REPORT DOCUMENTATION PAGE

AFRL-SR-BL-TR-01-

0633

1. AGENCY USE ONLY *(Leave blank)*	2. REPORT DATE	3. REPORT TYPE AND DATES
		FINAL REPORT SEPTEMBER 1999

4. TITLE AND SUBTITLE
A UNIVERSITY-INDUSTRY PARTNERSHIP FOR RESEARCH AND
TRANSITION OF GAMMA TITANIUM ALUMINIDES.

5. FUNDING NUMBERS
F49620-95-1-0359

6. AUTHOR(S)
TRESA M. POLLOCK
PAUL S. STEIF

7. PERFORMING ORGANIZATION NAME(S) AND ADDRESS(ES)
DEPARTMENT OF MATERIALS SCIENCE AND ENGINEERING
CARNEGIE MELLON UNIVERSITY
PITTSBURGH, PA 15213-3890

8. PERFORMING ORGANIZATION REPORT NUMBER

9. SPONSORING/MONITORING AGENCY NAME(S) AND ADDRESS(ES)
AIR FORCE OFFICE OF SCIENTIFIC RESEARCH
801 N. RANDOLPH STREET, ROOM 732
ARLINGTON, VA 22203

10. SPONSORING/MONITORING AGENCY REPORT NUMBER

11. SUPPLEMENTARY NOTES

20011220 114

12a. DISTRIBUTION AVAILABILITY STATEMENT

13. ABSTRACT *(Maximum 200 words)*

Cooling rates during casting have been shown to significantly influence yield strength, for the processing related research, tensile ductility and property variability in three different TiAl alloys. Variations in ductility are most sensitive to extrinsic defects such as porosity or the presence of large grains oriented for easy straining. A technique for quantitative analysis of surface connected porosity has been developed. Additionally, in the area of induction skull melting, fundamental information on the kinetics of aluminum vaporization has been established. Important differences in melt superheat and skull weight have been observed after casting in different melt atmospheres. A comprehensive study of the effect of preheat, stress-relief temperature, Al level and postweld heat treatment on the structure and properties of electron beam welds has also been completed. For deformation-related work, it has been found that the local plastic strain to failure increases significantly as the volume of plastically strained materials decreases based on the testing of notched and unnotched specimens. Moreover, plastic strain capabilities of even 0.8% have been found sufficient to blunt elastic stress concentrations up to $K_t = 2.3$. Strain mapping procedures developed in this program demonstrate that crack initiation is associated with groups of grains with intense plastic straining.

14. SUBJECT TERMS

15. NUMBER OF PAGES
64

16. PRICE CODE

17. SECURITY CLASSIFICATION OF REPORT	18. SECURITY CLASSIFICATION OF THIS PAGE	19. SECURITY CLASSIFICATION OF ABSTRACT	20. LIMITATION OF ABSTRACT
UNCLASSIFIED	UNCLASSIFIED	UNCLASSIFIED	

PRET:
A University-Industry Partnership for Research and Transition of Gamma Titanium Aluminides

Annual Report - September 1999

Principal Investigators:

Tresa M. Pollock (Department of Materials Science and Engineering)
Paul S. Steif (Department of Mechanical Engineering)

Department of Materials Science and Engineering
Carnegie Mellon University
Pittsburgh, PA 15213-3890

1. PRET Program Objectives

Among the intermetallics that have been investigated in recent years, gamma titanium aluminides are the most promising for their potential application in production aircraft engines. This research program focuses on fundamental issues of microstructure, processing and design that are directly relevant to the transitioning of gamma titanium aluminides into production aircraft components. The program participants include three universities (Carnegie Mellon University, Ohio State University, and the University of Michigan) and six companies (AlliedSignal, Allison Engine Company, General Electric Aircraft Engines, Howmet Corporation, Precision Castparts Corporation, and Rockwell International). The directions taken by this program are determined through a continuing dialogue between university and industry members of the research team. In general, the program focuses on areas where there is great uncertainty regarding the performance of gamma titanium aluminides in aircraft engines and where fundamental research at universities can play a significant role in reducing that uncertainty. The program consists of seven individual projects each carried out by a student and an advising faculty member. The projects are related to one another and fall into three broad areas: local deformation and microstructure, damage and fatigue, and processing.

1.1 Status of Effort

The induction skull melting (ISM) of Ti-48Al-2Cr-2Nb type alloys in an atmosphere of 500Torr Argon suppressed the vaporization of Al and maximized both the yield and melt bath temperature. On the other hand, significant Al vaporization occurred during the ISM of Ti-48Al-2Cr-2Nb type alloys at vacuum levels on the order of $3 - 6 \times 10^{-3}$Torr. The overall reaction rate for Al vaporization was $\sim 2.4 \times 10^{-4}$ g/(cm^2 s). Aluminum vaporization and the subsequent condensation of Al on the crucible walls during vacuum melts enhanced the formation of the skull leading to larger skulls, increased contact between the skull and the walls of the crucible leading to higher rates of heat extraction, and resulted in melt bath temperatures 20 to 30°C colder than melts conducted in atmospheres of 500Torr Argon. The difference in melt bath temperatures can be explained by the heat of vaporization.

To investigate the origins of property variability, several TiAl alloys investment cast with local solidification times varying between 24 and 235 s have been studied. Tensile ductility has been found to decrease and to become more variable as cooling rates during casting decrease. While slow cooling rates promote the retention of fully lamellar microstructures, recent annealing experiments on "48-2-2" type alloys show that increases in grain size, rather than higher fractions of lamellar structure, are detrimental to ductility. Weibull moduli obtained from statistical analyses of room temperature failure strengths are substantially higher than those typically encountered in ceramic materials, particularly in grain-refined and/or fast cooled materials. In addition, a link has been established between cooling rate during casting and the resulting texture for a series of binary alloys, and for samples from the baseline I (48-2-2) material, cooled at different rates.

Detailed SEM fractographic and AEM microstructure analysis of fractured tensile and fracture specimens was performed to develop correlations between the microstructure, mechanical properties, deformation mechanisms, and fracture behavior of electron beam welds in Ti-(46-48)Al-2Cr-2Nb in the postweld stress-relieved and heat-treated conditions. In these welds, mechanical properties and fracture paths were influenced primarily by the principal microstructural constituents, i.e., proportions of lamellar gamma/alpha-two constituent versus equiaxed gamma grains, with a greater proportion of lamellar constituent in the stress-relieved welds and at lower Al contents promoting translamellar fracture with some interlamellar splitting, and greater toughness. A higher proportion of equiaxed gamma grains with alpha-two located primarily at grain boundaries increased ductility, but reduced toughness due to transgranular, cleavage fracture.

The role of ductility in the design of gamma components with large stress concentrators has focused on notch strengthening effects in both near-gamma and lamellar TiAl alloys. Results have shown that notch strengthening (where monotonically loaded notched specimens exhibit notch root failure strains that are higher than failure strains seen in unnotched specimens) is exhibited by 48-2-2 and WMS alloys. It is thus likely a characteristic of TiAl alloys in general. The existence of notch strengthening can directly impact how TiAl components are designed and tested. Displacement mapping during in-situ tensile testing in a SEM of smaller notched and un-notched samples has revealed a correlation between microstructural features and localized strain; this correlation will be further analyzed using texture and orientation imaging microscopy analysis.

Finite element simulation of high speed, small particle impacts on NASA/GE cast-to-shape blade simulative specimens have been carried out. The extent of observed rear face cracking has been compared with FEA predictions linking the impact event to crack initiation. These comparisons have shown the usefulness of a crack initiation criterion combining plastic strain and tensile stress. Damage due to impacts on machined leading edge simulative specimens which have been developed in the PRET program have been characterized. These impacts are being carried out for a wider range of impact locations near the leading edge, providing a more stringent test of the crack initiation criterion. Thus far, the extent of cracking on the rear face of the impacted leading edge in these specimens shows good correlation with finite element simulations.

Results of elevated temperature, step-loading fatigue tests on impact damaged duplex 48-2-2 and near-lamellar WMS have revealed good agreement with a threshold-based approximation of fatigue strength. Further analysis has indicated the need to incorporate the effects of residual stress, small cracks and crack geometry into a threshold-based design approach.

Casting and Processing Defects and Impurities

.a Rishel
.. Cramb
.a Pollock
rnegie Mellon University
n Kelly
General Electric Aircraft Engines

2.1 Introduction

Gamma titanium aluminide alloys are currently being critically evaluated as alternative materials to nickel base superalloys for gas turbine, automotive and diesel applications. Gamma titanium aluminide ingots are produced by vacuum arc remelting, induction skull melting and to a lesser extent plasma arc melting processes. Gamma titanium aluminides are typically cast to near net shape in investment molds [Colvin et al., 1991, Larsen et al., 1992, Larsen et al., 1994, Wagner et al., 1995] or permanent molds [Jones et al., 1995, Jones and Eylon, 1995, Keller et al., 1997] following vacuum arc remelting or induction skull melting/remelting. In both processes, the control of alloy chemistry is a challenge due to the vaporization of aluminum and chromium or manganese, depending on the alloy composition. Yet, subsequent cast structure and properties are very sensitive to aluminum level [Austin and Kelly, 1993, Pollock and Steif, 1998, Raban et al., 1999]. Understanding the parameters which influence changes in melt chemistry during the melting of gamma titanium aluminides will enable the control of melt chemistry during the processing of these materials.

While cold crucible technologies are well suited to reducing melt contamination of reactive alloys such as gamma titanium aluminides, melting in a cold crucible can make it difficult to achieve the degree of melt superheat needed to fill thin section castings [Larsen et al., 1992]. Higher mold preheat temperatures and increased mold insulation are two means of minimizing the heat lost to the mold during filling, compensating in part for lower melt superheats. However, vacuum arc remelting experiments conducted in the first year of the program [Pollock and Steif, 1996, Pollock and Steif, 1997, Pollock and Steif, 1998, Rishel et al., 1997] demonstrated that there are limits to the degree of mold preheat and mold insulation which can be used without introducing negative effects. It was found that mold preheat temperatures on the order of 2200°F (1200°C) used in combination with mold insulation resulted in undesirably slow solidification and solid state cooling rates which resulted in the formation of large gamma grains. In addition, undesirably slow cooling rates increased the tendency for mold/metal reaction [Rishel et al., 1997, Pollock and Steif, 1998]. Large gamma grains and surface connected porosity have a detrimental effect on ductility [Pollock and Steif, 1998, Rishel et al, 1998, Raban et al., 1999]. Similar results would be expected for induction skull melted material cast under similar conditions. Given the above limits to mold preheat temperature and mold insulation, control of the cast structure in gamma titanium aluminides will also require an understanding of the thermal characteristics of the process and the factors which influence, and ultimately maximize, the degree of melt superheat in cold crucible technologies.

Thus, two key issues for the successful processing of gamma titanium aluminides are the control of melt chemistry and achieving optimal cooling rates during casting through the control of processing parameters such as melt superheat, mold preheat and mold insulation. The Carnegie Mellon University (CMU) induction skull melting (ISM) and casting facility acquired in the first year of the program, has uniquely equipped the Gamma Titanium Aluminide PRET program to study these and other issues for induction skull melted materials. One advantage of induction skull melting over vacuum arc melting is that small batches of material can be directly melted from elemental formulations and cast to near net shape, greatly reducing component cost.

2.2 Objectives and Approach

Our major objective for the past year has been to use the CMU induction skull melting and casting facility to study the important processing issues outlined above for induction skull melted gamma titanium aluminides. This has been a twofold objective, involving both an investigation of the effect of melt atmosphere on the induction skull melting of gamma titanium aluminides and an investigation of the effect of processing parameters on solidification rate, subsequent solid state cooling rates, and the resulting structure and properties of cast gamma titanium aluminides. A secondary objective has been to use the CMU ISM to produce alloys for other projects within the program.

To address the first component of our primary objective, we have continued our analysis of the effect of melt atmosphere on changes in aluminum level and the thermal response of the system during the induction skull melting of gamma titanium aluminides. The results are summarized in Sections 2.3. To address the second component of our primary objective, a significant effort has gone into the preparation of a series of cooling rate experiments to be conducted in the CMU ISM with instrumented investment molds. We will be conducting the actual experiments as this report goes to press. The experimental outline and our progress to date are summarized in Section 2.4. Finally, we have taken advantage of the fact that the water cooled crucible in the induction skull melting unit is essentially a water cooled mold and have used the unit to conduct solidification experiments in the crucible to directly measure thermal cooling profiles as the melt solidifies in the crucible. We have melted a series of binary Ti-Al alloys ranging from 45 to 52 at.% Al. These alloys have been used to study the development of as cast texture (Section 4) and are presently being used to characterize the high temperature portion of the Ti-Al binary phase diagram using differential thermal analysis.

2.3 Induction Skull Remelting of Gamma Titanium Aluminides

In the third year of the program we began a study of the effect of aluminum vaporization on the induction skull melting of gamma titanium aluminides. This work was performed in response to earlier questions and concerns about the control of aluminum level and the degree of melt superheat posed by both General Electric Aircraft Engines and Howmet Corporation. Tilt pour experiments were conducted with Ti-48.9Al-2Cr-2Nb alloys to investigate changes in aluminide melt chemistry during induction skull melting in both vacuum and Argon atmospheres. Experiments were conducted at vacuum levels on the

order of 5×10^{-3} Torr (5 microns) and in approximately 500 Torr of Argon. The Ti-48.9Al-2Cr-2Nb melts were also used to study the effect of the volatilization of aluminum on the thermal response of the induction skull melting process, which was characterized by the size of the skull, the rate at which heat was removed from the crucible, and the temperature of the melt bath.

This year we continued our analysis of the effect of melt atmosphere on changes in aluminum level and the thermal response of the system during the induction skull melting of gamma titanium aluminides. A video system and dedicated data acquisition system were added to the ISM so that melts could be monitored and recorded. This year we also analyzed the geometry of skull cross-sections to assess the amount of solid formed and we measured changes in aluminum level through skull cross-sections. A series of in-crucible solidification experiments were conducted with Ti-47.7Al-2Cr-2Nb to measure the melt bath temperatures earlier in the process in both vacuum and Argon atmospheres. A series of tilt pour experiments were conducted with Ti-6Al-4V to better understand the effect of volatilization on the process. In addition, we attempted to reduce the heat extracted from the crucible through the use of alumina disks placed in the bottom of the crucible during induction skull melts. A summary of all of the results to date along with a discussion of the effect of the volatilization of aluminum on the induction skull melting of gamma titanium aluminides is presented in the sections that follow.

2.3.1 Experimental Approach

Melting experiments were conducted in the Carnegie Mellon University vacuum induction skull melting and casting facility. Details about the induction skull melter and melting procedures have been reported elsewhere [Pollock and Steif, 1996, Pollock and Steif, 1998, Rishel et al., 1999].

Four different heats of pre-alloyed ingot of Ti-48Al-2Cr-2Nb type materials were used (Table 2.1). Heat 1 was supplied by General Electric Aircraft Engines, Heats 2 and 4 were purchased from the Flowserve Corporation and Heat 3 was supplied by Rockwell International. Heats 1 and 2 were closely matched in composition. Heat 3 was slightly lower in Al and Heat 4 was slightly higher in Al. Cylindrical ingots, 3.4" dia. x 4.5" high, were cut and machined to size for tilt pour experiments. Cylindrical ingots, 3.2" dia. x 4.5" high, were electric discharge machined to size for in-crucible solidification experiments. Three inch diameter Ti-6Al-4V ingots were supplied by Timet Corporation. This material is designated as Heat 5 and a typical chemistry is shown in Table 2.2. The Ti-6Al-4V ingots were machined to 6" lengths for tilt pour experiments. Charge ingot weights ranged from 2805 to 2850g for the Ti-48.9Al-2Cr-2Nb and Ti-49.6Al-2Cr-2Nb tilt pour experiments, ~2400g for in-situ solidification experiments and 3065g for Ti-6Al-4V tilt pour experiments.

Three series of tilt pour experiments were conducted with Ti-48.9Al-2Cr-2Nb alloys: Series I - Heat 1 in vacuum; Series II - Heat 2 in vacuum; and Series III - Heat 2 in Argon.

Table 2.1. Ti-48Al-2Cr-2Nb Type Alloy Ingot Chemistries for Series I, II, III, IV and VI Experiments (atomic percents)

Heat	Al	Cr	Nb	Fe	Si	C	O	N	H
1	48.89	1.94	1.94	0.01	<0.01	0.0193	0.1393	0.0074	0.0191
2	48.91	1.98	1.96	0.04	0.03	0.0321	0.1589	0.0132	0.1032
3	47.67	1.98	1.95	0.06		0.0140	0.1915	0.0055	0.0821
4	49.60	2.15	2.01	0.04	0.07	0.0450	0.1539	0.0123	0.0343

Table 2.2. Ti-6Al-4V Ingot Chemistries for Series V Experiments (atomic percents)

Heat	Al	V	Ni	Fe	Si	O	N	H	Cl
5	10.38	3.63	0.02	0.17	<0.05	0.4206	0.0228	0.0317	<0.01

Nominal hold times were 3, 6 and 9 minutes for vacuum melts and 3, 6 and 8 minutes for Argon melts. Two in-crucible solidification experiments were conducted: Series IV - Heat 3 in vacuum and Heat 3 in Argon. Nominal hold times were 2.5 minutes. Two tilt pour experiments were conducted with Ti-6Al-4V: Series V - Heat 5 in vacuum and Heat 5 in Argon. Nominal hold times were 4 minutes for both melts. Finally, four 6 minute tilt pour experiments were conducted with Ti-49.6Al-2Cr-2Nb: Series VI - Heat 4 in vacuum, in Argon, vacuum with an alumina disk in the bottom of the crucible and Argon with an alumina disk in the bottom of the crucible. Alumina disks for Series VI experiments were made from extruded high purity alumina, 99.8 wt. % Al_2O_3. The disks, which were nominally 3.5" in diameter and 0.16" thick, were placed in the center of the bottom of the crucible before charging the Ti-49.6Al-2Cr-2Nb ingots.

The melt power schedule for each experiment was as follows: 35kW, 80kW and 120kW each for 1 minute, 150kW until the ingots were fully molten, and 150kW for the duration of the experiment. Melt hold times were defined as the time at maximum power beyond the time it was visually determined that the charge was fully molten. At the end of the hold, the melt was tilt poured into a dried 7.6cm (3") diameter, room temperature, low carbon steel mold or solidified in the crucible.

Samples for chemical analysis were taken at mid-radius, 2.5 cm from the bottom of the tilt poured and cast ingots from Series I, II, III and V experiments. Chemical analyses were performed by Howmet Corporation's Operhall Research Center; X-ray fluorescence was used for Ti, Al, Cr, Nb and Leco Combustion for O, N and H. Radial sections through the skulls were taken for structural and chemical analyses. Samples were etched with a modification of Kroll's reagent: 100ml H_2O, 35ml H_2O_2, 5ml HNO_3 and 10ml HF. Relative chemistry changes were analyzed by Energy Dispersive Spectroscopy in a Philips XL-30 scanning electron microscope. Spot measurements were taken in the plane of section from the bottom to the top of the skull at a location approximately 2cm from the side of the skull. The conditions were as follows: 600 grit sample finish, 20kV, 150X, 0.9nA beam current, 300s acquisition time. Scrapings removed from deposits on the wall of the

crucible were analyzed by semi-quantitative X-ray fluorescence and/or by glow discharge mass spectroscopy.

Crucible water and melt bath temperatures were monitored during Series II through VI[†]. Thermocouples were positioned in the crucible inlet and outlet water lines approximately 0.5m (20") from the crucible. Melt bath temperatures were measured by the direct immersion of thermocouples at different times during the melt hold. As a means of validating melt bath temperature measurements, two different thermocouples were used in Series II, III and IV experiments: one W/W-26%Re (type G) thermocouple with 0.25mm diameter wire and one Pt-30%Rh/Pt-6%Rh (type B) thermocouple with 0.2mm diameter wire. Given the good agreement between the two thermocouple types and the reliability of the W/W-26%Re thermocouple, only type G thermocouples were used for the Ti-6Al-4V melts. One to three immersions were made per melt, each lasting approximately 5 seconds. Depending on the hold time, immersions were made approximately 120, 300, and 450 seconds after the material was fully molten (or ~ 360, 540, and 690 seconds into the experiment) for the tilt pour experiments. For in-crucible solidification experiments, immersions were made 30 to 40 and 110 seconds after the material was fully molten. Water temperatures, melt bath temperatures and vacuum levels were recorded on a data acquisition system.

2.3.2 Results and Analysis

Experimental conditions, skull fractions (skull weight / charge weight) and a measure of skull height are presented in Table 2.3. Final melt chemistries obtained from ingots cast after tilt pouring are shown in Tables 2.4 and 2.5. Melt observations, changes in melt chemistry and process monitoring results are presented and discussed in the sections that follow.

2.3.2.1 Melt Observations

During heat up, radial liquation cracks developed on the top surface of the charged ingot. Melting later initiated somewhere between the mid-height and bottom of the ingot during the hold at 120kW. Once the molten material reached a high enough temperature, it flowed around the unmelted portion of the ingot in contact with the bottom of the crucible, and solidified on the crucible wall forming the sides of the skull. Finally, the top portion of the ingot was incorporated into the bath and melted. Melt baths tended to oscillate about the vertical axis of the crucible, and if the oscillation of the bath brought the melt in contact with the copper walls and/or skull, additional skull formed. Images captured from video tapes of Ti-48Al-2Cr-2Nb and Ti-6Al-4V induction skull melts in both Argon and vacuum atmospheres are shown in Figure 2.1. As shown in the figure, the melt baths were significantly levitated and the shape of the baths approximated paraboloids of revolution.

[†] The new PC data acquisition system was used for Series V and VI experiments.

2 - 5

Table 2.3. Experimental Conditions and Skull Parameters

Melt #	Material	Atmosphere, Torr	Charge Weight, gms	Time to Melting, sec	Hold Time at 150kW, sec	Fraction Skull[1]	Average Finger Height, cm
	Series I	Vacuum					
1	Heat 1	5.4×10^{-3}	2810	223	180	0.33	5.15
2	Heat 1	4.0×10^{-3}	2803	245	360	0.34	5.73
3	Heat 1	3.4×10^{-3}	2827	255	513	0.38	6.67
	Series II	Vacuum					
4	Heat 2	4.3×10^{-3}	2845	244	180	0.35	6.58
5	Heat 2	4.7×10^{-3}	2805	249	366	0.39	7.70
6	Heat 2	4.1×10^{-3}	2834	245	540	0.37	6.65
	Series III	Argon					
7	Heat 2	~500	2839	248	160	0.22	3.33
8	Heat 2	~500	2841	232	360	0.22	3.21
9	Heat 2	~500	2848	230	480	0.26	3.40
	Series IV						
10	Heat 3	5.5×10^{-3}	2405	256	156	---	---
11	Heat 3	Argon (~500)	2413	262	150	---	---
	Series V						
12	Ti-6Al-4V	4.7×10^{-3}	3065	287	240	0.19	5.35
13	Ti-6Al-4V	Argon (~500)	3065	280	240	0.15	4.88
	Series VI						
14	Heat 4	4.7×10^{-3}	2837	231	360	0.32	6.11
15	Heat 4	Argon (~500)	2850	255	360	0.24	3.64
16	Heat 4	4.7×10^{-3} + disk[2]	2841	259	360	0.23[3]	6.54
17	Heat 4	500Torr Ar + disk[2]	2814	225	360	0.12[3]	3.76

[1] Skull fraction is the ratio of the skull weight to the charge weight.

[2] Melts conducted with an alumina disk in the bottom of the crucible.

[3] The alumina disk was removed from the skull before determining the skull fraction.

Melt atmosphere strongly influenced the appearance of the aluminide melt bath surfaces. In Argon, melt baths reached a near steady state profile soon after melting and remained relatively constant for the duration of the melt. Melts conducted in Argon were brighter in appearance than those conducted in vacuum and the crucible wall remained clean during melting. Vacuum melts resembled Argon melts for approximately the first 90 seconds. Then, while the levitated vacuum melts still resembled paraboloids of revolution, the maximum profile height began to decrease, profiles broadened as contact with the side walls increased and the bath color darkened. This difference in the shape of the melt baths is illustrated graphically in Figures 2.1c and 2.1d, respectively. Additionally, aluminum vaporized from the melt bath in vacuum and condensed on the crucible wall. As the condensate thickness increased, some spalling occurred.

Table 2.4. Final As-Cast Ingot Chemistries for Series I, II and III Experiments

Melt #	Al[1] at. % (wt. %)	Cr at. %	Nb at. %	Fe at. %	Si at. %	C at. %	O[2] at. % (wt. %)	N at. %	H at. %
	Series I								
1	48.16 (33.54)	1.94	1.94	0.01	0.01	0.0161	0.1140 (0.0471)	0.0066	--------
2	47.52 (32.98)	1.93	1.95	0.01	0.01	0.0194	0.1023 (0.0421)	0.0086	0.0154
3	47.17 (32.67)	1.92	1.95	0.01	0.01	0.0195	0.0891 (0.0366)	0.0064	0.0232
	Series II								
4	48.13 (33.52)	1.98	1.96	0.04	0.03	0.0258	0.1337 (0.0552)	0.0136	0.0115
5	47.98 (33.38)	1.98	1.97	0.04	0.03	0.0355	0.1079 (0.0445)	0.0141	0.0077
6	47.65 (33.10)	1.98	1.96	0.04	0.04	0.0323	0.0983 (0.0405)	0.0147	0.0116
	Series III								
7	48.53 (33.90)	2.00	1.96	0.04	0.03	0.0418	0.1608 (0.0666)	0.0143	0.0498
8	48.62 (33.98)	1.99	1.96	0.04	0.04	0.0386	0.1585 (0.0657)	0.0132	0.0383
9	49.02 (34.34)	2.00	1.96	-----	0.03	0.0321	0.1656 (0.0688)	0.0149	0.0382

[1] Initial aluminum levels were 34.21 wt. % for melts 1 thru 3 and 34.27 wt. % for melts 4 thru 9.
[2] Initial oxygen levels were 0.0577 wt. % for melts 1 thru 3 and 0.0660 wt. % for melts 4 thru 9.

Table 2.5. Final As-Cast Ingot Chemistries for Series V Experiments

Melt #	Al[1] at. % (wt. %)	V at. %	Ni at. %	Fe at. %	Si at. %	O[1] at. % (wt. %)	N at. %	H at. %	Cl at. %
	Series V								
12	10.56 (6.25)	3.52	0.02	0.11	<0.05	0.5374 (0.1886)	0.0260	0.0633	<0.01
13	10.75 (6.38)	3.48	0.02	0.12	<0.05	0.5291 (0.1862)	0.0260	0.2481	<0.01

[1] Initial aluminum and oxygen levels were 6.13 and 0.1473 wt. % , respectively.
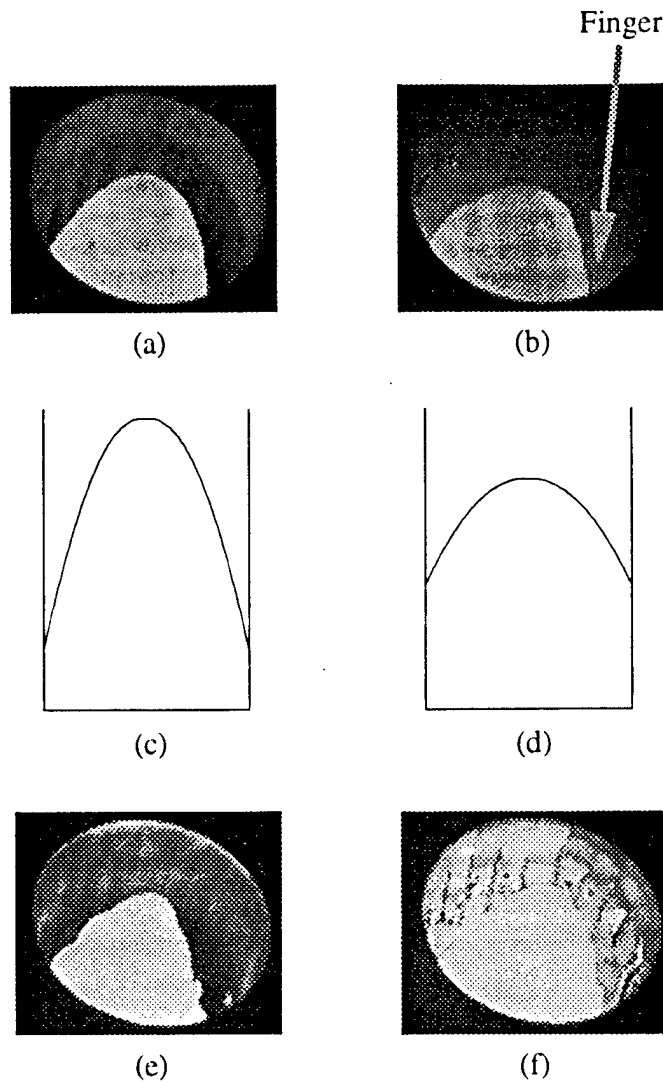
Figure 2.1   Photographs of a Ti-48Al-2Cr-2Nb melts in a) Argon and b) vacuum after 6 minute holds. Graphical melt profiles of Ti-48Al-2Cr-2Nb in c) Argon and d) vacuum. Ti-6Al-4V melts in e) Argon and f) vacuum after 4 minute holds.

Scrapings of the condensate which deposited on the crucible wall during Ti-48.9Al-2Cr-2Nb vacuum melts were analyzed by semi-quantitative X-ray fluorescence and found to be greater than 90 wt. % Al with up to 10 wt. % Cr in the Series·I experiments. The thickness of the condensate increased nearly linearly with hold time to a thickness of 7mm after the 9 minute holds.

Melt atmosphere did not strongly affect the Ti-6Al-4V melt bath profiles for the hold times investigated. Melt baths in both atmospheres reached near paraboloidal profiles soon after melting and remained relatively constant for the duration of the melts.   A thin layer

consisting of approximately 20 wt. % Ti and 80 wt. % Al was vapor deposited on the crucible wall; however the deposition rate was less than that of Al from the aluminide melts, averaging approximately 0.044 mm/min versus 0.076 mm/min.

Photographs of skulls from Ti-48.9Al-2Cr-2Nb melts in both Argon and vacuum atmospheres are shown in Figure 2.2. Skulls consisted of a portion of unmelted ingot on the bottom (Fig. 2.2c), material which solidified on the vertical copper cooling segments resembling "fingers", and a pour extension formed during tilt pouring. A deposit of Al was often visible on the outside surfaces of fingers on vacuum skulls. Table 2.3 and Figure 2.3 report the skull size as fraction skull for each experiment. The Ti-48.9Al-2Cr-2Nb aluminide skulls obtained from vacuum melts were approximately 1.5 times larger than those obtained from Argon melts. In addition, skull fractions were similar for a given atmosphere, tending to increase in size with melt hold time. Skull fractions for the Ti-6Al-4V melts did not exhibit the same sensitivity to melt atmosphere for the melt hold times investigated. The skull fraction for the melt conducted in vacuum was approximately 10% larger than that of the melt conducted in Argon.
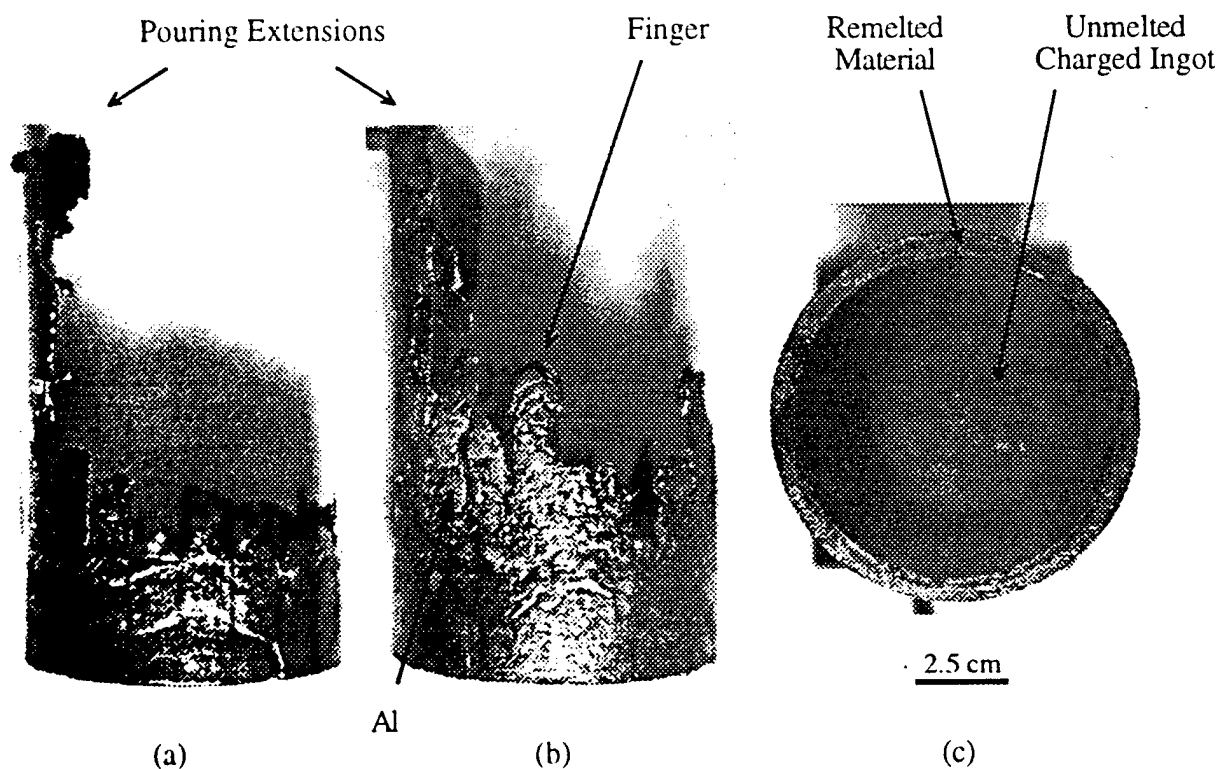
Figure 2.2 Side views of Ti-48.9Al-2Cr-2Nb skulls formed after 3 minute molten holds in a) Argon and b) vacuum; c) a bottom view of a skull formed after a 3 minute molten hold in vacuum showing unmelted charge. Note the pouring extensions indicated in a) and b) formed as the metal solidified on the crucible wall during tilt pouring. Also note that material solidified on the copper cooling segments resembled fingers and that Al was often visible on the outside surfaces of fingers on vacuum skulls.
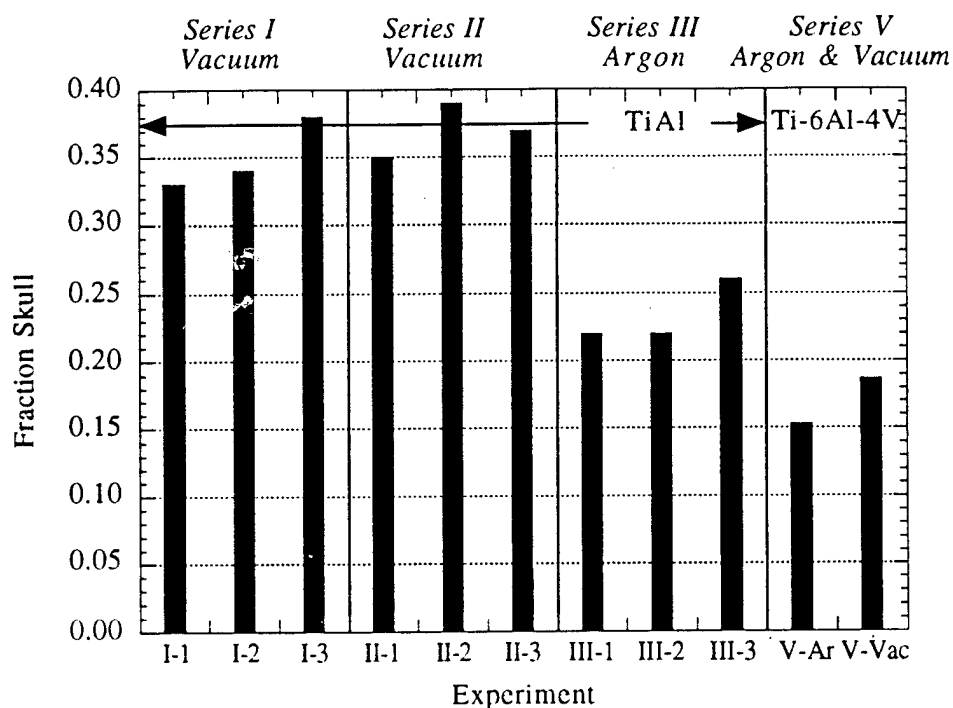
Figure 2.3   Skull fractions for Ti-48.9Al-2Cr-2Nb Series I, II and III melts and Ti-6Al-4V Series V melts.

As shown in Figure 2.2, skulls from Ti-48.9Al-2Cr-2Nb vacuum melts exhibited increased contact with the side wall of the crucible as compared with those from Argon melts. This is consistent with melt observations and with the significantly higher skull fractions for vacuum melts. In addition, the thickness of the fingers were slightly greater in the skulls obtained from vacuum melts. Ti-6Al-4V skull fractions were less than those obtained from aluminide melts conducted in Argon, finger heights were greater but the thickness of the skull and fingers were less.

The nominal contact area between the skull and side walls of the crucible was estimated by measuring individual finger heights from a given skull and then averaging the finger heights. Pour extensions were not included in this measure. Two different estimates of the nominal contact area between the skull and the crucible were then determined: 1) the total contact area which included the unmelted bottom of the charged ingot (Fig. 2.2c) and 2) the remelted contact area which excluded the unmelted bottom of the charged ingot. Skull fractions are plotted in Figure 2.4 as a function of the estimated remelted contact area between the skull and the crucible for Series I, II, III, V and VI melts. For the aluminides, skull size increased with increasing contact area; the trend is primarily due to the different melt atmospheres. Skull fractions for the Ti-6Al-4V Argon and vacuum melt results were similar, but differed from those of the aluminide melts in either Argon or vacuum atmospheres, indicating that material properties are also important. Similar trends were observed when skull fractions were plotted against finger heights and estimates of the total contact area between the skull and the crucible.
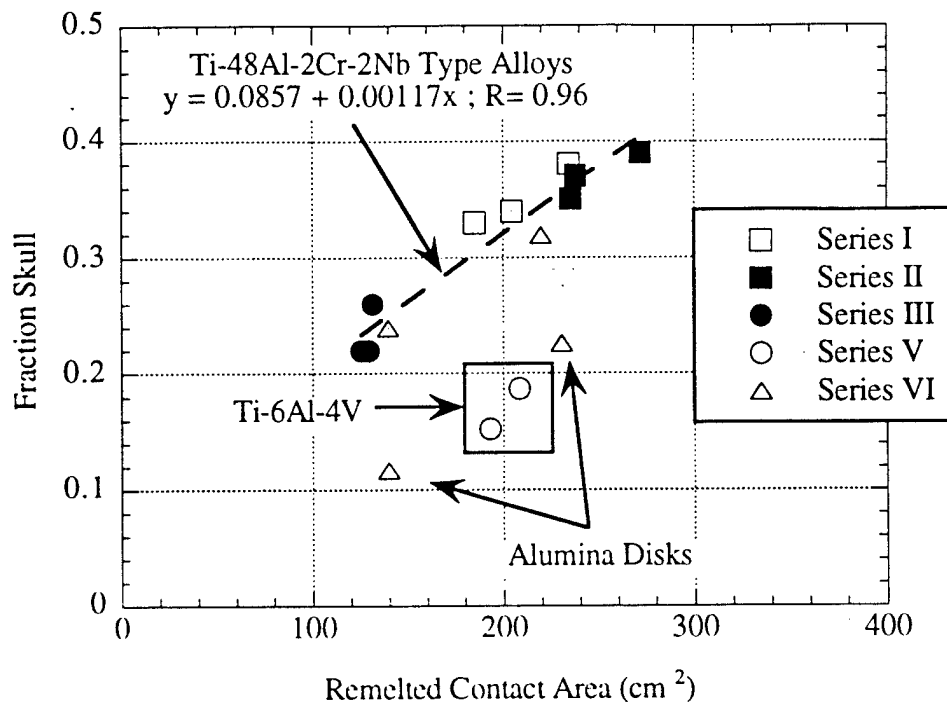
Figure 2.4 Skull fraction versus estimated remelted contact area for Series I, II, III, V and VI melts.

As shown in Table 2.3 and Figure 2.4, a similar dependence on melt atmosphere was observed for melts conducted with alumina disks in the base of the crucible (Series VI melts 16 and 17); however, skull fractions were shifted to lower values. Finger heights and thicknesses were similar to melts conducted without alumina disks. However, the base of the aluminide portion of the skull was thinner due to the underlying alumina disk. As a result, the combined cross-section of the aluminide skull and the underlying alumina disk was similar to that of skulls formed without alumina disks. Disks remained intact and there was little evidence of reaction between the melt and the alumina disk.

Photographs of macroetched radial sections from Ti-48.9Al-2Cr-2Nb skulls from melt 9 (8 minutes in Argon) and melt 6 (9 minutes in vacuum) are shown in Figures 2.5a and 2.5b, respectively. A photograph of a macroetched radial section taken from a Ti-47.7Al-2Cr-2Nb ingot solidified in the crucible after in-situ melting and freezing in vacuum (melt 10) is shown in Figure 2.5c. Several different regions are visible in the macrostructures of Figure 2.5: a region of unmelted charge material consistent with Fig. 2.2c (A), material which flowed and re-solidified around the charge (B), material which is believed to have deposited or solidified during the melt hold (C), and material which solidified during or after pouring for the tilt pour experiments (D) or after powering down for the in-situ solidification experiments (E). Note that the base of the vacuum skull (Fig. 2.5b) is thicker than that of the Argon skull (Fig. 2.5a) and this increased thickness is primarily due to the increased thickness of region C. Also, note that the skull region in Figure 2.5c is clearly different from the columnar structure formed as the melt solidified at the end of the
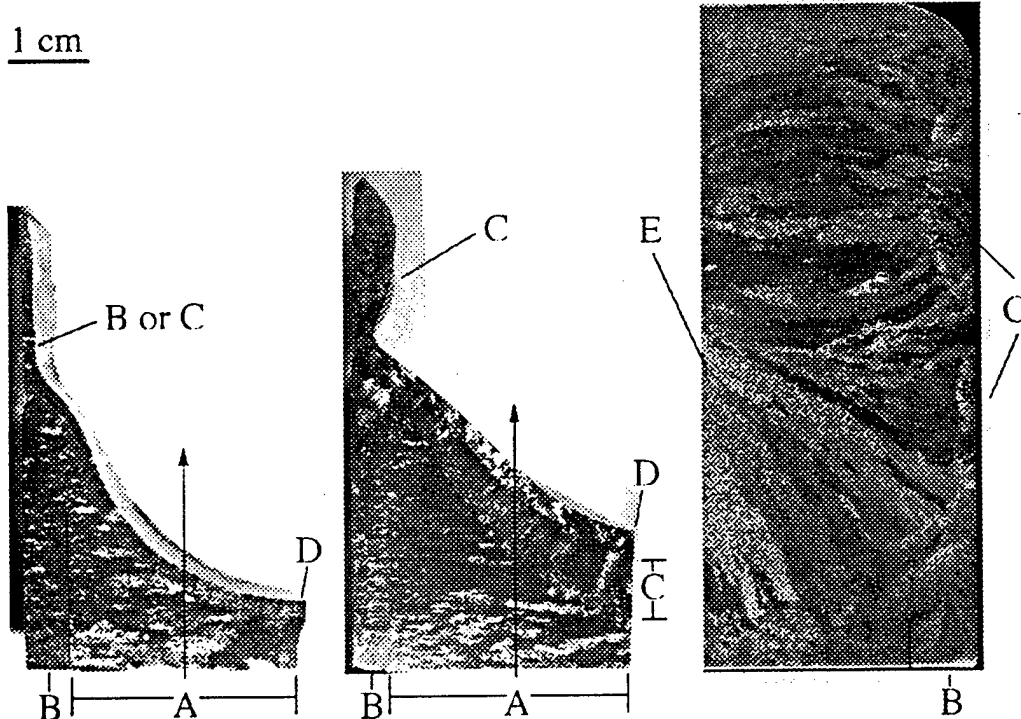
Figure 2.5   Macroetched radial sections through Ti-48.9Al-2Cr-2Nb skulls from a) an 8 minute molten hold in Argon (melt 9) and b) a 9 minute molten hold in vacuum (melt 6). Macroetched radial section through an ingot solidified in the crucible after a 2.5 minute molten hold in vacuum melt 10 (c).   Arrows indicate the location of EDS measurements. [A: unmelted ingot; B: flowed and re-solidified around the charge; C: formed during the molten hold: D: solidified during or after tilt pouring and E: solidified in the crucible after powering down]

in-situ experiment and that some melt back of the skull occurred as the liquid above it solidified in the crucible.

2.3.2.2 Changes in Chemistry

Changes in melt chemistry can be monitored by sampling the liquid bath either by removing small samples at specified times in the hold or by removing the entire liquid bath and repeating the experiment for a series of hold times. The latter approach was used in this work because it is difficult to remove small samples from the liquid bath in a vacuum unit and also because it was not necessary to correct for changes in the mass of the system as samples were removed.   Final melt chemistries analyzed using this technique are summarized in Tables 2.4 and 2.5.

A significant and repeatable aluminum loss was observed in vacuum gamma titanium aluminide melts. The Al loss increased with melt hold time to between 1.2 to 1.5 wt. % for the 9 minute holds in vacuum. The average rate of Al loss was approximately 2.7g/min, or ~24g after 9 minutes. A minimal Al loss was detected in Argon, on average 0.55g/min,

d this loss was almost within the reported three sigma repeatability of this measurement
nique for Al, +/-0.21 wt. %. It is also worth noting that the Al loss could be closely
ximated from estimates of the amount of Al which condensed on the walls of the
nle above the skull, indicating that the most of the lost Al condensed on the walls of
crucible.

nucible scrapings indicated that Cr was lost in the Series I vacuum melts. However, the
loss was also on the order of the reported three sigma repeatability of this measurement
technique for Cr, +/-0.045 wt. %. Nb levels remained unchanged in each set of
experiments.

Figure 2.6 shows a significant and repeatable oxygen loss for the Ti-48.9Al-2Cr-2Nb
Series I and II melts in vacuum. The oxygen loss increased with melt hold time to between
210 and 255 wppm for the 9 minute holds in vacuum. The rate of oxygen loss was
approximately 0.048g/min. No oxygen loss was observed for the Argon melts. As shown
in Figure 2.7, there was a direct correlation between aluminum and oxygen losses in both
vacuum and Argon. Note that Nitrogen levels remained essentially the same for a given
heat of material (Tables 2.1 and 2.4).

Aluminum vaporization from the aluminide melts followed first order reaction kinetics.
The rate expression is shown in Equation 2.1; where m_i is the mass of aluminum, A is the
bath surface area and V is the liquid volume. Rewriting Equation 2.1 in terms of weight
percents and integrating yields the relationship shown in Equation 2.2; where $wt.\%_o$ and
$wt.\%_i$ refer to the weight percent of Al in the starting material and that measured in the ingot
poured after time, t. The slope of a plot of $\{ln[wt.\%_i] - ln[wt.\%_o]\}$ versus time then
provides a measure of $-k(A/V)$, which can be solved for the overall reaction rate constant
for Al vaporization, k [cm/s], if the melt bath surface to volume ratio [1/cm] is known.
The corresponding flux of Al from the melt [g/(cm² s)] can be determined from Equation
2.3 using the measured rate constant and the Al composition of the liquid, c_m. In this
analysis, c_m is the initial Al composition in the liquid with units of g/cc which is calculated
according to $X_m n_{tot} MW \rho_{melt} / W_{tot}$; where X_m is the initial Al mole fraction, n_{tot} is the total
number of moles of liquid, MW is the molecular weight of Al, ρ_{melt} is the density of the
melt bath and W_{tot} is the weight of the liquid. Alternatively, the flux of Al can be calculated
directly from the measured rate of Al loss using the average grams of Al lost, the average
melt hold time and an estimate of the surface area during the melt hold.

$$\frac{1}{A}\frac{dm_i}{dt} = \frac{-km_i}{V} \tag{2.1}$$

$$ln[wt.\%_i] - ln[wt.\%_o] = \frac{-kA}{V}t \tag{2.2}$$
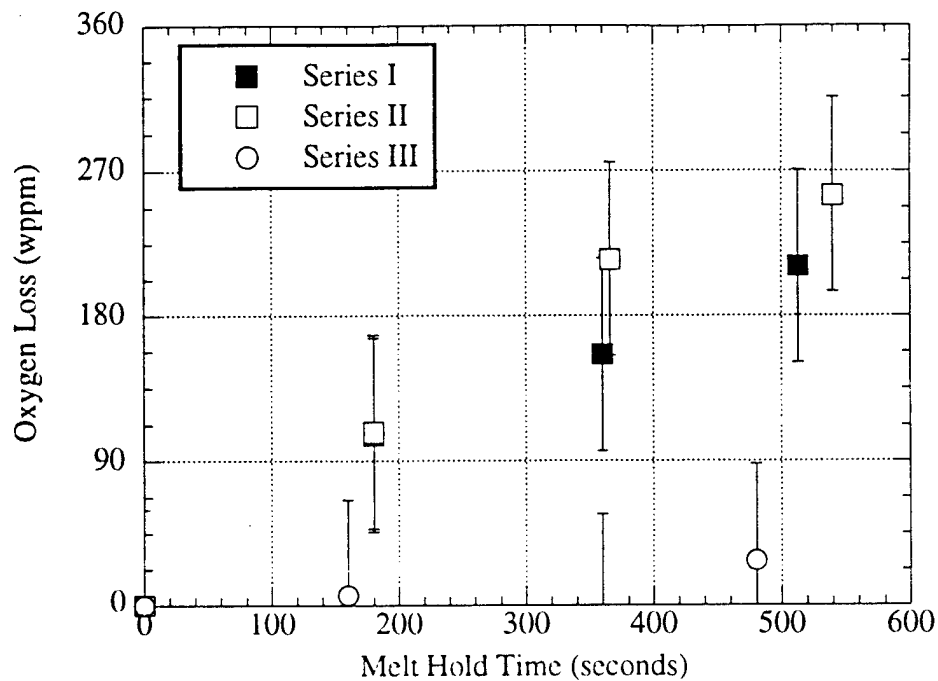
$$\Phi = k\,c_m \tag{2.3}$$

Figure 2.6   Oxygen loss as a function of melt hold time for Series I, II and III Ti-48.9Al-2Cr-2Nb aluminide melts. Bars indicate the stated three sigma accuracy of the measurement technique, +/- 60wppm.
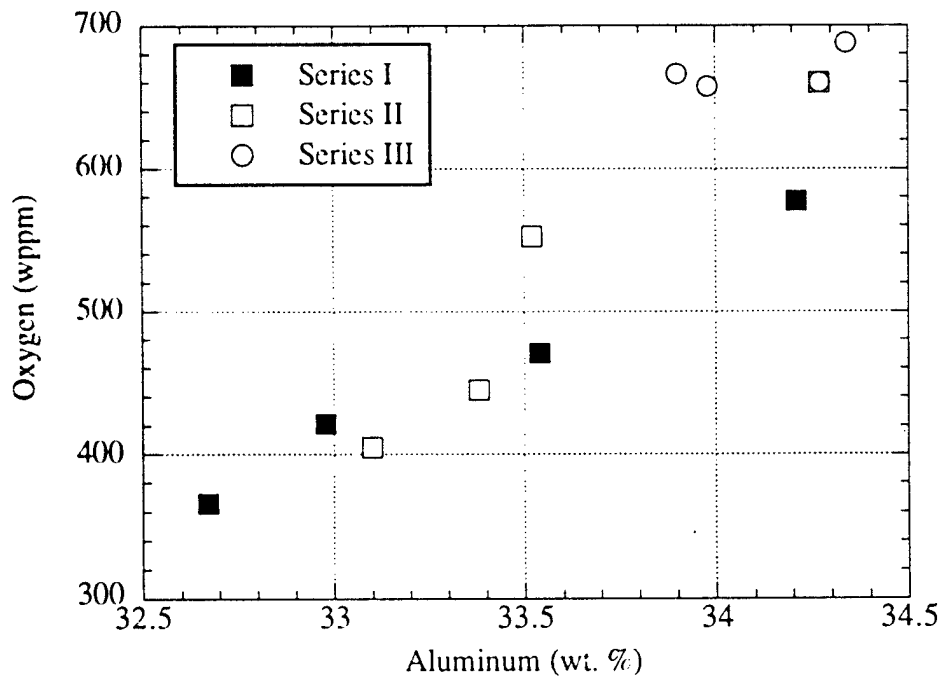

Figure 2.7   Oxygen content as a function of Aluminum level for Series I, II and III Ti-48.9Al-2Cr-2Nb aluminide melts.

Given the good agreement between Ti-48.9Al-2Cr-2Nb Series I and II vaporization experiments, the results were treated together in the manner described above to determine a value for the overall reaction rate constant for the loss of Al. The slope of a plot of $\{\ln[\text{wt.}\%_i] - \ln[\text{wt.}\%_o]\}$ versus time for the combined data was $-8.24\times10^{-5}\text{s}^{-1}$ and the regression coefficient of the curve fit was 0.9.

As mentioned in Section 2.3.2.1, aluminide melt profiles changed with time during vacuum melts, so the surface area was changing with time as well. An average surface area of the melt bath was determined by averaging an estimate of the melt bath surface area in Argon with the estimated average surface areas of the two series of vacuum melts. To facilitate an estimate of the melt bath surface area, the melt profile was described mathematically by a paraboloid of revolution using the charge volume, estimated bath height and average finger height (excluding the pour extension) as geometric boundary conditions. Surface area was then estimated from the surface integral of this function. Liquid volume was determined by subtracting the estimated volume of the skull from the total volume. For an estimated average melt bath surface to volume ratio of approximately 0.4, the reaction rate constant was $\sim 2\times10^{-4}$cm/s. The corresponding overall reaction rate for Al vaporization from gamma titanium aluminide melts was $\sim 2.4\times10^{-4}$g/(cm^{2}s).

For the Ti-48.9Al-2Cr-2Nb Series III experiments conducted in 500Torr of Argon, the slope corresponding to Eqn. 2.2 was $-9.9\times10^{-6}\text{s}^{-1}$. Using a surface to volume ratio of approximately 0.44, the overall reaction rate constant for Al vaporization was $\sim 2.3\times10^{-5}$cm/s and the corresponding overall reaction rate was $\sim 3\times10^{-5}$g/(cm^2 s). The kinetics of Al loss in 500Torr of Argon were an order of magnitude slower than those obtained in vacuum.

Oxygen also appeared to follow first order reaction kinetics in aluminide melts conducted in vacuum. The slope corresponding to Eqn. 2.2 was $-9.3\times10^{-4}\text{s}^{-1}$, the reaction rate constant was 2.3×10^{-3}cm/s and the overall reaction rate was approximately 5.5×10^{-6}g/(cm^{2}s).

Changes in Al level were measured through radial cross-sections of skulls by EDS spot measurements taken in the direction of the arrows shown in Figures 2.5a and 2.5b. Results for measurements taken through the skulls from melts 4 and 6 (Series II) in vacuum and melts 7 and 9 (Series III) in Argon are shown in Figure 2.8. Aluminum measurements through the skulls obtained from vacuum melts show that the Al level was essentially equal to that of the original ingot (34.27 wt. % Al) for approximately the first 1.5 cm from the bottom of the skull and then decreased gradually through the skull (region C of Fig. 2.5b) until it reached a composition similar to that of the final composition of the liquid measured in the poured ingots (region D of Fig. 2.5b). With one exception, the Al level remained essentially constant through the Argon skulls.
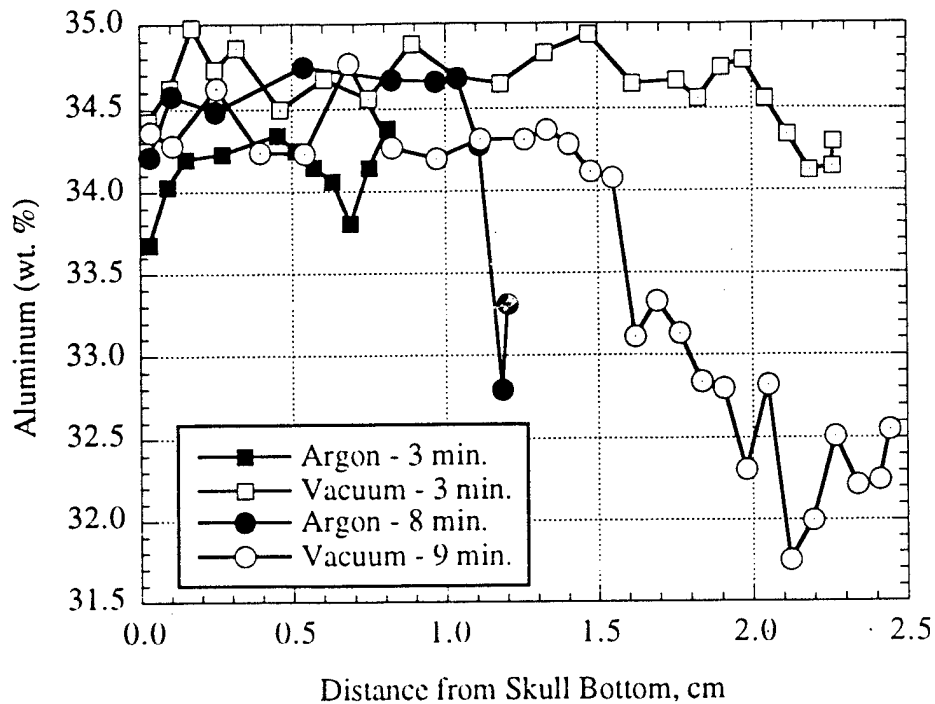
Figure 2.8   Aluminum level versus distance from the bottom of the skull for Ti-48.9Al-2Cr-2Nb Series II melts 4 and 6 in vacuum and Series III melts 7 and 9 in Argon. Measurements were taken through radial sections at a location 2 cm from the side of the skull as indicated in Figures 2.5a and 2.5b.

2.3.2.3 Process Monitoring

Crucible inlet and outlet water temperatures, melt bath temperatures and vacuum levels were monitored for melts 4 through 17 of Table 2.3[*]. The rate at which heat was removed from the crucible was estimated using the measured crucible water temperatures and Equation 2.4, where Q is the rate of heat transferred, ρ is the density of water, c_p is the specific heat of water, G is the volumetric flow rate and T is the temperature.

$$Q = \rho\, G\, c_p\, (T_{outlet} - T_{inlet})$$ (2.4)

Figure 2.9 shows the heat transfer rate to the melt furnace, as determined from the power schedule assuming no losses, and the rate of heat removed from the crucible as estimated

---

[*] Crucible water and melt bath temperatures for Series VI experiments were recorded on a different data acquisition system. Unfortunately, ground loops encountered during the Series VI experiments interfered with the crucible water temperature measurements preventing the accurate determination of the rate of heat transfer from the crucible. Melt bath temperature readings were not greatly affected. Ground loop issues on the new system have since been resolved.
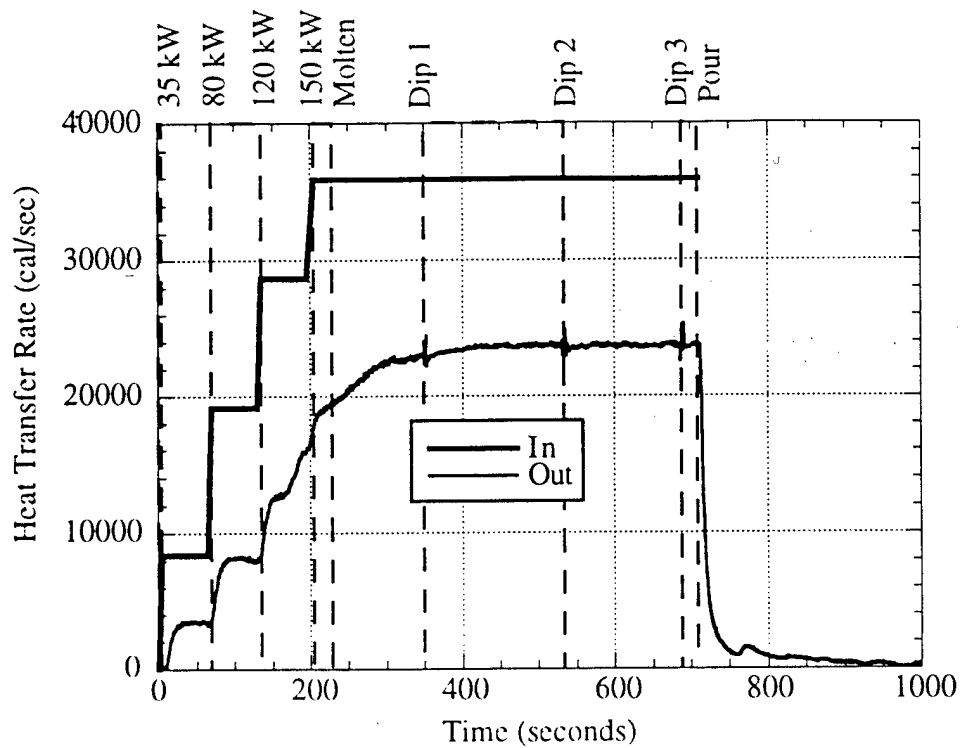
Figure 2.9   Heat transfer rates to the melt furnace (In) and from the crucible (Out) versus total elapsed time for Series III melt 9 (8 minutes in Argon).
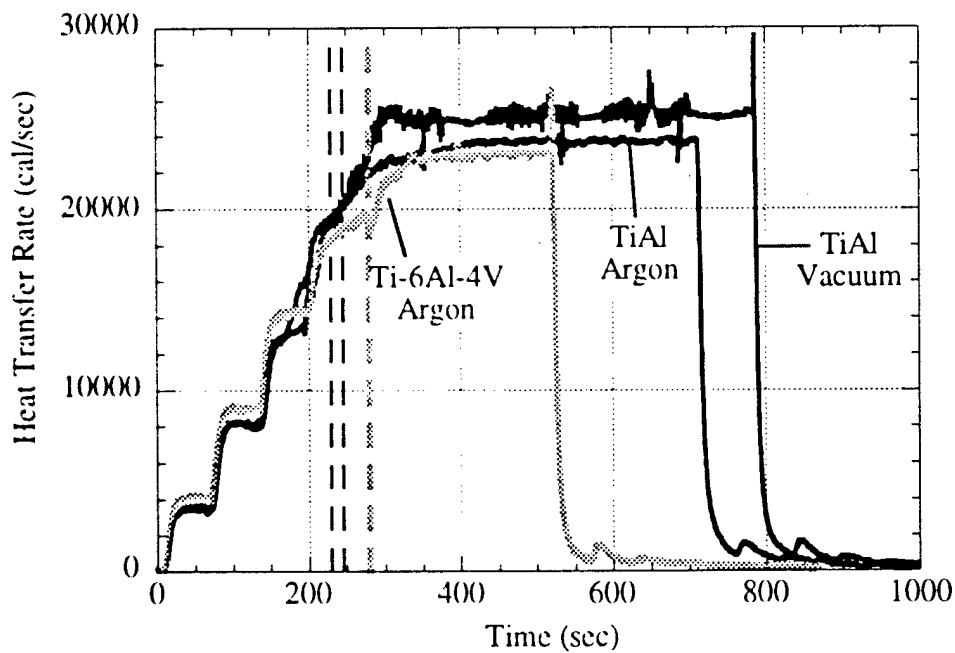

Figure 2.10 Measured heat transfer rates from the crucible versus total elapsed time for Series II melt 6 (9 minutes in Vacuum), Series III melt 9 (8 minutes in Argon) and Ti-6Al-4V Series V melt 13 (4 minutes in Argon). Vertical lines indicate the time at which the charge was fully molten.

from Equation 2.4, for the duration of melt 9. As shown in Figure 2.9, the heat transfer rate from the crucible is less than the heat transfer rate to the unit. The difference between the two is attributed to transmission losses of the field to the melt bath and to radiative losses from the melt bath surface. Cooling of the crucible outlet water temperature before it reaches the thermocouple may also introduce a loss, but temperature sensitive labels placed directly on the crucible have shown that this difference is small.

As shown in Figures 2.9, the induction skull melting process achieved, or was approaching, a steady thermal state at a given power level, except during the actual transformation from solid to liquid. Another important observation was that the process is highly repeatable for a given power schedule, charge geometry and charge weight. For example, Table 2.3 shows that the time it took to completely melt Ti-48Al-2Cr-2Nb type charges ranging in size from 2805 to 2850g varied from 223 to 255 seconds. This is a strikingly reproducible observation, especially given the fact that the decision as to whether or not the charge was fully molten was a visual one. Melt times for the smaller 2400g charges (melts 10 and 11) were similar (260 seconds), but greater than those for the larger charges. Despite the significantly higher melting temperature of Ti-6Al-4V, melt times for Ti-6Al-4V charges were again similar ranging from 280-290 seconds. Average melting rates for all of the experiments were 9.2 to 12.6g/s (0.55 - 0.75kg/min).

For the Ti-48.9Al-2Cr-2Nb experiments, heat transfer profiles obtained from crucible water temperature measurements were highly repeatable for a given melt atmosphere, with curves lying on top of one another for each atmosphere [Rishel et al., 1999]. However, as shown in Figure 2.10, 60 to 90 seconds after melting occurred, the heat transfer rate was 1500 to 2000 cal/sec higher for Series II melts conducted in vacuum than it was for Series III melts conducted in Argon, indicating that more heat was removed from the vacuum melts. The onset of increased heat extraction in vacuum coincided with the change in bath shape and the build up of the Al condensate on the crucible wall. Prior to this, the curves were nearly identical for the two atmospheres. Heat transfer profiles for the Ti-6Al-4V melts conducted in Argon and vacuum were nearly identical and similar to those from the Series III Ti-48.9Al-2Cr-2Nb melts conducted in Argon (Figure 2.10). This observation is consistent with the similar appearance of the melt baths and similar skull sizes.

Vacuum levels recorded during the Ti-48.9Al-2Cr-2Nb melts were also very repeatable for a given charge weight. Vacuum levels increased with time prior to melting, peaked just after the bath was fully molten, and then gradually decreased with time. Peak vacuum levels ranged from 0.02 to 0.04Torr Hg. The vacuum level for the Ti-6Al-4V melt in vacuum peaked at 0.14Torr Hg.

Given the dynamic nature of the melt baths, the highly curved surfaces, the inability to power down without significant freezing and a different emissivity in vacuum and Argon, optical pyrometry was not a viable option for bath temperature measurements in this work. Instead, melt bath temperatures were measured by the direct immersion of thermocouples at full power. Temperature measurements in the Ti-48.9Al-2Cr-2Nb Series III melts conducted in Argon were always higher than those measured in the corresponding Series II

s conducted in vacuum. Good agreement was obtained between type B and type G
mocouples.

re was also good agreement between immersions made at a particular time into the melt
a given melt atmosphere. For example, the 3 sets of temperature data recorded in the
8.9Al-2Cr-2Nb Series II melts 4, 5, and 6, just after the melts were molten for 120
nds, were in good agreement with one another. The data was then averaged to obtain
more statistically significant measure of the melt bath temperature at this time into a
vacuum melt. Similarly, the 2 sets of data recorded for melts 5 and 6 just after the melts
were molten for 300 seconds were in good agreement with one another and were averaged
together. Finally the single set of data recorded from melt 6 just after the melt was molten
for 450 seconds was averaged. A similar analysis of the data was performed for the Ti-
48.9Al-2Cr-2Nb Series III experiments conducted in Argon. Average values are presented
in Table 2.6 for the different types of thermocouples in each of the two atmospheres
studied.

Temperature measurements taken 30 to 40 seconds after melting in the in-situ Ti-47.7Al-
2Cr-2Nb solidification experiments yielded a bath temperature of approximately 1545°C for
both vacuum and Argon atmospheres (in-situ melts 10 and 11). The observed similarity in
melt bath temperatures is consistent with similar melt bath appearances and heat flux
curves.

While thermal similarity exists between the two melt atmospheres in the early stages of
aluminide melt holds, the difference between the two atmospheres is very obvious after 2
minutes into the holds (Series II and III). As shown in Table 2.6, melt bath temperatures
measured in vacuum (Series II) were 21 to 27°C colder than those measured in Argon
(Series III). Using liquidus temperatures for the binary TiAl system from the work of
McCullough [McCullough et al, 1989], superheats are estimated to be 15°C for the vacuum
melts and 35°C for the Argon melts 2 minutes into the melt hold. At a later time, 7.5
minutes into the melt hold, melt superheats had increased to approximately 20 and 50°C for
vacuum and Argon melts, respectively. Lower measured melt bath temperatures in vacuum
are consistent with the increased removal of heat from vacuum melts shown in Figure 2.10,
increased skull size (Fig. 2.3), increased contact with the crucible wall (Fig. 2.4) and an
endothermic heat of vaporization for Al [JANAF, 1986].

Average melt bath temperatures for the Ti-6Al-4V melts in Argon and vacuum melts
recorded 120 seconds after the melts were fully molten were nearly identical, 1687 and
1686.3°C, respectively. Again, the observed similarity in melt bath temperatures is
consistent with similar melt bath appearances, skull sizes and heat flux curves. Reported
values for the liquidus temperature of Ti-6Al-4V range from approximately 1650 to 1690°C
[Engineering Alloy Digest, Handbook of Ternary Phase Diagrams], indicating anywhere
from 0 and 37°C superheat.

Thermal measurements from Series VI experiments exhibited similar trends between
vacuum and Argon atmospheres. The presence of the alumina disks in the bottom of the
crucible had little effect on the thermal results.

Table 2.6 Average melt bath temperature measurements in Argon and vacuum
atmospheres for Series II, III and IV experiments

Approximate Time into Melt Hold[1], sec	Argon		Vacuum		Averages of Type G[2] and B[3]		Argon vs Vacuum
	Type G (°C)	Type B (°C)	Type G (°C)	Type B (°C)	Argon (°C)	Vacuum (°C)	Difference (°C)
Series IV							
30 - 40	1545	1546	1547	1542	1546	1544	none
110	1538	-----	1546	1542	1538	1544	none
Series I and II							
120	1532	1536	1511	1514	1534	1513	21
300	1536	1545	1515	1521	1541	1518	23
450	1546	1550	1519	1523	1548	1521	27

[1]Time after the melt was fully molten. [2]W/W-26%Re thermocouple type.
[3]Pt-30%Rh/Pt-6%Rh thermocouple type.

2.3.2.4 Effect of the Heat of Vaporization on the Melt Bath Temperature of Gamma Titanium Aluminide Melts

The control volume shown in Figure 2.11 was defined to calculate the effect of the heat of vaporization on the melt bath temperature during induction skull melting. Initially the control volume is entirely liquid. At the end of the hold the control volume is assumed to consist of liquid plus new solid which formed during the melt hold. Due to intense stirring, the liquid is assumed to be of uniform temperature at any given time. An analysis of the change in temperature due to the volatilization of Al for Ti-48.9Al-2Cr-2Nb Series II melt 6 follows.
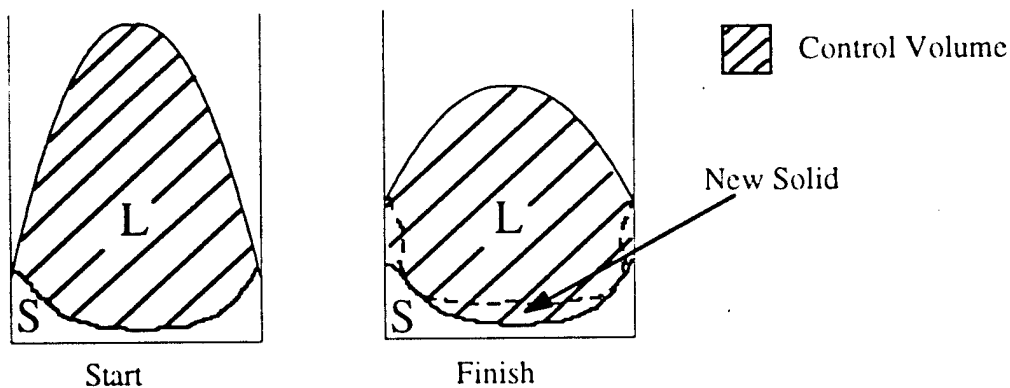

Figure 2.11 Schematic illustrating the control volume at the start and finish of an induction skull melt in vacuum.

Based on temperature measurements in Argon atmospheres, the initial melt bath temperature is assumed to be 1550°C. The amount of new solid formed was determined from the difference in the weight of the skull obtained from melt 9 and the skull obtained from melt 6. This difference was approximately 380 grams. The Al loss was 21 grams. Enthalpy data for this analysis was obtained from Howmet Corporation. The heat balance is summarized in Table 2.7.

Table 2.7 Heat Balance for the Effect of the Heat of Vaporization on the Melt Bath Temperature During Induction Skull Melting

Initial Temperature, °C	1550
Initial Heat Content, cal	**745010**
Molar Heat of Vaporization, cal/mole	-71969
Moles of Aluminum Lost	0.778
Heat of Vaporization, cal	**-56015**
Heat of Fusion, cal/g	84.76
New Solid Formed, g	380
Heat of Solidification, cal	**32210**
Final Heat Content, cal	**721206**

$$H_{final} = f_{solid} \, H_{solid} + f_{liquid} \, H_{liquid} \qquad\qquad (2.6)$$

The final heat content listed in Table 2.7 corresponds to a liquid temperature of 1512°C. However, the final enthalpy is the average enthalpy for the control volume which now consists of liquid and solid. It can be calculated using Equation 2.6, where H refers to enthalpy and f refers to the fraction of liquid or solid as designated. If it is assumed that the temperature of the new solid is close to the liquidus temperature. The enthalpy of the liquid can then be determined using the known fraction solid and fraction liquid of the control volume. The result is an enthalpy which corresponds to a temperature of 1517°C. The temperature drop due to vaporization is then 33°C which is close to the temperature drop reported in Section 2.3.2.3. If the heat of solidification and fraction solid are ignored are ignored, the analysis yields a temperature drop of 70°C.

2.3.3 Discussion

The results presented herein demonstrate that induction skull melting can be a highly reproducible process for a fixed charge material, ingot charge geometry, power schedule and melt atmosphere. Moreover, induction skull melting is a steady state, or near steady state, thermal process.

The plateaus in the heat transfer profiles shown in Figures 2.9 and 2.10 illustrate that for a given power level, induction skull melting reaches a steady, or near steady, thermal state in the absence or presence of volatilization. A steady state thermal profile implies a steady state skull profile. When the power level is changed, a new steady state is reached and the thermal profile and skull profile adjust themselves to the new power level and associated heat flux. However, the specific thermal response after melting is influenced by the vaporization of volatile constituents and the subsequent vapor deposition of the volatile constituents on the cold wall of the crucible. The result is that while the system reaches a steady, or near steady, thermal state in each case, the final steady state heat transfer rates are different.

For instance, the induction skull melting of gamma titanium aluminides in ~500Torr of Argon prevented the evaporation of aluminum; consequently, the melt profiles changed little with time. Increases in skull size with melt hold time are primarily due to random contact with the copper wall resulting from melt oscillations. The random character of the growth of the skull in the absence of volatilization explains the increased time it takes to reach a steady thermal state after the charge is molten (Figure 2.10).

On the other hand, the induction skull melting of gamma titanium aluminides in vacuum levels less than the equilibrium vapor pressure of aluminum, approximately 100 microns at 1520°C, resulted in a significant aluminum loss from the melt bath and the vapor deposition of aluminum on the cold walls of the copper crucible. The vaporization of aluminum led to changes in the chemistry of the melt bath, and hence its liquidus temperature. In addition, this loss in aluminum influenced the thermal response of the system not only through its heat of vaporization and changing liquidus temperature, but also through the vapor deposited layer which formed on the crucible wall.

The melt appearance and the thermal response of the gamma titanium aluminide melts conducted in vacuum were similar to those conducted in Argon for approximately the first 90 seconds, or until the thickness of the vapor deposited layer exceeded 0.11mm. Although tilt pour experiments were not conducted in the early stages of the melts, finger heights on ingots solidified in the crucible after 2.5 minute holds in Argon and vacuum were similar. This would suggest that the skull sizes were similar at this time. Once vaporization was well underway (~120 seconds into the melt hold), the degree of superheat in the bath changed both due to the endothermic heat of vaporization and the increase in liquidus temperature with Al loss. The estimated heat of vaporization of Al from titanium aluminides is approximately 72 kcal/mole [JANAF, 1986]. As shown in Section 2.3.2.4, this corresponds to a temperature drop of approximately 30°C which is similar to the measured temperature difference between melts conducted in vacuum and Argon.

While the endothermic heat of vaporization accounts for the temperature difference between melts conducted in vacuum and Argon, it does not explain the increased heat transfer rate from the crucible in vacuum. As shown in Section 2.3.2.4, the change in heat content due to the vaporization of Al is small, approximately -56kcal, and would account for only 100cal/sec when averaged over the duration of the melt, 540s. But more importantly, the

vaporization reaction is an endothermic reaction, so the heat of vaporization should decrease the heat content of the bath. Thus, for the same contact area, less heat should be removed from the crucible in vacuum, not more.

The increased heat transfer rate in vacuum can be explained by increased contact between the skull and the crucible in vacuum (Figure 2.4). The condensed layer of aluminum on the crucible wall enabled the skull to form to higher finger heights by reducing the gap between the bath and the wall/condensate. This increased the chance that a melt oscillation would contact the wall/condensate where it would solidify and form part of the skull. The melt bath is also likely to wet a vapor deposited layer of aluminum more readily than a bare copper surface and the heat of condensation may play a role in the local wetting phenomenon. As contact between the skull and the crucible increased, more heat was extracted from the melt. Moreover, as shown in Figure 2.10, the steady state heat transfer rate was reached more quickly in vacuum melts where condensate assisted skull formation occurred. Condensate assisted skull formation in vacuum is supported by the observation of finger growth during the molten hold and subsequent meniscus lines on the "fingers" of skulls (Fig. 2.2b).

An increase in the heat extracted from the crucible should result in an increase in the thickness of the skull. Such an increase was observed in cross-sections of skulls taken from vacuum melts, for example Region C in Figure 2.5b. But, as shown in the macrographs of Figure 2.5, the complex geometry of the skull would require computational modeling to predict the exact change in the thickness of the skull.

Ti-6Al-4V melts conducted in vacuum and Argon were similar for the melt hold times investigated, but skull fractions and finger heights were slightly, but noticeably, larger after melting in vacuum. A vapor deposited layer of Al and Ti formed during the vacuum melt, but the rate of formation was approximately 0.6 times that observed for the aluminum deposition during the aluminide melts. At the end of the melt holds the scale thickness was approximately 0.18mm. This thickness is just above the 0.11mm at which condensate assisted skull formation was observed in the Ti-48.9Al-2Cr-2Nb melts conducted in vacuum atmospheres. The scale thickness and slightly larger size of the vacuum skull suggest that condensate assisted skull formation was just becoming a factor. It is likely that if longer melt hold times were investigated, the vapor deposited layer of Al and Ti would build up to a critical thickness and condensate assisted skull formation would become significant.

The placement of an alumina disk in the bottom of the crucible (Series VI melts) did not significantly alter the heat transfer rate from the crucible. This observation indicates that most of the heat is lost through the portion of the skull which formed from the melted charge, and the sides of the skull account for most of this material. Presumably, material which solidified on the crucible wall would have better contact with the crucible than the machined bottom of the charged ingot and this would result in a higher heat transfer rate and a higher heat transfer coefficient. The difference in heat transfer coefficients between the bottom and sides of the skull is large enough that the presence of the alumina disk, which introduces another interface, has little impact on the rate of heat transfer. This

explains the excellent correlation between the finger heights and the size of the skull, as well as the apparent similarities in skull profiles with and without the alumina disks.

In the CMU ISM, the bottom of the induction coil is at the same elevation as the bottom of the crucible. Consequently, the major benefit of the alumina disk was that it elevated the charge so that the bottom of the charge melted, since it was now within the induction coil. This resulted in a significant reduction in skull size (Table 2.3 and Figure 2.4) and a marked increase in yield.

As mentioned in Section 2.3.2.1, disks remained intact, but skull removal was difficult since the disks prevented shrinkage of the material which formed between the sides of the alumina disks and the crucible walls. Disks designed to fit in the bottom of the crucible should minimize, or eliminate, the amount of material formed between the sides of the alumina disk and the crucible wall, making it easier to remove the skull. Finally, there was little evidence of reaction between the melt and the alumina disk, but oxygen analyses have not yet been conducted to verify this finding.

Changes in chemistry within the skull and the liquid may arise due to partitioning and/or solute washing as the liquid solidifies to form additional skull (i.e. at the solid/liquid interface). Changes in the liquid chemistry will also occur if volatile species are lost in vacuum (i.e. at the liquid/gas interface). It is not clear whether the change in composition in the vacuum melts shown in Figure 2.8 is due to partitioning and solute washing or if this represents the changing composition of the liquid.

Macrosegregation bands in the skull may result from changes in the power level. For example, powering down may result in a solute depleted band such as the one shown in the 8 minute Argon profile in Figure 2.8.

Tracking changes in chemistry is a complex endeavor. However, if it can be assumed that most of the skull is near the original composition of the charge (i.e. region C in Figure 2.6 is small), the diffusion boundary layer of the volatile species in the liquid is small and the liquid bath is of nearly uniform composition due to intense mixing, then the composition of the liquid bath closely approximates the average melt chemistry. Changes in melt chemistry can then be monitored, as in this work, by sampling the liquid bath and repeating the experiments for a series of hold times to determine the overall vaporization kinetics.

While the vaporization of Al from the melt involves a number of steps; the overall reaction rate is determined by the rate limiting step or steps. Following the approach used by Ward [Ward, 1963], the rate limiting steps for the vaporization of Al in the ISM process may include 1) transport to the non-turbulent boundary layer, 2) transport of Al in the melt bath across the non-turbulent boundary layer to the free surface of the melt, 3) desorption of Al from the melt free surface to the gas phase, 4) transport of gaseous Al across the gas boundary layer, 5) transport in the gas phase, and 6) condensation. Due to the intense stirring action of the melt bath in ISM, transport of Al in the bulk liquid (step 1) is not rate limiting. In vacuum, low pressures and continuous pumping enhance the transport of Al through the gaseous phase and away from the melt bath so that steps 4 and 5 are not rate

Finally, the cold wall of the copper crucible, as well as the chamber, provide ...ant surface area for condensation, so that condensation (step 6) is not rate ...ing. The rate limiting steps are the transport of Al across the non-turbulent ...ry layer to the free surface of the melt (step 2) and desorption of Al from the free ... of the melt (step 3).

... measured rate of Al vaporization from gamma titanium aluminide melts in vacuum was compared with the maximum rate of free vaporization for Al (step 3), W_{Al}, calculated using the Langmuir-Knudsen expression [Pehlke, 1979] shown in Equation 2.5; where α is the condensation coefficient, p_{Al}° is the equilibrium vapor pressure of pure Al, γ_{Al} is the activity coefficient of Al, M is the molecular weight of Al, R is the gas constant and T is the temperature. The nearly linear increase in condensate thickness indicated that condensation was not rate limiting; therefore, the condensation coefficient was assumed to be unity. An equilibrium vapor pressure for pure Al of 9.4×10^{-4} atm was calculated using thermodynamic data for the vaporization of liquid Al [15] at the average bath temperature of 1520°C. Finally, an activity coefficient of 0.28 was determined from the activity calculated by the Thermocalc software package and the mole fraction. The maximum rate of free vaporization was estimated to be 6×10^{-4} g/(cm^2 s), three times greater than the measured rate of 2.4×10^{-4} g/(cm^2 s) obtained using Equation 2.3; where c_m is the initial melt composition. This is very good agreement for this type of analysis.

$$W_{Al} = \alpha \, p_{Al}^{\circ} \, \gamma_{Al} \sqrt{\frac{M}{2\pi RT}} \qquad (2.5)$$

Note that the reaction rate constant reported here can be applied to other ISM units to predict Al loss from gamma titanium aluminide melts, if the rate controlling steps are the same and the surface to volume ratio has been determined. As shown in Equation 2.2, Al loss is proportional to the surface to volume ratio, consequently larger diameter crucibles which have smaller surface to volume ratios should exhibit smaller Al losses.

Oxygen also appeared to follow first order reaction kinetics for O(l) → O(g). This was a surprising finding. The direct vaporization of oxygen from an aluminide melt with ~34 wt. % Al is unlikely, rather first order reaction kinetics and the relation between Al and O levels shown in Figure 2.7 suggest that the solubility of oxygen is decreasing with decreasing Al content. Another possible explanation is that Al in the Al rich boundary layer is deoxidizing the melt bath and forming a volatile constituent such as AlO(g). While the mechanism is not understood at this time, the finding that oxygen is lost in vacuum is important since lower oxygen levels negatively impact creep properties.

This is the first detailed study of the thermal and chemical response of induction skull melting of gamma titanium aluminides. Important differences between melting in vacuum levels less than the vapor pressure of Al and in Argon levels well above the vapor pressure of Al have been noted. Melting in Argon has certain advantages over melting in vacuum. The observed increase in superheat in Argon melts could be significant when attempting to fill thin wall castings. Lower skull weights after Argon melting translate to increased yield.

The crucible remains cleaner, slowing the build up of the skull. Melt chemistry does not change. However, when melting and pouring in Argon, there is the risk of gas entrainment in the pour stream. Melting in vacuum offers the possibility of outgassing during melting and eliminates the risk of atmosphere entrainment during pouring. While changes in chemistry occur in vacuum, especially Al and O levels, the changes are repeatable and consequently should be predictable.

Although melts conducted in Argon exhibited higher melt superheats than those conducted in vacuum, superheats reported here for ISM are still significantly less than those obtained in conventional VIM which utilizes refractory crucibles. The values reported here are also less than the 50°C superheat measured in the pour stream by Clites and Beall during tilt pouring of vacuum induction slag melted titanium from a 5" diameter x 8" high, 32 segment crucible [Clites and Beall, 1975]. The additional superheat reported by Clites and Beall is undoubtedly due to the insulating effect of the slag layer between the skull and the crucible wall.

One of the process goals for the induction skull melting of gamma titanium aluminides is to melt elemental formulations and directly pour into near net shape castings. Packing a crucible with chunks and pellets of elemental formulations will result in increased contact with the crucible wall, so the time before complete melting will increase. The size of the skull may also increase if constituents adhere to the crucible walls. Clearly, the charge geometry used in this work is an ideal geometry, not the preferred geometry; nevertheless, it has permitted the detailed, systematic study of the induction skull melting of titanium aluminides reported here.

2.3.4 Conclusions

1. Induction skull melting is a steady state, or near steady state, thermal process. The thermal response of the system is highly repeatable for a fixed charge material, charge geometry and power cycle. The highly repeatable nature of ISM has important implications for process control.
2. Significant aluminum vaporization occurs during the induction skull melting of gamma titanium aluminides at vacuum levels on the order of 3 - 6 x 10^{-3} Torr. The overall reaction rate for aluminum vaporization is ~2.4x10^{-4}g/(cm^2 s).
3. The condensation of aluminum on the crucible walls enhances the formation of the skull and influences the thermal response of the system. Condensate assisted skull formation results in increased contact with the walls of the crucible which leads to larger skulls, less yield and higher rates of heat extraction from the crucible. Melts conducted in atmospheres less than the vapor pressure of aluminum are colder than melts conducted in atmospheres which prevent vaporization. Differences in temperature of approximately 20 to 30°C were observed in our system for hold times of 2 and 7.5 minutes, respectively.

2.4 Future Work

A significant effort has gone into the preparation of a series of cooling rate experiments to be conducted in the CMU ISM with instrumented investment plate molds. Twelve plate molds like the one shown in Figure 2.12 were purchased from Howmet Corporation. Plate dimensions are 4" high x 6" long x 0.5" thick. Provisions were made for two thermocouples in the casting cavity and 3 thermocouples at various depths of the investment wall in six of the molds. Mold insulation will be used to minimize gradients in the molds. Planned experiments are listed in Table 2.8 along with estimates of the local solidification time and the time above the eutectoid temperature. The cooling rate experiments have been designed to attempt to duplicate results obtained from previous experiments conducted at Howmet Corporation using both their on-site vacuum arc remelting and induction skull melting facilities (Section 5). In addition, we will attempt to fill in gaps in the cooling rate data that we have attained to date for plate thicknesses of 0.5", and the resulting material will be used by the Microstructure Origins of Damage and Property Variability Project to complete our property/cooling rate data base. As shown in Table 2.8, we will also produce a series of slowly cooled binary Ti-Al alloys ranging from 45 to 52 at.% Al for use by the Microstructure Evolution and Characterization Project for an evaluation of the effect of cooling rate on as cast texture. We have conducted the first fully instrumented Ti-48Al-2Cr-2Nb, 315°C mold preheat, experiment and will be completing this casting work in the near future.

Finally we will characterize the high temperature portion of the Ti-Al binary phase diagram using differential thermal analysis on Ti-45Al, Ti-48Al and Ti-52Al binary alloys. The results will be compared with cooling curves obtained during in-crucible solidification experiments conducted in the CMU ISM. Samples taken from the Series II vaporization experiments will also be analyzed using differential thermal analysis.

Table 2.8   Planned Cooling Rate Experiments for the CMU ISM along with Estimates of the Local Solidification Time and the Time Spent above the Eutectoid Temperature

Alloy	Aim Preheat °C	$t_{f, surface}$ ** sec	$t_{f, center}$ sec	$t_{eut, surface}$ sec	$t_{eut, center}$ sec	Thermo-couples	HIP
48-2-2*	315	11	26	54	39	surface	yes
48-2-2	540	24	37	603	592	surface	yes
48-2-2	650	30	42	878	869	surface	yes
48-2-2	315††	11	26	54	39	yes	no
48-2-2	540	24	37	603	592	yes	no
48-2-2	650	30	42	878	869	yes	no
48-2-2	900	84	101	1259	1248	yes	no
Ti-45Al	900	84	101	1259	1248	surface	no
Ti-48Al	900	84	101	1259	1248	surface	no
Ti-52Al	900	84	101	1259	1248	surface	no

*   Ti-48Al-2Cr-2Nb   ** t_f refers to the local solidification time
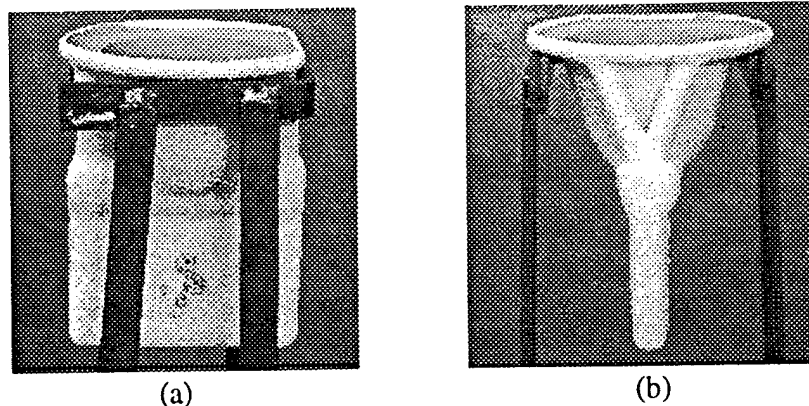† t_{eut} refers to the time spent above the eutectoid temperature
††   Completed

Figure 2.12 Photographs of an investment plate mold for use in the CMU cooling rate experiments a) long side view showing holes for thermocouples and b) short side view.

Acknowledgments

References

Austin, C. M. and Kelly, T. J., Structural Intermetallics, eds. R. Darolia, J. J. Lewandowski, C. T. Liu, P. L. Martin, D. B. Miracle and M. V. Nathal, TMS, Warrendale, PA, p. 143, (1993).

Claxton, R. J., Journal of Metals, Feb., pp. 14-16, (1975).

Clites, P. G. and Beall, R. A., Proc. of the Fifth International Symposium on Electroslag and Other Special Melting Technologies, eds. G. K. Bhat and A. Simkovich, Carnegie Mellon Institute, Pittsburgh, pp. 477-496, (1975).

Colvin, G., Ciani, M., Kleyn, B. and VanderLeest, L., Microstructure/Property Relationships in Titanium Aluminides and Alloys, eds. Young-Won Kim and Rodney Boyer, TMS, Warrendale, PA, p. 361-369 (1991).

Engineering Alloy Digest, Upper Montclair, N.J. Ti-60.

Gabathuler, J. P., and Weinberg, F., *Metallurgical Transactions B*, Vol. 14B, pp. 733-741, (1983).

Gabathuler, J. P., Weinberg, F., Modeling of Casting and Welding Processes II, eds. J. A. Dantzig and J. T. Berry, AIME, pp. 127-132, (1984).

Handbook of Ternary Phase Diagrams, eds. P. Villars, A. Prince and H. Okamoto, ASM International, Vol. 4, pp. 4388-4396, (1995).

JANAF Thermochemical Tables, Third Edition, American Chemical Society and the American Institute of Physics, (1986).

Jones, P. E., Porter III, W. J., Eylon, D. and Colvin, G., Gamma Titanium Aluminides, eds. Y-W. Kim, R. Wagner and M. Yamaguchi, TMS, Warrendale, pp. 53-62, (1995).

Jones, P. E. and Eylon, D., Titanium '95, Vol. I, Institute of Materials (UK), pp. 225-232, (1996).

Keller, M. M., Porter, W. J., Jones, P. E. and Eylon, D., 30th ISATA, Materials for Energy-Efficient Vehicles; Paint and Powder Coating Applications in the Automotive Industries, Automotive Automation Limited, Croydon (England), pp. 611-618, (1997).

Larsen, Jr., D. E., Wheeler, D. A. and London, B., Proc. of the Seventh World Conference on Titanium, ed. F. H. Froes, TMS/AIME (USA), (1992).

Larsen, Jr., D. E., Wheeler, D. A. and London, B., Processing and Fabrication of Advanced Materials III, eds. V. A. Ravi, T. S. Srivatsan and J, J, Moore, TMS, Warrendale, pp. 631-641, (1994).

McCullough, C., Valencia, J. J., Levi, C. G. and Mehrabian, R., *Acta Metall.*, Vol. 37, no. 5, pp. 1321-1336, (1998).

Pehlke, R. D., Unit Processes of Extractive Metallurgy, Elsevier, NY, pp. 130-138, (1979).

Pollock, T. M. and Steif, P. S., PRET: A University-Industry Partnership for Research and Transition of Gamma Titanium Aluminides, AFOSR/PRET Annual Report, Carnegie Mellon University, Pittsburgh, PA, Sept. 1996.

Pollock, T. M. and Steif, P. S., PRET: A University-Industry Partnership for Research and Transition of Gamma Titanium Aluminides, AFOSR/PRET Annual Report, Carnegie Mellon University, Pittsburgh, PA, Sept. 1997.

Pollock, T. M. and Steif, P. S., PRET: A University-Industry Partnership for Research and Transition of Gamma Titanium Aluminides, AFOSR/PRET Annual Report, Carnegie Mellon University, Pittsburgh, PA, Sept. 1998.

Raban R., Rishel, L. L. and Pollock, T. M., Mat. Res. Soc. Symp. Proc. Vol. 487, MRS, accepted for publication in June 1999.

Rishel, L. L., Pollock, T. M., Cramb, A. W. and Larsen, D. E., Proc. Intl. Symp. on Liquid Metal Processing and Casting, eds. A. Mitchell and P. Auburtin, American Vacuum Society, p. 214, (1997).

Rishel, L. L., Biery, N. E., Raban, R., Gandelsman, V., Pollock, T. M., and Cramb, A. W., *J. of Intermetallics*, **6**, p. 629, (1998).

Rishel, L. L., Pollock, T. M., Cramb, A. W. and Larsen, D. E., Proc. Intl. Symp. on Liquid Metal Processing and Casting, eds. A. Mitchell, L. Ridgway and M. Baldwin, American Vacuum Society, p. 287, (1999).

Sasaki, K., Sugitani, Y., Kobayashi, S. and Ishimura, S., *Iron and Steel Institute of Japan. Transactions*, Vol. 19, p. 134, (1979).

Wagner, R., Appel, F., Dogan, B., Ennis, P. J., Lorenz, U., Mullauer, J., Nicolai, H. P., Quadakkers, W., Singheiser, L. and Smarsly., W., Gamma Titanium Aluminides, eds. Y-W. Kim, R. Wagner and M. Yamaguchi, TMS, Warrendale, pp. 405-414, (1995).

Ward, R. G., *Journal of the Iron and Steel Institute*, Vol. 201, pp. 11-15, (1963).

Section 4. Microstructural Evolution and Characterization

N. Biery
M. De Graef
T. Pollock
Carnegie Mellon University

4.1 Overview

In Year I of this project, dogbone samples from a single HIP'ed and heat-treated slab of Baseline I material were subjected to a series of tension enexperiments. These experiments revealed that the tensile ductility in the faster cooled regions of the slab was a factor of four higher than that in the slower cooled regions. In the second year of the project we investigated this microstructural variability using more extensive mechanical tests on various sample geometries, again for the baseline I material. In addition we used *in-situ* straining experiments and strain mapping to correlate surface displacements with local surface strains. In the third year of the project we continued to investigate the deformation behavior of the baseline material and its relationship to the microstructure of the material, in particular the relationship with the as-cast structure. These experiments included further surface displacement mapping experiments as well as mechanical testing, Orientation Imaging Microscopy (OIM), and examinations of the cast texture present in these alloys.

In the project's fourth year, we have continued to collect information using the strain mapping technique that we have developed, applying it to a wider range of alloys, and to different loading geometries. Alloys tested include the 'baseline I' 48Al-2Cr-2Nb alloy, the 48Al-2Cr-2Nb alloy from the plates cast in the first year (plates 2 and 5), and a 45Al-1.9Cr-1.9Nb-0.9B XD™ alloy from the first year (plate 11). These results, and the results obtained from further mechanical testing, have pointed to intrinsic microstructural features as the source of property variability. Because cast titanium aluminides typically solidify with columnar grain structures, cast texture is one key microstructural feature which has been characterized in detail. Texture measurements have been made on a range of binary Ti-Al Alloys, as well as on 48Al-2Cr-2Nb alloys with different cooling rates (including the 'baseline I' alloy). Recent results on strain mapping and texture development are reviewed in the following sections.

4.2 Displacement and Strain Mapping

The surface displacement mapping technique developed in the first and second years of the program (Pollock and Steif, 1996, Pollock and Steif, 1997) has been applied to double-notched and un-notched tensile samples of various cast gamma alloys using an *in-situ* straining stage mounted in a Philips XL30 field emission scanning electron microscope. Notched samples were sheet-type double v-notched specimens with a 0.25mm notch radius; un-notched specimens were sheet-type dogbone samples with gage

sections that measure 4mm wide by 2.5mm thick (3mm for the 'baseline I' specimens) by 13mm long. The bulk materials have plastic strain-to-failures in the 1-2.5% range, but all of the alloys exhibit some variability. The strain mapping technique, based on an enhanced version of the DAISIES algorithm (Wissuchek et al., 1996), was briefly summarized in 1998 report (Pollock and Steif, 1998).

After testing to failure in the SEM, the fracture surfaces of the samples were examined to locate the fracture origins on each sample surface. These observations were compared with the strain maps and the surface microstructure. Finally, the loading of the notched 48-2-2 samples was modeled using finite element modeling (FEM), and the strains predicted by FEM were compared with those obtained experimentally. The FEM used the properties obtained from tensile specimens of the same alloy with the same heat treatment. The specimen was assumed to be under plane stress conditions for the analysis (a reasonable assumption for modeling surface strains in a 2mm thick specimen with a 250µm radius notch).

4.2.1 Observations of Notched Samples

In each of the tested samples, the development of strain followed a systematic progression as the sample load increased (Figure 4.1). As the load increased, the strain increased in the entire region of the notch root, but it increased more rapidly in small regions of the sample, resulting in significantly elevated strains localized to only a few grains at the notch root.
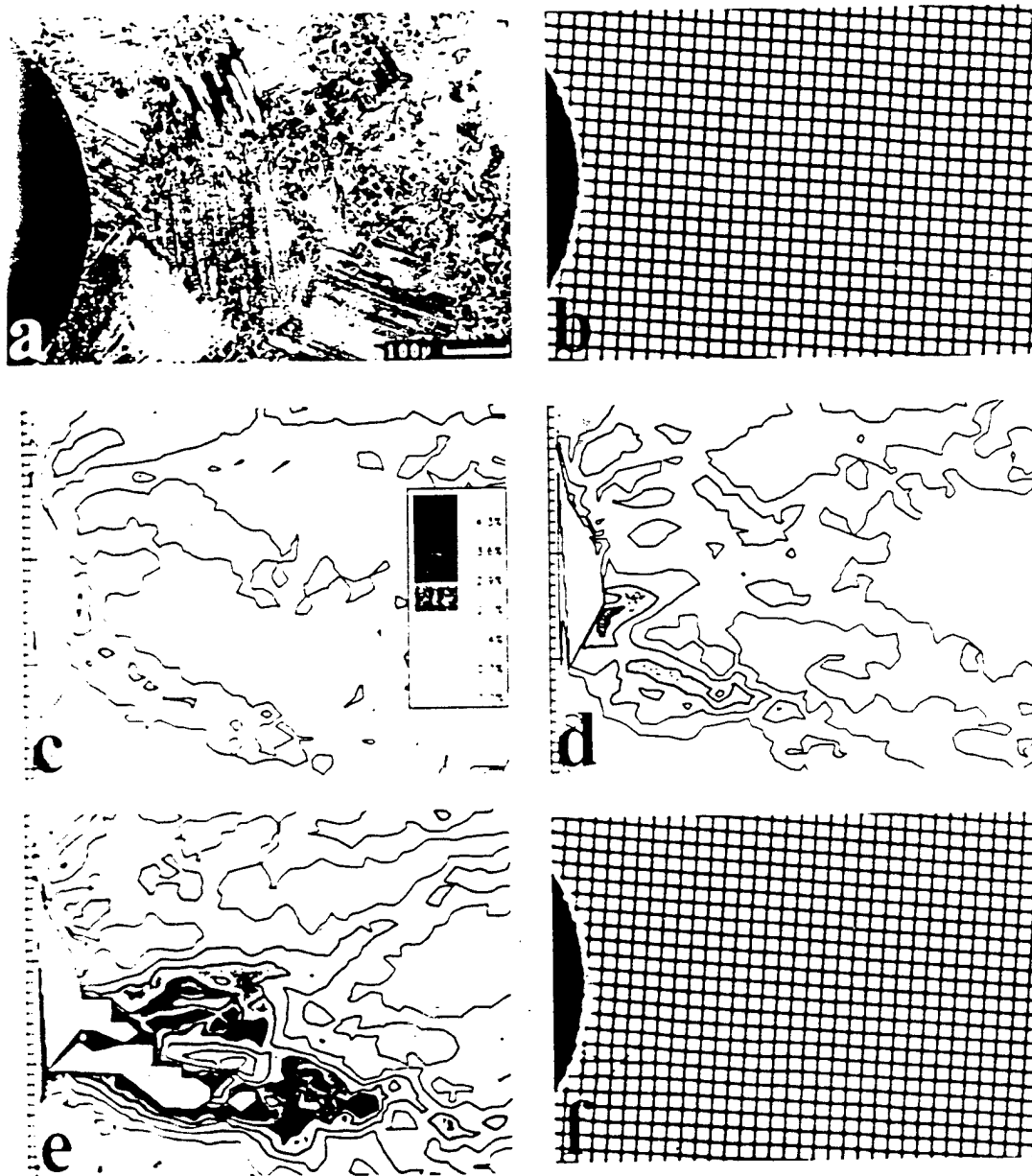
Figure 4.1 - a) SEM BSE image of the microstructure of the 48-2-2-1 alloy near the notch root. b) grid before loading; strain maps and corresponding BSE images for net section stresses of c) 550MPa, d) 600MPa, and e) 651MPa. f) A crack is visible at the highest applied load, the strains around the crack exceed the threshold for the strain map (light areas in the crack region).

In the 48-2-2 samples, the strains at the notch root reached quite high levels before the initiation of cracking (greater than 4% in all cases). This level of strain is quite a bit higher than the value obtained in bulk tension tests (1-2.5%). This indicates that strains at stress concentrators may be quite significantly higher than those in bulk samples, so that designing on the basis of bulk tensile strains could be conservative under plane stress conditions.

When the strain maps were compared to the microstructures of the 48-2-2 samples (Figure 4.2), it was observed that the high strain regions were concentrated near the notch root and that the magnitude of the peak strain was similar to that predicted by the continuum model. However, the contours were strongly influenced by the local microstructure (they were not as smooth as those generated by FEM). Cracking was first observed in the grains with the highest strains rather than at the boundary between grains that are deforming and those that are not. Examination of the crack path showed that it was primarily transgranular, although there are some regions of grain boundary cracking (Figure 4.3). The dominance of transgranular cracking may indicate that the accumulation of strain within a grain is more likely to initiate cracking than the interface between a deforming and a non-deforming grain.
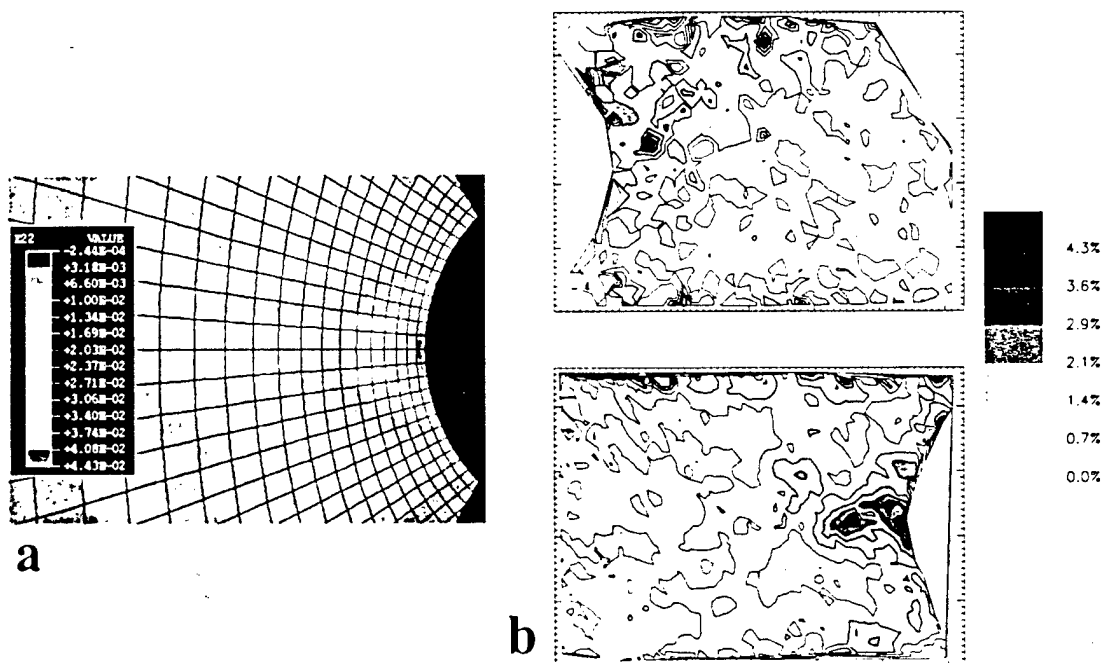
Figure 4.2 - a) Finite element ε_{yy} strain contour map for a 250μm notch and a net section load of 410MPa. The maximum strain at the notch root is 4.4%; b) experimental ε_{yy} strain maps for the left (top) and right (bottom) side notches of a 48-2-2 near-γ alloy with maximum strains of over 5%. Strains are scaled between 0 and 5% in this and all following figures.

Whether the initiation is at a boundary between a highly strained grain and its nearby undeformed neighbor or in the highly strained grain itself, the result points to the potential importance of sample texture. If more grains are favorably oriented for slip at the stress concentration, the plastic deformation will be distributed over a larger volume, or there may not be an incompatibility problem. Either way, a texture that favors deformation of many neighboring grains should have a positive effect on damage tolerance in these alloys. It is known that cooling rate affects textures in these alloys

(McCullough et al., 1989, De Graef et al., 1999), and so this may be a mechanism contributing to the known variation in ductility with cooling rate in these alloys (Raban et al., 1999).
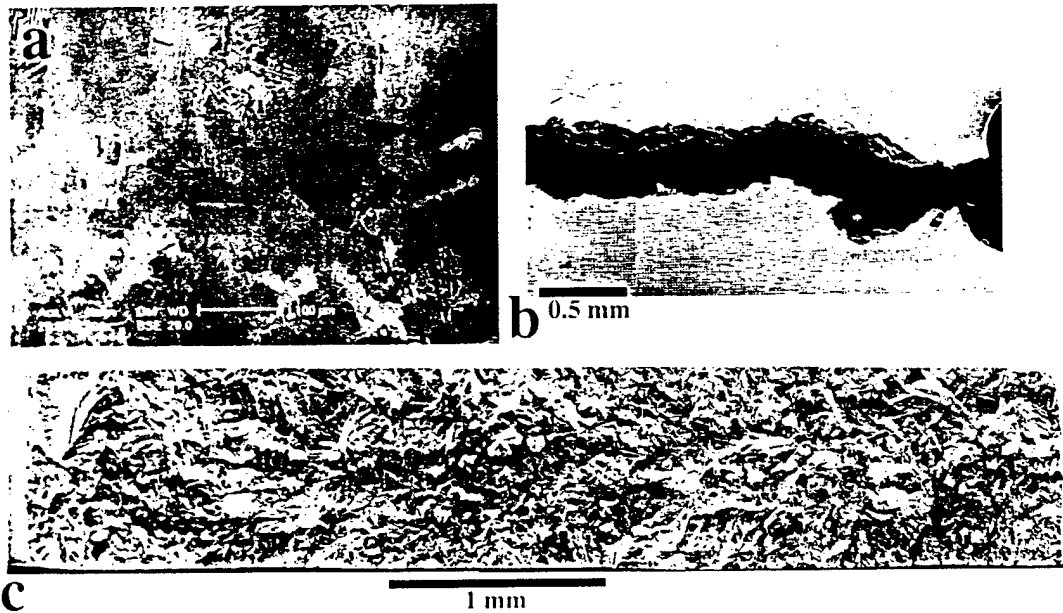

Figure 4.3 - a) SEM back-scatter image of the microstructure of the 48-2-2 near-γ alloy at the notch root: b) SEM secondary electron image of the sample after fracture: c) SEM micrograph of the fracture surface.

In these 48-2-2 samples it was also observed that the samples failed immediately, or almost immediately, after the initiation of a crack: no cracks were observed on the surface of the samples prior to final failure, and no stable crack growth was observed. This is in contrast to earlier experiments on samples of the same alloy, where stable crack growth was sometimes observed (Pollock et al., 1996). The difference in behavior may be due to the difference in the elastic stress concentration factor between the two sets of experiments. The stress away from the notch root was higher in these samples after crack initiation, leading to the catastrophic propagation of cracks once initiated. Occasionally, cracks that did not intersect the main crack on the surface were observed after testing, cracks that may have occurred before the failure event, but these cracks were not observed during the test. It was also found that when one of the two notches showed higher levels of strain, cracking was first observed at this site. The cracks propagated predominantly transgranularly through the γ grains in the sample, and they tended to pass along rather than through the γ-α2 boundaries.

In the nearly lamellar 47-2-2-1 sample that was tested (Figure 4.1), high strain contours were observed along lamellar colony boundaries and in a region containing a number of small, equiaxed γ grains. Very little strain was present in the lamellar colonies, although one colony right at the notch root (with a favorable orientation for slip) did show some evidence of deformation before failure (Figure 4.1). This colony appeared to be oriented

such that its lamellae were at around 45° tilt with respect to the loading axis, an orientation which has been shown to provide maximum ductility and minimum yield strength in poly-synthetically twinned (PST) experiments (Inui et al.. 1992). Maximum strains at the notch root prior to crack initiation were greater than 4%, which is quite a bit higher than the approximately 1% plastic strain that is seen in bulk samples of this material. Stable crack growth in the 48-2-2-1 material was observed in a crack at the notch root during testing. As the load neared the failure load, the crack was visibly growing, but this crack did not propagate and cause the sample to fail (Figure 4.4). Instead, another crack that initiated at the other notch caused the failure. However, both of the cracks present after failure passed through the high strain regions in the strain maps of this sample.
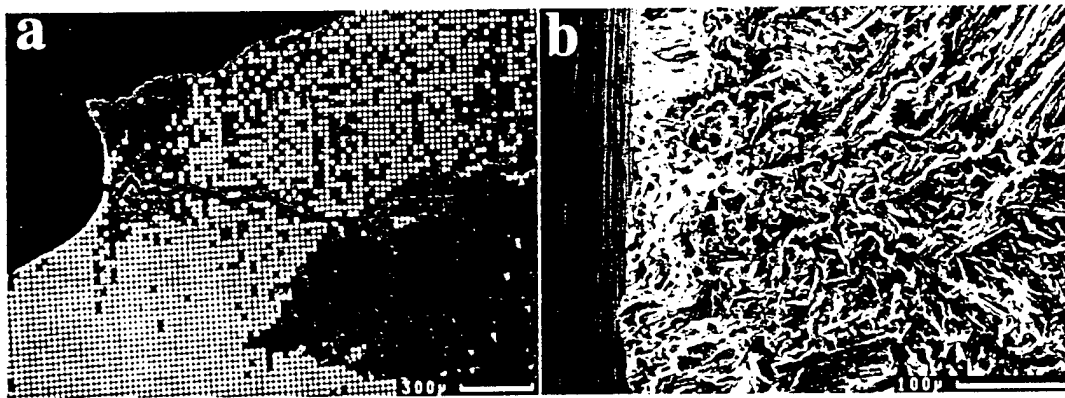
Figure 4.4 - a) SEM BSE micrograph of the 47-2-2-1 sample used in Figure 4.1 after fracture, an attempt was made to remove the markers after testing, but was abandoned to avoid damaging the fracture surface; b) SEM micrograph of the fracture surface, showing the probable fracture origin.

An examination of the fracture surface proved more fruitful in locating the fracture origin. Fortunately, the lamellar sample did contain some small γ-grains, the cleavage facets of which could be tracked back to a probable fracture origin (Figure 4.4). The origin was located in a region that consisted of several small γ or α, grains rather than in a lamellar colony. However, this region was not on the polished and gridded surface of the sample, and so even if this notch was under observation, the actual crack origin could not have been observed during the test. Nevertheless, the strain mapping technique successfully identified a feature of the microstructure associated with enhanced local straining and failure did indeed occur at the same type of feature in the sample interior.

4.2.2 Observations of Dogbone Samples

There were three different microstructures observed in these samples, and the strain mapping results were different in each. These results will be broken up into the three categories to separate the features identified with each microstructure, but similarities between the tests will also be noted.

In all of the tests, the strain distribution was quite non-uniform, but the degree of non-uniformity depended on the microstructure of the sample. In the lamellar sample, the distribution of strain was quite a bit more uniform than in the segregated duplex material or in the near gamma material, but the average strain level was also much lower when failure occurred. The segregated material showed the largest disparities, but it also displayed a relatively high level of strain. The near-γ material showed peak strain similar to that in the segregated material, but with less variation.

An attempt was made to relate the apparent orientation of the lamellae in the lamellar samples to the distribution of strain in the microstructure. It was hypothesized by analogy with the polysynthetically twinned results of Prof. Yamaguchi's group (Fujiwara et al., 1990) that the sample with the lamellae oriented at approximately 45° to the tensile axis would display the lowest yield and the highest degree of strain prior to failure. Unfortunately, an analysis of the test results failed to turn up a definitive correlation between the degree of strain and the apparent orientation of the lamellae. An explanation for this discrepancy is the lack of information on the out of plane orientation of the lamellae.

For the samples with the more segregated microstructure it was noticed that there was less strain in the 'lighter' (more α_2) regions of the microstructure than in the darker (more γ) regions. To check this hypothesis, the strain at each marker was plotted vs. the average intensity of the SEM BSE photo of the microstructure (Figure 4.5). A positive correlation was noticed, and a 2-D Gaussian function was fit to the data. The fit function had a long axis oriented such that higher strains fell in the darker regions of the sample. This was also clear from an image of the microstructure with the strain contours plotted over it: the lowest strain contours lie in the brightest regions where there is significant α_2 present, and the highest contours are in the regions of the sample where there is very little or no α_2 present.

For the near-γ baseline I samples, it was not possible to relate the local strain to the grain orientation because the grain orientation was unknown. Furthermore, in the dogbone baseline samples, the crack never passed through the areas under observation, so the crack path could not be compared with the highly strained regions. It was noted, however, that there was a significant anisotropy of strain between adjoining grains, and that the strain contours followed the features present in the microstructure.
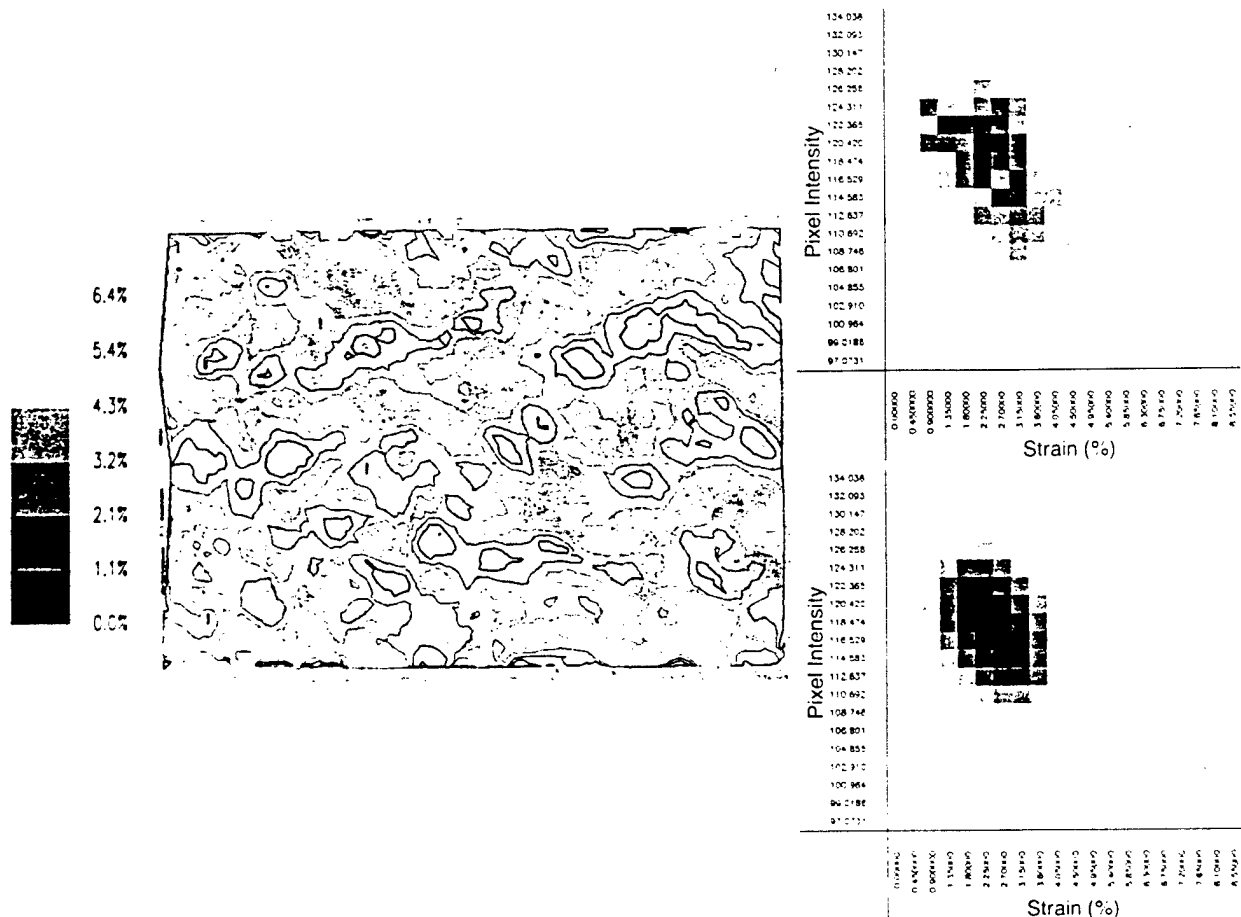
Figure 4.5 - SEM BSE micrograph of a 48-2-2 sample with overplot of strain contours. The low strain (dark) contours tend to overlay the bright (predominantly α_2) regions of the microstructure, while the high strain (light) contours overlay the dark (predominantly γ) regions. The plots at right show the variation of strain with pixel intensity and a 2D Gaussian fit to that data. Darker regions show greater number of pixels with that pixel intensity and strain. As strain levels increase, the average pixel intensity decreases; the average intensity of the pixels with the highest strains is lower than that of the pixels with the lowest strains.

.3 Microstructure and Texture Characterization of As-Cast Alloys

he year 2 program report (Pollock and Steif, 1997) and in (Muraleedharan et al., ``) we described how the cooling rate during casting is a primary factor in `ining the as-cast microstructure. While all as-cast samples exhibited a columnar ostructure, only slower cooling rates during casting produced a typical lamellar icrostructure in the as-cast material. Faster cooling rates, however, resulted in a fully γ, ..mellar-like `.iicrostructure with significant deviations from the standard orientation relationships between adjacent lamellae. In the year 3 report we presented evidence that the cooling rate affected the texture of the cast material as well. In year 4 we have continued to perform experiments investigating the texture of cast gamma samples using x-rays to obtain better statistics than in the OIM scans reported previously, and have applied texture analysis to a wider range of materials, including materials with known solidification rates.

The as-cast microstructure is important because it affects the evolution of microstructure and texture in this class of alloys. The importance of texture on the mechanical and plastic flow properties of PST crystals has been analyzed in (Bartels and Uhlenhut, 1998). It is important to point out that PST crystals are always solidified at a relatively slow rate, so the corresponding cooling rate is rather slow. Johnson, Inui and Yamaguchi (Johnson et al., 1998) have recently reported calculations which indicate a transition from β to α primary dendrites as a function of cooling rate (interface velocity) and Al-content; the interface velocity above which β dendrites are replaced by α dendrites varies by 2 orders of magnitude for a change in Al-content of 1 at%. Johnson et al. (Johnson et al., 1998) also provide evidence for the $[00.1]$ solidification direction of the α phase in alloys produced by the floating zone technique.

Texture analysis can be performed by means of standard x-ray diffraction methods, resulting in an orientation distribution function (ODF) from which pole-figures can be derived. The information contained in such a description is purely statistical and averaged over the volume of the sample exposed to the x-ray beam. An alternative method for the determination of solidification textures is the use of Orientation Imaging Microscopy (OIM). This technique provides a pointwise set of Euler angles, relating the local grain orientation to a standard reference frame. The grain orientation is determined from an electron backscatter pattern (EBSP), and the complete dataset (typically containing several tens of thousands of points) can then be used to determine local orientation variations or to compute the ODF and related pole figures.

4.3.1 Experimental Procedure

Several different alloys spanning a range of aluminum levels and solidification times/cooling rates were obtained for analysis. The binary alloys were (balance Ti, atomic %): 46.5 Al, 48 Al, 52 Al, and 58 Al. These numbers are the average of two chemical analyses performed at Howmet and Sherry Labs, rounded to the nearest half percent to avoid over-quantifying the values (the variation in Al level was between 0.7 to 1% except in the case of the 58Al alloy, where there is a lack of good standards and the variation between the two results was almost 4%).

A number of alloys with the composition 48Al-2Cr-2Nb were also tested (referred to hereafter as 48-2-2); one relatively fast cooled sample, one relatively slowly cooled sample, one from a batch of slabs ('Baseline I') that have been studied extensively in other work (Muraleedharan et al., 1997, Steif et al., 1997, knaul et al., 1999), and one cast in the same manner (at the same cooling rate) as the binary alloys. The binary samples and one of the 48-2-2 samples were obtained from as-cast cylindrical ingots (diameter greater than 100mm, each longer than 90cm), while the other 48-2-2 samples were obtained from cast and HIP'ed rectangular slabs (100x150x12mm). A columnar solidification structure was revealed by macroetching in each of the ingots with the exception of the 56Al binary (Figure 4.6). In each case the surface analyzed for texture was a 25 by 25mm square perpendicular to the solidification direction (~12mm above and parallel to the bottom of the cylindrical ingots, 1.5 mm inside and parallel to the surface of the rectangular ingots, see schematic in Figure 4.7. The samples were removed from larger sections using either a low speed abrasive saw with a pressed SiC grit blade (all samples except for the fast and slow cooled 48-2-2) or by wire EDM. The samples were then wet ground to a 600-grit finish using standard metallographic preparation techniques.
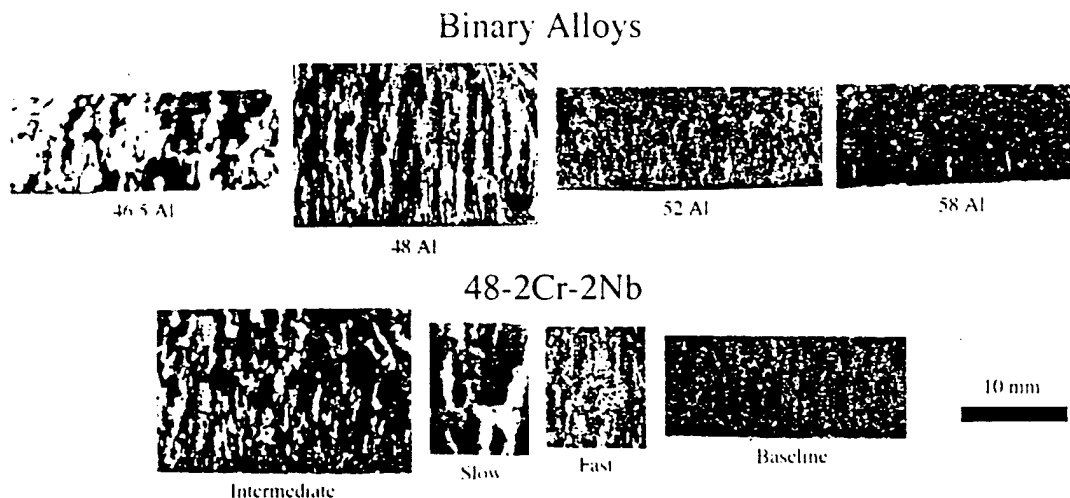
Binary Alloys

48-2Cr-2Nb

Figure 4.6 - Macrostructures of samples adjacent to the samples used for texture analysis. Note that the columnar structure is visible in all of materials except for the 58 Al binary.

despite the phase transformations that occurred on cooling to room temperature and the effects of HIP in some of the samples.
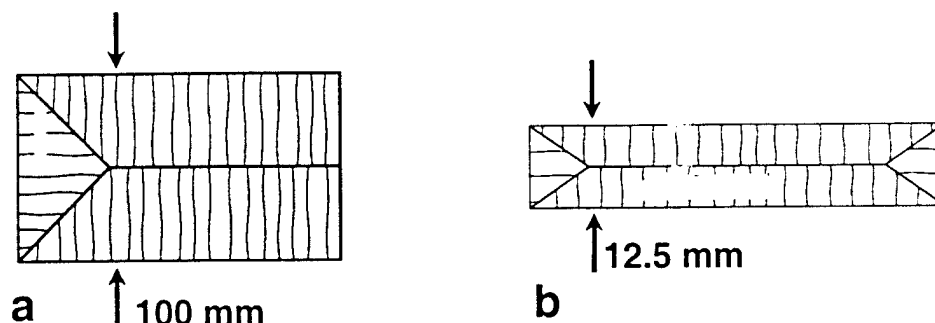

Figure 4.7 - Schematic of the location and orientation of the rectangular samples (gray rectangles) cut for texture measurements. The orientation of the columnar grains within the plates is shown schematically. Note that all samples were approximately the same size.

Texture was characterized using the TSL-OIM package on a Phillips XL-40 FEGSEM and using Rigaku x-ray diffractometer with a 2-axis goniometer. Samples were removed from several as-cast ingots, as well as from some post-HIP material, and examined using the OIM. The results obtained from these samples are detailed below.

Due to some limitations of the OIM used, which is insufficiently sensitive to index the patterns correctly using the tetragonal unit cell, each sample was indexed as generic FCC. Furthermore, only one phase at a time can be indexed currently, so each sample was indexed as if it only contained 'FCC' γ-TiAl, ignoring the presence of the α_2 phase. However, since the close-packed planes of the γ phase should the parallel to the close-packed planes of any parent phases, the information available by indexing in this simple fashion should still help us determine the solidification and transformation path of the alloys of concern.

For each sample, 2θ scans and [111], [200], and [202] pole figures were obtained (these peaks were chosen because they are the strongest peaks in the 2θ scan for γ-TiAl) using a Rigaku Diffractometer equipped with a goniometer suitable for pole figure collection. Cu-K$_\alpha$ radiation was used in conjunction with a graphite crystal monochromator, and parallel focusing optics were used to minimize the effect of sample misalignment. Pole figures presented in this paper represent raw data and no extensive data analysis was attempted.

4.3.2 Observations and Discussion

4.3.2.1 Crystallographic Analysis

Before discussing the observed textures as a function of alloy composition and cooling rate, it is useful to summarize the orientation relation between the various phases and how the solidification texture relates to the primary solidified phase. We will use the graphical depictions in Figure 4.8(a-c) to illustrate how the both the primary phase and the orientation relationship determine the final texture.
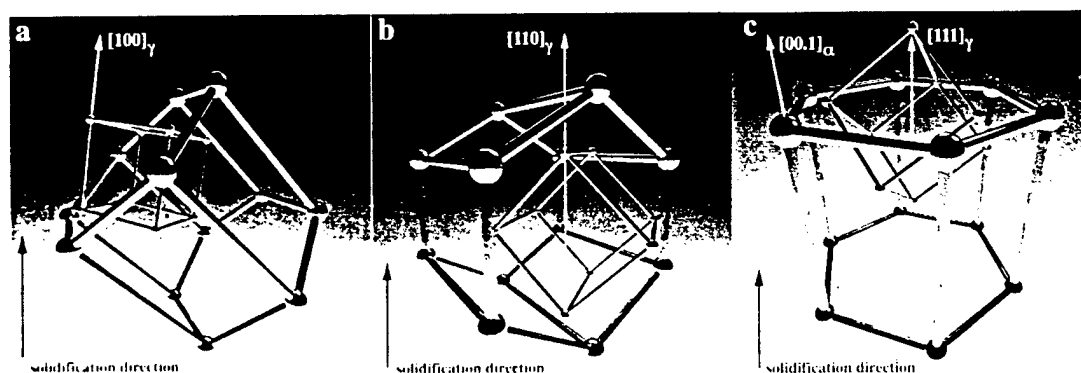

Figure 4.8 - Orientation of the γ-phase unit cell (cube with small spheres at vertices) with respect to the solidification direction (vertical direction) and the α_2 unit cell, assuming a) primary [100]-β solidification, b) primary [10.0]-α solidification, and primary [00.1]-α solidification.

The standard orientation relation between the α_2 and γ phases shows that the close-packed $(00.1)_\alpha$ planes are parallel to the $\{111\}_\gamma$ planes. These planes are in turn parallel to the $\{110\}_\beta$ planes. If the β-phase is the first phase to solidify, and its primary dendrite growth direction is of the $\langle 100 \rangle$ type, then the resulting γ-texture perpendicular to the growth direction (after going through two solid state phase transformations with the above orientation relations) will be of the $\langle 100 \rangle$ type. This is illustrated in Figure 4.8a, which shows a unit cell of the γ-phase (small cube) and three cells of the α_2-phase. The $\langle 100 \rangle$ texture is not sharply peaked since there is a small angle between the plate normal/solidification direction (the vertical direction in the figure) and the cube directions. The absence of a sharp peak in the $\{100\}_\gamma$ pole figure may make it difficult to recognize the primary solidification phase as the phase, but often four-fold dendrites can be observed which unambiguously point to primary β solidification.

If the β-phase does not dominate the growth of the columnar grains, then there are two possible resulting textures for the γ-phase, depending on the primary solidification direction of the α-phase:

4-12

- primary solidification along the $[\bar{1}0.0]_\gamma$ direction, shown in Figure 4.8b. In this growth mode the hexagonal c-axis lies perpendicular to the growth direction, in the chill plane. This is a common solidification direction for hexagonal systems and it is intuitively easy to understand since the close packed planes grow laterally much faster than along their normal. The resulting γ-texture is then of the $\langle 110 \rangle$ type.

- primary solidification along the $[00.1]_\gamma$ direction, shown in Figure 4.8c. This growth mode is less likely than the previous one, but it has nevertheless been reported by McCullough and coworkers (McCullough et al., 1989) for faster dendrite tip velocities (0.083cm/s, Ti-Al, floating zone method). Johnson et al. (Johnson et al., 1998) have also reported this growth mode based on calculations of the interface velocity versus Al-content. The resulting γ-texture is then of the $\langle 111 \rangle$ type.

We conclude from this brief crystallographic analysis that there are three possible textures for the final phase: $\langle 100 \rangle$, indicating that the growth is dominated by β solidification, and $\langle 110 \rangle$ or $\langle 111 \rangle$, both consistent with a strong influence of α solidification, with growth along $[\bar{1}0.0]_\gamma$ or $[00.1]_\gamma$, respectively.

4.3.2.2 Texture Measurements

We will review the results for the binary alloys first in order of increasing aluminum content, followed by the 48-2-2 alloys. The range of aluminum levels was chosen to compare with the binary phase diagram. The binary alloy ingots were cast into room temperature cylindrical steel molds, resulting in a relatively short solidification time. One of the 48-2-2 alloys shared this processing route. The cooling rates for the binary alloys and the similarly cast 48-2-2 alloys should be similar due to the identical processing route. These will be followed by the various 48-2-2 alloys, which vary only in cooling rate and the presence or absence of a HIP treatment step, a process which weakens but does not completely remove the original cast texture.

The pole figures for the 111, 200, and 202 reflections are shown in each of the graphs of Figures 4.9 and 4.10. The pole figures are represented by gray scale renderings in a stereographic projection, with the random texture as the reference state. The 2θ scan for a perfectly random γ-TiAl powder is shown in 4.11, for the range $2\theta=35-70°$.

The 46.5% Al sample showed a very strong $\langle 111 \rangle_\gamma$ texture (Figure 4.9a), indicative of the second type of α solidification (growth along the $[00.1]_\gamma$ direction). The observed texture for the 46.5% Al sample is consistent with the relatively short solidification time of the ingot. This finding is at odds with the equilibrium phase diagram, which would predict β-solidification for this aluminum level. Orientation imaging microscopy was also performed on this sample (Pollock and Steif, 1998).
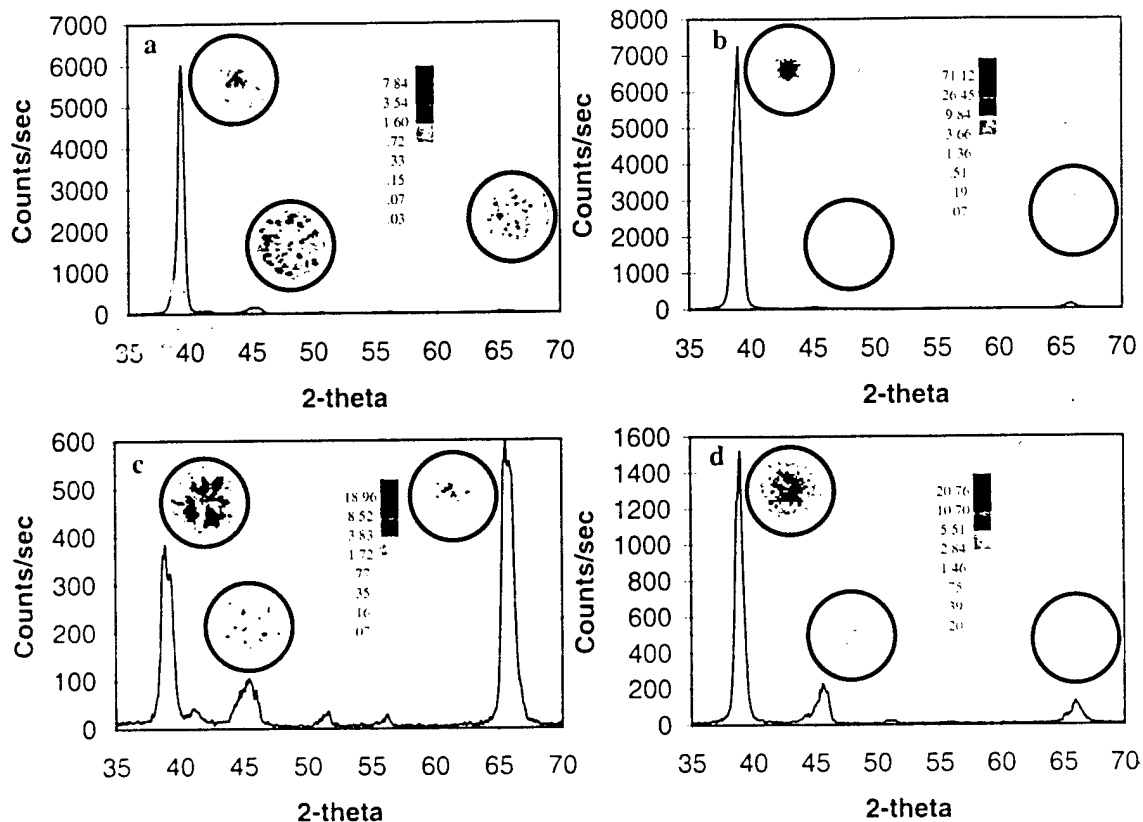
Figure 4.9 - Scans and pole figures for the (111), (200), and (202) planes (from left to right) for the binary alloys a) 46.5 Al, b) 48 Al, c) 52 Al, and d) 58 Al. All alloys solidified at approximately the same cooling rate. Note the varying intensity scales.
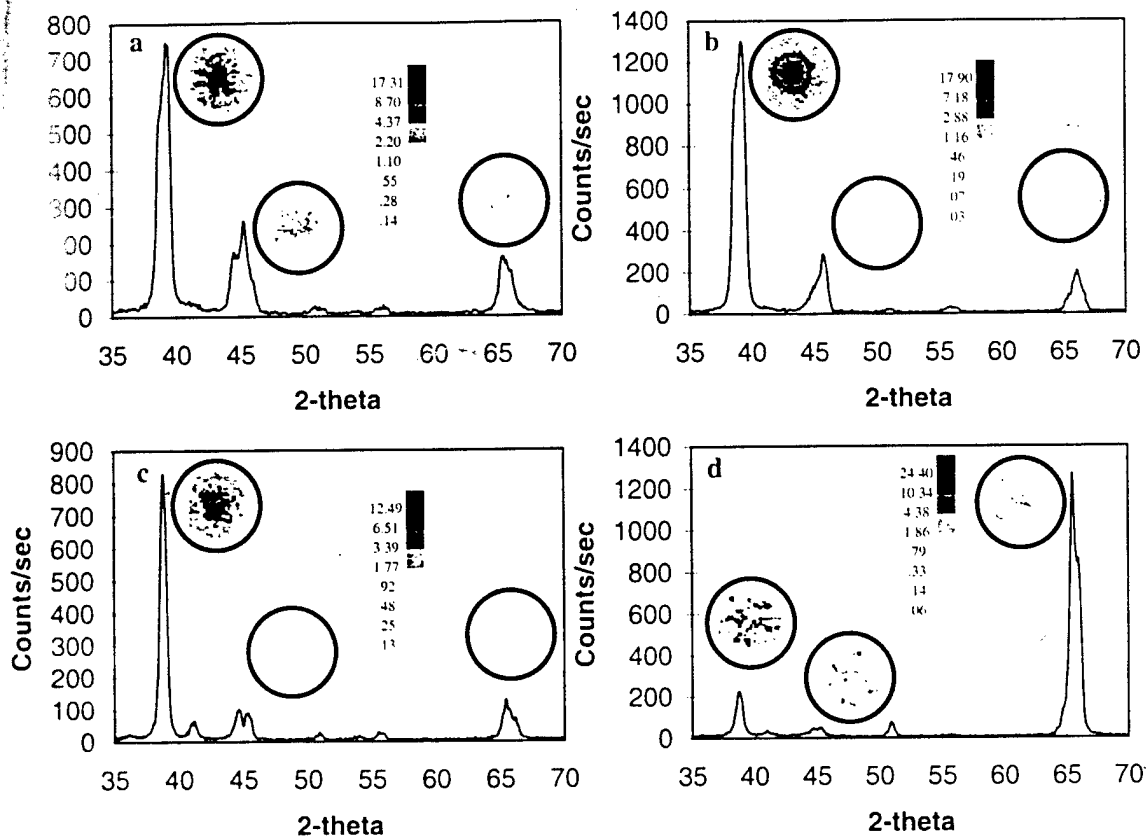
Figure 4.10 - 2θ scans and pole figures for the (111), (200), and (202) planes (from left to right) for a) 48-2-2, b) baseline alloy, c) 48-2-2 fast cooled, and d) 48-2-2 slow cooled.
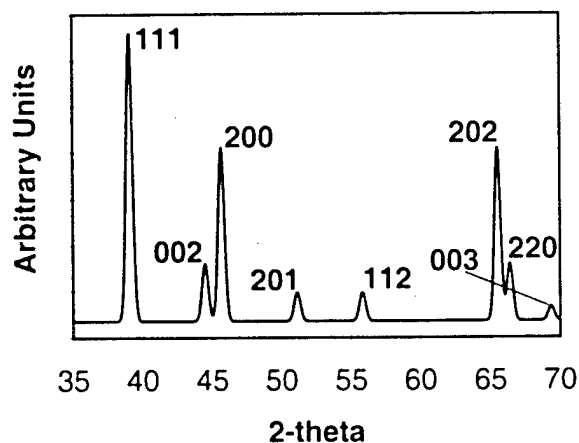
Figure 4.11 - Calculated and indexed 2θ powder pattern for a perfectly random γ-TiAl powder, using Cu-K$_\alpha$ radiation.

The 48% Al sample showed a texture (Figure 4.9b) very similar to that of the 46.5% Al sample, but when the 2θ scan was examined, it was noted that the 202 peak was twice as intense as the 200 peak, indicating that there was a preferential alignment of the (202)

planes parallel to the sample surface. This may indicate that both types of α-solidification are simultaneously occurring. but that $[10.0]$, growth is dominant.

The 52% Al sample exhibited a marked $\langle 101 \rangle$, type texture (Figure 4.9c). which is consistent with primary solidification along $[10.0]$, as detailed above. There is still a weak presence of the $[00.1]$, texture. since the 111 peak is higher than it should be relative to the 200 peak in a randomly oriented material. Therefore, both types of α solidification are operative in this material, but $[10.0]$, growth is now dominant.

The 58% Al sample showed a surprising texture (Figure 4.9d): a relatively strong $\langle 111 \rangle$, texture. but in the 2θ scan the 200 peak is significantly stronger than the 202 peak. when they should have equal heights for a random texture. So the trend of increasing proportions of $[202]$, oriented grains with increasing aluminum content reverses. indicating that the composition may be in a portion of the phase diagram where different solidification phenomena are operative. In fact. the composition is close to the intermetallic γ phase, which may require an extension of our rather simplified texture discussion presented above.

The 48-2-2 alloys from the cylindrical ingot showed a much less pronounced texture than that present in the binary alloys presented so far (Figure 4.10a). In fact. this alloy showed only a mild $\langle 111 \rangle$, texture. in contrast with the binary 48.5 Al sample. which showed a strong $\langle 111 \rangle$, texture. Cr and Nb are β stabilizers and may be affecting the β-phase boundary).

The 'baseline' 48-2-2 sample (a sample of the same material studied in Muraleedharan et al.. 1997. Steif et al.. 1997) showed a texture (4.10b) very similar to that of the 48-2-2 alloy in 4.10a. The nearly isotropic character of both the $\{200\}$, and $\{202\}$, pole figures indicates that this is a strongly uniaxial texture. with the majority of $\{111\}$, planes very nearly parallel to the chill plane.

The most significant cooling rate effect is observed when fast and slow cooled samples of the 48-2-2 material are compared (Figure 4.10c-d). The most rapidly cooled 48-2-2 sample displays (Figure 4.10c) a pronounced $\{111\}$, texture. whereas the slow cooled alloy (Figure 5.10d) displays a $\{202\}$, texture. This difference is in good agreement with microstructural observations. which reveal that the lamellar colonies are aligned nearly perpendicular to the columnar growth direction in the fast cooled alloy (Muraleedharan 1997).

It is instructive to compare the texture measurements on the 48-2-2 alloy with the calculated results for interface velocity vs. aluminum content by Johnson et al. (Johnson et al.. 1998). From PROCAST simulations (Muraleedharan et al.. 1997) of the cooling curves at the center of cast plates. the local solidification time was calculated to be about

10-25 seconds for the fast cooling rate, and about 186-222 seconds for the slowest cooled plate. The interface velocities at the surface and center of these two slabs were determined to be 3.26 and 1.32 mm/sec for the fast cooled plate, and 1.72 and 1.25 mm/sec for the slow cooled plate (interface velocities calculated from temperature gradients using the PROCAST models). The computations by Johnson et al. (Johnson 1998) predict a transition from β to α dendrites at an interface velocity of about 0.83mm/sec for binary alloys with an aluminum content of 48at%; the interface velocities for both of these samples fall into the α region which is in agreement with this analysis. However, in this case there was a transition from basal plane to c-axis growth. It is worth noting that although four-fold dendrites oriented normal to the columnar growth direction have been observed at the surfaces of baseline material (Muraleedharan et al., 1997), the final texture of the casting is not dominated by $\langle 100 \rangle_\beta$. Further work is under way to elucidate the nature of this transition in these alloys.

4.5 Future Plans

We are currently writing up a journal manuscript about the displacement mapping method. The IDL routines are being converted to Java, and will be distributed as open source code. Plans have been made to use OIM to measure the relative orientations of grains in the regions of observation. Further investigations of texture will be made to verify the results obtained to date, with an emphasis on samples solidifying with a primary β texture. Further experiments investigating the effects of microstructural inhomogeneity and local crystallographic orientation with be performed using the in-situ stage and strain mapping in conjunction with OIM of the samples. The overall objective of these experiments is to identify microstructural features associated with enhanced local strain.

References

Bartels A., and Uhlenhut H., "Anisotropy of plastic flow in strongly textured gamma-TiAl based alloys," Intermetallics, **6**, pp. 685-688 (1998)

De Graef M., Biery N.E., Rishel L.L., Pollock T.M., and Cramb A., "On the relation between cooling rate and solidification microstructure in as-cast titanium aluminides," 1999 TMS Annual Meeting, International Symposium on Gamma Titanium Aluminides, to be published in the session proceedings, (1999)

Fujiwara T., Nakamura A., Hosami M., Nishitani S.R., Shirai, Y. and Yamaguchi M., "Deformation of polysynthetically twinned crystals of TiAl with a nearly stoichiometric composition," Phil. Mag. A, **61**, pp. 591-606 (1990)

Inui H., Oh M.H., Nakamura A., and Yamaguchi M., "Room temperature tensile deformation of polysynthetically twinned (PST) crystals of TiAl," Acta Mater., **40**, pp. 3095-3104 (1992)

Johnson D.R., Inui, H. and Yamaguchi Y., "Crystal Growth of TiAl Alloys," Intermetallics, **6**, pp. 647-652 (1998)

Knaul, D.A., Beuth, J.L. and Milke, J.G., "Modeling and measurement of the notched strength of gamma titanium aluminides under monotonic loading," Met. Trans., **30A**, pp. 949-959 (1999).

McCullough C., Valencia J.J., Mateos H., Levi C.G., Mehrabian R., and Rhyne K.A., "The high temperature alpha field in the titanium-aluminum phase diagram," Scripta Metall. Mater., **22**, pp. 1131-1136 (1988)

Muraleedharan K., Rishel L.L., De Graef M., Cramb, A.W., Pollock T.M., and Gray, G.T. III, "The effect of cooling rate during casting on microstructural development in Ti-48Al-2Nb-2Cr type alloys," in "Structural Intermetallics 1997", edited by Nathal M.V., Darolia R., Liu C.T., Martin P.L., Miracle D.B., Wagner R., and Yamaguchi M., pp. 215-224, The Minerals, Metals and Materials Society (1997)

Pollock T.M., Mumm D.R., Muraleedharan K., and Martin P.L., "In-situ observations of crack initiation and growth at notches in Ti-48Al-2Cr-2Nb," Scripta Metall. Mater., **35**, pp. 1311-1316 (1996)

Pollock T.M. and Steif P.S., PRET: A University-Industry Partnership for Research and Transition of Gamma Titanium Aluminides, AFOSR-PRET program Annual report 1, Carnegie Mellon University, Pittsburgh PA, September 1996.

Pollock T.M. and Steif P.S., PRET: A University-Industry Partnership for Research and Transition of Gamma Titanium Aluminides, AFOSR-PRET program Annual report 2, Carnegie Mellon University, Pittsburgh PA, September 1997.

Pollock T.M. and Steif P.S., PRET: A University-Industry Partnership for Research and Transition of Gamma Titanium Aluminides, AFOSR-PRET program Annual report 3, Carnegie Mellon University, Pittsburgh PA, September 1998.

Steif P.S., Jones J.W., Harding T., Rubal, M.P., Gandelsman V.Z., Biery N., and Pollock T.M., "Surface damage due to impact and fatigue strength reduction in gamma titanium aluminides," in "Structural Intermetallics 1997", edited by Nathal M.V., Darolia R., Liu C.T., Martin P.L., Miracle D.B., Wagner R., and Yamaguchi M., pp. 435-442, The Minerals, Metals and Materials Society (1997)

Wissuchek D.J., Mackin T.J., De Graef M., Lucas G.E., and Evans A.G., "A simple method for measuring surface strains around cracks," Journal of Experimental Mechanics, 36, pp. 173-179 (1996).

ction 5. Property Variability

ael Raban   Andrew Elliott
nolas Biery   Linda Rishel
sa Pollock   Marc De Graef

arnegie Mellon University

5.1 Overview

The overall objective of this project is to identify the microstructural origins of property variability in cast gamma titanium aluminides. The approach has been to study in detail the development of macro- and microstructure as a function of casting conditions and with variations in subsequent HIP and heat treatment cycles. In terms of property variability, the focus has been on tensile ductility, since this is one of the properties of greatest concern with regard to structural applications. A range of alloys has been studied, including Ti-48Al-2Cr-2Nb type alloys and "grain-refined" XD alloys.

One of the major results of the studies within this project in previous years is that tensile ductility, and importantly the variability in this property, is strongly influenced by cooling rate during investment casting. Unfortunately, variations in cooling rate during casting influence a number of potentially important features of cast microstructure, including texture, segregation, initial grain size and volume fraction of lamellar grains. In Section 4 we outlined the results of studies on texture and the influence of segregation on the distribution of strain in the microstructure. In this section, recent studies on the influence of cooling rate on other features of cast structure are reported, along with results of tensile testing. While both the grain size and the initial fraction of lamellar structure following HIP and heat treatment are strongly influenced by cooling rate during casting, grain size is shown to have a more pronounced influence on ductility. Heat treatments that establish an equivalent fraction of lamellar structure in fast and slow cooled materials have shown that the increase in grain size caused by a tenfold increase in local solidification time reduces tensile ductility by a factor of approximately four.

A second objective in the previous year has been to quantify the variability in tensile properties in a range of compositions and microstructures with the use of Weibull statistical analyses. Alloys studied in previous years of the program have been included in this study. Additionally, two new alloys cast in collaboration with the Howmet Corporation have been added to the program on variability: Ti-47Al-2Cr-1.9Nb (fast and slow cooled) and Ti-45Al-2Nb-1.3Mn + 1.1at%B XD™. In the "48-2-2" type materials, the Weibull moduli varied from 10 to 95, with the higher values associated with samples machined from a single plate of smaller grained (faster cooled) material. The XD material, with the finest grain size and most uniform microstructure, also had a high modulus of 50. These results collectively suggest that fine-grained material is desirable in terms of minimizing property variability and for obtaining the highest levels of ductility for a wide range of composition and microstructure.

5.2 Microstructure and Tensile Properties as a Function of Casting Cooling Rates

In this section we examine cast structure and tensile property variability for three alloys with nominal compositions of Ti-48Al-2Cr-2Nb, Ti-47Al-2Cr-1.9Nb and Ti-47Al-2Cr-2Nb+0.5at%B. Depending on the cooling rates, extent of segregation and the hot isostatic pressing (HIP) temperature, alloys in this composition range form either fully lamellar microstructures composed of α_2/γ lamellar grains, or duplex microstructures consisting of lamellar grains and varying volume fractions of γ grains. The objective of this study has been to examine the evolution of structure as a function of cooling rate and determine its influence on tensile properties. The results reported here build on prior work reported in the 1998 Annual Report (Pollock and Steif, 1998).

5.2.1 Materials and Experimental Procedures

A series of 8 investment cast plates (plates 1 through 8) with dimensions 10.2 cm x 10.2 cm x 1.27 cm (0.5 inches thick) were utilized in this study. Additionally, two investment cast plates (plates 1-II and 3-II) with dimensions 10.2 cm x 15.2 cm x 1.91 cm (0.75 inches thick) were produced for this experiment. Investment mold preheat temperature and the degree of mold insulation were varied in order to influence cooling conditions. For plates 1 through 8, three mold preheat temperatures, 315°C, 815°C and 1204°C, were used along with varying degrees of mold wrapping with Kaowool insulation. These experiments are described in greater detail elsewhere (Rishel et. al. 1997; Muraleedharan et. al. 1997). For plates 1-II and 3-II, two mold preheat temperatures of 370°C and 650°C were utilized along with an insulating wrap around the cluster.

To estimate cooling rates during casting, a one-dimensional heat transfer analysis was performed utilizing the UES ProCAST simulation package. Measured plate and shell thicknesses were used to establish the casting and mold geometry. Due to lack of thermal data for Ti-48Al-2Cr-2Nb or Ti-47Al-2Cr-2Nb+0.5at.%B alloy, thermal properties for Ti-45Al-2Cr-2Nb+0.9at.%B were utilized in the analysis. Liquidus temperatures obtained from the binary TiAl phase diagram (Kattner et. al. 1992) and a non-equilibrium solidus temperature of 1438°C were used for casting simulations. Investment shell properties were provided by Howmet Corporation. Measured shell temperatures at the outer shell surfaces of the cast plates were used as thermal boundary conditions. A variable interface heat transfer coefficient between the metal and the mold was assumed and this same interface condition was used for all simulations.

Following casting, plates 1 through 8 were subjected to a HIP cycle (hot isostatic pressing) of 1260°C / 170 MPa / 4h. Plates 1-II and 3-II were given a lower temperature HIP of 1093°C / 170 MPa / 4h. A summary of casting conditions is presented in Table 5.1 along with the estimated range of calculated local solidification times and cooling times to the binary equilibrium eutectoid temperature (1125°C) for plates 1 through 8.

Table 5.1: Mold preheat/wrap conditions and estimated cooling rates for 1.27 cm thick (plates1 - 8) and 1.91 cm (labeled x - II) thick plates.

Plate #	Alloy	Casting Conditions (Mold Preheat/Wrap Condition)	HIP treatment °C / MPa / hrs	Estimated Range of Local Solidification Time (sec) *	Time to 1125°C (sec) ♦
1	48-2-2	315 °C / Full Wrap	1260 / 170 / 4	11 - 26	39
2	48-2-2	315 °C / Partial Wrap	1260 / 170 / 4	10 - 25	39
3	48-2-2	815 °C / No Wrap	1260 / 170 / 4	13 - 30	55
4	48-2-2	1204 °C / Partial Wrap	1260 / 170 / 4	20 - 47	178
5	48-2-2	1204 °C / Full Wrap	1260 / 170 / 4	186 - 222	1097
6	Int. B	315 °C / No Wrap	1260 / 170 / 4	10 - 24	35
7	Int. B	815 °C / Partial Wrap	1260 / 170 / 4	13 - 31	60
8	Int. B	1204 °C / Full Wrap	1260 / 170 / 4	202 - 235	1217
1-II	47-2-2	650 °C / Cluster Wrap	1093 / 170 / 4	--	--
3-II	47-2-2	370 °C / Cluster Wrap	1093 / 170 / 4	--	--

* Range indicates times at surface and centerline, respectively.
♦ Time between non-equilibrium solidus and binary eutectoid (1125°C) temperatures at plate centerline.

Mechanical testing was conducted using an Instron constant extension-rate tensile testing machine with a nominal strain rate of 10⁻⁴/s. A total of 85 cylindrical tension specimens with a gage diameter of 4 mm and gage length of 19 mm were machined in accordance with low stress grinding procedures. Specimens were removed from each plate according to the illustrations shown in Fig. 5.1. Four specimens were removed from plates 1 through 8, with the exception of plate 2, where only one specimen was removed. In plate 2, the specimen position corresponds to the specimen labeled "4" in Fig. 5.1a. After testing, fracture surfaces were characterized in a scanning electron microscope (SEM). Subsequently, each specimen was sectioned transversely directly below the fracture surface for further microstructural characterization. These specimens were prepared metallographically and documented either with a light optical microscope or by SEM in backscattered electron mode (BSE).

Heat treatments described in this study were performed in air. Specimens were coated with a yttria slurry to reduce oxygen diffusion. All quantitative microstructural data was obtained from the specimen interiors well beyond the oxygen-affected surface regions of the 1 cm³ annealed samples. Grain size measurements were performed via the linear intercept method. The volume fraction of gamma grains in duplex microstructures was measured by the point counting method. It is important to note that each individual volume fraction measurement must sample a sufficient area given the inhomogeneity of the gamma grain distribution. In this study, volume fraction measurements were found to be reproducible provided that a minimum area of 3.5 mm² was sampled for each data point. In cases where samples were heat treated prior to mechanical testing, a tantalum

foil wrap was used and heat treatment was performed in a vacuum of 10^{-6} Torr. All reported oxygen analyses in this study were measured via Leco combustion analysis at the Howmet Corporation.
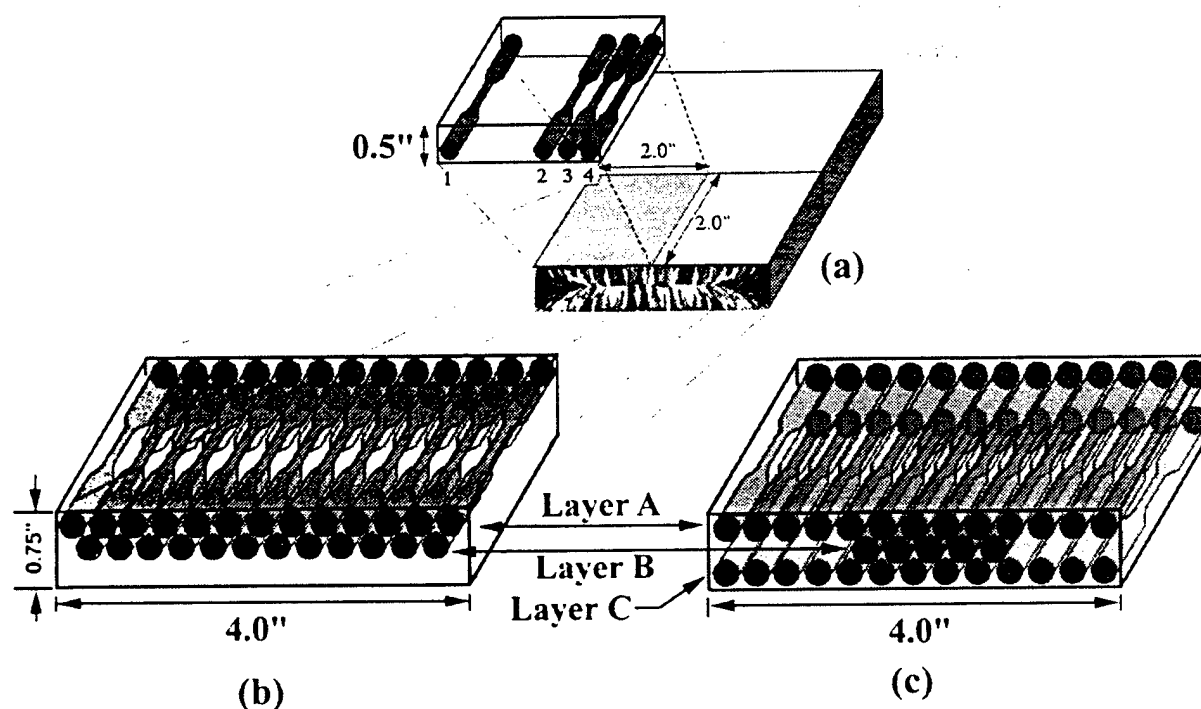

Fig. 5.1 -- Specimen configurations: plates 1 through 8 (a), plate 1-II (b), and plate 3-II (c).

5.2.2 Development of Macrostructure

Table 5.1 and the cooling curves shown in Fig. 5.2 demonstrate that a wide range of local solidification times and cooling rates are attainable by varying mold preheat and wrap conditions. Macrostructures as a function of cooling rate are shown in Fig. 5.3. It is apparent that the width of the columnar grains varies considerably from the fastest to the slowest cooled plates (Pollock and Steif, 1997; Muraleedharan et. al, 1997). Likewise, as expected from the estimated local solidification times in Table 5.1, there is relatively little macroscopic variation between plates 1 through 4 (Ti-48Al-2Cr-2Nb) and plates 6 and 7 (Ti-47Al-2Cr-2Nb + 0.5at%B). The slowest cooled plates, 5 and 8 (1204°C preheat / full wrap), on the other hand, solidified five to eight times slower and thus exhibit a correspondingly coarser columnar structure. Note also that the degree to which the columnar grains extend from the end of each plate (marked by "X" in Fig. 5.3) varies

to some degree with cooling rate. For the two 1.91 cm thick 47Al-2Cr-1.9Nb plates (1-II and 3-II), a higher mold preheat temperature increased the extent of the centerline equiaxed structure.
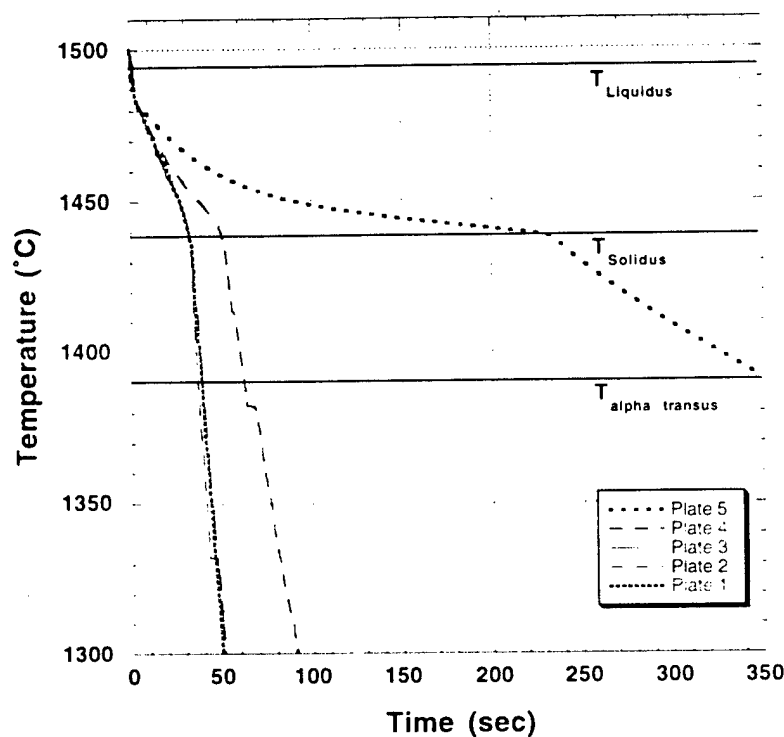
Fig. 5.2 -- 48-2-2 alloy cooling curves at 4 mm from mold wall estimated using UES ProCAST simulation. Liquidus, solidus and transus temperatures from the binary phase diagram (Kattner, 1992).

5.2.3 Development of Microstructure

The develpoment of microstructure in (47-48)Al-2Cr-2Nb plates depends on the cooling conditions during casting as well as on the HIP cycle. Fig. 5.4 illustrates the variation in HIPed microstructures for the fastest and slowest cooled plates of each alloy. As-cast microstructures for all ten plates were either fully lamellar (FL) or nearly fully lamellar (NFL), similar to Figs. 5.4b, d, and f. For the 48-Al-2Cr-2Nb alloy plates cast with relatively rapid cooling conditions, plates 1 through 4, HIPing in the $\alpha + \gamma$ phase field at 1260°C/170 MPa/4h results in a duplex microstructure composed of a mixture of γ grains and lamellar α_2 +γ grains (Fig. 5.4a). Ti-47Al-2Cr-2Nb+0.5at.%B alloys cast with approximately the same cooling conditions and processed with the same HIP cycle, plates

6 and 7, also had duplex microstructures; however, the gamma phase fraction was lower due to the lower aluminum content of this alloy.

When cooled slowly (local solidification times of the order of 200s), both alloys possessed a coarse fully lamellar as-cast microstructure that was retained even after subsequent HIP and heat treatment (Fig. 5.4b and 5.4f). At higher cooling rates, the volume fraction of gamma grains following HIP varied considerably with cooling conditions, particularly in the higher aluminum 48-2-2 alloy. Table 5.2 shows the average volume fraction of gamma grains in HIPed Ti-48Al-2Cr-2Nb material as a function of the approximate local solidification time at the plate centerline for plates 1 through 4. A twofold increase in local solidification time resulted in a 30% increase in the average lamellar fraction (and corresponding decrease in gamma grain fraction).

The micrographs in Fig. 5.4 also demonstrate that the HIP temperature influences final microstructure. Figs. 5.4c and 5.4d show the microstructure of the 47Al-2Cr-1.9Nb alloy following the 1093°C HIP cycle. Compared to the 47Al-2Cr-2Nb+0.5at.%B plates HIPed at 1260°C (Figs. 5.4e and 5.4f), it is apparent that a higher proportion of gamma grains are present. For both alloys, γ grains, when present, are located at aluminum rich interdendritic regions, as indicated by the BSE images in Fig. 5.4. Figs. 5.4e and 5.4f also reveal the presence of boride flakes within interdendritic regions for the 47Al-2Cr-2Nb+0.5at.%B alloy.

Given the increased solubility of titanium in the gamma single phase region near the eutectoid temperature, heat treatments at approximately 1093°C (just below the binary eutectoid temperature) maximize the fraction of gamma phase in 48-2-2 type alloys (Austin and Kelly, 1993; Austin et. al, 1997). The variation of the volume fraction gamma phase as a function of heat treatment time (after HIP) is shown in Fig. 5.5 for fast and slow cooled 48Al-2Cr-1.9Nb plates. Heat treatment times of 2 hours yielded only a minor increase in the gamma phase fraction for both the fast and slow cooled materials. At 4 and 6 hours, the gamma phase fraction increased by 8% and 14.5%, respectively, for the slow cooled plate 5. After 14 hours, the gamma phase fraction in the slow cooled plate increased by about 48%, compared to 23% for the fast cooled material. Comparison of plate 1 and plate 5 curves in Fig. 5.5 also indicates that the kinetics of the gamma transformation are sensitive to the starting structure. Transformation kinetics are slower at higher initial gamma phase fractions (plate 1), apparently due to the fact that the interdendritic regions highest in aluminum concentration had already transformed to gamma during HIP treatment.

Fig. 5.6 illustrates the evolution of duplex microstructure during HIP and heat treatment. The initially fully lamellar as-cast structure (Fig. 5.6a) begins to transform via a process of α_2 lamellae dissolution (Fig. 5.6b) within high aluminum regions. This is followed by formation of gamma grains (Fig. 5.6c).
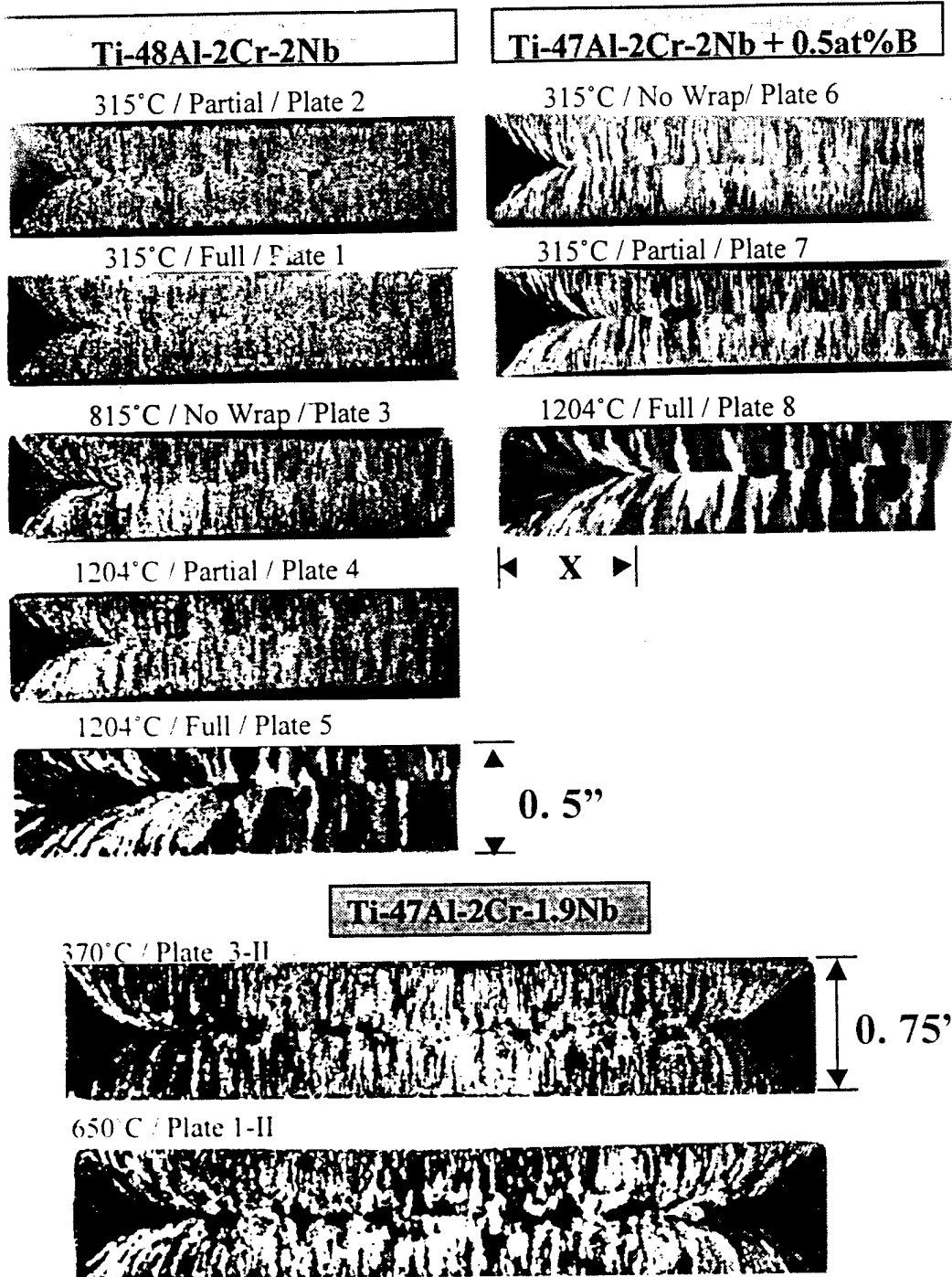
Fig. 5.3 -- Macrostructures of investment cast plates following HIP. Transverse cross-sections are shown with mold preheat / wrap / plate # listed above plate. Ti-48Al-2Cr-2Nb and Ti-47Al-2Cr-2Nb+0.5at.%B plates HIP'ed at 1260°C / 170 MPa / 4h. The Ti-47.9Al-2Cr-1.9Nb plates were given a lower temperature HIP of 1093°C / 170 MPa / 4h.
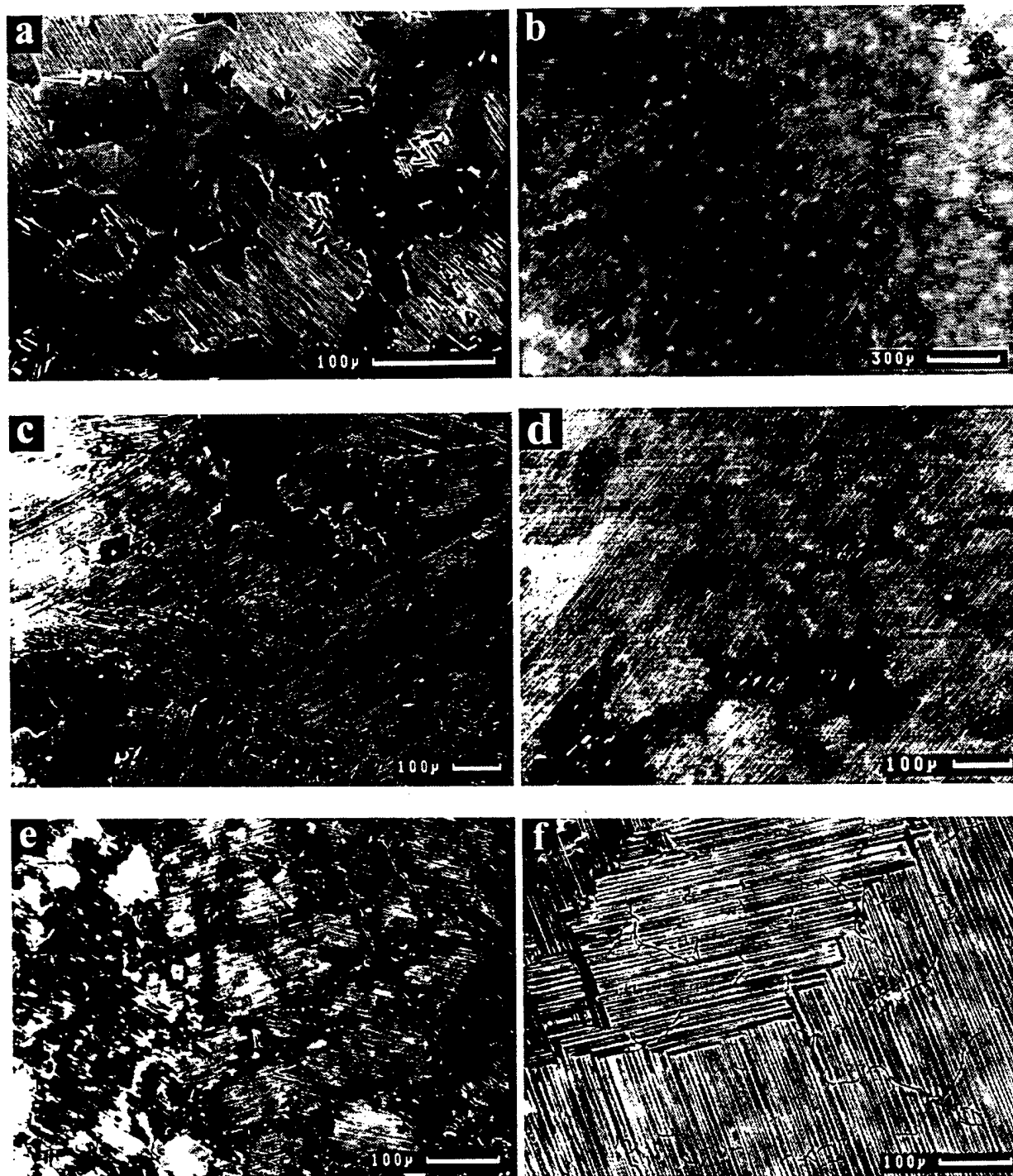
Fig. 5.4 -- Range of microstructures for 48Al-2Cr-2Nb HIP'ed at 1260°C, plate 1 (a) and plate 5(b); 47Al-2Cr-1.9Nb HIP'ed at 1093°C, plate 3-II (c) and plate 1-II (d); and Ti-47Al-2Cr-2Nb+0.5at.%B HIP'ed at 1260°C, plate 7 (e) and plate 8 (f).

Table 5.2 -- Variation of lamellar fraction with local solidification times at plate centerlines for 48-2-2 plates following HIP cycle of 1260°C/170MPa/4h.

Plate Number	Estimated Local Solidification Time at Plate Centerline (sec)	Average Lamellar Fraction (%)
2	25	43
1	26	45
3	30	55
4	47	60
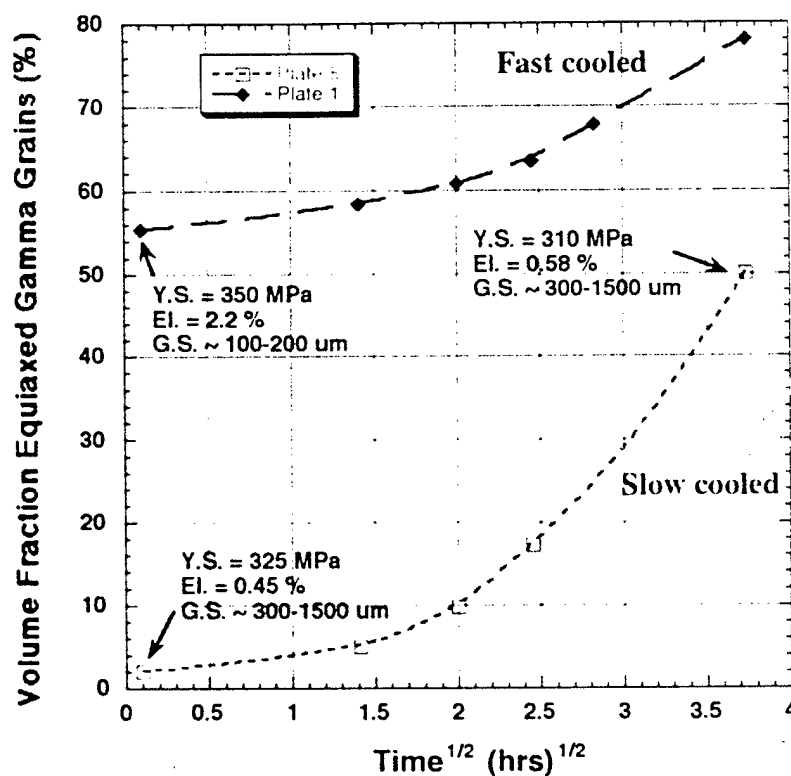
Fig. 5.5 -- Gamma transformation kinetics at 1093°C for two 48-2-2 castings; Plate 1 (fast cooled, initial gamma fraction = 55%) and Plate 5 (slowest cooled, nearly fully lamellar).

Microstructural variations within cast plates are illustrated in Fig. 5.7 and 5.8 for the 1.91 cm thick Ti-47Al-2Cr-1.9Nb plates (1-II and 3-II). For the slower cooled plate 1-II shown in Fig 5.7, the microstructure remains fully lamellar to a distance 4 mm below the surface of the casting. On the other hand, Fig 5.8 reveals that for the faster cooled plate 3-II, the fully lamellar microstructure transforms to duplex structure at approximately a 2 mm depth. These variations in surface structure may be due to differences in cooling rate during casting. Another possible factor influencing the stability of the lamellar structure in the slower cooled plate may be that higher mold preheat temperature and slower cooling promote surface diffusion of oxygen from the investment mold, thus stabilizing the alpha phase. However this is not supported by the oxygen analyses in Fig. 5.9, which shows oxygen enhancement to depths of only 0.5 to 0.8mm.
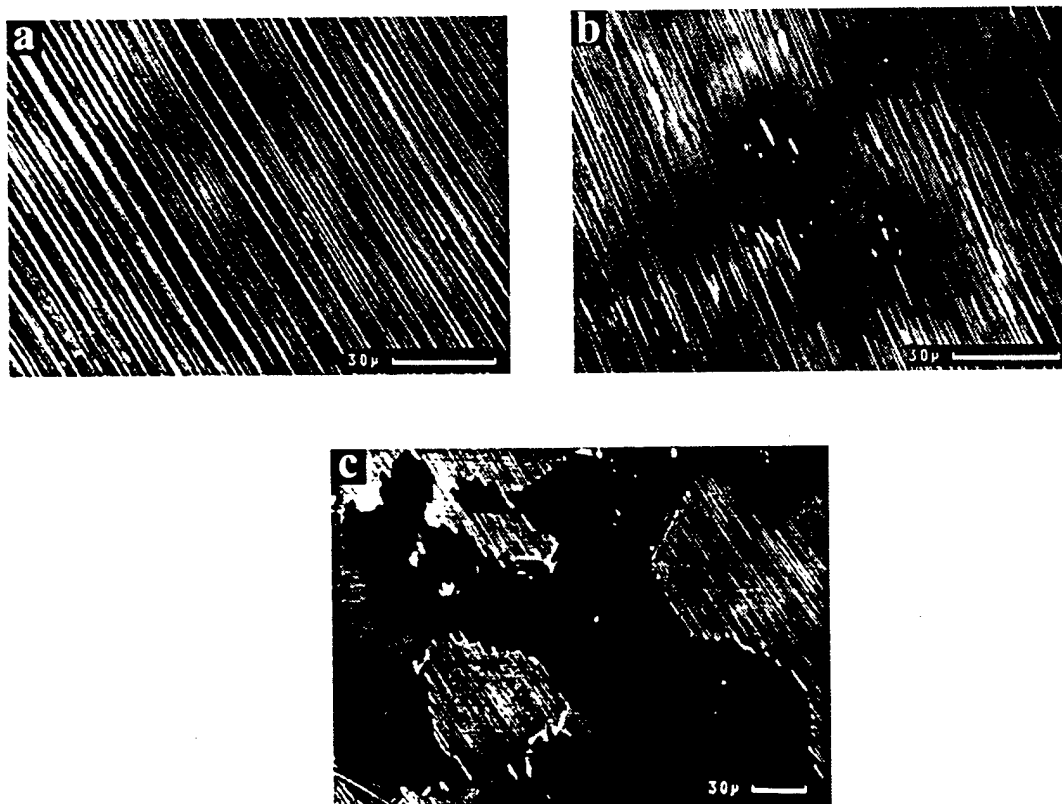
Fig. 5.6 -- Evolution of duplex structure during casting and HIP treatment; BSE micrograph revealing initially fully lamellar as-cast microstructure and composition gradients evidenced by the dark, Al-rich regions (a); Dissolution of α_2 lamellae within Al-rich regions during cooling or during HIP (b); Characteristic duplex microstructure following HIP or heat treatment between 1093°C and 1260°C (c).

5-10

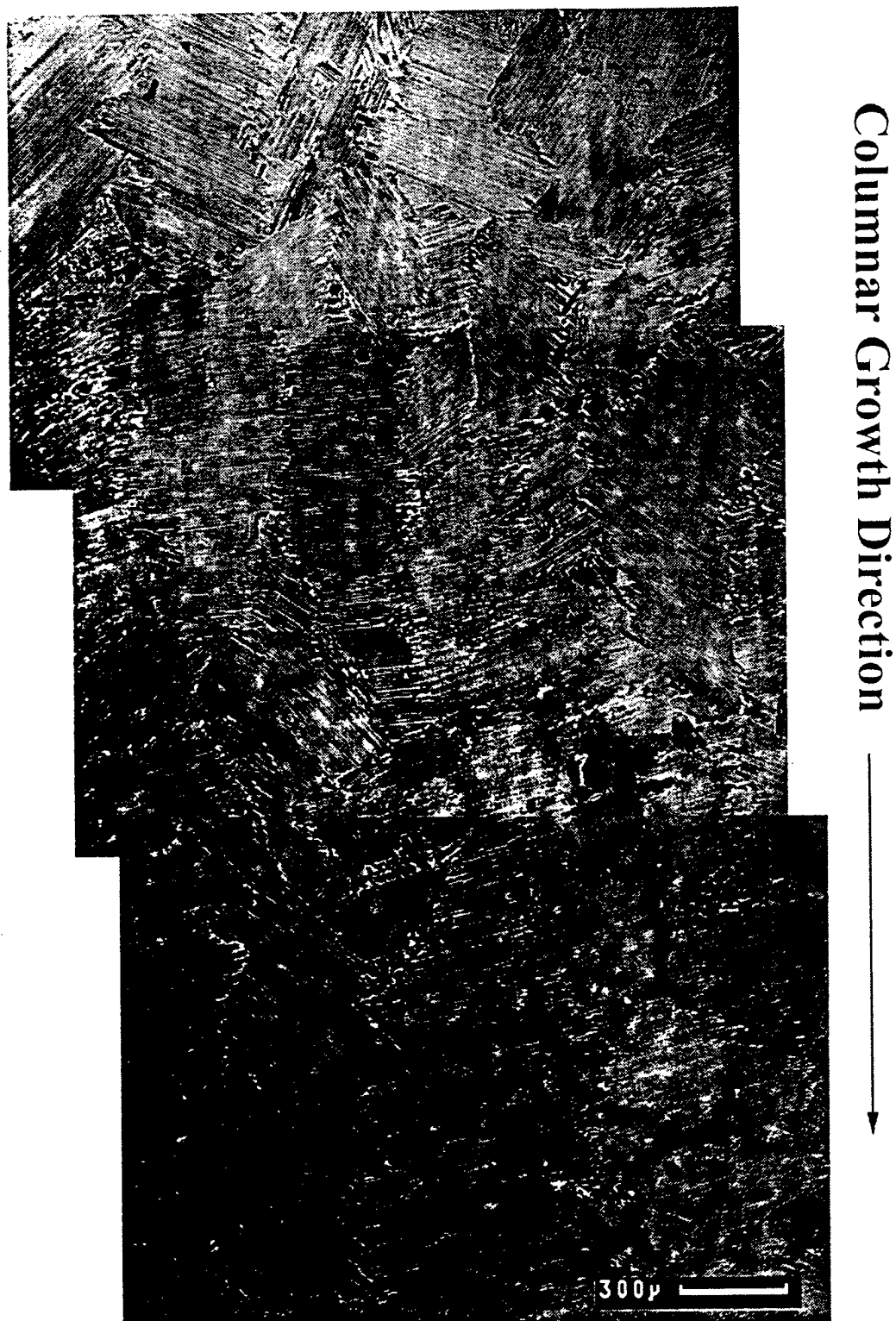**Columnar Growth Direction**

Fig. 5.7 - Plate 1-II (slow cooled Ti-47Al-2Cr-1.9Nb) microstructure from plate surface (top) towards plate interior. Note: interior microstructure is duplex (not shown).

Columnar Growth Direction

Fig. 5.8 - Plate 3-II (fast cooled Ti-47Al-2Cr-1.9Nb) microstructure from plate surface (top) towards plate interior.

.4l-2Cr-2 Nb

.tal of 17 tension tests were conducted on samples from Ti-48Al-2Cr-2Nb plates 1
.;gh 5. Specimen locations were configured in order to sample microstructural
.ility within each plate (Fig. 5.1). For example, a faster cooling rate is expected at
..e specimen #1 location shown in Fig. 5.1 due to accelerated heat transfer at plate ends.
With regard to the surface oxygen effects illustrated in Fig. 5.9, it is worth noting that
even specimens taken near the surface are unaffected by high surface oxygen levels since
this material was removed during machining.
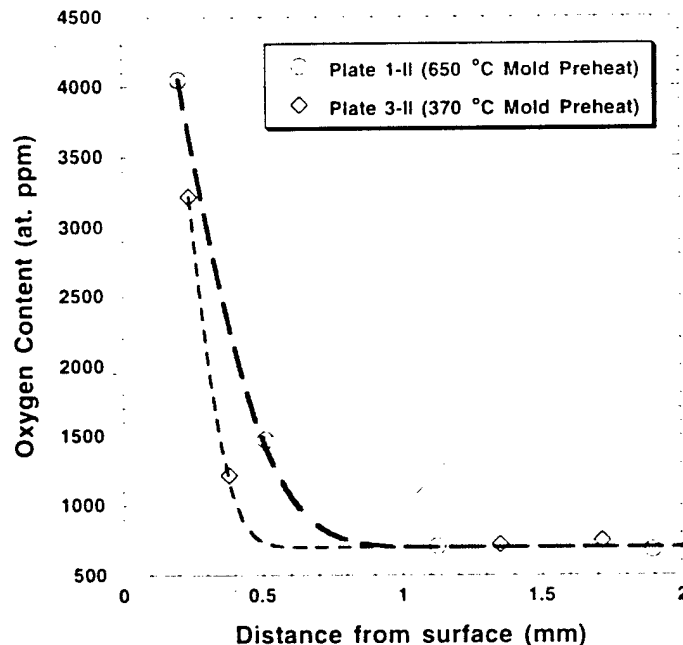
Fig. 5.9 -- Variation in oxygen concentration between the surface and interior of the cast
plate. Dashed curves represent error function fits to the experimental data. Data obtained
by Leco combustion test. Measurement error approx. +/- 60 wppm.

Room temperature tensile data is plotted in Fig. 5.10 as a function of position from the
end of the plate. Fig. 5.10a reveals that the yield strength does not exhibit a strong
variation with position in the plate with the exception of the slowest cooled plate 5 where
very low yield strengths were observed for interior plate specimens (specimens 2 through
4). Tensile ductility was more sensitive to position within the plate. Strains to failure for
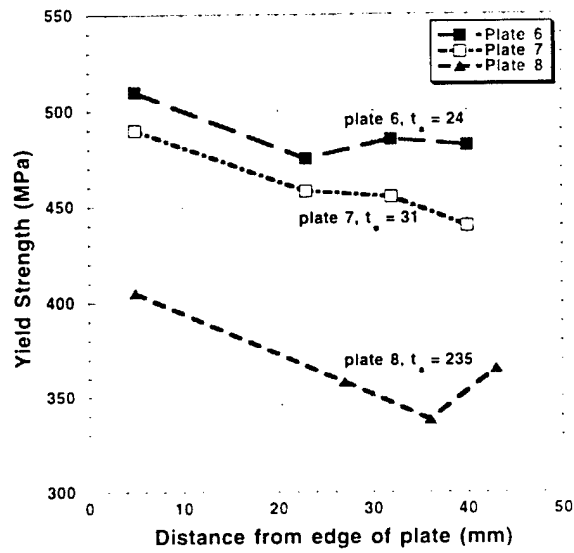samples in the interior regions of the plates, were lower, particularly for slower cooling
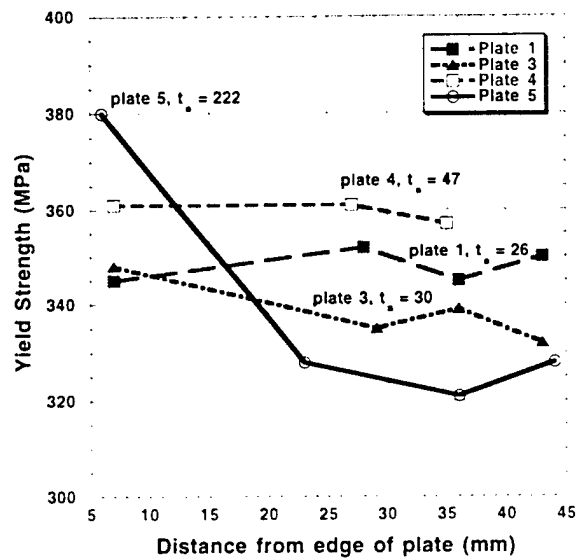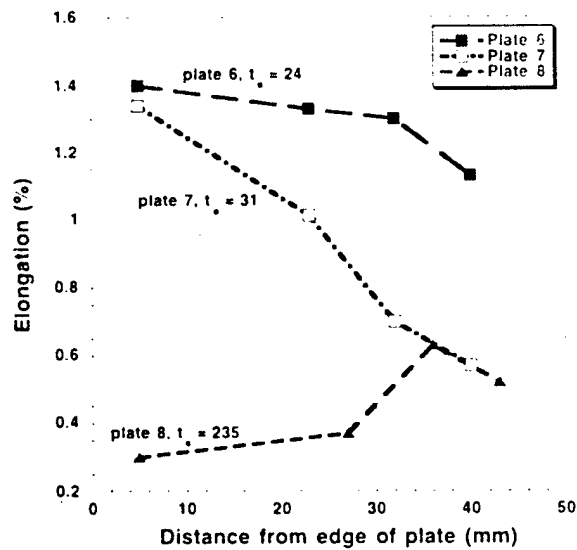
(a)
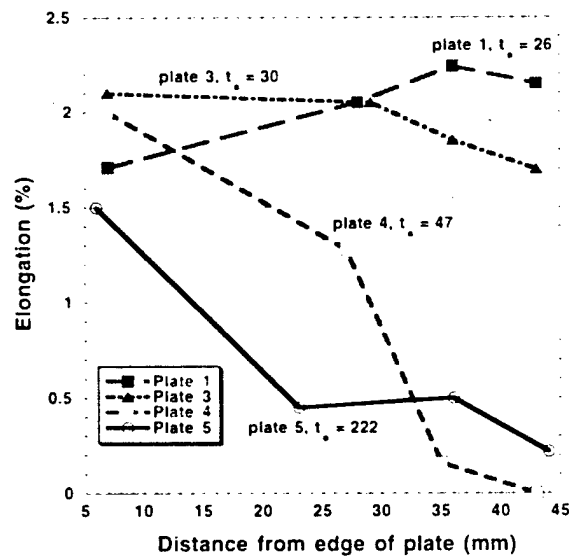
(b)

Fig. 5.10 -- In-plate variabillity for Ti-48Al-2Cr-2Nb alloy plates 1 through 5: yield strength (a), elongation (b). (t_s indicates local solidification time at the plate centerline)

(a)

(b)

Fig. 5.11 -- In-plate variability for Ti-47Al-2Cr-2Nb+0.5at.%B alloy plates 6 through 8: yield strength (a), elongation (b). (t_s indicates local solidification time at the plate centerline)

rates. For example, the ductility of plate 5 varied from 1.5% at the surface to 0.2% in the interior. Ductilities for plate end specimens exhibited a range of about 0.6% with a minimum of 1.5%. Examination of fracture surfaces revealed a characteristic transgranular and translamellar fracture mode associated with the faster cooled, duplex γ grain/lamellar microstructure (plate 1). The interior plate 4 specimens with tensile ductilities of <0.2% failed prematurely due to the presence of surface connected porosity that was not 'healed' during HIP treatment. For the slowest cooled plate (plate 5), interlamellar fracture was observed in low ductility specimens, apparently due to very large grains at the plate interior.

Ti-47Al-2Cr-2Nb+0.5at.%B

Microstructure variation in 47Al-2Cr-2Nb+0.5at.%B plates also results in a corresponding variation in tensile properties. Comparison of yield strengths in fast cooled plates with data obtained by Austin and Kelly (1993) for the same aluminum level, as well as data presented in the next section for Ti-47Al-2Cr-1.9Nb, shows that the addition of 0.5 at.% Boron to Ti-47Al-2Cr-2Nb alloys may result in yield strength improvement of up to 60 MPa. However, while high yield strengths were observed in fast cooled plates, a considerable yield strength variation of 170 MPa (with a minimun of 340 MPa, close to the faster cooled 48-2-2 material) was discovered over the range of cooling rates obtained in this study (Fig. 5.11a). Likewise, tensile ductility in plate 7 fell sharply at specimen locations in the interior of the plate (specimens 2,3,4), while ductilities in the slowest cooled plate remained uniformly low (Fig. 5.11b). Failure surfaces were dominated by interlamellar fracture at very large grains.

In Fig. 5.12, the average tensile ductility of Ti-48Al-2Cr-2Nb is compared to 47Al-2Cr-2Nb+0.5at.%B over a range of similar cooling rates. The average is taken from the interior specimens (2, 3 and 4, Fig. 5.1a). While the Ti-48Al-2Cr-2Nb alloy exhibited markedly higher ductility, it is interesting to note that the slowest cooled specimens for both alloys had a similarly low ductility of ~ 0.5%. For the same approximate range of cooling rates, variability in the ductility of the 47Al-2Cr-2Nb+0.5at.%B material was lower compared to the Ti-48Al-2Cr-2Nb alloy.

Ti-47Al-2Cr-1.9Nb

The thicker plate geometry of the 47Al-2Cr-1.9Nb plates (1.91 cm) allowed for sampling of surface as well as centerline microstructures (Figs. 5.1b and 5.1c). Yield strengths as a function of sample position in the plate are shown in Fig. 5.13a for layers A (surface) and B (center) of plates 1-II and 3-II. There is less variability in yield strengths for the faster cooled plate 3-II for layers A and B, labeled 3A and 3B, respectively. In the slower cooled material, the yield strengths of the samples along the plate centerline (layer 1B) were somewhat lower and more variable. Tensile ductility along the centerline (layer B) and surface (layer A) of the slow cooled plate 1-II are ranked from highest to lowest in

Fig. 5.13b. The variability in tensile ductility is much higher along the centerline of the plate, compared to the surface for the slow cooled plate. There is considerably less variability in ductility of the faster cooled plate in both the surface and centerline layers. Fig. 5.13c. Weibull analyses of these samples are shown in Section 5.3. Examinations of fracture surfaces revealed that high ductilities corresponded to translamellar/transgranular modes of failure, while low ductilities generally corresponded to interlamellar fracture.
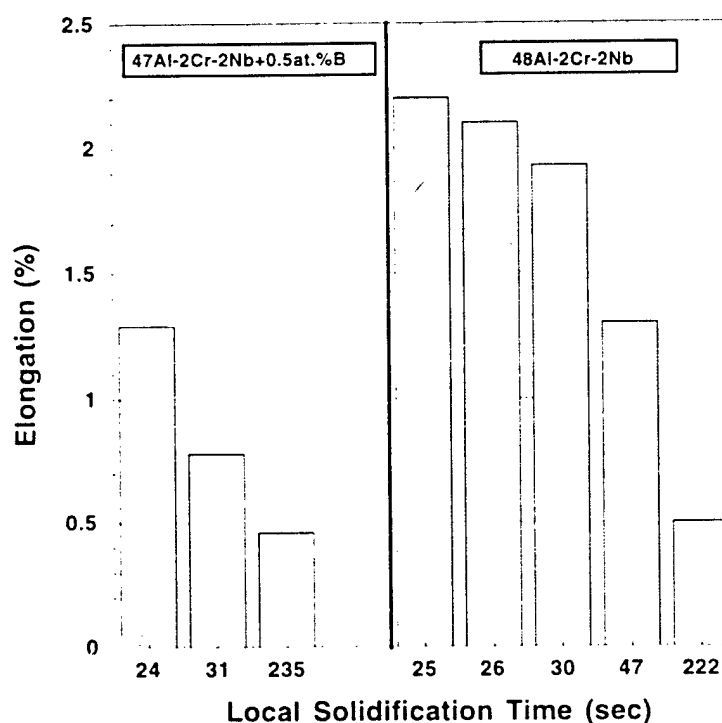

Fig. 5.12 -- Variation of average elongation for plate interior specimens with cooling rates for 48Al-2Cr-2Nb and 47Al-2Cr-2Nb+0.5at.%B alloys. (Samples which failed due to surface connected porosity in plate 4, local solidification time = 47s were excluded from the average).

5.2.5 Discussion: Microstructure and Property Variability in "48-2-2" Alloys

This study has shown that a considerable degree of variability in tensile properties, and in particular tensile ductility, results from variations in investment casting process parameters such as mold preheat and wrap. In Ti-48Al-2Cr-2Nb type alloys it has previously been shown that duplex structures exhibit higher ductility at room temperature compared to fully lamellar structures, though not necessarily at a constant grain size

(Huang, 1991). In other alloys, tensile ductility has been found to be sensitive to grain size (Kim, 1992, 1995; Dimiduk et. al, 1998). In this study, both grain size and the proportion of lamellar grains have been found to vary with the initial cooling rate during casting. From this it is apparent that a detailed understanding of the evolution of microstructure during casting and subsequent HIP and heat treatment cycles is needed in order to control (and reduce) property variability.
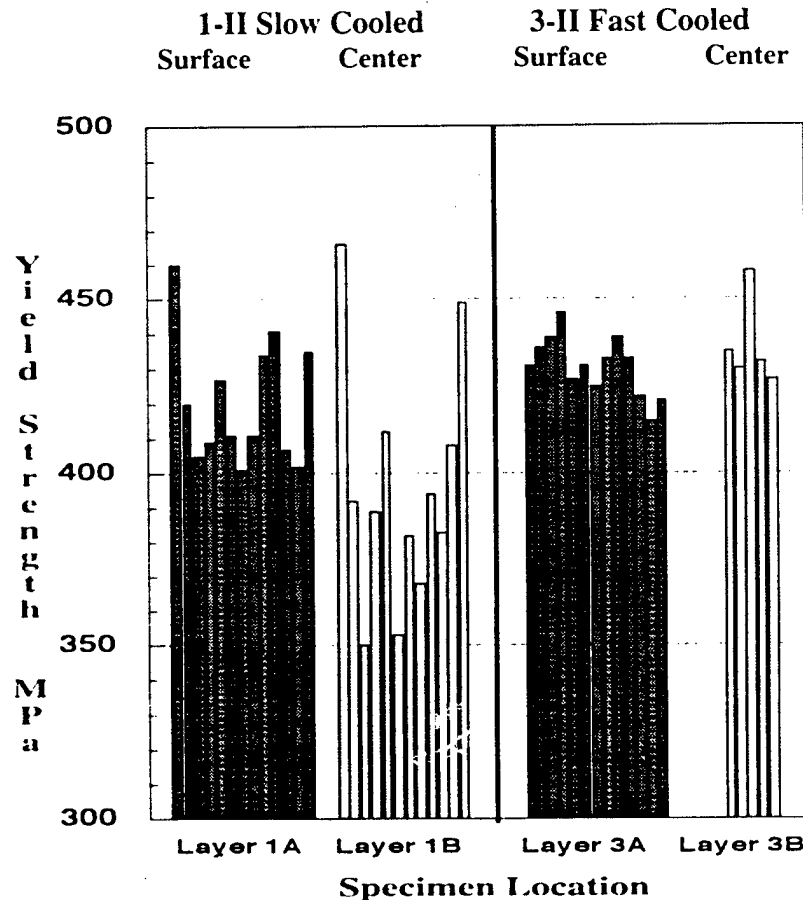

Fig. 5.13 -- Gamma fraction vs. position 1-II (a). yield Strength vs. position for plated 1-II (slow cooled) and 3-II (fast cooled)

Gamma transformation kinetics from an initially as-cast. fully lamellar microstructure will depend on the mechanism of formation of gamma grains. Here, it is proposed that gamma transformation occurs in multiple stages. Initially, aluminum segregation is present due to partitioning during solidification. The alignment of the residual α_2 phase in Al-rich regions shown in Fig. 5.6b with the surrounding lamellar structure suggests that α dissolution follows the formation of lamellar structure in the $\alpha+\gamma$ region. This
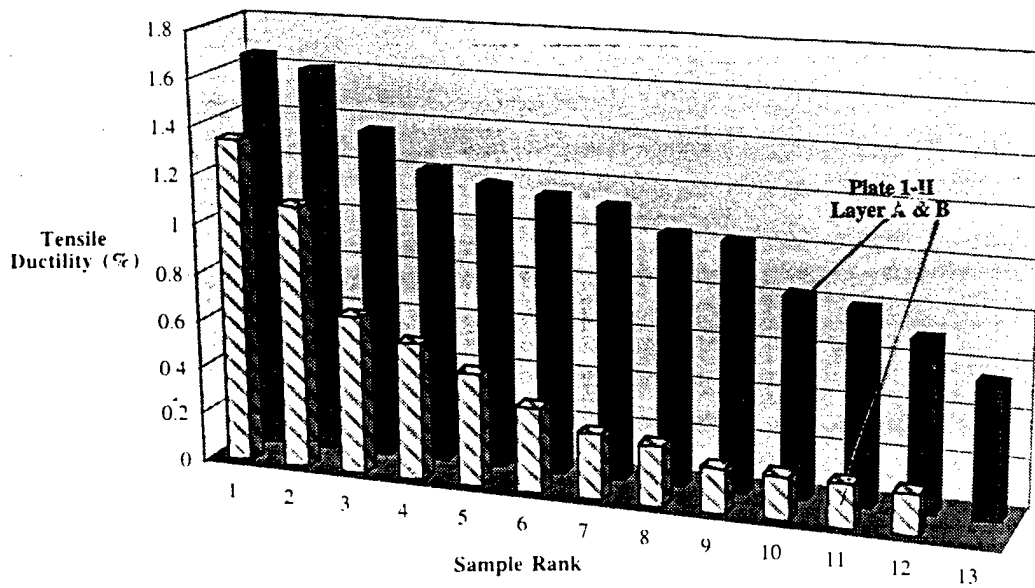
(b)
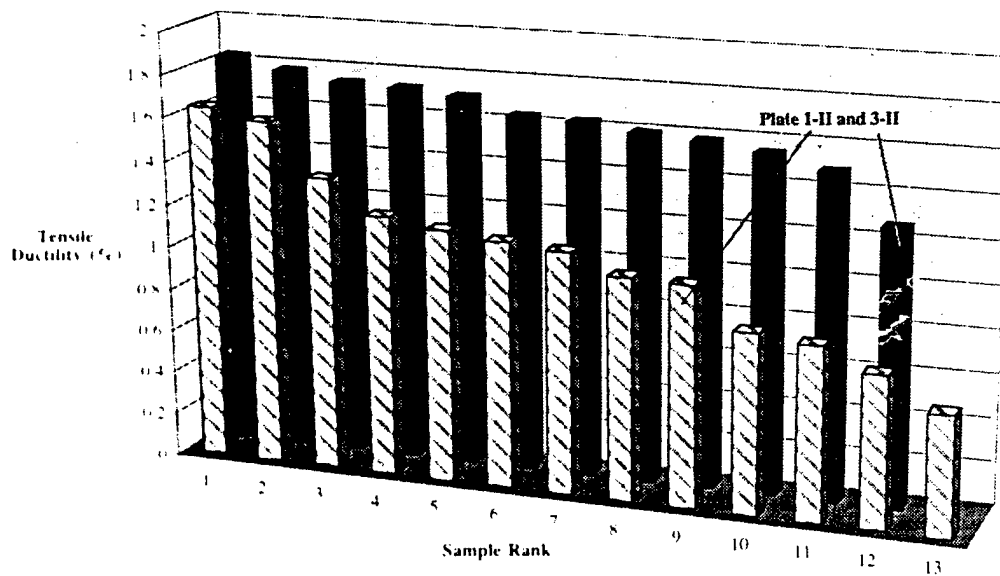
(c)

Fig. 5.13 – Yield strength vs. position 1-II (slow cooled) for Layers A and B (a), the influence of cooling rate on tensile ductility of layer A samples in plate 1-II (slow cooled) and 3-II (fast cooled) (b). Specimen locations are described in Fig. 5.1b & 1c. For example. 'Layer 1A' refers to specimens removed from Layer A positions in plate 1-II.

does not occur discontinuously along a reaction front (Mitao and Bendersky, 1995), but instead appears to proceed by the lateral shrinkage and breakup of laths, Fig. 5.6b. Upon complete dissolution of α_2 lamellae in the Al-rich interdendritic regions during HIP or heat treatment, two possible mechanisms for the formation of the equiaxed gamma grains include either recrystallization or coarsening of γ lamellae. It is presently unknown which process is more important, since changes in the crystallographic orientation of the gamma grains within the interdendritic gamma phase regions have not yet been investigated.

It is expected that the stability and thickness of the α_2 lamellae is enhanced at slow cooling rates due to a considerable amount of time spent in the high-temperature regime of the $\alpha + \gamma$ phase region. Moreover, subsequent dissolution of α_2 is more difficult in slower cooled plates given the larger lamellar spacings and correspondingly longer diffusion distances. Hence, a fully lamellar microstructure can be retained following HIP provided that the as-cast cooling rates are sufficiently slow. However, it has been shown that heat treatment of fully lamellar HIPed microstructures at 1093°C can result in gamma phase fraction increases of 8% and 14.5% after 4 and 6 hours, respectively (Fig. 5.6). Therefore, while it is possible to decompose the lamellar structure in the slowest cooled plates, the time scale for significant decomposition is beyond the length of a typical HIP cycle. For faster cooled plates, the development of gamma grains following HIP of fully lamellar 48Al-2Cr-2Nb plates is also sensitive to cooling conditions. Table 5.2 shows that for a range of local solidification times between 25 and 47 seconds, the average gamma fraction varied by 17%. Likewise, average gamma fractions within the slow cooled 47Al-2Cr-1.9Nb plate ranged from 22% near the plate ends (faster cooling conditions), to 8% at the plate interior.

For the 47Al-2Cr-2Nb+0.5at.%B alloy, boride flakes are located at interdendritic areas. For boron concentrations greater than 0.5 at.%, borides have been found to act as heteronucleants resulting in the formation of a uniform equiaxed microstructure rather than a columnar structure (Christodoulou et. al. 1988). However, for the 47Al-2Cr-2Nb+0.5at.%B alloy examined here, the boron addition appears to have a minimal effect on the final macrostructure (Fig. 5.3) or microstructure. While it has been shown that boride particles suppress grain growth for heat treatments above the alpha transus (Saha et. al. 1990, De Graef et.al 1997); observation of grain size in slow cooled 48Al-2Cr-2Nb and 47Al-2Cr-Nb+0.5at.%B plates (Figs. 5.4b and 5.4f) indicates that the formation of large grains during solidification is not impeded by the presence of interdendritic boride flakes.

Tensile Properties

The primary factor that influences tensile properties is the scale of the microstructure. Finer grain sizes in fast cooled materials contribute to enhanced ductility by limiting the maximum size of an initiation crack to the dimensions of the grain. This is consistent

with the observation of higher tensile ductilities in fine-grained thermomechanically processed materials (Fuchs, 1992). Fig. 5.13 illustrates that a variation in mold preheat temperature of only 270°C between plate 3-II (faster cooled, 370°C preheat) and plate 1-II (slower cooled, 650°C preheat) significantly influences properties. For the faster cooled plate 3-II, not only is ductility enhanced compared to the slower cooled plate 1-II, but variations in both yield strength and elongation as a function of position are reduced as well. For plate 1-II, slow cooling resulted in particularly low ductilities at the plate centerline, where fracture within large grains was observed to be largely interlamellar in character. Faster cooling resulted in increased gamma grain fractions following HIP, resulting in a characteristic transgranular/translamellar fracture mode.

It is clear that large lamellar colonies that develop as a result of very slow cooling rates represent the most significant source of property variability for all three alloys in this study. This is readily apparent by comparison of the range of ductilities observed in Ti-47Al-2Cr-1.9Nb fast cooled plate 3-II and slow cooled plate 1-II, Fig. 5.13b. In the next section, this variability due to cooling rates is captured in Weibull analyses of tensile properties. Large grains in plate 8 and at the interior of plate 7 also resulted in a sizable reduction in yield strength and elongation (Fig. 5.11). It is worth noting that the most slowly cooled Ti-48Al-2Cr-2Nb plate 5 exhibited less variability in ductility, but had a uniformly low tensile ductility due to the large lamellar colony size. The deleterious effects of large lamellar colonies was also apparent in the fracture surfaces of specimens originating from the slowest cooled regions of all three alloys. SEM analyses indicated that interlamellar delamination occurred preferentially at lamellar colonies oriented at angles near 45° with respect to the tensile axis. Since plastic straining strongly depends on the orientation of lamellar interfaces with respect to the tensile axis (Zin et. al. 1997, Umakoshi et. al. 1992) variations in the yield strength and ductility are expected, particularly considering the large colonies observed in the slowest cooled plates.

The deleterious effects of large grains in the 48Al-2Cr-2Nb alloy persist, even after significant duplex structure formation resulting from a 14 hour heat treatment at 1093°C (Fig. 5.6). Fig. 5.6 illustrates that when the slow cooled, large grain, plate 5 was heat treated at 1093°C for 14hrs, the fraction of gamma grains was similar to the fast cooled plate 1. However, the ductility and yield strength of the heat treated plate 5 specimen were essentially unaltered, in spite of the high gamma grain fraction. This observation suggests that the prior as-cast lamellar colony size is the primary factor controlling the ductility of duplex microstructures.

To accurately measure the average or minimum properties of large-grained microstructures which evolve from an initial columnar cast structure, larger samples of various orientations should be utilized. However, it is also important to note that components such as turbine airfoils may only contain several grains in their cross-section.

Finally, an additional cause of low ductility and increased variability in the 48Al-2Cr-2Nb alloy is surface connected porosity. The existence of surface connected porosity in slow cooled castings arises primarily due to high mold preheat temperatures (Rishel et. al, 1997). Fig. 5.10 shows low tensile ductility for the two innermost specimens (3 and 4) in slow cooled plate 4: this was a result of the presence of surface connected porosity that did not close during HIP. Thus it is apparent that slow cooling rates during casting may be detrimental due to the formation of very coarse microstructures and/or due to the likelihood that surface connected porosity will be present.

5.3 Quantification of Variability and Weibull Analyses

The experiments of the previous section have shown that titanium aluminides may be subject to substantial property variability over the range of conditions likely to be encountered in industrial casting processes. The limited tensile ductility coupled with the variability in this property and the mounting evidence for a dependence of the ductility of γ-titanium aluminides on strained volume (Knaul et al., 1999, Pollock and Steif, 1997) suggests that a probabilistic approach to the prediction of fracture strengths may be useful. This type of analysis is often used when evaluating the properties of ceramics that are "flaw sensitive" materials. Extrinsic flaws such as surface connected porosity and machining damage have been found to be particularly detrimental to tensile properties (Pollock and Steif, 1997, 1998, Rishel et. al, 1998). As discussed in the previous sections, intrinsic features of microstructure of most importance to tensile properties include grain size, γ/α_2 volume fraction and distribution, texture and segregation. To quantify the contributions of these features of TiAl castings to property variability, Weibull analyses of tensile data generated over the course of this program have been conducted.

A Weibull analysis assumes that the properties of a material are related to flaws that are distributed at random throughout the material. As a consequence, the average properties of a material will decrease as the sample volume (or sample area, depending on the flaw type) increases, and vice versa, because a larger amount of material will contain more flaws than a smaller one. This behavior is typical in ceramics (Savitz, 1999), but has also been observed in conventional metals such as duplex stainless steels (Besson et al., 1997). The situation is less severe in a material that exhibits some ductility; a flaw may not lead to any significant reduction in strength if there is sufficient ductility to reduce the stress concentration associated with the flaw. Gamma titanium aluminides, like other relatively ductile intermetallics, lie somewhere between the brittle behavior of a ceramic and the ductile behavior of a metal. Thus an additional question is whether such an analysis can be utilized for the prediction of the behavior of samples with different strained volumes. This question is addressed in Section 6.

To remove as many sources of variation as possible, the first analysis was conducted on samples from a single plate of "Baseline-1" Ti-47.9Al-2Cr-2Nb material. A total of 34 cylindrical threaded samples, each with a gage diameter of 4 mm (0.160") and gage length of 19 mm (0.75") were machined at Metcut Research Associates with standard low

stress grinding procedures. The results of these tests are shown in Table 5.3. The ductility variation for this particular plate was relatively low, ranging from 1.2% to 2.2%.

In a Weibull analysis, the probability of failure, F, is:

$$F = 1 - \exp\left[-\frac{1}{V_o} \int \left(\frac{\sigma - \sigma_\mu}{\sigma_o} \right)^m dV \right]$$

where σ is the failure stress, σ_μ is a threshold stress below which no failures occur (taken as zero in the analysis, to be consistent with analyses conducted on ceramic materials). σ_o is a characteristic strength of the distribution (in this case the stress at which the probability of failure is 63.2%), V is the volume of the strained gage section and m is the Weibull modulus. A higher Weibull modulus is associated with a lower degree of variability in the failure strength of the material. The Weibull modulus and characteristic strength can be extracted from a dataset by first ranking specimens on the basis of their failure stress to obtain a failure probability, F:

$$F = \frac{n}{(N+1)}$$

where n is the sample rank and N is the total number of samples. The failure probability as a function of failure stress is then plotted on a logarithmic scale, as shown for the Baseline-1 plate in Figure 5.14. It can be seen that the Weibull modulus for this slab of material is quite high (over 90); no sample failed at a load less than 415 MPa and none failed above 445 MPa.

To evaluate the additional influence of plate to plate variation within a single heat of material, tensile data from an additional 4 plates of material cast from the same "Baseline-1" heat of material (under nominally constant casting conditions) were tested with the same cylindrical specimen configuration. The results, shown in Table 5.4, reveal a considerably lower Weibull modulus of $m = 22$. Analyses of fracture surfaces of the Baseline-1 samples revealed occasional large grains in the vicinity of the fracture initiation sites, but no "extrinsic" failure origins, such as porosity. Including dogbone sheet-type specimens from several additional Baseline-1 plates further reduces the modulus to $m = 12.3$. The sheet specimens had gage section volumes up to a factor of 2.5 higher than the cylindrical specimens, but were subjected to different low stress grinding procedures. It is important to note that variability in failure strengths may increase when sampling multiple plates due to differences in microstructure that affect the yielding and subsequent plastic flow properties and/or differences in the plastic strains to failure (for a constant yield strength). In this Baseline-1 dataset, variability arises to a greater degree from variations in the yield strength from plate to plate, rather than from large shifts in

tensile ductility. This is most likely due to subtle differences in the investment casting process, as this set of plates were not all cast in a single mold.

Table 5.3 – Summary of Mechanical Tests on Specimens from a Single Ti-47.9Al-2Nb-2Cr "Baseline-1" Cast Plate.

SPECIMEN	UTS (MPA)	EL (%)*	SPECIMEN	UTS (MPA)	EL (%)*
A01	441	2.2	B01	429	1.8
A02	436	1.8	B02	442	2.1
A03	424	1.6	B03	440	2.0
A04	435	1.8	B04	417	1.2
A05	436	1.8	B05	439	1.8
A06	435	1.8	B06	441	1.9
A07	435	1.6	B07	435	1.7
A08	443	2.1	B08	418	1.3
A09	429	1.6	B09	423	1.4
A10	442	1.8	B10	436	1.7
A11	438	1.9	B11	437	1.6
A12	437	1.8	B12	437	1.8
A13	441	1.9	B13	441	1.8
A14	438	1.8	B14	437	1.9
A15	433	1.7	B15	440	2.0
A16	428	1.7	B16	434	2.0
A17	431	2.0	B17	440	2.1

* Plastic Strains to Failure
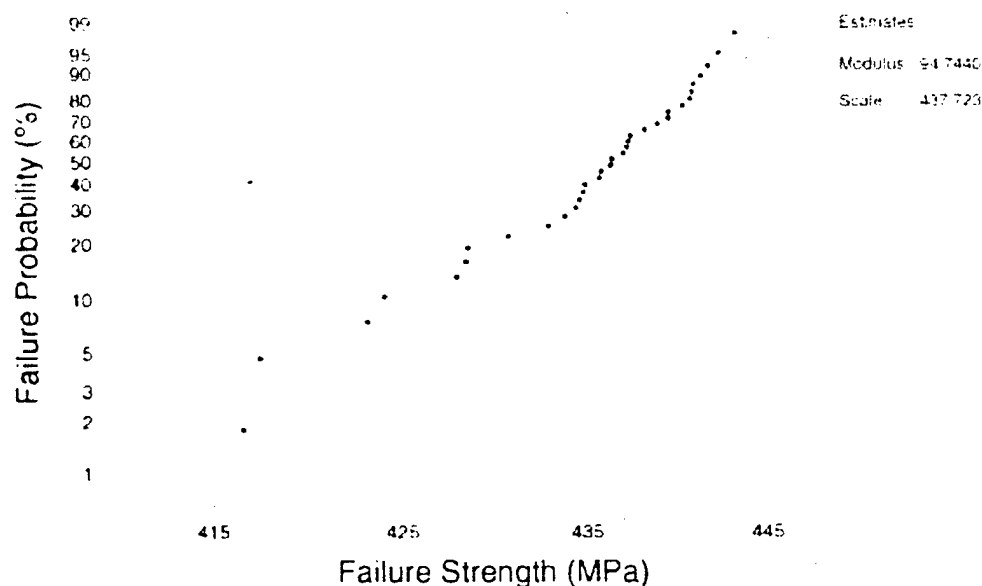
Fig. 5.14 - Weibull plot for "Baseline-1" specimens machined from a single cast plate.

discussed in Section 5.2, cooling rates during casting have a strong influence on microstructure and properties. Thus we have also analyzed the tensile data for Ti-47Al-1.9Nb plates I-II (slow cooled) and 3-II (fast cooled), Figs. 5.3 and 5.13. The results of Weibull analysis are shown in Figure 5.15(a) and (b). The Weibull modulus is substantially lower for the slow cooled material (10 vs. 36), which also has a lower average tensile ductility of 0.8%, compared to 1.5% for the faster cooled material.

The final set of tension experiments were on a Ti-45Al-1.3Mn-2Nb+1.1at%B XD plate cast with the higher mold preheat temperature of 648°C (1200°F). Compared to the Ti-47Al-2Cr-1.9Nb alloy cast under the same conditions, the Weibull modulus of the XD material is a factor of 5 higher, Table 5.4. The average tensile ductility of the slow cooled XD material was 0.8%, which is the same as that measured for the slower cooled 47 Al material. Thus it is apparent that while XD alloys have lower average tensile ductilities compared to "48-2-2" type alloys at higher casting cooling rates, under slow cooling conditions their average tensile ductility is comparable, and far less variable than "48-2-2" alloys.

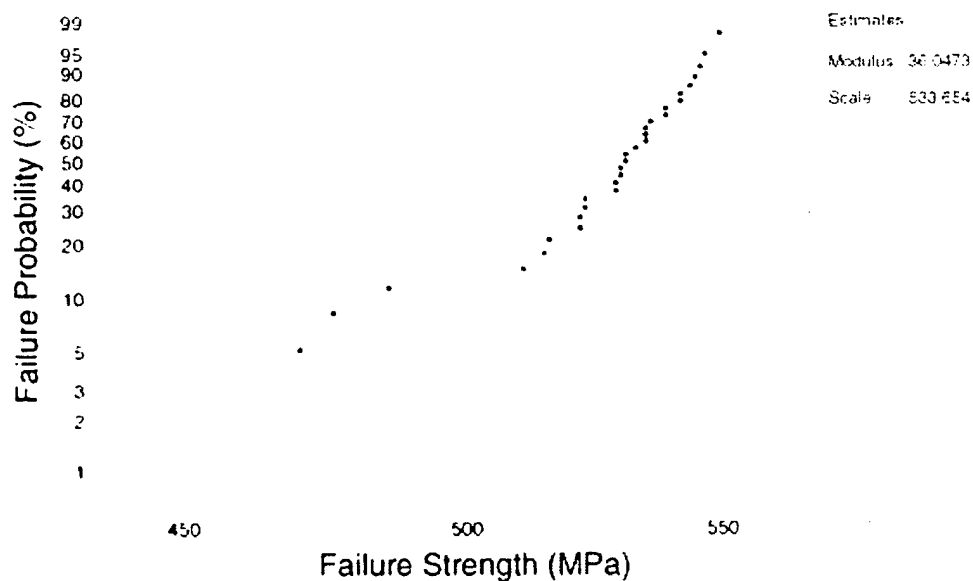Table 5.4 – Weibull Moduli of Gamma Alloys Compared to Several Advanced Ceramics

Material	Specific Elastic Modulus (GPa/g/cc)	Range of Failure Stress (MPa)	Range of Tensile Ductility (%)**	Weibull Modulus
"Baseline-1" Ti-47.9Al-2Cr-2Nb, Single Plate	44	417 - 433	1.2 – 2.2	95
"Baseline-1" Ti-47.9Al-2Cr-2Nb, Multiple Plates	44	370 - 434	1.4 – 2.1	22
"Baseline-1" Ti-47.9Al-2Cr-2Nb, Multiple Plates, Cylindrical and Sheet Specimens	44	310 - 434	0.4 – 2.1	12.3
Slow-Cooled Ti-47Al-1.9Nb-2.0Cr	44	349 - 549	0.2 – 1.7	10
Fast-Cooled Ti-47Al-1.9Nb-2.0Cr	44	440 - 550	0.3 – 2.2	36
Slow-Cooled Ti-45Al-2Mn-2Cr+0.9at%B XD™	44	508 - 557	0.5 – 1.0	50
*GS-44 Si_3N_4	97	--	--	20-35
*AS800 Si_3N_4	94	--	--	20-30
*SiC	125	--	--	7-10
*Al_2O_3 99.5%	99	--	--	5-25
*ZrO_2 (PSZ)	36	--	--	15-30

*Savitz, M., 1999   ** Plastic Strains to Failure

Estimates

Modulus 10.1381

Scale 480.757

Failure Probability (%)

Failure Strength (MPa)

(a)

Estimates

Modulus 36.0473

Scale 533.654

Failure Probability (%)
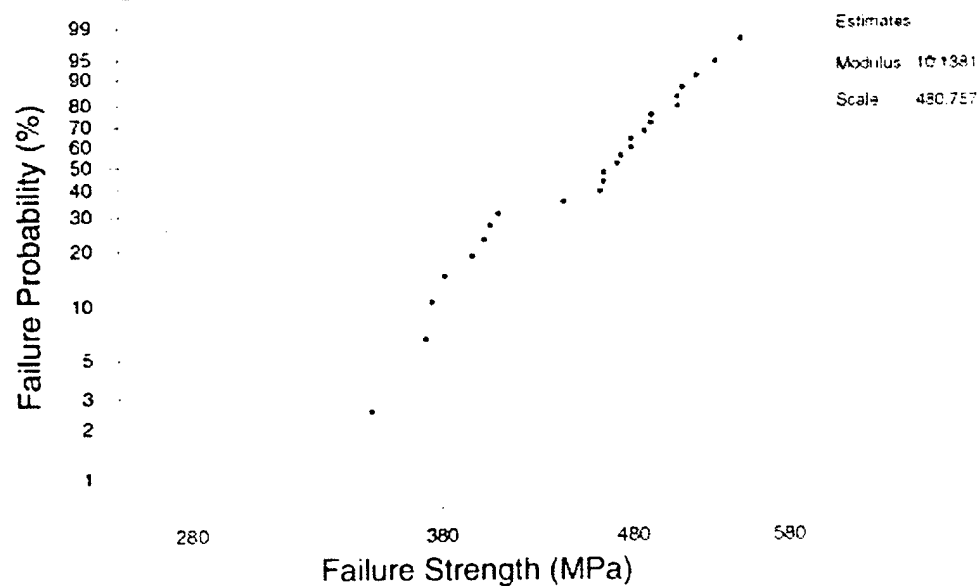
Failure Strength (MPa)

(b)

Fig. 5.15 - Weibull plots for slow-cooled Ti-47Al-2.0Cr-1.9Nb (a) and fast-cooled Ti-47Al-2.0Cr-1.9Nb (b).

5-26

Finally, it is worthwhile to note that the Weibull moduli in this set of cast TiAl alloys are generally higher than most advanced ceramics, Table 5.4. However, materials that cool slowly during casting do approach the same level of variability in failure strength as observed in ceramics. Nevertheless, even when high levels of strength variability are observed, the advantage of TiAl alloys is the small (though finite) level of tensile ductility, which leads to reductions in elastic stress concentration factors (Knaul et. al. 1999).

5.4 Future Work

Further studies on the decomposition of as-cast lamellar structure will be pursued; this process is important as it determines the final grain size of the cast material, which in turn has a strong effect on property variability. Cooling rate experiments to be conducted by the casting project in the CMU Induction Skull Melting unit are presently underway (Section 2.4). In the upcoming year we will examine the microstructure of cast plates as a function of cooling rate. Several binary and multicomponent compositions will be examined. These experiments will provide an important link to prior experiments that were conducted in the facilities at Howmet. Finally, additional effort will be aimed at measurement of Weibull moduli of various forms of material; the ultimate goal is to relate this to observations on local straining (Section 4.). As a part of this effort we will test cylindrical specimens with higher volumes in the strained gage section of the material. Finally, a comparison of the variability in cast plates and specimens removed from blade castings will also be made.

5.5 Acknowledgements

5.6 References

Austin C.M. and Kelly T.J., *Structural Intermetallics*, TMS, Warrendale, PA, (1993), 143-50.

Austin C.M., Kelly T.J., McAllister K.G. and Chesnutt J.C., *Structural Intermetallics*, TMS, Warrendale, PA, (1997), 413-25.

Besson J. and Pineau A., in "Recent Advances in Fracture", edited by Mahidhara R.K., pp. 125-136, The Minerals, Metals and Materials Society (1997).

Christodoulou L., Parrish P.A., Crowe C.R., *High Temperature, High Performance Composites*, ed. S.D. Lemkey, 120, Pittsburgh, PA, (1988), 29-34.

De Graef M., Hardwick D. A., and Martin P. L., *Structural Intermetallics*, TMS, Warrendale, PA, (1997), 185.

Dimiduk D.M., Hazzledine P.M., Parthasarathy T.A., Seshagiri S., and Mendiratta M.G., *Metall. Mater. Trans. A.*, 29A, (1998), 37-47.

Fuchs G.E., *Titanium '92*, Froes F.H. and Caplan I., eds., TMS, Warrendale, PA (1992), 1275 – 1282.

Huang S-C. and Shih, D.S., *Microstructure/Property Relationships in Gamma Titanium Aluminides and Alloys*, ed. Y-W. Kim and R.R. Boyer, TMS, Warrendale, PA, (1991), 135-48.

Jin Z., Gray G. T. and Yamaguchi M. *Structural Intermetallics*, TMS, Warrendale, PA, (1997), 225.

Kattner U., Lin J.C. and Chang Y.A., *Met. Trans. A*, 23A, (1992), 2081.

Kim Y-W., *Acta Metall. Mater.*, 40, (1992), 1121-34.

Kim Y-W., *Gamma Titanium Aluminides*, ed. Y.W. Kim, R. Wagner, and M. Yamaguchi, TMS, Warrendale, PA, (1995), 637-54.

Knaul D.A., Beuth J.L. and Milke J.G., Metall. Trans., **30A**, pp. 949-959 (1999).

Mitao S. and Bendersky L.A., *Gamma Titanium Aluminides*, Kim Y.-W., Wagner, R., and Yamaguchi, M., eds., TMS, Warrendale, PA, (1995), 181-188.

Muraleedharan K., Rishel L.L., De Graef M., Cramb A.W., Pollock T.M. and Gray G.T., *Structural Intermetallics*, TMS, Warrendale, PA, (1997), 215-224.

Pollock, T.M. and Steif P.S., AFOSR-PRET Annual Report, (1997).

Pollock, T.M. and Steif P.S., AFOSR-PRET Annual Report, (1998).

Rishel L.L., Pollock T.M., Cramb A.W., and Larsen D.E., *Proc. Of the International Symposium on Liquid Metal Processing and Casting*, Vacuum Metallurgy Division of AVS, (1997), 214-225.

Rishel L.L. , Biery N.E., Raban R., Gandelsman V.Z., Pollock T.M. and Cramb A.W., Intermetallics 6, (1998), 629 – 636.

Savitz M., *Ceramic Bulletin*, (1999), 53 – 56.

Umakoshi Y., Nakano T. and Yamane T., *Mat. Sci. Eng*, A152, (1992), 81-88.

6. Notch Strengthening in Titanium Aluminides Under Monotonic Loading

Jack L. Beuth
Jorge G. Milke
Carnegie Mellon University

6.1 Introduction

Titanium aluminides are seen as potential replacements for nickel superalloys in some aircraft engine components. TiAl components have been tested in both civilian and military aircraft engines, and low-pressure turbine blades in commercial aircraft engines are an initial application being pursued for these materials[1]. An important potential drawback for titanium aluminides is their limited ductility, particularly at room temperature. Another related issue is the variability in ductility currently observed in TiAl alloys. Although average total strains at failure in uniaxial tests are often in the range of 1 to 2 percent (which places them outside traditional definitions for ductile metals), it is also common for occasional specimens to exhibit monotonic tensile failure at a fraction of 1 percent total strain. Such variations can occur even in specimens machined from a single cast slab or component. Ductility limits and variability are of particular concern in the design of components having notches or other stress concentrators, where plastic flow may not be sufficient to reduce large stress concentrations. This suggests that some of the conservatism inherent in the design of components made out of more ductile superalloys may not exist in analogous TiAl components.

The control of process parameters to achieve consistent material properties throughout a TiAl casting is an important area of current research. Relationships between the control of casting parameters and the control of tensile ductility are considered directly by Raban, et al.[2] Work by Knaul, et al.[3] has shown that the ability to consistently achieve failure strains of 1 percent or more is sufficient to make TiAl components nearly notch insensitive under monotonic loading for components with elastic stress concentration factors as high as 2.4. This is an important barrier to overcome in notched component design and suggests that the average ductility seen in TiAl alloys, though significantly lower than that seen in the nickel superalloys they are meant to replace, is sufficient. Methods are also outlined by Knaul, et al.[3] for quantifying effects of average ductility and ductility variations on the load-carrying capability of notched components.

Notched specimen tensile tests performed in the work of Knaul, et al.[3] also indicate that the cast Ti-47.9Al-2.0Cr-2.0Nb alloy tested exhibits notch strengthening, where maximum strains at failure in notched specimens are, on average, larger than strains at failure in uniaxial tensile (unnotched) specimens. Increases in maximum failure strains correlated well with estimated decreases in the volume of material subjected to large strains, suggesting a size effect. Notch strengthening effects in fatigue are seen in most structural alloys and have been observed in TiAl alloys.[4] Under monotonic loading, notch strengthening and size effects are well-documented in brittle materials and Weibull statistical methods are commonly used to exploit this in the design of ceramic components.[5] Size effects have also been observed and modeled in the ductile rupture of carbon and stainless steels.[6] The review article by Bazant and Chen[7] provides a comprehensive

of material size effects, with an emphasis on quasi-brittle materials that exhibit stable
with before failure. The goal of this study is to further explore the issue of notch
ning or size effects in TiAl alloys with a methodical set of tests and detailed modeling
is includes tests on not only the near-gamma alloy considered by Knaul, et al.[11], but also
dominantly lamellar TiAl alloy to determine if such effects are alloy or microstructure
nt. If it exists, notch strengthening can provide designers of TiAl components an added
f conservatism when using failure strains obtained from tests on large, unnotched tensile
ens in their design criteria. It is even possible that statistics could be incorporated into TiAl
ng and design methods to allow designers to exploit this phenomenon, analogous to what is
done in ceramic component design.

In the next section, specimen geometries are described. Details of specimen preparation, including
locations within cast slabs from which specimens were taken, are also detailed. In the succeeding
section, results from tests performed on notched and unnotched specimens are presented.
Numerical models are used to relate the failure strains in notched specimens to those observed in
unnotched specimens. Plots showing failure stresses and strains as a function of specimen elastic
stress concentration are used to demonstrate the existence of notch strengthening. Volumes of
material subjected to large strains are estimated for each of the notched specimen types, and the
correlation between failure strain and highly strained volume is explored. Finally, experimental
results are compared with predictions of notch strengthening based on Weibull statistical methods.

6.2 Experimental Procedures and Specimen Geometries

Two alloys are considered in this study. The first has the composition Ti-47.9Al-2.0Cr-2.0Nb
and will be referred to from this point on as 48-2-2. This alloy was investment cast at the Howmet
Corporation and subjected to a heat treatment of 1093°C for 5 hours, HIPing at 1205°C and 172
MPa for 4 hours, and a final heat treatment of 1205°C for 2 hours, followed by rapid cooling. As
seen in the micrograph shown in Fig. 6.1, the microstructure for this alloy consists predominantly
of equiaxed γ grains with some small α_2 grains and approximately 7 volume percent lamellar grains
of γ and α_2. The average size of the gamma grains is on the order of 70 μm. The second alloy
considered has a composition of Ti-47.3Al-2.2Nb-0.5Mn-0.4W-0.4Mo-0.23Si and will be
referred to as WMS. The WMS material was investment cast at the Howmet Corporation and
subjected to a HIP treatment at 1260°C and 172 MPa for 4 hours, followed by a heat treatment at
1010°C for 50 hours. As seen in the micrograph shown in Fig. 6.2, the microstructure of this
alloy is fully lamellar with some β_2 and α_2 phases. The lamellar colony size is also on the order of
70 μm.

Specimens for each material type were machined from a single cast slab as shown in Fig. 6.3a.
Both slabs measured approximately 100 x 140 x 11 mm. Unnotched flat dogbone and notched flat
specimens with notch radii of 2 mm, 4 mm and 8 mm (further referred to as R = 2 mm, R = 4 mm,
and R = 8 mm specimens, respectively) were machined from each slab. Additionally, four 140 x
11 x 1.5 mm rectangular specimen "blanks" were machined in case results suggested another
notched specimen geometry should be considered. These blank specimens were not used. Also,
shorter, cylindrically shaped unnotched specimens conforming to a standard used by General

Electric Aircraft Engines were machined from locations closer to the center of the slab. These specimens were tested to relate their failure strains to those from flat dogbone specimens for a separate study of machining effects. They also provided additional stress vs. strain data for each material tested. Four specimens of each type were machined. All specimens are machined with their tensile axis along the longest dimension of the slab, designated as the x direction in Fig. 6.3a. Flat specimens were taken in the following order from each edge to the center of the slab: dogbone, blank, R = 2 mm, R = 4 mm and R = 8 mm.
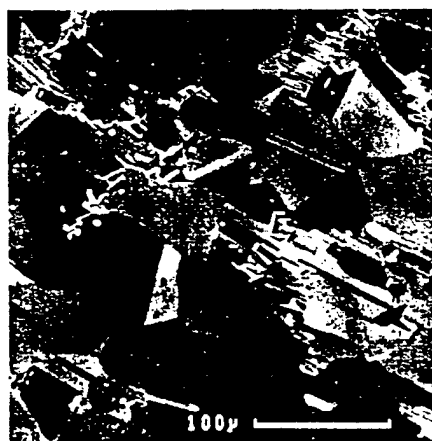
Figure 6.1   Micrograph typical of the near-notch region of the cast 48-2-2 alloy tested in this study.
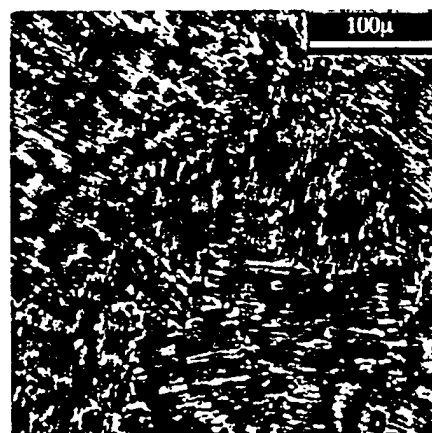

Figure 6.2   Micrograph typical of the near-notch region of the cast WMS alloy tested in this study.

Figures 6.3b through 6.3e detail the geometry of each flat specimen. All flat specimens (dogbone and notched) have a thickness of 1.5 mm, a total length of 140 mm, a maximum width (at the grip section) of 11 mm, and a minimum width (gage section width or distance between notches) of 6 mm. This consistency in flat specimen design meant that the only change from specimen to specimen was its y location in the slab and the radius of the notch used to create the 6 mm reduced section width. Furthermore, any significant changes in properties with y location could be discerned from the series of tests on flat dogbone specimens. The standard GE specimen (not

6-3

shown in Fig. 6.3) is a cylindrical specimen with threaded ends. The specimen's overall length is approximately 51 mm and the its gage section is 19.1 mm long and 2.03 mm in diameter.

a)

b)

c)

d)

e)
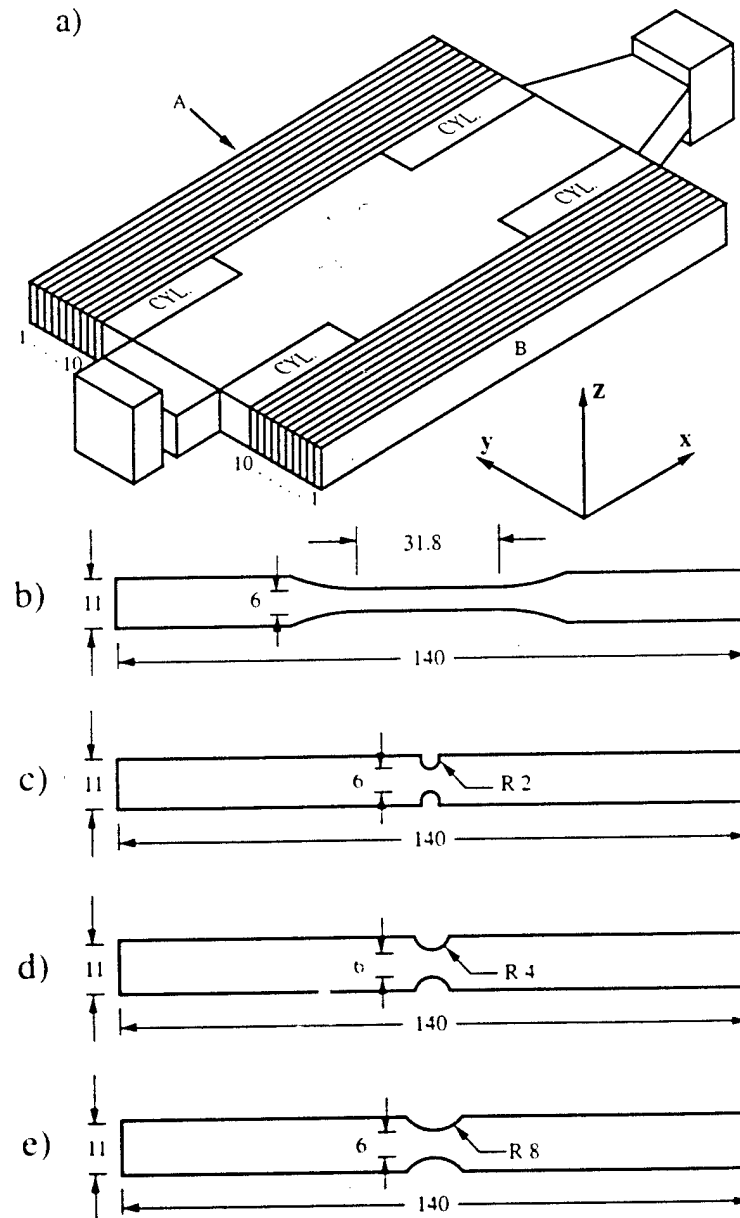
All Measures in mm
All Specimens 1.5 mm Thick

Figure 6.3   a) Specimen machining diagram;
              b) Dogbone specimen geometry (specimens #1 and #6);
              c) 2 mm radius notched specimen geometry (specimens #3 and #8);
              d) 4 mm radius notched specimen geometry (specimens #4 and #9);
              e) 8 mm radius notched specimen geometry (specimens #5 and #10).

The notched geometries were chosen to provide specimens with a range of elastic stress concentration (K_t) values and volumes of highly strained material. K_t values that resulted were 1.00 (for the unnotched specimens), 1.23, 1.47 and 1.85. In particular, the stress concentration of 1.23 for the 8 mm specimen was so mild that compared to a dogbone specimen the dominant effect of the notch was to cause failure to occur between the notches instead of anywhere along the dogbone specimen gage length. Thus the volume of highly strained material was reduced without introducing a significant gradient of stress or strain in the region experiencing failure. Estimates of the resulting volumes of highly strained material for each specimen are given in a later section and they indicate a wide range of values for these specimens. Specimens were machined by wire electrodischarge machining and machine ground with a 600 grit grinding wheel to a depth of at least 0.1 mm on all surfaces. This was followed by hand grinding with 320, 400 and 600 grit sandpaper. Specimens were then electropolished in a solution containing 30 ml perchloric acid, 175 ml n-butanol, and 300 ml methanol[8].

All testing was conducted on an Instron screw-driven testing machine. Flat specimens were held by 25.4 mm (1 in) wide self-tightening mechanical grips and were aligned within the grips through the use of specially machined spacers. For all flat specimens the loading rate was equal to 0.04 mm/min and displacements were measured using a 25.4 mm (1 in) gage length extensometer. In the notched (flat) specimen tests, the displacement was measured along the tensile axis, with the gage centered across the notch and across the specimen width. Cylindrically shaped unnotched specimens were held by threaded adapters. The loading rate for these shorter specimens was equal to 0.02 mm/min and displacements were measured using a 12.7 mm (0.50 in) gage length extensometer.

6.3 Experimental Results

Experimental results are summarized in Figs. 6.4 through 6.7 and in Table 1. For the specimen designations used in the table and figures, the letter (A or B) indicates the side of the slab from which the specimen was taken and the number (1-10) indicates the position of the specimen within each side, from edge to center (Fig. 6.3a). Figure 6.4 summarizes the stress vs. strain results from tests on all of the dogbone-shaped flat and GE cylindrical specimens for both alloys (for all unnotched geometries) and also shows the input stress-strain curve used in the finite element models. Unnotched specimen failure strains are given in Table 1, however the results from the GE cylindrical specimens are omitted for brevity. Overall, total strains at failure and hardening rates are similar for the two alloys; however, the WMS alloy has a yield stress on the order of twice that of the 48-2-2 alloy. For the 48-2-2 material, all specimens failed between 0.8% and 1.8% total strain and the stress vs. strain response is essentially the same for all specimens tested. For WMS, failure occurred between 0.6% and 1.5% total strain and the stress vs. strain behavior is more variable than for 48-2-2. There is some correlation between changes in yield stresses and failure strains and the distance of some specimens from the slab centerline; however, no consistent trend in results is seen for all specimens. Input curves were obtained by fitting a Ramberg-Osgood stress vs. strain law to experimental true stress vs. true strain curves:

$$\varepsilon = \frac{\sigma}{E} + \alpha \frac{\sigma_Y}{E} \left(\frac{\sigma}{\sigma_Y} \right)^{1/n} . \tag{1}$$

The parameter α is taken as equal to 3/7 and σ_y and n are fit to the data. Use of values of $\sigma_y = 252$ MPa and n = 0.128 for 48-2-2 and $\sigma_y = 488$ MPa and n = 0.088 for WMS resulted in the fitted curves shown in Fig. 6.4, which are reasonable representations of the "average" stress vs. strain behavior for each alloy.
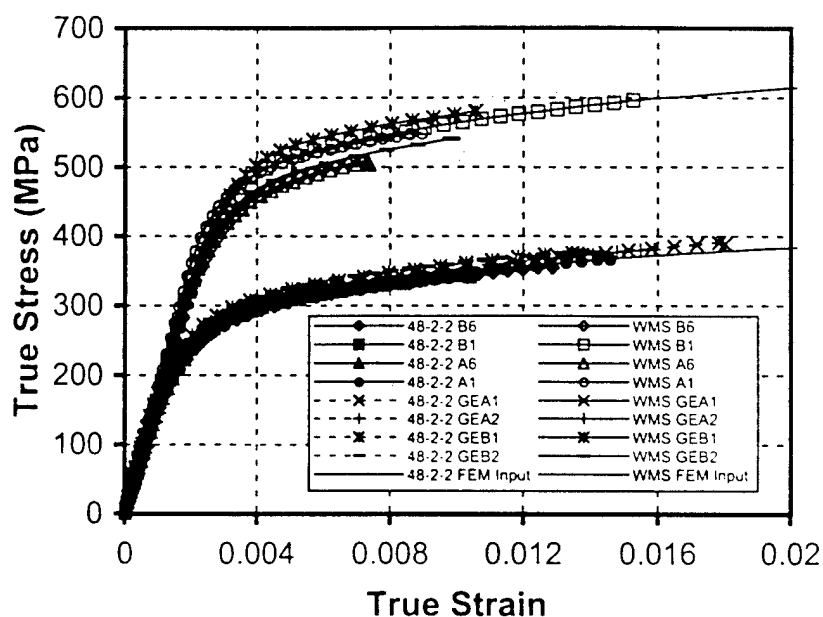

Figure 6.4   Stress vs. strain results from unnotched uniaxial tension specimens for 48-2-2 and WMS, including the curve used as input for the finite element models.

In Figs. 6.5-6.7, experimental load vs. displacement results from the R = 2 mm, R = 4 mm and R = 8 mm specimens are presented for both alloys, along with results predicted by the finite element models. Values of Load/A_{net} are plotted as a function of displacement along the tensile axis measured across the notch using a 25.4 mm gage length. Finite element models used in this study are highly similar to those used by Knaul, et al.,[8] using eight-noded quadratic displacement interpolation plane stress elements within the ABAQUS finite element package. Presented results were checked against those from models having double the element resolution in directions normal to and along the periphery of the notch, with no significant changes seen. As further checks of mesh resolution near the notch root, elastic stress concentration factors agreed well with approximate values provided graphically in the stress concentration handbook of Peterson[9] and plots of elastic-plastic normal stress vs. strain in the loading direction at the notch root (where the stress state is uniaxial for a fully refined mesh) reproduced the input curves used in the models. As seen in Figs. 6.5-6.7, overall the finite element predictions agree well with the measured results. It is important that the predictions agree reasonably well with the experimental data, so that accurate estimates of failure strains at the notch root can be obtained from the finite element models. For all of the notched specimens, finite element predictions for the 48-2-2 material tend to agree better with the test results than for the WMS material. This is likely due to the difficulty in choosing the input properties for WMS, because the unnotched test stress vs. strain results are somewhat scattered. No consistent trends were seen in the experimental data for a single alloy that would indicate a clear change in properties as one moves through a single cast slab.
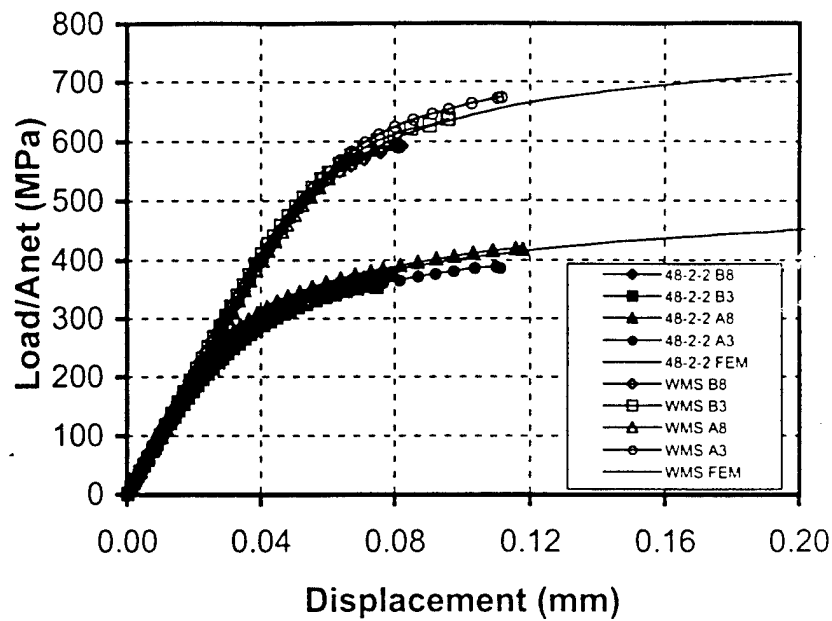
Figure 6.5   Experimental Load/A_net vs. displacement across the notch using a 25.4 mm gage length, with numerical predictions superimposed, for the R = 2 mm specimens.
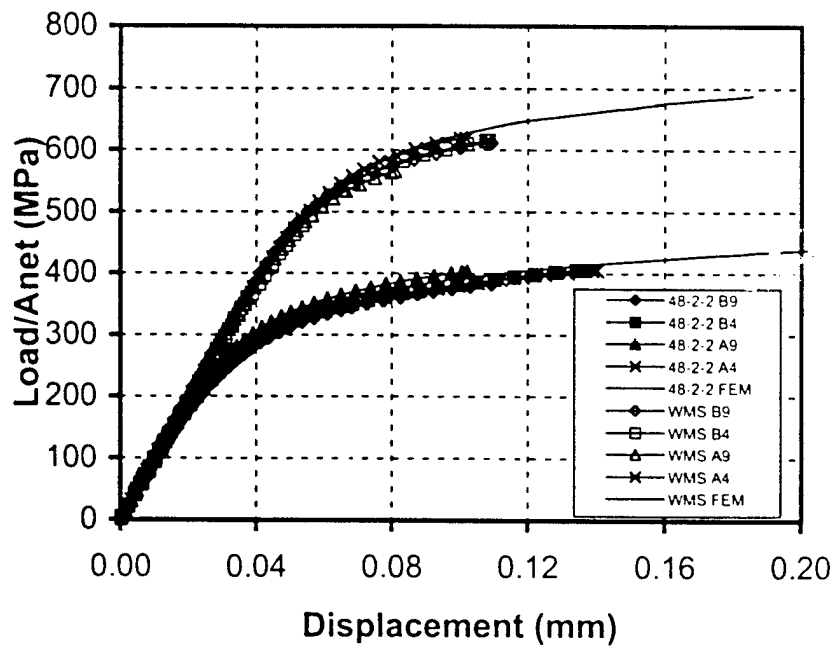

Figure 6.6   Experimental Load/A_net vs. displacement across the notch using a 25.4 mm gage length, with numerical predictions superimposed, for R = 4 mm specimens.
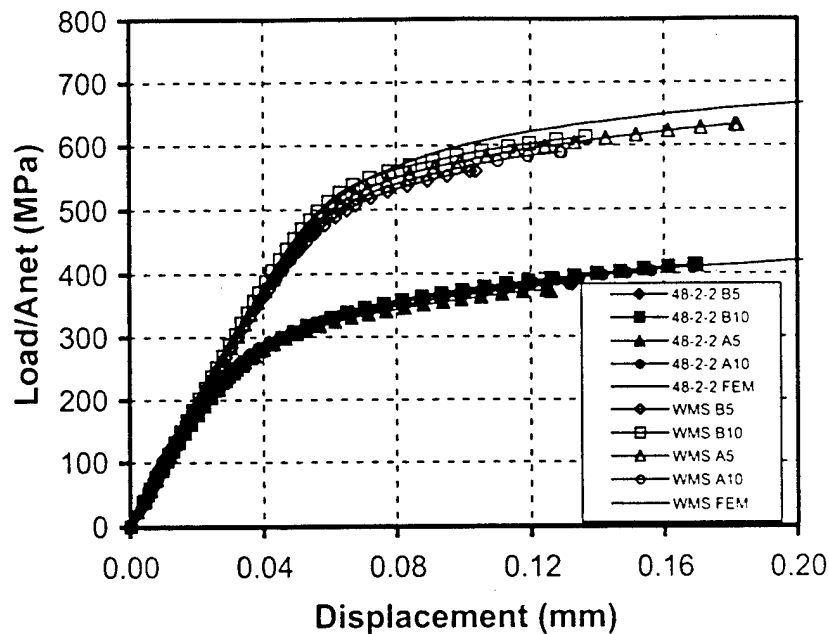
Figure 6.7   Experimental Load/A_{net} vs. displacement across the notch using a 25.4 mm gage length, with numerical predictions superimposed, for R = 8 mm specimens.

Measured values of Load/A_{net} and displacement at failure from all flat specimen tests and notch root strains at failure for each notched specimen test, as inferred from the finite element models, are presented in Table 1. Two values for the strain at failure for the notched specimens are given. Values without parentheses are determined from measured displacements at failure using numerically determined plots of displacement vs. notch root strain, and values with parentheses are determined by an analogous procedure using net section stresses at failure. Because net section stress vs. notch root strain plots are relatively flat for large notch root strains, the values obtained from net section stresses at failure are generally less accurate than those obtained from displacements at failure. However, because there is some variability in the load vs. displacement results for each specimen type, it is important to show failure strains obtained from both methods. The actual failure strain at the notch root will lie between these two values.

As seen in Table 1, for both alloys there is a clear trend of notch root strains at failure being larger than failure strains seen in the unnotched dogbone-shaped specimens. Also, for both alloys there is a tendency for the notch root strains to be highest in the R = 2 mm specimens, lower in the R = 4 mm specimens, and the lowest in the R = 8 mm specimens. The failure strain values for one of the R = 2 mm WMS specimens (specimen A3) are particularly large. For this specimen, load and displacement methods give significantly different failure strain predictions; however, both values (3.29% and 4.29%) are large compared to values near 1% seen in the dogbone specimens.

Table 1 Stresses and strains at failure for notched and unnotched tensile specimens.

Specimen	Unnotched Specimens			Notched Specimens			
	Axial Stress at Failure (MPa)	Axial Strain at Failure (Pct)	Plastic Strain at Failure (Pct)	Net Section Stress at Failure (MPa)	25.4 mm Gage Displacement at Failure (mm)	Notch Root Strain at Failure (Pct)*	Notch Root Plastic Strain at Failure (Pct)*,**
48-2-2							
A1 (doghone)	366	1.46	1.24	----	----	----	----
A3 (R=2mm)	----	----	----	388	0.111	3.41 (2.36)	3.16 (2.12)
A4 (R=4mm)	----	----	----	408	0.140	2.88 (2.46)	2.64 (2.22)
A5 (R=8mm)	----	----	----	375	0.126	1.78 (1.24)	1.55 (1.03)
A6 (doghone)	341	1.04	0.83	----	----	----	----
A8 (R=2mm)	----	----	----	420	0.118	3.64 (3.80)	3.39 (3.55)
A9 (R=4mm)	----	----	----	405	0.102	1.91 (2.30)	1.68 (2.06)
A10 (R=8mm)	----	----	----	406	0.156	2.39 (2.32)	2.15 (2.08)
B1 (doghone)	332	0.84	0.64	----	----	----	----
B3 (R=2mm)	----	----	----	357	0.075	1.92 (1.47)	1.69 (1.25)
B4 (R=4mm)	----	----	----	407	0.136	2.63 (2.46)	2.39 (2.22)
B5 (R=8mm)	----	----	----	385	0.133	1.91 (1.62)	1.68 (1.39)
B6 (doghone)	354	1.29	1.08	----	----	----	----
B8 (R=2mm)	----	----	----	378	0.079	2.20 (2.00)	1.97 (1.77)
B9 (R=4mm)	----	----	----	384	0.109	2.13 (1.66)	1.90 (1.43)
B10 (R=8mm)	----	----	----	415	0.170	2.54 (2.75)	2.30 (2.51)
WMS							
A1 (doghone)	549		0.58	---	----	----	----
A3 (R=2mm)	----	----	----	677	0.112	3.29 (4.29)	2.91 (3.90)
A4 (R=4mm)	----	----	----	621	0.102	1.76 (1.71)	1.41 (1.36)
A5 (R=8mm)	----	----	----	637	0.182	2.72 (1.77)	2.35 (1.42)
A6 (doghone)	504	0.74	0.45	----	----	----	----
A8 (R=2mm)	----	----	----	598	0.081	1.95 (1.78)	1.59 (1.43)
A9 (R=4mm)	----	----	----	567	0.081	1.23 (0.95)	0.89 (0.62)
A10 (R=8mm)	----	----	----	593	0.129	1.72 (1.00)	1.37 (0.67)
B1 (doghone)	596	1.54	1.19	----	----	----	----
B3 (R=2mm)	----	----	----	641	0.096	2.66 (2.75)	2.29 (2.38)
B4 (R=4mm)	----	----	----	618	0.108	1.94 (1.62)	1.58 (1.27)
B5 (R=8mm)	----	----	----	562	0.104	1.23 (0.76)	0.89 (0.44)
B6 (doghone)	508	0.72	0.42	----	----	----	----
B8 (R=2mm)	----	----	----	594	0.082	2.04 (1.71)	1.68 (1.36)
B9 (R=4mm)	----	----	----	613	0.109	2.00 (1.50)	1.64 (1.16)
B10 (R=8mm)	----	----	----	617	0.137	1.82 (1.40)	1.47 (1.06)

*The values in these columns for notch root strain at failure are as determined using the displacement at failure (the first entry, not in parentheses) and the net section stress at failure (the second entry, in parentheses)

**All plastic strains are calculated using the following Young's moduli: $E_{48-2-2}=165$ GPa, $E_{WMS} = 171$ GPa

Notch strengthening can be demonstrated graphically by comparing notch root strains and net section stresses at failure between specimen geometries. Figure 6.8 provides a plot of (total) failure strains vs. elastic stress concentration factor, K_t, for the 48-2-2 alloy. The results plotted in Fig. 6.8 show a steady increase in failure strain with increasing K_t, with the greatest scatter seen in the results for the highest K_t specimen (R = 2 mm). These results are similar to those cited in previous notched specimen tests on the 48-2-2 material[3] and they suggest a notch strengthening or size effect. Specimens with smaller volumes of highly strained material (higher K_t values) will exhibit, on average, larger strains at failure because it is less likely that this smaller volume will contain a ductility reducing feature or flaw (e.g., a poorly oriented grain or a pore). This argument also explains the larger amount of scatter in failure strain results for higher K_t specimens. Occasionally, even small highly strained volumes will contain a severe ductility-reducing feature or flaw, and a low strain at failure will result. Figure 6.9 provides a plot of total failure strain vs. K_t analogous to that given in Fig. 6.8, but for the WMS material. The trends in the results are similar to those seen for the 48-2-2 specimens, showing an increase in average failure strain values and in variability with K_t. Figure 6.10 provides a plot of measured net stress (Load/A_{net}) at failure vs. K_t for all notched specimens, which shows that there is no significant decrease in load carrying capability with increasing K_t for either material. This counter-intuitive, directly measured result would not be possible without increases in notched specimen failure strains with increasing K_t.
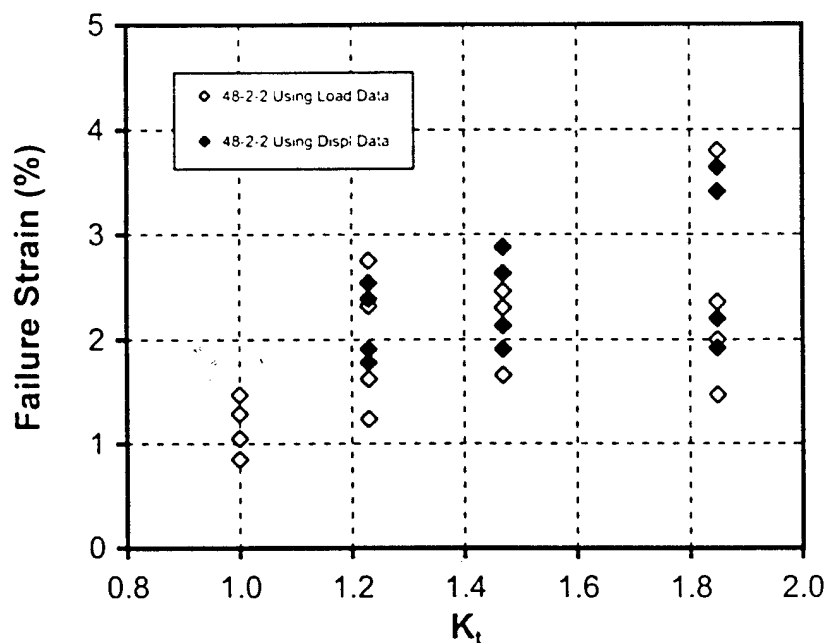

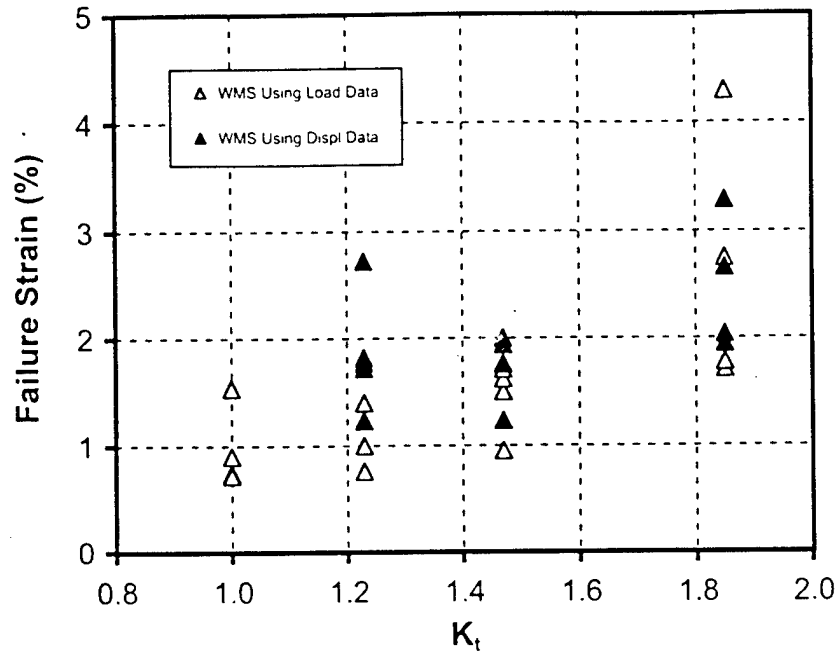Figure 6.8   Failure strains (total) vs. K_t for 48-2-2 specimens.

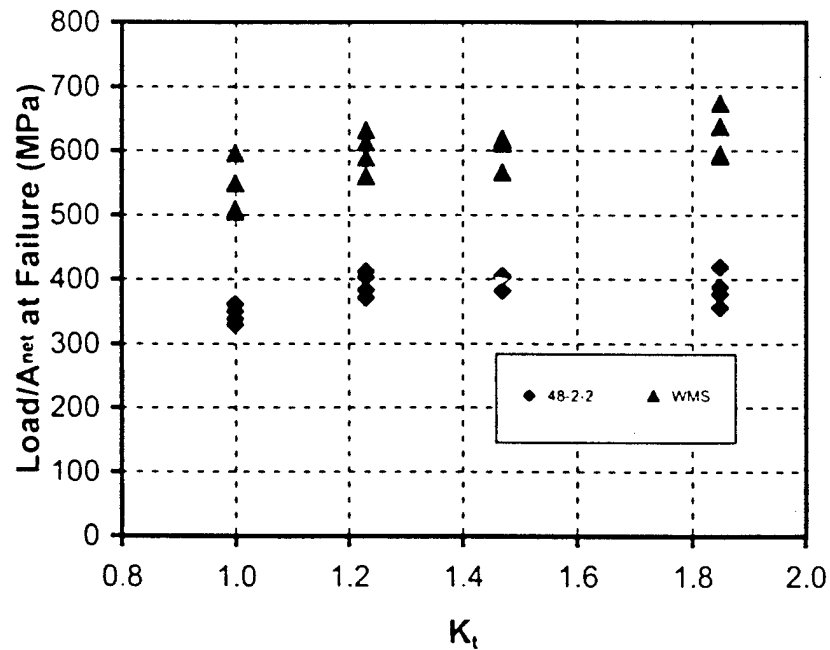Figure 6.9   Failure strains (total) vs. K_t for WMS specimens.

Figure 6.10   Failure Load/A_{net} vs. K_t for all specimens.

6.4 Volume Estimates and the Use of Weibull Probability Theory

The notched specimens used in this study have elastic stress concentrations of 1.23, 1.47 and 1.85. This range of K_t values and the range of notch radii would suggest that these specimens

have a significant variation in volume of highly strained material among them. Apart from using finite element models to back out failure strains from experimentally measured loads and displacements at failure, a principal goal of specimen modeling has been to quantify volumes of highly strained material in the specimens. In this section, two methods of calculating highly strained volumes are used. One involves the use of plastic strain contour plots to determine the volume of material subjected to strains greater than or equal to a defined percentage of the maximum plastic strain at the notch root. The second method involves use of Weibull probability theory to calculate an equivalent volume of uniformly strained material.

To illustrate how highly strained volumes were estimated, contour plots of quarter models of an R = 4 mm 48-2-2 specimen showing normalized equivalent plastic strains are provided in Fig. 6.11. To obtain the normalized equivalent plastic strain, strains within the specimen are divided by the maximum equivalent plastic strain, which occurs at the notch root. Figure 6.11 contains two contour plots, taken at notch root plastic strain levels close to the upper and lower bounds of the experimentally observed notch root plastic strains at failure (at 1.43 and 2.64 pct.). Contour boundaries equal to normalized equivalent strain values of 0.50, 0.70, and 0.90 are shown in each of the plots. Points taken along the contours were used to calculate the contour areas as irregular polygons. Volumes having as low as 50% of the maximum plastic strain at failure were chosen based on the argument that ductility variations in TiAl make it possible for failure to initiate in a specimen at a location that is subjected to as little as 50% of the maximum equivalent plastic strain.

Lower bound   Upper bound

NS = Normalized Equivalent $0 < NS < 0.5$
Plastic Strain $0.5 < NS < 0.7$
                                   $0.7 < NS < 0.9$
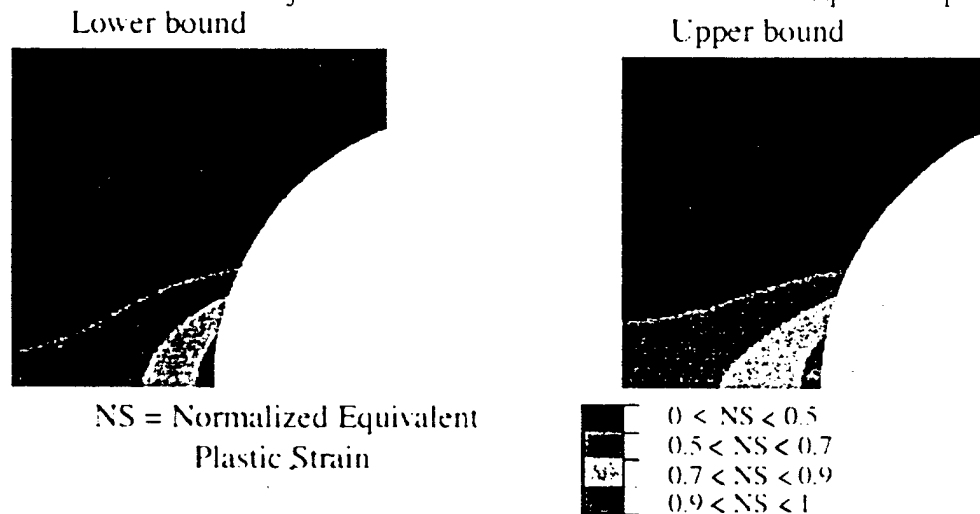 $0.9 < NS < 1$

Figure 6.11   Contour plots of normalized equivalent plastic strain for an R = 4 mm 48-2-2 specimen for notch root plastic strains at the lower and upper bounds of notch root plastic strains at failure seen in tests.

Weibull statistics offer another way of estimating highly strained volumes in the notched specimens. A Weibull statistical approach is based on a weakest link theory of failure, assuming that a given volume of material will fail at the most severe flaw. Size effects result due to the decreased probability of a small volume containing a severe flaw. The probability of failure, F, as a function of volume is

$$F = 1 - e^{-\frac{1}{V_0}\int\left(\frac{\sigma-\sigma_\mu}{\sigma_0}\right)^m dV} \qquad (2)$$

σ is the applied stress, V is the volume of stressed material and V_0 is a reference volume for the Weibull parameters m, σ_μ and σ_0 are determined. The parameter σ_μ is the threshold the stress below which the probability of failure is zero), σ_0 is a normalizing parameter ly selected as the stress at which the probability of failure is 63.2%), and m is the Weibull us (which can be used to quantify the variability of the material with respect to failure s).[10,11] Raban, et al.[12] have successfully extracted values of m and σ_0 parameters from a set of tensile test data on the 48-2-2 alloy, assuming a value of σ_μ equal to zero (which is only done for ceramic materials). Their work shows that plotting of 48-2-2 test data on standard axes of $\ln\left(\ln\left(\dfrac{1}{1-F}\right)\right)$ vs. $\ln\left(\sigma - \sigma_\mu\right)$ does result in an essentially linear distribution of test data points. The values for Weibull parameters obtained from their work (assuming $\sigma_\mu = 0$ MPa) are $\sigma_0 = 390$ MPa and m = 12.3. Limits in the amount of available unnotched test data preclude estimating Weibull parameters for the WMS alloy.

The criterion used herein to estimate the volume of highly strained material is to define it as the "equivalent" volume V_{equiv} of a specimen under uniform stress $\sigma = \sigma_{max}$ such that the probability of failure is the same as that of the notched specimen with $\sigma = \sigma_{max}$ at the notch root. For the notched specimen we have

$$F_{notched} = 1 - e^{-\frac{1}{V_0}\int\left(\frac{\sigma - \sigma_\mu}{\sigma_0}\right)^m dV} \tag{3}$$

For the uniformly stressed specimen with $\sigma = \sigma_{max}$, the probability of failure is given by

$$F_{uniform} = 1 - e^{-\frac{1}{V_0}\left(\frac{\sigma_{max} - \sigma_\mu}{\sigma_0}\right)^m V_{equiv}} \tag{4}$$

Setting $F_{notched} = F_{uniform}$ and solving for V_{equiv} yields

$$V_{equiv} = \frac{\int\left(\dfrac{\sigma - \sigma_\mu}{\sigma_0}\right)^m dV}{\left(\dfrac{\sigma_{max} - \sigma_\mu}{\sigma_0}\right)^m} . \tag{5}$$

Using this expression, numerical values for V_{equiv} for all 48-2-2 notched specimens have been obtained from the finite element models by performing a piecewise integral over the notched specimen volume using maximum principal stresses for the variable σ. The use of maximum principal stresses in the calculations is consistent with the fact that a Weibull probability law can be derived by assuming a uniform distribution of crack-like flaws of differing lengths[13]; however, it also implies a brittle failure process in TiAl.

Table 2 provides a summary of highly strained volumes for all notched specimens as obtained from contour plots of equivalent plastic strain, as well as equivalent volumes for 48-2-2 specimens calculated using Weibull statistics. Also included are calculations for 48-2-2 double-notched specimens tested by Knaul, et al.,[3] which are designated as r/W = 1/3 and r/W = 1/10, where r is the notch radius and W is the specimen's total width. The r/W = 1/3 specimens had W = 12 mm and were 3 mm thick. The r/W = 1/10 specimens had W = 20 mm and were 1.5 mm in thickness.

All specimens were 140 mm in total length. These specimens had elastic stress concentration factors of 1.3 and 2.4, respectively. Lower bound and upper bound values correspond to values calculated at the lowest and highest notch root failure strains seen in the tests. In most cases, lower and upper bound values are similar, so that the volume values are not a strong function of the notch root failure strain.

Table 2 Calculated volumes of highly strained material for notched specimens.

Notched Specimen	Lower Bound Volume (mm³)				Upper Bound Volume (mm³)			
	NS≥0.5	NS≥0.7	NS≥0.9	V_{equiv}	NS≥0.5	NS≥0.7	NS≥0.9	V_{equiv}
48-2-2								
R = 2mm	3.4	1.1	0.18	15	4.1	1.4	0.24	18
R = 4mm	21	6.0	0.85	29	25	8.1	1.2	27
R = 8mm	43	28	8.5	31	44	31	16	29
r/W=1/10	3.0	1.0	0.16	37	3.4	1.2	0.16	39
r/W=1/3	30	13	2.1	27	35	23	4.3	24
WMS								
R = 2mm	2.7	0.93	0.16	N/A	4.1	1.4	0.21	N/A
R = 4mm	7.5	2.8	0.45	N/A	19	5.8	0.92	N/A
R = 8mm	3.2	15	2.5	N/A	35	24	7.4	N/A

Notes NS denotes normalized plastic strain.
   V_{equiv} denotes equivalent volume as determined by Weibull statistical methods using $\sigma_u = 0$, $\sigma_o = 390$ and m = 12.3.

Highly strained volume estimates based on normalized plastic strain contours (columns in Table 2 with "NS" in their labels) show a correlation with failure strain results from the experiments (Table 1 and Figs. 6.8 and 6.9). Specimens with smaller highly strained volumes tend to exhibit larger notch root failure strains. Except for the r/W = 1/10 specimen, calculated equivalent volumes using Weibull statistics agree reasonably well with the graphically obtained highly strained volume values using a 0.50 normalized plastic strain limit (the columns labeled "NS≥0.5" in Table 2). This correlation seems reasonable in that Weibull statistics will assign a high probability of failure only to portions of the specimen experiencing stresses near the maximum stress value (at 90% or more of the maximum stress, perhaps); however, for elastic-plastic deformation a reduction in stress level on the order of 10% could correspond to a reduction in plastic strains as great as 50% from the maximum value. For the r/W = 1/10 specimen, the correlation between Weibull equivalent volumes and highly strained volumes calculated using a 0.50 normalized plastic strain limit breaks down. For this specimen the Weibull method is including more material away from the notch root than the plastic strain contour methods are, and this specimen had a much greater width between the notches (16 mm) than the other specimens considered herein.

Given that Weibull parameters can be successfully extracted from test data for 48-2-2,[112] and can then be used to calculate equivalent volume values, the final issue considered herein is whether Weibull methods can be used to predict the notch strengthening observed in TiAl specimen tests. In Figs. 6.12 and 6.13 the data from Raban, et al.[112] are plotted as solid circles on standard $\ln\left(\ln\left(\frac{1}{1-F}\right)\right)$ vs. $\ln(\sigma - \sigma_\mu)$ axes. As previously cited, a linear fit of this data yields their values

of $\sigma_0 = 390$ MPa and m = 12.3 (assuming $\sigma_\mu = 0$ MPa). According to Weibull theory, test results plotted from specimens having a smaller volume will have the same slope (Weibull modulus, m) as those of larger specimens, but the results will be shifted to the right on the x axis. This can be interpreted as an effective change in the parameter σ_0, which can be calculated directly from the y-axis intercept.

Predictions for the shift of notched specimen results based on the lower bound values of Weibull equivalent volumes given in Table 2 are designated by lines plotted in Figs. 6.12 and 6.13. Also included in Figs. 6.12 and 6.13 are experimental results for the corresponding notched geometries, where the notch root failure stress for each specimen is determined from the average of the notch root failure strains given in Table 1. Figure 6.12 gives results and predictions for r/W = 1/3 and r/W = 1/10 specimens[3] and Fig. 6.13 gives results and predictions from samples in the current study (R = 2 mm, R = 4 mm, R = 8 mm). The results plotted in Figs. 6.12 and 6.13 show that the predictions based on Weibull theory lie to the right of the experimental notched specimen results. This is particularly true for the results plotted in Fig. 6.13. Weibull theory predicts a greater increase in notch root failure stress than is seen in the experimental data and is thus predicting a more significant notch strengthening or size effect than is seen in 48-2-2. The magnitude of the difference is typically large, which is not necessarily clear from the log scale of the plotted x axis values.
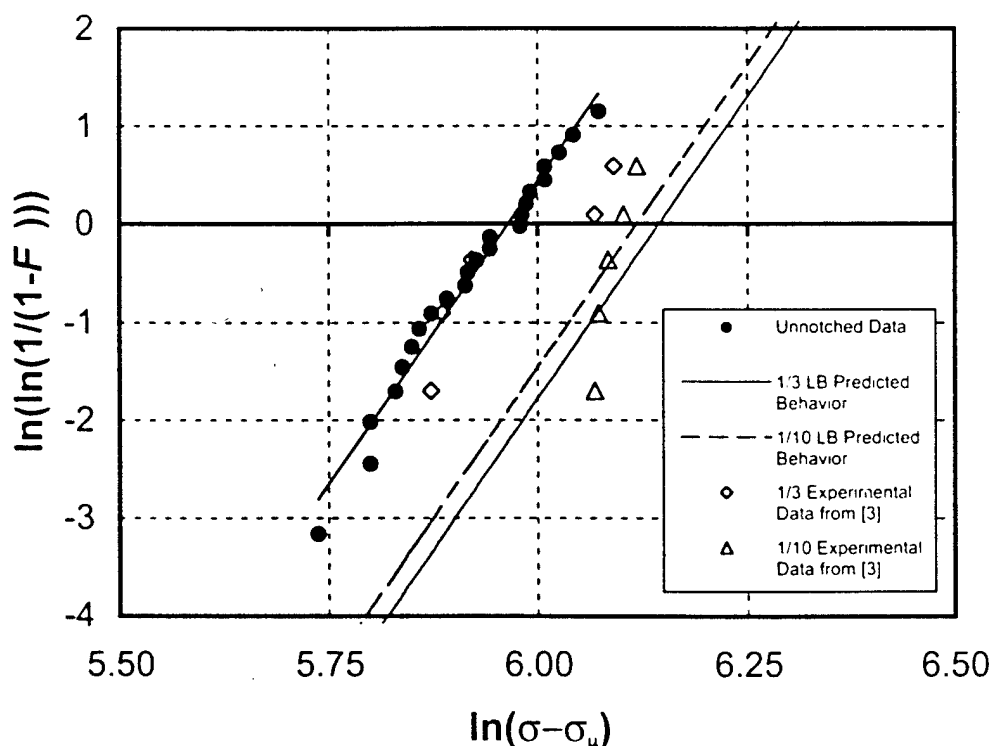

Figure 6.12   Experimental results and predicted behavior using Weibull probability theory for r/W = 1/3 and r/W = 1/10 48-2-2 specimens from Knaul, et al.[3].

As previously noted, results in Figs. 6.12 and 6.13 are generated based on distributions of maximum normal stress throughout the tested specimens in order to be consistent with the notion

of a size effect caused by a distribution in the material of crack-like flaws of differing lengths (from which Weibull statistical formulas can be derived[113]). Although a cause for a size effect in TiAl alloys has not been identified, there is evidence that failure initiation sites are correlated with a grain or a group of grains oriented in such a way that they experience much larger plastic strains than their neighbors. There also appears to be a correlation between low ductility and large grain or lamellar colony sizes. Thus a size effect in TiAl alloys could be due to distributions of grain orientations or grain sizes in tested specimens.[114] Because a notch strengthening or size effect in TiAl alloys is not necessarily related to brittle propagation of crack-like flaws, the authors have also generated analogous plots to those of Figs. 6.12 and 6.13 based on Von Mises equivalent stresses and equivalent plastic strains and using nonzero values of the parameter σ_μ. In all cases, the shift in results predicted by Weibull theory is significantly larger than that seen in the notched specimen experiments. Because a single set of unnotched specimen data has been used to apply Weibull theory, some caution should be exercised in making broad conclusions based on the results presented herein. However, results of this study consistently suggest that although TiAl alloys exhibit low ductility compared to nickel superalloys and they exhibit size effects similar to those seen in ceramics and other brittle materials, the magnitude of the effect is not as great as is seen in fully brittle materials.
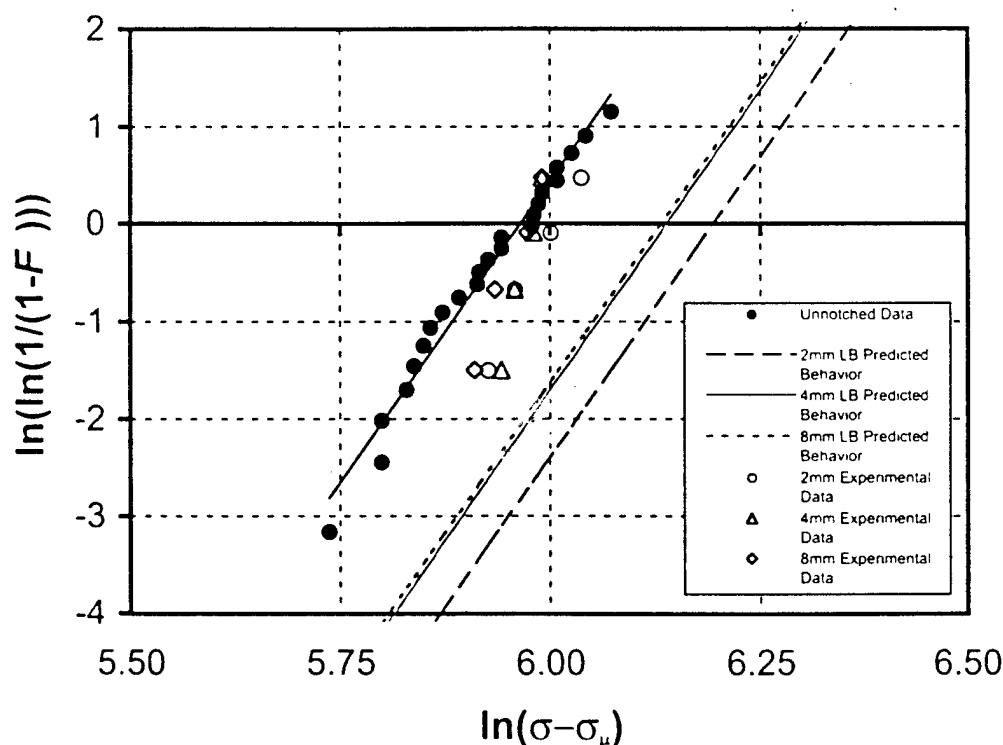

Figure 6.13   Experimental results and predicted behavior using Weibull probability theory for R = 2 mm, R = 4 mm, R = 8 mm 48-2-2 specimens.

6.5 Result Summary

Calculated highly strained volumes have been used to produce a single plot of failure strain vs. highly strained volume using test data for both the 48-2-2 and WMS TiAl alloys. This includes tests on the 48-2-2 alloy from Knaul, et al.[1] and tests on cylindrically shaped GE standard

unnotched tensile specimens. The plot is shown in Fig. 6.14, with highly strained volumes in notched specimens defined as the volume of material subjected to 50% or more of the maximum equivalent plastic strain at failure (using lower bound values). Again, two failure strain data points are generated for each notched specimen test, corresponding to strains obtained from the load or displacement at failure. The highly strained volume data (x axis) is plotted on a log scale to efficiently fit all the data points on a single plot. Although the data for each alloy could be plotted separately, the fact that both alloys exhibit similar strains-to-failure makes plotting them on a single set of axes reasonable. The plotted data fit well together and show a trend of increasing average failure strain values and variability with decreasing values of highly strained volume.
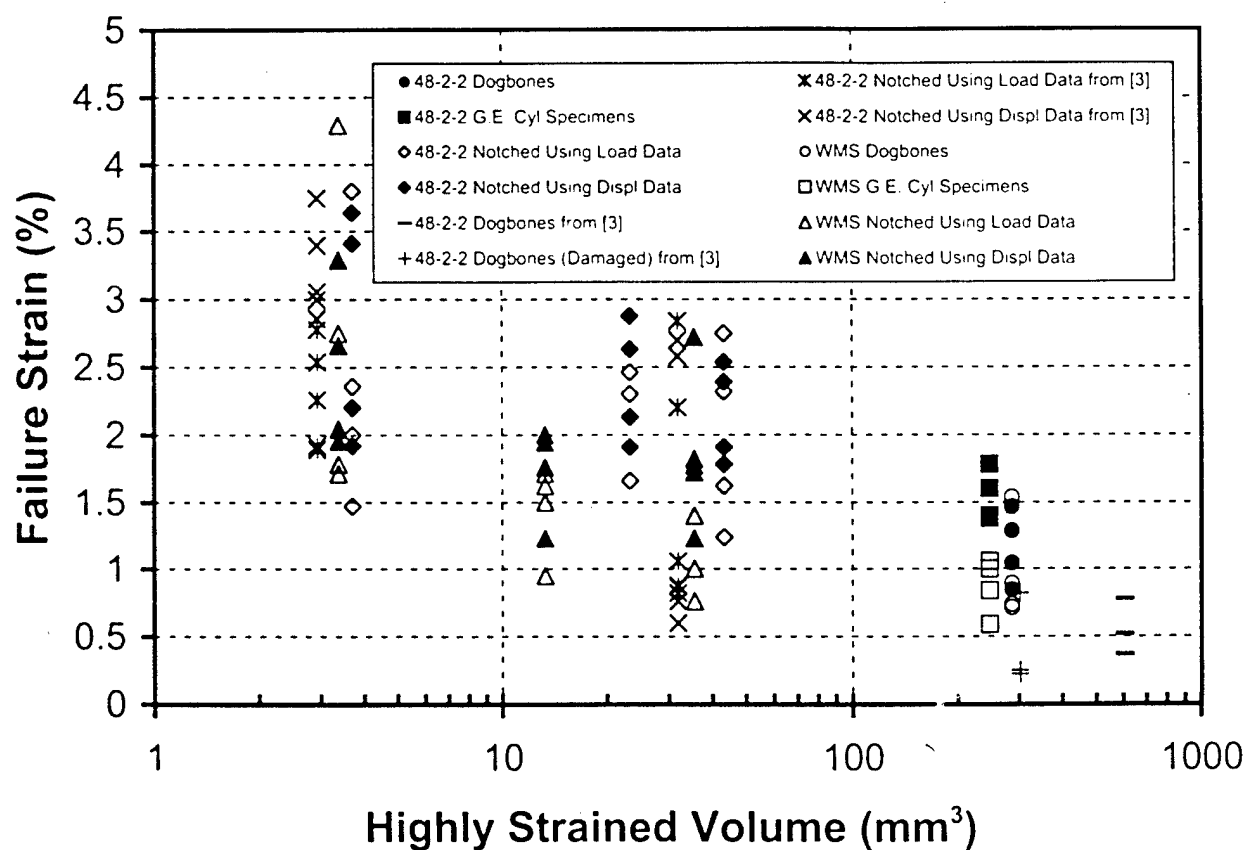

Figure 6.14   Summary plot of failure strain vs. highly strained volume for all specimens (both alloys).

It should also be noted that some of the failure strains from unnotched (dogbone shaped) specimens from Knaul, et al.[3] were very small (see the data points at the far right side of the plot of Fig. 6.14). Subsequent fracture surface evaluation of these specimens revealed evidence that some of them had machining damage. Although some of these low ductility specimens did not show clear evidence of damage, it is still suspected that damage may have been imparted to them through machining. This apparent damage existed in spite of extensive efforts in specimen preparation made to reduce the likelihood of any grinding damage remaining in finished specimens. The specimens where machining damage has been noted have been flat, unnotched specimens which were ground along the specimen length. In such grinding operations, a small area of the

specimen is in contact with the grinding wheel at any one time. In contrast, cylindrical specimens and the notch in notched flat specimens are ground in a direction normal to the specimen length using a shaped wheel, where a relatively large area of the wheel always in contact with the specimen. It is suspected that machining damage is easier to induce for grinding operations involving small contact areas, perhaps due to larger temperatures and thermal gradients near the point of contact.

6.6 Conclusions

A series of notched and unnotched specimens has been designed to methodically test for the existence of notch strengthening in near-gamma 48-2-2 and lamellar WMS alloys. This includes use of finite element model predictions to estimate volumes of highly strained material for each notched specimen (based on physically reasonable definitions for "highly strained" material). Specimens were designed so that the stress concentrations and volumes of highly strained material varied over a wide range. Results verify notch strengthening seen in earlier tests on 48-2-2. Notch strengthening for the WMS alloy appears to be at least as great as that seen in the 48-2-2 material.

Use of Weibull statistics to predict notch strengthening in the 48-2-2 alloy has shown that strengthening is not as great as would be predicted by this brittle, weakest link theory. This is consistent with the notion that TiAl alloys, though less ductile than the nickel superalloys they are positioned to replace, are still far from exhibiting characteristics of truly brittle materials. It also suggests, however, that well-established Weibull statistical methods, though perhaps useful in characterizing TiAl variability, cannot be applied directly to exploit notch strengthening in the design of TiAl components containing stress concentrators. Even if knowledge of TiAl notch strengthening is not directly integrated into design practice, the effects documented in this study can still offer some additional margin of safety for notched component designs based on unnotched failure strains or stresses. In testing small numbers of notched specimens, the effect has been significant enough to allow average Load/Net Section Area values at failure to actually increase with an increase in elastic stress concentration.

6.7 Acknowledgments

6.8 References

1. Austin, C.M. and Kelly, T.J., "Development and Implementation Status of Cast Gamma Titanium Aluminide," *Structural Intermetallics*, R. Darolia, J.J. Lewandowski, C.T. Liu, P.L. Martin, D.B. Miracle, and M.V. Nathal, eds., TMS, Warrendale, Pa, 143-150 (1993).

2. Raban, R., Rishel, L.L. and Pollock, T.M., "The Dependence of Tensile Ductility on Investment Casting Parameters in Gamma Titanium Aluminides," *High-Temperature*

rdered Intermetallic Alloys VIII, E.P. George, M. Yamaguchi and M.J. Mills, eds., **552**, ٢S, Warrendale, Pa, 55-60 (1999).

aul, D.A., Beuth, J.L. and Milke, J.G., "Modeling and Measurement of the Notched ٠ngth of Gamma Titanium Aluminides under Monotonic Loading," *Met. Trans.*, **30A**, ٠)-959 (1999).

ail, S.J. and Bowen, P., "Effects of Stress Concentrations on the Fatigue Life of a ٠amma-Based Titanium Aluminide," *Mater. Sci. Eng.*, **A192/193**, 427-434 (1995).

5. Richerson, D.W., *Modern Ceramics Engineering*, 2nd Edition, Marcel Dekker, Inc., NY, (1992).

6. Besson, J. and Pineau, A., "Numerical Simulation of Ductile Rupture: Analysis of Experimental Scatter and Size Effect," *Recent Advances in Fracture*, R.K. Mahidhara, A.B. Geltmacher, P. Matic and K. Sadananda, eds., TMS, Warrendale, Pa, 125-136 (1997).

7. Bazant. Z.P. and Chen, E-P., "Scaling of Structural Failure," *Appl. Mech. Rev.*, **50**, 593-627 (1997).

8. Blackburn, M.J. and Williams, J.C., "The Preparation of Thin Foils of Titanium Alloys," *Trans. TMS-AIME*, **239**, 287 (1967).

9. Peterson, R.E., *Stress Concentration Factors*, John Wiley and Sons, New York, NY, (1974).

10. Weibull, W., *The Phenomenon of Rupture in Solids*, Royal Swedish Institute for Engineering Research, Stockholm, 31-43 (1939).

11. Weibull, W., "A Statistical Representation of Fatigue Failures in Solids," *Proc. Royal Inst. Tech.*, **27**, 31-37 (1949).

12. Raban, R., Elliott, A., Biery, N., Pollock, T. and De Graef, M., "Property Variability" *PRET: A University-Industry Partnership for Research and Transition of Gamma Titanium Aluminides Annual Report*, Chapter 5 (1999).

13. Freudenthal, A.M., "Statistical Approach to Brittle Fracture," *Fracture: An Advanced Treatise, Vol. II: Mathematical Fundamentals*, H. Liebowitz, ed., Academic Press, New York, 591-619 (1968).

14. Biery, N.E., De Graef, M.J. and Pollock, T.M., "Study of Localized Strain at Notches in Gamma TiAl Alloys Using Displacement Mapping and Microstructural Characterization," *Proc. Intl. Symp. on Gamma Titanium Aluminides II*, Y.W. Kim, M. Yamaguchi and D.M. Dimiduk, eds., TMS, Warrendale, Pa, in press (1999).

7. Surface and Foreign Object Damage

Paul S. Steif
Volus T. McKenna
Carnegie Mellon University

7.1 Introduction

The overall goal of this portion of the PRET project has been to assess the threat to gamma components associated with surface damage. Our focus has been in-service impacts of small particles on rotating parts (e.g., on compressor or turbine blades). Here we describe the work carried out at CMU that addresses the relation between impact events and the resulting surface damage. The project at University of Michigan addresses the reduction in fatigue strength associated with surface damage and is described in Section 8. Our studies have attempted to simulate damage in the laboratory, with a balance between sufficient realism to be relevant and sufficient simplicity to be reproducible and characterizable.

The situation of greatest concern is that of an impact on the leading edge of a blade. Observations of the damage associated with impacts on the leading edge of gamma blade simulative specimens (Draper, Pereira and Nathal, 1997) have pointed to a complex pattern of damage: cracking exists on the rear and impacted faces, though cracking on the rear face can occur for less severe impacts. Since a blade may have to be designed so as to keep this first level of damage under control, our studies of small particle impacts focus primarily on the rear face damage.

Rear faced damage that is produced by a front side impact has been studied in a progressive fashion in the PRET program. Our studies have begun with a simpler geometry of impacts at the center of flat plate with edge effects eliminated. This simpler geometry has allowed us to produce damage in a reasonably reproducible manner, and to readily carry out finite element analyses of the impact event. It has also allowed us to draw some conclusions regarding the usefulness of tensile ductility in predicting crack extent.

Next, we have turned to the study of impacts at the edge of specimens that are shaped to simulate a blade leading edge. Two classes of specimens have been considered. Impacts on cast-to-shape, blade-simulative specimens, which have been studied in another program (Draper, Pereira and Nathal, 1997), have been analyzed here. In addition, a new machined, leading-edge simulative specimen has been developed in this program. High speed impacts on these specimens have been performed, together with the accompanying analysis. Details of these activities are described below.

7.2 Material Properties, Preparation, and Experimental Procedures

7.2.1 Material Properties and Validation

Two gamma TiAl alloys have been used to date in investigating the damage associated with high-speed impacts. These alloys are designated 47.9 Al baseline (a near gamma microstructure) and WMS (a fully lamellar microstructure) and were described previously.

The true-stress true-strain responses of the two gamma alloys at large strains were measured quasistatically (from 0.001 to 0.1s^{-1}) and at high rates (from 1000 to 8000 s^{-1}) at Los Alamos National Laboratories. The results of these tests were then fit to a Zerilli-Armstrong model (Zerilli and Armstrong, 1987). The flow stress as a function of the plastic strain were fit to the following forms:

for the 47.9 Al alloy:

$$\sigma = 270 + 660\exp\left[-0.00350T + 0.0001750T\ln(\dot{\varepsilon})\right] + 3000\varepsilon_p^{0.96} \qquad (1)$$

for the WMS alloy:

$$\sigma = 525 + \left(4125\varepsilon_p^{\cdots}\right)\exp\left[-0.0015T + 0.000055T\ln(\dot{\varepsilon})\right] \qquad (1)$$

where σ is the stress in MPa, $\dot{\varepsilon}$ denotes the strain rate, ε_p is the plastic strain, and T is temperature in K. One feature of interest to point out is that WMS is significantly harder than the 47.9 Al alloy at low rates; although at higher rates their flow stresses become more similar.

Two independent tests of the appropriateness of the above fits to the high strain-rate data were performed. The first test involved determining the coefficient of restitution of WMS, and was carried out by Ken Vecchio of UCSD. The experiment involved clamping a 1.75 mm thick plate of WMS against a copper block containing two 180 W cartridge heaters. Steel balls of 1.9 mm diameter were propelled at approximately 88 m/s at the target assembly from a gas gun. Actual values of incident and return velocity of the steel balls were determined using a passive electromagnetic coil detection system, situated between the gun muzzle and the target. Velocities were calculated from the time intervals between successive voltage pulses obtained from two individual coils in the detector. The coefficient of restitution is the ratio of the return velocity to the incident velocity. Three measurements were taken at room temperature, leading to three estimates of the coefficient of restitution: 0.27, 0.27 and 0.30.

The impact was simulated using ABAQUS EXPLICIT (Hibbit Karlsson and Sorenson, Inc.). The copper block and the restraining apparatus were modeled as rigid and

treats the copper block and the restraining apparatus to be rigid. Comparing the incoming velocity with the FEA predicted outgoing velocity, we predicted the coefficient of restitution to be .31, which is quite close to the measured value. Approximating the backing as rigid will tend to raise the prediction of the coefficient of restitution, since in the experiment there may be some energy lost from the sphere that is transferred to vibration of the backing. Still, the comparison lends credence to the stress-strain law adopted for the WMS material.

The second test was performed by Rusty Gray at LANL to test the assumed stress-strain response of 47.9 Al baseline at high rates. Here a cylinder of 47.9 Al baseline material was fired at a large AF1410 steel block. The cylinder was initially 2.000" long and 0.299" diameter, and was given an initial velocity of 549.6 ft/s. Of principal interest is the final length of the cylinder after the impact event. It was measured to be 1.884". The finite element simulation of the test was carried out using ABAQUS EXPLICIT. The event was modeled as axisymmetric, and the steel block taken to be elastic. The FE model predicted the length after impact to be 1.87", lending some confidence to the stress-strain law adopted for 47.9 Al baseline material.

7.2.1 Material Preparation and Experimental Procedures

Impacts geometries studied in this program are shown schematically in Figure 7.1 and are discussed in more detail below. The specimens were electro-discharge machined from the cast plates into rectangular flat plates of two thicknesses (1.75 mm and 2.25 mm). All samples were subsequently low stress ground and then subjected to conventional mechanical polishing by hand using sandpaper with a series of grits up to 600 grit. All samples were then electropolished in a solution containing 300ml methanol, 175ml n-butanol and 30ml perchloric acid maintained at -50°C.
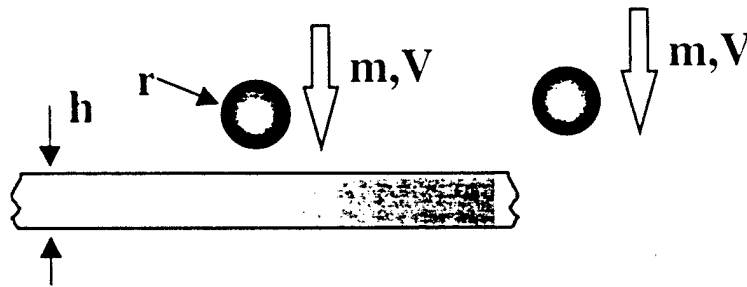

Figure 7.1. Center plate impact geometry and leading edge impact geometry

High speed impact damage was produced using a ballistic impact facility at NASA Glenn Research Center which has been described previously. The spheres were 1.587 mm in diameter and had velocities ranging from 75 m/s to 305 m/s. As described previously, finite element simulations of the impacts were carried out using ABAQUS EXPLICIT.

7.3 Results

7.3.1 Center plate impacts

The relation between small particle impact and the resulting cracking was initially studied in this project for the simplified, though representative geometry of a spherical particle impinging on the center of a thin plate. If sufficiently energetic, this impact can produce cracking on the rear face of the plate. In light of the rear face cracking that occurs in leading edge impacts, rear face cracking in plates impacted in their centers was deemed worthy of study. New data on rear face cracking due to center plate impacts, together with accompanying analyses, are presented here.

Backscatter electron images of cracking on the rear face are shown in Figure 7.2 for two representative impacts on WMS; the nature of rear face cracking is similar in the 47.9 Al baseline alloy. Typically, the cracking zone consists of larger cracks at the center with smaller cracks at the periphery. The radius of the smallest circle that contains all the visible cracking is taken as a linear measure of cracking extent. The radial extent of rear face cracking as a function of impact energy is plotted as the circular marks in Figure 7.3. These data correspond to plates of 47.9 Al baseline, with a thickness of nearly 1.7 mm.
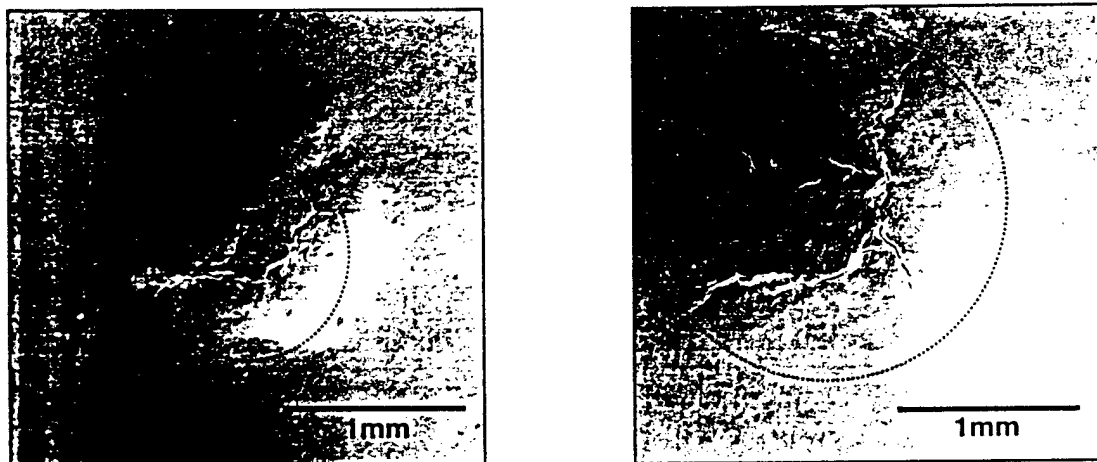

Figure 7.2. Backscatter electron images of typical cracking on rear face of impacted WMS plates. Circles define the cracking zone radius for each impact.

As in past years, we have investigated whether the extent of cracking can be predicted based on FE analysis and on a simplified cracking criterion based on accumulated plastic strain. To that end, a series of calculations were performed taking the plate thickness to be fixed at 1.7 mm, the particle at 1.5875 mm, and varying the impact speed. Using the FE simulations, we calculate the accumulated plastic strain on the rear face of the plate as a function of the radial distance from the center of impact. Then, presuming a constant value of the critical plastic strain for crack initiation, the FE results allow us to predict cracking extent as a function of impact velocity. These calculations were repeated for several values of the critical plastic strain. As can be seen from Figure 7.3, the data is bounded by the curves corresponding to 0.75% and 1.25% plastic strain, with 1% giving

7-4

a reasonable prediction. Results presented in previous reports also showed that predictions based on 1% critical plastic strain were in reasonable agreement with experiments. Data accumulated thus far has argued persuasively for a cracking criterion based on a critical plastic strain. at least for center plate impacts.
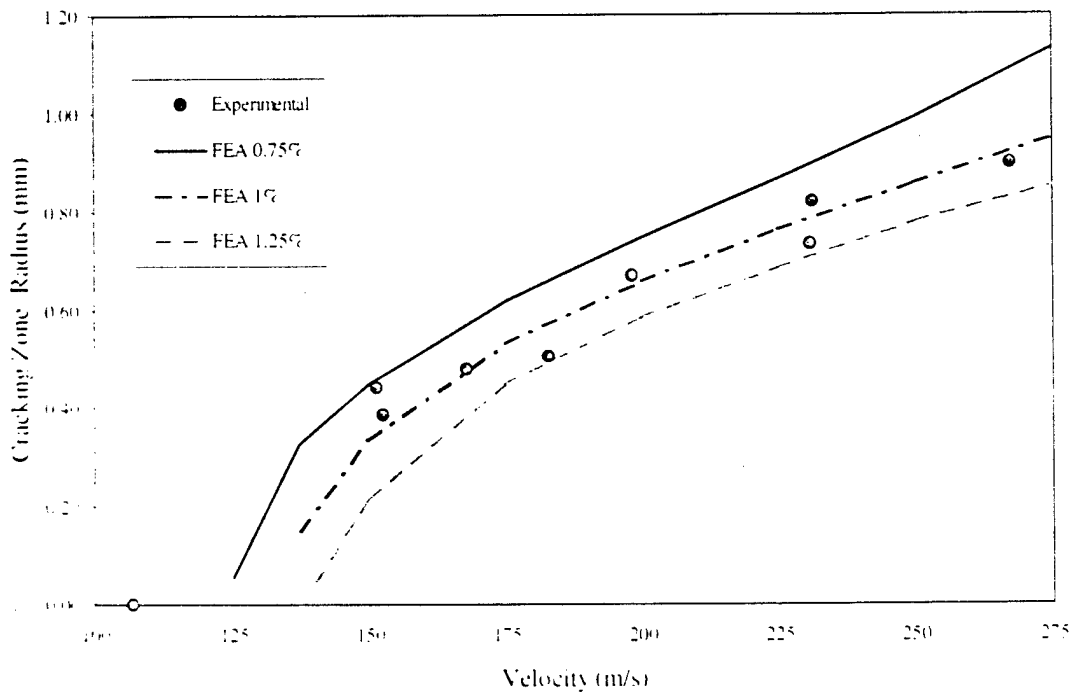

Figure 7.4. Cracking zone radius vs. impact velocity: comparison between observations and predictions for the 1.70 mm thick 47-9 baseline alloy.

7.3.2 Impacts on Leading Edges

The configuration of greatest interest in contemplating gamma for use in blades is impact near the leading edge. It would be immensely valuable to have a reliable model that permits a blade designer to entertain "what if" scenarios for various contemplated blade geometries. To develop that model. we have: (i) simulated leading edge type impacts under controlled experimental conditions and (ii) carried out calculations to see if the observed cracking can be predicted based on a reasonable failure criterion. As will be seen below. the observed cracking can be rationalized. During the final year we hope to translate that rationalization into a model useful to design engineers.

7.3.2.1 Cast-to-Shape, Blade Simulative Specimens

Our studies have been based on two sources of leading edge impacts. A significant and valuable set of data has emerged from the NASA Glenn Research Center (formerly Lewis Research Center). Susan Draper. Michael Pereira, and Bradley Lerch have been studying impacts on cast specimens with contours simulating a GE airfoil design These

:cimens, nominally of the same composition as our 47.9 Al alloy, were cast to shape then chemical milled to have a gage section that is flat with a contoured edge to late the leading edge of a turbine blade. NASA has generated data on the effects of .tile hardness, diameter, and velocity, impact location, specimen thickness, ture at impact, and the effect of a superimposed tensile stress.

r studies have focused on a subset of the NASA data, which includes two specimen .iicknesses (3.56 mm and 2.10 mm). The impacts were associated with hardened ball bearings of radius 1.587 mm; the impacts were carried out at room temperature, with zero superimposed tensile stress. Each impact event is represented by a circle in Figure 7.5 (corresponding to the two thicknesses). The impact energy is symbolized by the diameter of the circles. The y-coordinate of the circle center corresponds to the length of the longest rear face crack resulting from that event (some impacts produce multiple rear face cracks). The x-coordinate of the circle center corresponds to the distance from the impact center to the tip.
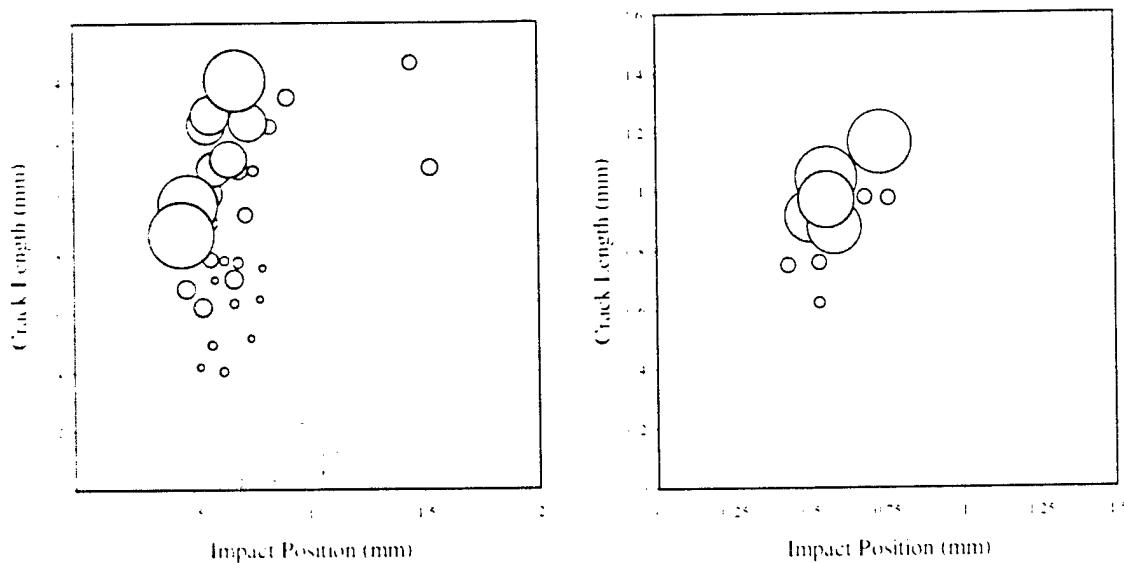

Figure 7.5. Length of longest rear face crack produced by leading edge impact (NASA data) as a function of location of impact center from blade tip. The energy of impact scales with circle diameter. The left plot is for 3.56 mm thick specimens; the right plot is for 2.10 mm thick specimens.

As part of our effort to understand the connection between impact events and damage, we have simulated a series of impacts spanning those depicted in Figures 7.5. Our simulations considered a range of impact velocities (from 150 m/s to 350 m/s) and distances from tip (~0.5 mm to ~2 mm). The critical results extracted from the finite element simulations were plastic strain and tensile stress (acting parallel to the blade axis), both as functions of position and time. Typical results for contours of plastic strain and contours of axial tensile stress shown in Figure 7.6 and 7.7, respectively. The contours of axial tensile stress are highly sensitive to the time; the stresses depicted in

Figure 7.7 are meant to be near to their maximum values. The time incrementing in ABAQUS Explicit is not adjustable by the user; typically there are only a few time steps over the range of interest (when the stresses are near their maximum). Moreover, the stress at each spatial point reaches its maximum at a different instant of time. Thus, one can say the stresses may exceed those depicted in Figure 7.7, but probably only slightly.
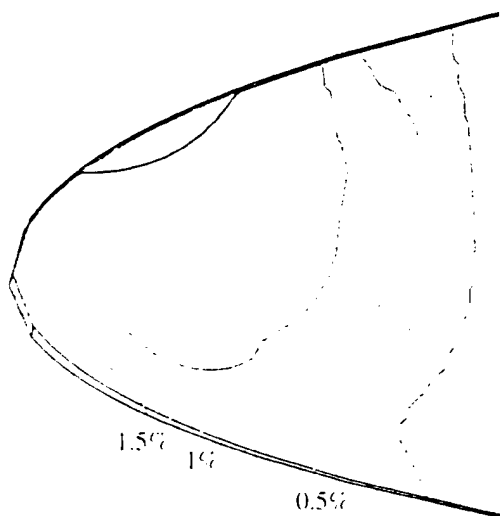

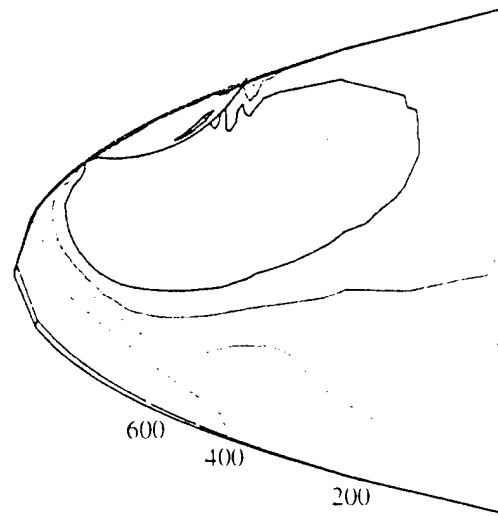Figure 7.6. FEA predicted contours of plastic strain at end of impact.

Figure 7.7. FEA predicted contours of maximum tensile stress (MPa).

As described in the previous report, impacts can produce very different combinations of stress and strain depending on the position of the impact. For example, if the impact is of high energy, but close to the tip, there can be a large plastic strain far from the tip. However, this plastic strain occurs due to bending of the blade in the cross-section; in fact, the stresses at the position of high plastic strain are compressive. One suspects that cracking would not occur under such conditions. Thus, while results for the center plate impacts presented in the last section suggest that plastic straining dictates cracking, the center plate impact geometry always leads to tensile stresses accompanying plastic straining. As just pointed out, plastic straining may involve tensile or compressive stress.

Still contours of plastic strain and stress can be a basis for predicting the extent of cracking. For example, one can posit that, for a given impact, cracking occurs along the back face up to a point at which the plastic strain no longer exceeds, say, 1%. Alternatively, one can assume that cracking occurs along the back face up to a point at which the tensile stress no longer exceeds, say, 300 MPa. Perhaps more realistically, one can posit that cracking requires both plastic strain and tensile stress. Accordingly, Figure 7.8 shows the prediction of cracking extent as a function of impact position, for a fixed impact velocity and specimen geometry. The predictions are based on three criteria: achieving 300 MPa, achieving 1% plastic strain, and achieving both 300 MPa and 1% plastic strain. It is seen that the plastic strain criteria limits cracking extent for impacts

7-7

that occur farther from the tip; the stress criteria limits cracking for near tip impacts. One can also see how, for a given speed, cracking may disappear as impacts occur far enough away from the edge, depending on whether a center plate impact of that speed would cause cracking.
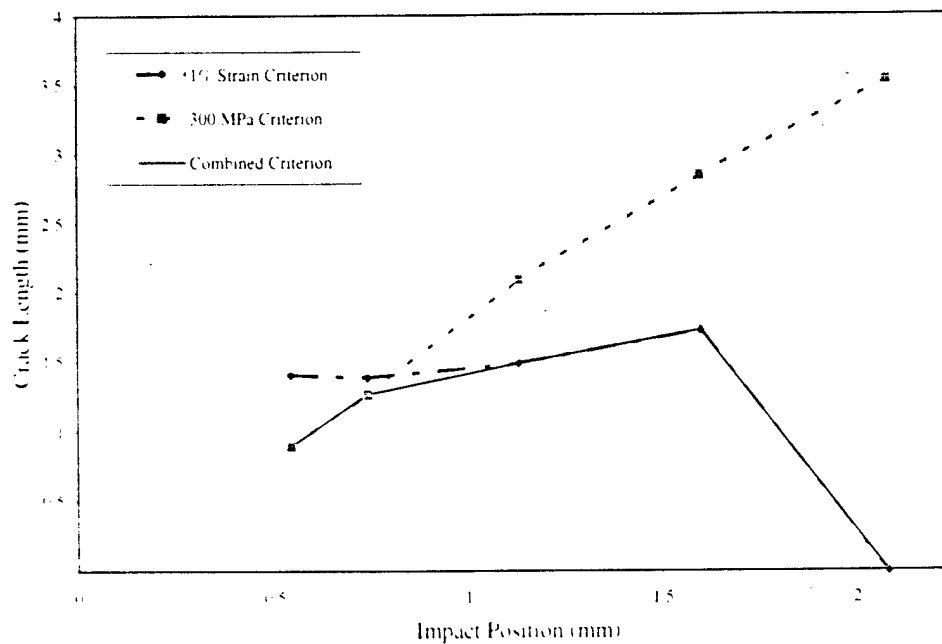

Figure 7.8. Finite element prediction for length of rear face crack as a function of impact position given three cracking criteria. (1.587 mm sphere at 275 m/s on 3.56 mm thick specimen)

FEA predictions are compared with the observed rear face cracking in Figures 7.9 and 7.10 for thicknesses of 3.56 mm and 2.1mm respectively. The experimental data are plotted as the shaded circles; the predictions based on the combined plastic strain- tensile stress criteria are plotted as the empty circles. There is clearly significant scatter in the experimental data; moreover, the impacts did not occur over a wide enough range of positions to truly test the predicted variation with impact position. The comparison between this set of data and the FEA predictions does leave open the question of the validity of the proposed combined cracking criterion. Still, there are some features that are worth pointing out. First, for impacts in the range of 0.5 to 1.0 mm (where most of the experimental data lie), the cracking extent is not strongly dependent on the impact energy. This is also seen in the predictions: for near tip impacts, where the stress criterion controls, the cracking is not sensitive to impact energy. Second, there is some indication for the lower energy impacts that cracking extent decreases when the impacts are very far from the tip. This is also predicted; impacts in this regime are controlled by the plastic strain. Thus, one sees some indications that the combined criterion provides useful insight into the patterns of cracking in leading edge impacts.
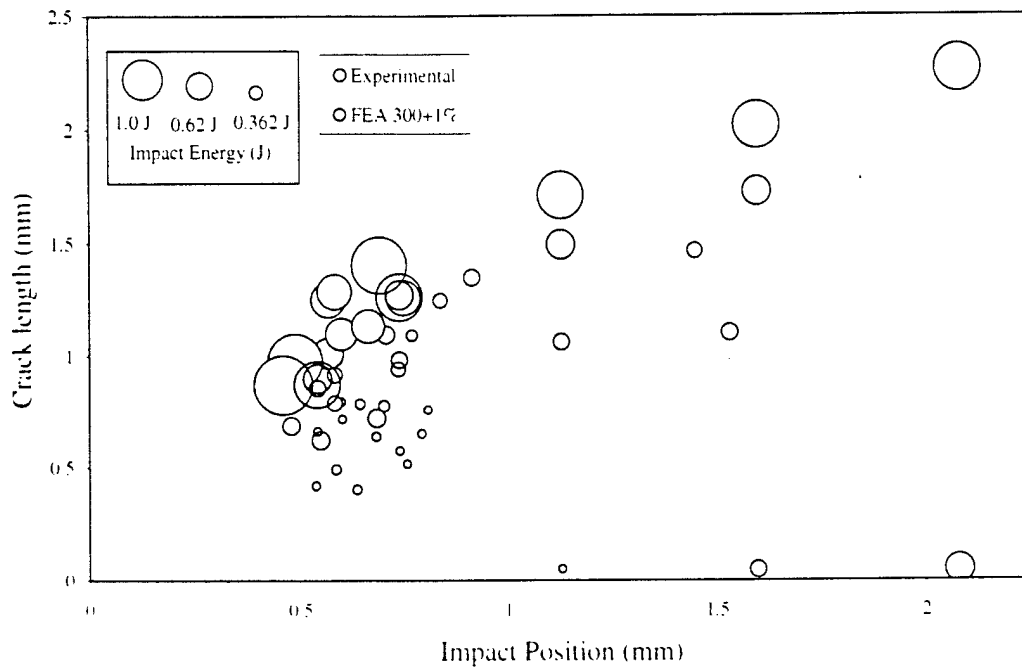
Figure 7.9. Comparison of crack lengths on rear face of impacted 3.56 mm thick
NASA specimens with FEA predictions based on a combined cracking criterion.
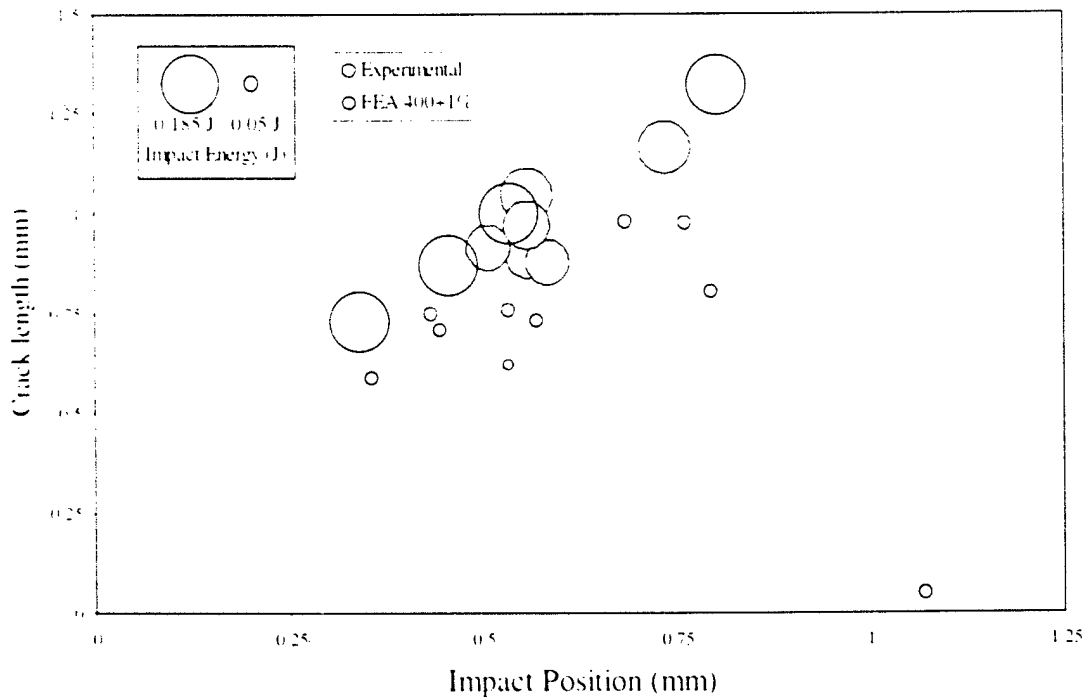(300 MPa tensile stress and 1% plastic strain)

Figure 7.10. Comparison of crack lengths on rear face of impacted 2.10 mm thick
NASA specimens with FEA predictions based on a combined cracking criterion.
(400 MPa tensile stress and 1% plastic strain)

7.3.2.2 Machined, Leading Edge Simulative Specimens

The experiments on the cast-to-shape blade-simulative specimens have been an invaluable beginning for our studies of the leading edge impacts. However, our additional goals of exploring a variety of materials and providing damaged specimens for the fatigue studies carried out at University of Michigan dictate that we have a leading edge specimen which can be machined from flat plates. To that end, we have devised a machined, leading-edge simulative specimen involving a rectangular plates with four corners chamfered (shown in Figure 7.11). Specifically, these specimens were first prepared as were the rectangular plates. After sanding the rectangular samples to 400 grit, the four long edges were chamfered at 14° by low stress grinding. Then, all surfaces were sanded up to 600 grit and then electropolished. The electropolishing leads to minimal rounding of the sharp corners of the specimen. As can be seen from Figure 7.12, which depicts an impact of 93 m/s on the chamfer of a 47.9 Al baseline specimen, the leading-edge simulative specimen exhibits the same rear face cracking as exhibited by the NASA cast-to-shape blade-simulative specimens.
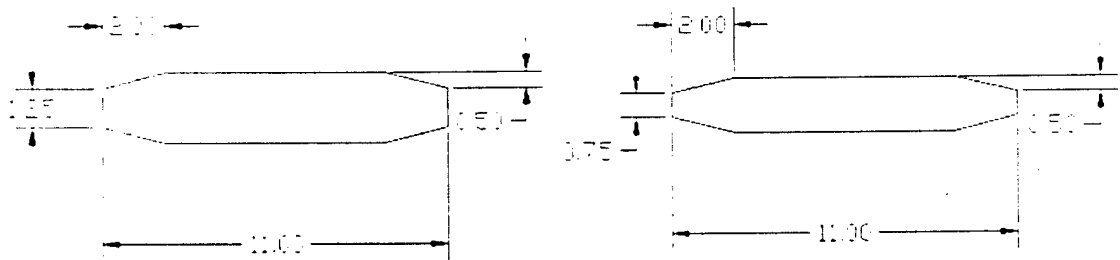

Figure 7.11. Machined leading-edge geometry

Thus far, impact data has been obtained for a single 47.9 Al baseline specimen of thickness 1.7 mm. The observed extent of the largest rear face crack is plotted as the shaded circles in Figure 7.13. Predictions based on the combined plastic strain-tensile stress criterion are also plotted in Figure 7.13 as the empty circles. It can be see that the general variation of the data with respect to impact position and energy is well captured by the combined cracking criterion. Additional impact data on leading-edge simulative specimens now being gathered will help to test further the usefulness of this cracking criterion.
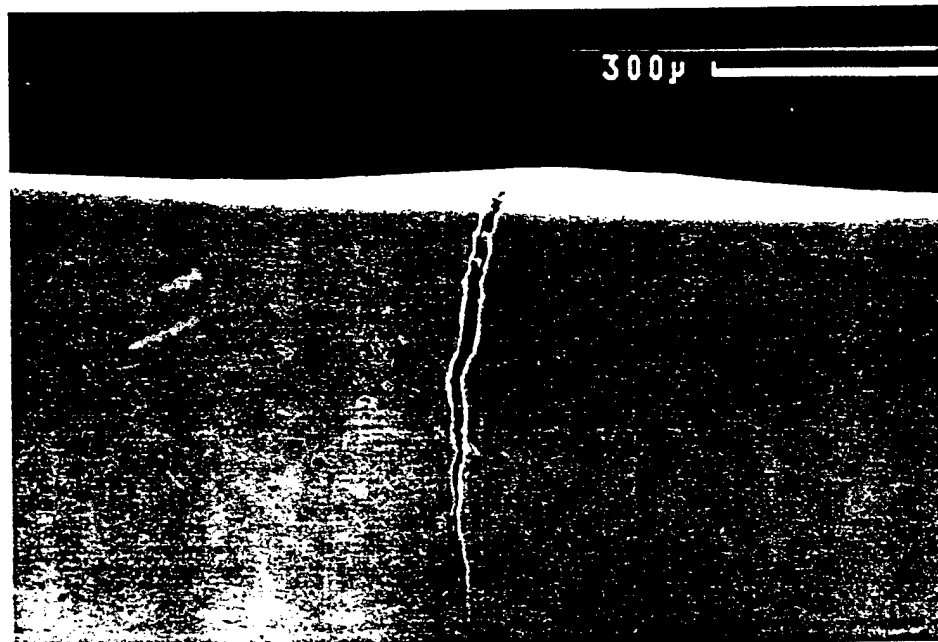
Figure 7.12. Rear face of chamfered 47.9 Al baseline specimen impacted with 1.5875 mm diameter steel sphere at 93 m/s at a distance from the tip of 0.18 mm.
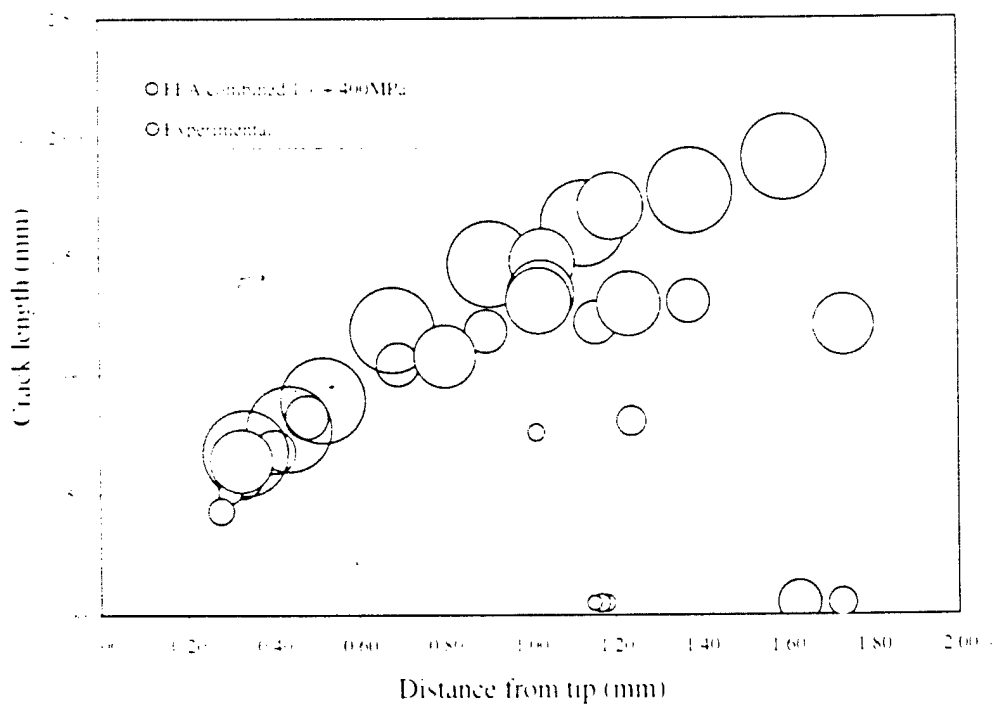

Figure 7.13. Experimental results with FEA predictions for chamfered 1.7 mm thick 47.9 Al baseline specimens.

Conclusions and Future work

king on the rear face of plates impacted at their center by small high-speed particles
es useful insight into the more relevant threat of leading edge damage of gamma
s. Studies of center impacts have shown that the overall extent of rear face
king is well predicted by finite element analysis, together with a critical plastic strain
erion for crack initiation. The most recent data indicates that the cracking extent in
he 47.9 Al baseline alloy is well bounded by predictions based on 0.75% and 1.25%
critical plastic strain. These strain levels compare well with the ductility inferred from
static uniaxial tensile tests on flat coupons.

Impacts on the leading edge of airfoils have been studied in two ways. First, an existing
set of impact data on cast-to-shape blade-simulative specimens which had been generated
by NASA Glenn Research Center (in a joint GE/NASA program) has been compared
with finite element analysis. Second, a new machined, leading edge simulative specimen
has been developed in this program. Initial impact testing has occurred and these have
been compared with finite element analysis.

In the case of impacts near leading edges, it has been found that areas of high plastic
strain do not necessarily have tensile stress. While a general multiaxial criterion for
crack initiation criterion has not been established for gamma, we have taken a
preliminary stab at this problem, at least in the context of leading edge impacts.
Specifically, we have considered a combined criterion in which cracking requires both a
minimum level of plastic strain and a minimum level of tensile stress. This criterion
leads to very interesting predictions regarding the variation of cracking with impact
energy and with position of impact relative to the tip. Very near the tip, the cracking is
relatively insensitive to impact energy; by contrast, it is quite sensitive to energy farther
from tip. In addition, for a fixed energy, the extent of cracking increases initially with
position from the tip, and then decreases. Comparison with the NASA data shows that
the general level of cracking is predictable; while there is some indication of the
predicted variation with position and energy, for the data set used impacts tended to be in
a narrow range of distances from the tip. Initial impact data from the new machined,
leading edge simulative specimen shows the cracking to be reasonably well predicted;
also, there is more evidence of the predicted variation with impact position.

During the final year, we first intend to continue to test the predictability of leading edge
cracking due to impact on both types of specimens on several material systems. Second,
providing the anticipated predictability is found, we intend to develop charts or
guidelines to aid in the accounting for FOD in the design of gamma airfoils.

7.5 Acknowledgements

7.6 References

Draper, S.L., Pereira. J.M. and Nathal, M.V.. 1997, HITEMP Review 1997, NASA CP-10192, Vol. II, pp.25-1 to 25-13.

8. Fatigue Behavior of Gamma TiAl

Trevor S. Harding
J. Wayne Jones
Ryan M. Smith
Elen G. Koharian
University of Michigan

8.1. Introduction

The drive to reduce aircraft gas turbine engine weight, while improving performance and efficiency, has positioned γ-TiAl alloys among leading candidates to replace current nickel-based super alloys as the material of choice for low pressure turbine blades. This is primarily a result of the lower density, high specific stiffness and elevated temperature strength retention, and good environmental resistance of γ-TiAl. The lower density in particular will lead to significant engine weight savings and reduced stresses on rotating components such as low pressure turbine blades (Perrin, 1998).

A significant drawback to γ-TiAl alloys, in terms of component design, is their limited fatigue crack growth resistance compared to nickel-based super alloys (Austin et al., 1997), (Huang and Chesnutt, 1994). In general, there is a small difference between the threshold stress intensity range of long cracks and the apparent toughness, leading to dramatically shortened lifetimes for small changes in applied stress should threshold be exceeded (Campbell et al, 1997), (Rosenberger et al., 1996), (Sadananda and Vasudevan, 1995), (Venkataswara et al. 1995). This is particularly troubling in the presence of an extrinsic damage mechanism since the initiation lifetime would be eliminated. The use of a damage tolerant approach to design for γ-TiAl alloys would then necessitate the use of more accurate crack detection methods and shorter inspection intervals, both of which add cost to engine operation. A preferable approach to designing with γ-TiAl is to use endurance limits and threshold stress intensity range values for determining acceptable operating stresses. This technique has the advantage of ensuring that components with pre-existing flaws will have a theoretically infinite life. In addition, this method reduces the effort at the design stage (i.e. there is no need for lifetime summation over complex engine loading spectra) and reduces the need for engine inspections (Perrin, 1998).

A serious limitation to a threshold-based design philosophy is that the anticipated size of any pre-existing flaws must be known accurately. In the case of assembly-related impacts or foreign object damage (FOD) this may prove difficult. The effects of simulated FOD on fatigue properties has been examined for conventional titanium alloys, as well as γ-TiAl, but to date none have examined impact damage in light of a threshold-based design approach (Lerch et al, 1999), (Roder et al, 1999), (Nicholas et al, 1980), (Hudak et al, 1999). The fatigue of γ-TiAl project of the PRET program examines the effects of both assembly-related ("shop floor") impact damage and FOD on fatigue strength and uses a threshold-based model to predict this response over a range of damage severities. Presently, the program has established a good correlation between fatigue strength and impact damage for assembly-related damage at both room and

elevated temperature for the duplex General Electric Ti-47.9Al-2.0Cr-1.9Nb alloy and the near-fully lamellar Allied Signal Ti-47.3Al-2.2Nb-0.6Mn-0.45W-0.46Mo-0.23Si alloy. Particular nuances such as the influence of residual stresses, small crack effects, lifetime modeling and inaccuracies in measuring the initial flaw size have been examined and are discussed in the present report. Future research will examine the effect of simulated FOD on both a duplex and fully lamellar alloy.

8.2. Objectives and Approach

The objectives for the past year in the fatigue of γ-TiAl project has been to complete step-loading fatigue tests at elevated temperature and evaluate the phenomenon which may be leading to a deviation from the threshold-based predictions, including small crack effects, residual stress effects and inaccuracies in crack shape measurement. Constant amplitude fatigue tests were conducted at 600°C on the 48-2-2 alloy to examine the role that the small crack effect plays in fatigue strength reductions from impact damage. Further modeling of the lifetime response of impact damaged material was conducted through a collaborative effort with the Materials Directorate at Wright Patterson Air Force Base.

Additional analysis was carried out to determine the effect residual stresses play in the experimental fatigue results. X-ray diffraction techniques, stress relieving of fatigue specimens and a modified threshold-based model were all used to address the residual stress effect.

Finally, quantitative fractographic analysis was used to produce a better idea of the shape and size of initial impact damage and the growth mechanisms of subsequent fatigue cracks. The method involved characterizing impact damage and fatigue cracks based on differences in the amount of heat tinting present on the fracture surfaces of failed specimens. The goal is to address the effect of impact damage crack shape on the threshold predictions of fatigue strength.

8.3. Summary of Results from Fourth Year of Fatigue Studies

The results presented in this report suggest that a threshold-based approach to elevated temperature design of γ-TiAl low-pressure turbine blades, with assembly related impact damage in mind, is feasible if several additional variables are taken into account. Namely these are residual stress effects, small crack effects and a difficulty in accurately portraying the shape and extent of impact damage in the interior of blades, or for that matter specimens. Step loading fatigue tests at 600°C have shown that simulated assembly related impact damage reduces the fatigue strength of both the Ti-47.9Al-2.0Cr-1.9Nb duplex alloy (48-2-2) and Ti-47.3Al-2.2Nb-0.6Mn-0.45W-0.46Mo-0.23Si near-fully lamellar alloy (WMS) in a way that can be generalized with a threshold-based prediction. However, the variables mentioned previously complicate the issue, specifically by making the threshold-based model conservative in the severe impact regime and non-conservative in the low to moderate impact regime.

To address the issue of a residual stress effect, numerical analysis was conducted on step loading fatigue test data to determine the residual stresses necessary to cause the increase in fatigue strength at severe impact levels. The effect of residual stresses in the duplex alloy was found to be small and only appeared to improve fatigue strength at the most severe damage levels. In the near-fully lamellar alloy, on the other hand, the residual stress effect was found to be significantly higher and effected the fatigue strength of specimens with moderate to severe impacts. This combination resulted in the near-fully lamellar alloy having higher fatigue strength for a given level of impact damage compared to either the duplex alloy or the threshold-based prediction for the alloy. X-ray diffraction techniques and specimen annealing failed to produce reliable results.

A small crack effect was suspected in causing the threshold-based model to be non-conservative for low to moderate severity impacts. To address this issue constant amplitude fatigue tests were conducted on the duplex alloy at 600°C, and their results predicted using curve fits of the long-crack fatigue crack growth behavior. The stress-lifetime response of specimens with low and severe impacts was compared. The curve fit accurately predicted the stress-lifetime response of the severely impacted specimens, suggesting that such damage levels are in the long-crack regime. However, modeling of the specimens with low severity impacts, and therefore, cracks in the small crack regime, required the same curve fit equation with an artificially constrained threshold of 3.3 MPa√m. This suggests that small cracks in the duplex alloy may begin propagating at stress intensities below the long crack threshold, but then accelerate quickly in a way similar to long-cracks.

Finally, a quantitative fractographic investigation of the actual appearance of impact damage and fatigue crack growth in step loading test specimens was conducted for both alloys. The results indicate that several of the threshold prediction assumptions regarding impact damage are erroneous. The extent of internal damage is generally overestimated from surface measurements when indent tip cracks are present on the specimen surface, and underestimated when they are not. Also, fatigue cracks propagating from the impact damage zone tend to do so as either quarter-elliptical corner cracks with an average aspect ratio of 0.75, or as surface cracks. A second set of threshold predictions were calculated based on the assumption that the impact damage could be treated as a corner crack with depth equivalent to the effective crack length and aspect ratio equal to the fatigue cracks. The actual fatigue results agreed well with this model, though additional data is needed to confirm it. However, a true representation of the impact damage would take into account that the indent itself should be treated as a through-thickness crack, while the indent tip crack may be a corner or surface crack. Thus, a more realistic threshold prediction would likely fall somewhere between the through-thickness crack prediction and the corner crack prediction on the Kitagawa plot. From the data, it appears that such a model would still need to take into account a reduced residual stress effect. Moreover, none of the threshold predictions accurately addresses the small crack effect for low to moderate severity impacts.

8.4. Review of Previous Work

In previous years of the fatigue of γ-TiAl project, the use of step-loading fatigue tests to determine the effect of simulated shop floor damage on fatigue strength has proven quite successful. Studies conducted on the General Electric cast 48-2-2 alloy and the Allied Signal cast WMS alloy at room temperature found good correlation between the experimental fatigue strength and threshold-based predictions. Tests at 600°C on the same alloy, for which a dedicated quartz lamp furnace was constructed, have also shown good correlation with threshold-based predictions. Prior to this report, however, tests on the WMS alloy had not been completed.

The final results did, however, show that the threshold-based prediction was somewhat conservative for large damage levels and non-conservative at very slight damage levels. The exact definition of these ranges is dependent on the alloy in question and, therefore, on the microstructure. The non-conservative nature of the prediction at small damage levels was expected to be a result of the small crack effect. Results of tests intended to examine this effect are presented in Section 8.7.2. Possible explanations for the conservative predictions at large damage levels included residual stresses and inappropriate assumptions regarding the shape and severity of the initial impact damage. Efforts aimed at analyzing these factors are discussed in Sections 8.7.1 and 8.7.3 respectively.

Finally, a more complete understanding of the effect of microstructure on the formation of impact damage and fatigue failure was developed. Impact damage was found to be dependent on both material and mechanical parameters for the simulated shop floor damage. Furthermore, local microstructural features, such as misoriented lamellar colonies and weak γ grain boundaries, could lead to larger damage levels than anticipated. Misoriented lamellar colonies could also have a dramatic effect on fatigue properties in the WMS alloy as well. Though the WMS alloy exhibited a greater resistance to impact damage and higher fatigue strength in the undamaged state, this advantage was lost when the impact damage interacted with an unfavorably oriented lamellar colony leading to rapid interlamellar failure.

8.5. Materials and Experimental Procedure

In the present study, two different gamma titanium aluminide alloys were examined. The first of these was provided by General Electric Aircraft Engines (Huang, 1991) and has a nominal composition of Ti-47.9Al-2.0Cr-1.9Nb (at.%). This alloy is referred to as "48-2-2" from this point. Plates were investment cast at Howmet Corporation with final dimensions of 12.5 mm x 100 mm x 140 mm. These plates were first heat-treated in vacuum at 1093°C for 5 h, followed by a hot isostatic press (HIP) at 1205 °C and 172 MPa for 4 h. A final heat treatment of 1205 °C for 2 h and rapid cool completed the processing. The final microstructure, shown in Figure 1 consisted of a duplex structure of equiaxed gamma grains, roughly 70 μm in size, and about 6 vol.% γ-α_2 lamellar colonies.

second alloy was originally developed by Allied Signal and had a nominal position of Ti-47.3Al-2.2Nb-0.5Mn-0.4W-0.4Mo-0.23Si (at.%), and is referred to as IS" from this point. The alloy was investment cast into plates with final dimensions 2.5 mm x 100 mm x 150 mm. Post-casting processing included a HIP treatment of °C and 172 MPa for 4 h, followed by a heat treatment of 1010 °C for 50 h. The microstructure produced by this processing is shown in Figure 2. Optical scopy revealed a near fully lamellar microstructure with lamellar colonies on the der of 165 μm in size and 10-20 μm gamma grains along lamellar colony boundaries.

Figure 1: Optical micrograph of duplex 48-2-2 alloy showing 70 μm equiaxed γ grains and a small fraction of lamellar (γ-α$_2$) colonies.
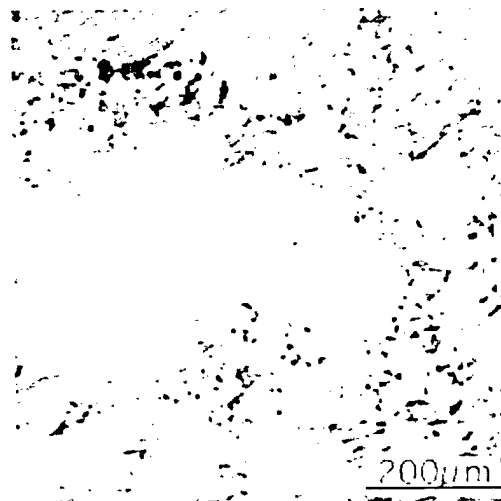
Figure 2: Optical micrograph of the lamellar WMS alloy revealing lamellar colonies of roughly 165 μm in size surrounded by small equiaxed gamma grains.

Assembly related ("shop floor") damage was introduced quasi-statically rather than in a dynamic impact. The reasons for this include the ability to accurately reproduce damage

levels based on the load of the indent. Quasi-static indentation and dynamic drop-weight impacts were found to produce qualitatively identical damage, only the quasi-static indents were far more reproducible. Quasi-static indents involved pressing a hardened steel wedge with a 60° flank angle into the specimen edge at a displacement rate of 0.25 mm/min. During the indentation the load was monitored with a load cell and when the desired load was reached the wedge was withdrawn. The indent results in a notch-like indent and, in the case of moderate to severe indents, an indent tip crack. A discussion of the correlation between peak load and damage, and the damage mechanisms can be found in the previous year's report.

8.6. Step Loading Fatigue Test Results

The reduction in fatigue strength following introduction of simulated impact damage is determined using the step-test method (Collins, 1993) and examined with a modified form of the Kitagawa plot (Kitagawa and Takahashi, 1976). Figure 3 compares the fatigue failure strength determined from step-tests conducted at 600°C with the effective crack length determined from pre-test measurements. The fatigue failure strength is defined as the highest stress level at which a specimen survived an entire stress block of 10^5 cycles during the step test. Given that the difference between the threshold stress intensity range and apparent toughness is small in γ-TiAl alloys, the fatigue failure stress is considered to be a reasonable approximation of the endurance limit.

Solid lines in Figure 3 represent the fatigue strength of undamaged material (slope = 0) and the predicted fatigue strength as determined from a long-crack threshold-based calculation (slope=-1/2). This prediction is based on the presumption that impact damage can be modeled as a through-thickness crack with depth equal to the effective crack length. The dashed line with slope of -1/2 represents a threshold-based prediction calculated from closure corrected, effective threshold stress intensity range data. Theoretically, the actual fatigue strength results should follow these lines. As a result, it is clear that despite lower fatigue strength in the undamaged state, the duplex 48-2-2 alloy should have a higher fatigue failure stress at moderate to severe damage levels because of its higher threshold stress intensity range. The fatigue strength of the undamaged material is determined in the same manner as damaged specimens. The fatigue strength of undamaged material was found to be 310 MPa and 490 MPa for the 48-2-2 and WMS alloys respectively at 600°C.

As can be seen from Figure 3, for relatively large effective crack lengths, the threshold-based approximation follows the general trends in the reduction of the fatigue strength. The fatigue data does not, however, follow the −1/2 slope of the threshold-based prediction as expected. Instead at large effective crack lengths, the measured fatigue strength is higher than the threshold-based model would predict. And, though the 48-2-2 alloy should have a higher fatigue failure stress for an equivalent effective crack length, the actual fatigue failure stress of the WMS alloy is considerably higher. Furthermore, for moderate effective crack lengths, the fatigue strength data is lower than the threshold-based model. This suggests that the model is conservative for large impact sites and non-conservative for smaller impacts, which would presumably be more difficult to detect in

engine inspections. It should also be pointed out that at effective crack sizes below the transitional flaw size the measured fatigue strength approaches the fatigue strength of undamaged material asymptotically from below. Therefore, despite a general correlation between the threshold-based approach to predicting fatigue strength reductions following impact and the actual data, there are some discrepancies. These will be discussed in the following section.
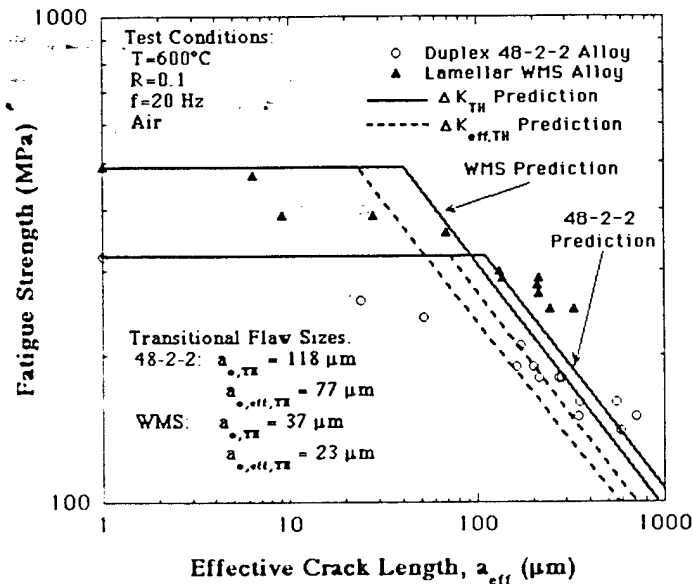

Figure 3: Modified Kitagawa plot of 48-2-2 and WMS at 600°C showing the reduction in fatigue strength as a function of effective crack length

The intersections of the line representing the undamaged material fatigue strength and the threshold-based or effective threshold-based lines are termed the transitional flaw sizes. $a_{o,TH}$ and $a_{o,eff,TH}$. Theoretically, $a_{o,TH}$ is a critical flaw size above which the threshold stress intensity range (ΔK_{TH}) can be reasonably considered a constant. In other words, cracks of size greater than $a_{o,TH}$ can be considered long cracks (Kitagawa and Takahashi, 1976). Likewise $a_{o,eff,TH}$ defines a critical flaw size above which the effective threshold stress intensity ($\Delta K_{eff,TH}$) can be considered constant. The values of $a_{o,TH}$ and $a_{o,eff,TH}$ are 118 μm and 77 μm respectively for 48-2-2. Compared with the duplex microstructure of the 48-2-2 alloy, $a_{o,TH}$ is roughly 1.5-2 times the average γ-grain size and $a_{o,eff,TH}$ is approximately equivalent to one grain diameter. For the WMS alloy these values are 37 μm and 23 μm. Neither of these transitional flaw sizes appears to correspond to the lamellar colony size, the dominant microstructural feature. However, the value of $a_{o,TH}$ is approximately 2 - 3.5 times the size of the γ-grains located at lamellar colony boundaries. The value of $a_{o,eff,TH}$ is 1 - 2.5 times the γ-grain size.

8.7. Analysis of a Threshold-Based Model of Fatigue Behavior

8.7.1. Residual Stress Analysis

One possible explanation for the conservative estimates of fatigue strength for large effective crack lengths is the existence of compressive residual stresses in the impact site which interact with the propagating indent tip crack to alter the driving force for further propagation. During the indentation, significant plastic deformation occurs to accommodate the formation of the indent, particularly in larger indents. This deformation would likely result in a zone of compressive residual stresses near the indent tip. Attempts to measure the residual stresses quantitatively with x-ray diffraction techniques proved infeasible given the small size of the damage zone relative to the x-ray beam, material cast texture and the presence of a non-uniform residual stress gradient. As a result, the approach taken was to estimate the residual stresses based on a modified threshold-based model and fatigue strength data from step-tests. In addition, a number of specimens of each alloy were impacted at various loads to produce a range of impact sites and then annealed at 800°C for 2 hours in an attempt to relieve the residual stresses. These specimens were then tested using the step-test method and compared with un-annealed specimens as another measure of the residual stress effect.

Development of a threshold-based model that incorporates a residual stress effect requires an understanding of the effect of residual stresses on the stress intensity range, ΔK. It must first be assumed that the sum of the reduction in ΔK due to the residual stress and the minimum ΔK in the applied load cycle is less than zero. The stress intensity range can then be reduced to the sum of the maximum nominal stress intensity and the stress intensity due to the residual stresses:

$$\Delta K = K_{max} - K_{min} = \left(K_{max}^{NS} + K^{RS}\right) - \left(K_{min}^{NS} - K^{RS}\right) \tag{1}$$

$$\Delta K = K_{max}^{NS} + K^{RS} \tag{2}$$

where K_{min}^{NS} and K_{max}^{NS} are the minimum and maximum stress intensity due to the nominal or applied stress and K^{RS} is the stress intensity factor due to residual stresses. Equation (1) can be reduced to equation (2) since the magnitude of K_{min} is less than zero and can be assumed to have no effect on crack propagation. However, a compressive residual stress component of the stress intensity will have an effect on the apparent load ratio. In these experiments, the applied load ratio was 0.1 for all tests. However, a compressive residual stress field would tend to reduce the apparent load ratio, which in turn would tend to increase the threshold stress intensity range of the material. An empirical equation was derived using threshold data for 48-2-2 and WMS at R=0.1 and threshold data for a representative γ-TiAl alloy (Larsen et al, 1996). This equation was assumed to be of the same form as that developed by Elber (Elber, 1971):

$$\Delta K_{th} = \frac{\Delta K_{eff,th}}{0.40R + 0.76} \tag{3}$$

The load ratio dependence of ΔK_{TH} was found to be identical for both the 48-2-2 and WMS alloys at 600°C. By combining equation (3) with a fracture mechanics calculation of σ_{TH} based on ΔK_{TH} and the load ratio one can arrive at the following:

$$\sigma_{TH} = \frac{\Delta K_{eff.TH}\left(\sigma_{max}^{NS} + \sigma^{RS}\right)}{K_{max}^{NS}\left(0.72\sigma_{max}^{NS} + 1.044\sigma^{RS}\right)} \qquad (4)$$

Equation (4) forms the basis of a new threshold-based model that incorporates the effects of a compressive residual stress field in the damage zone. However, in order to apply this model to the Kitagawa Plot, an assessment of the estimated residual stresses must be determined. Using numerical methods, equation (11) is solved for the residual stress term which best estimates the measured fatigue failure stress of a specimen with effective crack length, a_{eff}. In other words, equation (11) is not estimating the actual residual stresses at the indent tip, rather it is calculating a value of σ^{RS} which best corrects the discrepancies in the data observed in the Kitagawa Plot (Figure 3). In the case of the 48-2-2 alloy, the estimated residual stresses vary from –60 MPa to –90 MPa over a wide range of effective crack lengths, and thus impact severities. This suggests that the effect of residual stresses on the final fatigue behavior in 48-2-2 is small and is consistent from one impact to another. In the WMS alloy the range of estimated residual stresses is also narrow (-150 MPa to –200 MPa). However, the effect of residual stresses is 2 – 3 times greater than in the 48-2-2 alloy and there is a moderate dependence of residual stress effect on effective crack length, with the residual stress effect decreasing with increasing crack length. The greater residual stress effect in the WMS alloy is not suprising given that the WMS alloy has higher yield strength than the 48-2-2 alloy (503 MPa vs. 330 MPa at 23°C). Therefore, despite having a lower threshold, the greater strength of the WMS alloy results in residual stresses that retard fatigue crack growth and lead to higher overall fatigue failure stresses than in 48-2-2. It is worth restating here that the estimated residual stresses from equation (4) do not necessarily reflect actual residual stress magnitudes, but rather represent the relative effect that residual stress has on final fatigue behavior.

Figure 4 shows the effect that a compressive residual stress has on fatigue strength of the 48-2-2 alloy following impact. The curves shown represent the upper and lower bounds of compressive residual stresses estimated from equation (4). Figure 4 shows that the modified threshold-based model can accurately bound the actual fatigue results. Based on the upper bound, the residual stress effect appears to be limited to crack lengths greater than approximately 400 µm. Cracks of this size were present only in the most severely impacted specimens. At crack lengths less than 400 µm, the model still predicts that residual stresses are present at the damage zone. However, the residual stresses are small in comparison to the applied stresses necessary to cause failure in specimens with these smaller effective crack lengths. As a result, the residual stress effect on the Kitagawa plot is not apparent in these specimens.

The effect of residual stresses on the fatigue strength of impact damaged WMS is shown in Figure 5. Curves representing the upper and lower bounds of estimated residual stresses are shown in Figure 5 along with the threshold-based prediction. Again, the curves bound the measured fatigue strength data, suggesting that equation (11) is an effective way of predicting the effect of residual stresses on fatigue strength, if not actual residual stresses. Residual stresses do not appear to affect the fatigue strength of specimens with effective crack lengths smaller than 80 - 130 μm. Thus the benefit of residual stresses would be imparted on considerably smaller damage zones, and thus less severe impacts, in the WMS alloy than for the 48-2-2 alloy.
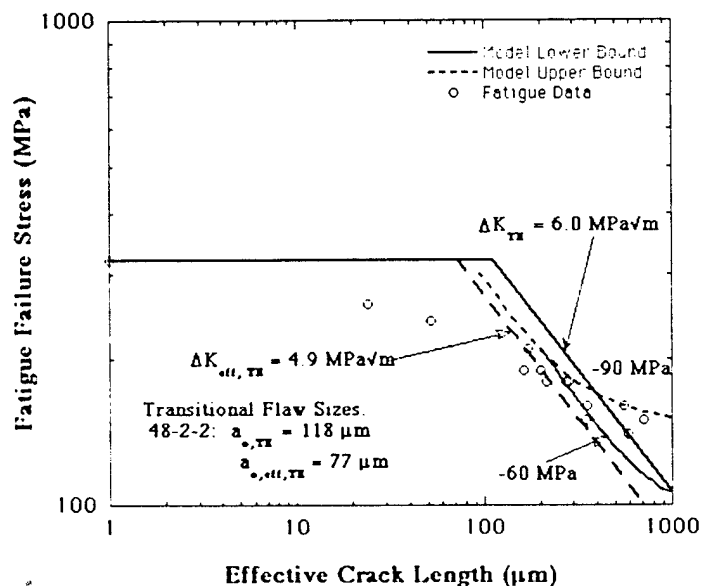

Figure 4: Effect of estimated compressive residual stresses on the threshold-based model of 48-2-2 at 600°C as shown in a modified Kitagawa plot

As mentioned previously several specimens were annealed at 800°C for 2 h following indenting in the hopes of relieving residual stresses around the indent tip. If successful, subsequent step-testing would reveal the reduction in fatigue strength resulting from the removal of residual stresses, and thus indicate the magnitude of the residual stress effect. The annealing appears to have had no affect on the subsequent fatigue results of the 48-2-2 alloy. It is possible that the anneal does not relieve the residual stresses. However, microstructural characterization of indents following annealing revealed a band of recrystallization around the indent, suggesting that the stress field had been relieved at least partly. This region of recrystallization is not expected to significantly alter the fatigue crack growth properties, since it is small in comparison to the size of the indent tip crack. This lack of a significant reduction in fatigue strength following annealing suggests that some other phenomenon may be causing the higher than predicted fatigue strength. One possible explanation is that the assumptions made in modeling the impact damage for the threshold prediction are in error.
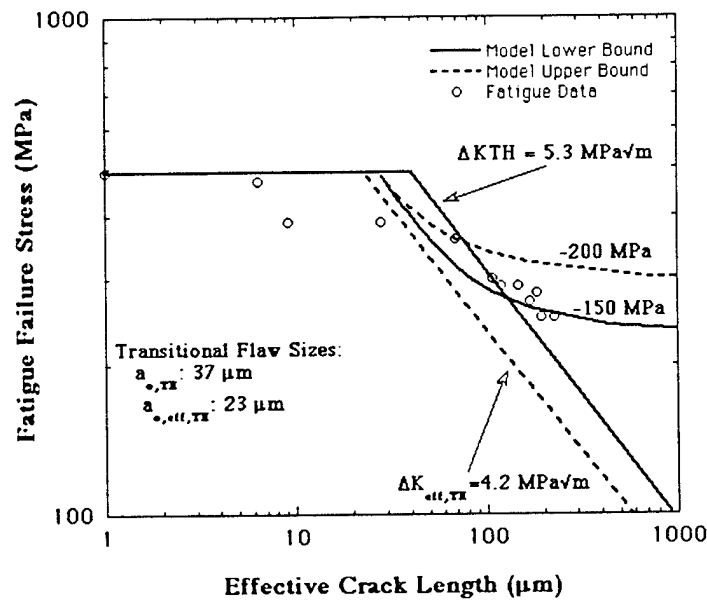
Figure 5: Effect of estimated compressive residual stresses on the threshold-based model of WMS at 600°C as shown in a modified Kitagawa plot

In the case of the WMS specimens, the fatigue strength of low and moderate severity impacts does not appear to be affected by the annealing. In the largest impact, however, the fatigue strength is significantly lower than specimens with similar effective crack lengths. Analysis of the estimated residual stress in this particular specimen following annealing indicates that the effect of residual stress could be estimated at -115 MPa. Which is less than the lower bound estimated for the standard WMS specimens. While this may suggest that the annealing reduced the compressive residual stress, it should also be pointed out that equation (4) predicts that the residual stress effect decreases with increasing effective crack length. Thus, it is unclear whether the annealing actually reduced the residual stress effect in either the 48-2-2 or WMS alloy.

8.7.2. Constant Amplitude Fatigue Testing and Analysis

As discussed previously, the measured fatigue strength data of small to moderate effective cracks lengths in both the 48-2-2 and WMS alloys is less than either the threshold-based model or the fatigue strength of undamaged material. A likely explanation for this behavior is that as the effective crack size diminishes the threshold stress intensity range is steadily decreasing. This decrease in threshold continues as the fatigue strength of impacted specimens gradually approaches the endurance limit of undamaged material, in which case fatigue crack growth is a stress controlled, rather than stress-intensity controlled phenomenon. Such behavior has been identified with small crack growth, either through a loss of closure in the case of $\Delta K_{eff,TH}$, or through a dependence of fatigue crack growth on non-continuum, microstructural factors.

xamine this phenomenon, standard constant amplitude fatigue tests were conducted
pact damaged 48-2-2 specimens at 600°C. Five specimens were impacted at
N to produce effective crack lengths in the small crack regime of the Kitagawa plot.
dditional five specimens were impacted at 3000 N to produce effective cracks in the
crack regime for comparison.

are 6 shows the results of the constant amplitude fatigue tests on impacted specimens
the 48-2-2 alloy. Stress-lifetime curves of specimens impacted at 1000 N and 3000 N
oth show a sudden transition from moderate lifetimes (~10,000-50,000 cycles) to run-
out at 10^7 cycles. Such behavior has been reported for other γ-TiAl alloys (Larsen et al,
1999), (Trail and Bowen, 1995), and is a result of the small difference between ΔK_{TH} and
the apparent toughness, ΔK_Q. In other words, a small increase in stress above the
endurance limit (10^7 fatigue strength) leads to a dramatic decrease in lifetime as crack
growth rates accelerate quickly. This observation makes a strong case for using cycle
blocks of 10^5 cycles in the step-test method to approximate the 10^7 endurance limit.

Figure 6 also demonstrates that impact damage, even low severity impacts, can lead to a
significant decrease in fatigue strength. The 10^5 fatigue strength of the undamaged
material was found to be 310 MPa using the step-test method. Assuming this is a
reasonable approximation of the endurance limit, impacts of 1000 N resulted in a 110
MPa reduction in fatigue strength. Specimens impacted at 3000 N had an endurance
limit of only 130 MPa, a 58% reduction from the undamaged material.
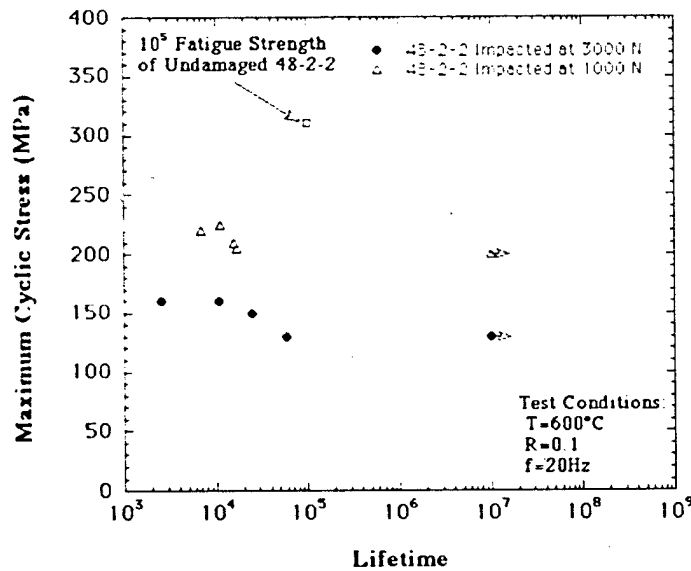

Figure 6: Results of constant amplitude stress fatigue tests at 600°C for specimens of the 48-2-2 alloy impacted at 1000 N and 3000 N

Examination of the small crack effect in 48-2-2 was accomplished by modeling the
stress-lifetime response of specimens tested in the constant amplitude tests with both
long-crack and small-crack fatigue crack growth equations. Both equations are discussed

in more detail by Larsen et al. (Larsen et al, 1996). The governing long-crack fatigue crack growth equation is referred to as the ATANH equation and is of the form:

$$\log(da/dN) = C_1 \arctan h \{C_2 [\log(\Delta K) + C_3]\} + C_4 \tag{5}$$

where C_1 to C_4 are constants dependent on material and test conditions determined by regression of long crack fatigue crack growth data. As Figure 7 demonstrates, the asymptotic nature of equation (5) accurately portrays the near-threshold fatigue behavior of the 48-2-2 alloy for both ΔK and ΔK_{eff}.
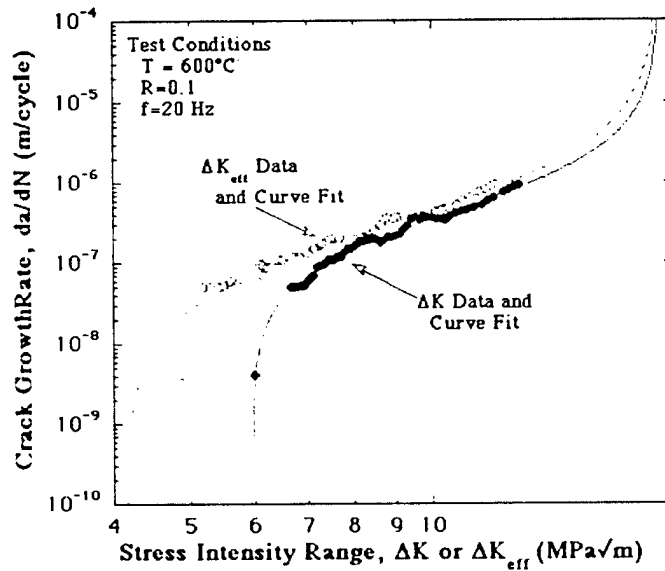
Figure 7: Regression of 600 °C fatigue crack growth data of the duplex 48-2-2 alloy using the ATANH equation. The equation has been extrapolated up to the toughness of the material for purposes of illustration.

The governing equation used to represent accelerated, sub-threshold small crack growth in 48-2-2 is termed the Small Crack equation (Larsen et al, 1996):

$$\log(da/dN) = C_1 \langle \exp\{C_2[\log(\Delta K) + C_3]\}$$
$$- \exp\{C_5[\log(\Delta K) + C_3]\}\rangle/2 + C_4 \tag{6}$$

The equation behaves in a manner similar to the ATANH equation, only that the overall equation is asymmetric, and the near-threshold response is non-asymptotic. This aspect of the small crack equation represents the accelerated crack growth of small cracks at stress intensity range values below ΔK_{th}.

The stress-lifetime response of the impacted 48-2-2 specimens can be estimated by inserting equations (5) or (6) into an equation of the form:

$$N_p = \int_{a_{eff}}^{a_c} \frac{da}{f(\Delta K)} \qquad (7)$$

where N_p is the propagation lifetime for a specimen with an effective crack length, a_{eff}, following impact damage and a critical flaw size to cause failure, a_c. Figure 8 shows the stress-lifetime curves generated by numerically integrating equation (5) for the 48-2-2 specimens impacted at 3000 N. Initial effective crack lengths of 400 μm, 500 μm and 600 μm were used for generating the curves since they bounded the measured effective crack lengths of the impacted specimens. The actual effective crack lengths for each specimen are identified for comparison with the generated curves. As Figure 8 indicates, the curves generated by equation (5) accurately bound the actual response of the damaged specimens. This result indicates that the use of the ATANH equation is valid for prediction of remaining lifetime in severely impact damaged 48-2-2 at 600°C, where cracks are likely in the long crack regime.
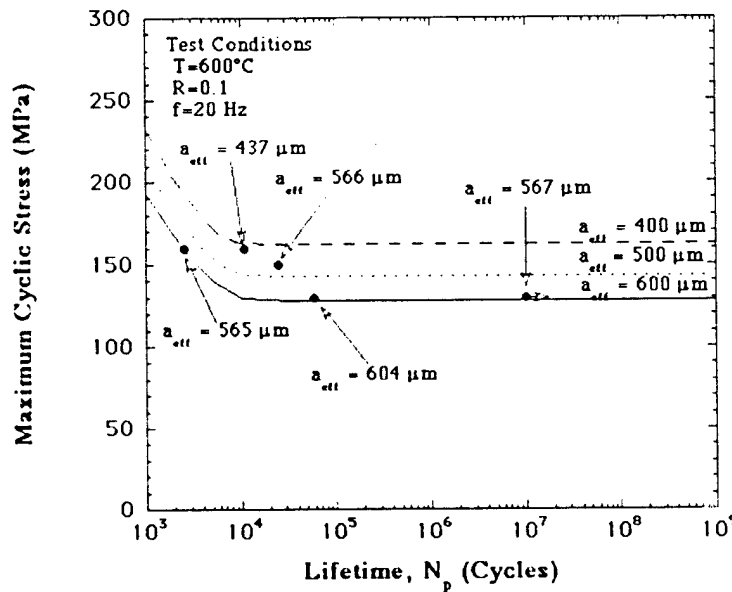
Figure 8: Comparison of stress-lifetime response of 48-2-2 specimens impacted at 3000 N and tested at 600°C with curves generated from the ATANH equation. The initial effective crack lengths of each specimen are shown for comparison with the ATANH curves, which bound the measured stress-lifetime response of these long cracks closely.

However, the use of the ATANH equation for generating stress-lifetime curves for effective crack lengths on the order of those generated by 1000 N impacts (~75 μm) proved invalid. The ATANH equation predicts that the endurance limit of specimens with effective crack lengths on the order of those impacted at 1000 N would be closer to 400 MPa, rather than the measured result of 200 MPa.

The lower than expected endurance limit for specimens impacted at 1000 N suggests growth at stress-intensity range values below the long crack threshold. Further attempts

at modeling the stress-lifetime response of these materials using the ATANH equation were made by recalculating the constants C_1 to C_4 for closure-corrected, long-crack fatigue crack growth data. Though this had the effect of reducing the predicted endurance limit from about 400 MPa for ΔK-based data to around 270 MPa for ΔK_{eff}-based data, it still over-predicted the measured endurance limit of impact damaged specimens. The Small Crack equation (6) was also used to model this behavior. As shown in Figure 9, equation (6) accurately predicts the endurance limit of specimens with effective crack lengths on average 75 µm in size. However, equation (6) significantly overestimates the fatigue strength at much shorter lifetimes ($10^3 - 10^5$ cycles), and does not correctly represent the flatness of the stress-lifetime curve of the actual data. This combination of results is due to the fact that equation (6) results in a threshold stress intensity value range representative of cracks on the scale of those seen in the specimens impacted at 1000 N, but does not represent the asymptotic near-threshold behavior that equation (5) does. Therefore, the behavior of these so-called "small cracks" can be described as exhibiting sub-threshold crack growth and yet still portraying the rapid acceleration in crack growth typical of long-crack behavior in 48-2-2.
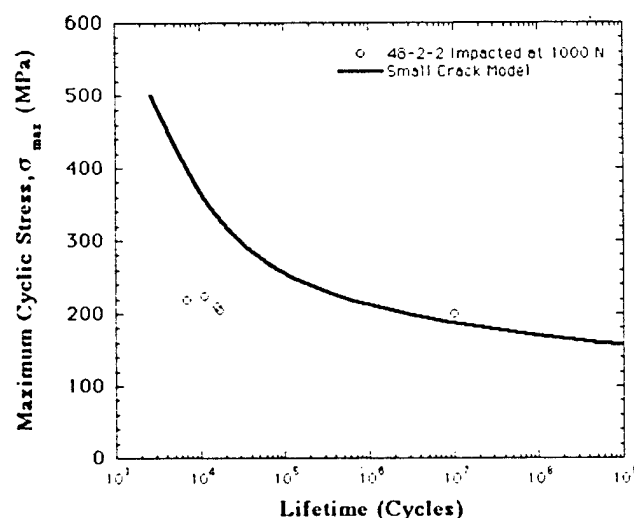

Figure 9: Modeling of the stress-lifetime response of 48-2-2 specimens impacted at 1000 N and tested at 600 °C using the Small Crack equation. The equation accurately predicts the endurance limit of these specimens, but fails to represent the behavior of these specimens at lower lifetimes.

To accommodate this apparently anomalous behavior, the ATANH equation was constrained to model the same closure-corrected, long-crack fatigue crack growth data shown in Figure 7 with an artificial threshold stress intensity range of 3.3 MPa√m. The results of this regression are shown in Figure 10 along with a regression without this artificial restraint. The resulting curve fit and set of parameters for equation (5) exhibit the small-crack "threshold" that accurately predicted the endurance limit using the Small Crack Equation, and the rapid acceleration of cracks that have begun to propagate represented by the ATANH equation.

The stress-lifetime curves generated for an average effective crack length of 75 µm using equation (5) with and without the artificially constrained threshold of 3.3 MPa√m is shown in Figure 11. It is clear from Figure 11 that the modified form of the ATANH equation not only accurately predicts the endurance limit of these small crack specimens, but also represents the behavior of these specimens at shorter lifetimes. It is worth noting that the threshold stress intensity range of 3.3 MPa√m was arbitrarily chosen to produce the best data fit in the stress-lifetime curves. However, this value is the same as that predicted by the Small Crack Model to fit the endurance limit determined experimentally. Moreover, Larsen et al., found that a threshold stress intensity range value of 3.3 MPa√m could be used to predict the behavior of specimens from a lamellar γ-TiAl alloy that were notched by electro-discharge machining (EDM) (Larsen et al, 1999). The authors related this threshold value to the minimum toughness in lamellar PST crystals for interlamellar cracking. The correlation between the stress-lifetime results in duplex 48-2-2 following impacts at 1000 N and a value for the minimum toughness of lamellar PST crystals may be coincidental. However, it points to the necessity for a more complete understanding of the effects of local microstructural features (e.g. lamellar plate orientation) in the near-threshold fatigue crack propagation of cracks on the scale of those observed following impacts of 1000 N.
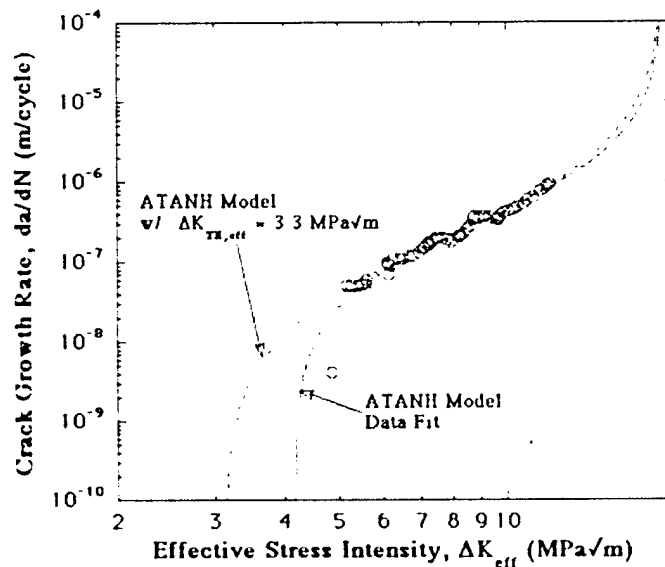
Figure 10: Data regression using the ATANH model for the 48-2-2 alloy tested at 600 °C. Regression fit for the long-crack data is shown along with a fit for data artificially constrained to have a threshold of 3.3 MPa√m.

8.7.3. Effect of Impact Damage Crack Size and Shape Measurements

In addition to qualitative analysis, each fracture surface was examined to map out the shape and size of the indent, indent-tip crack and fatigue crack. The method used to perform this analysis involved optical measurement of the extent of heat tinting on the

fracture surface using a color CCD camera. This was compared with SEM examination of changes in the fracture morphology. Much of the theory behind the threshold-based model of fatigue strength prediction is based on three assumptions:

1. Indent tip-cracks are through-thickness and behave as such during fatigue.
2. When no cracking is evident at the indent tip from surface observations. no cracks are anticipated in the specimen interior.
3. Fatigue cracks propagate from the indent-tip crack as through-thickness cracks.

The fractographic analysis, however, has revealed that none of these assumptions are true.
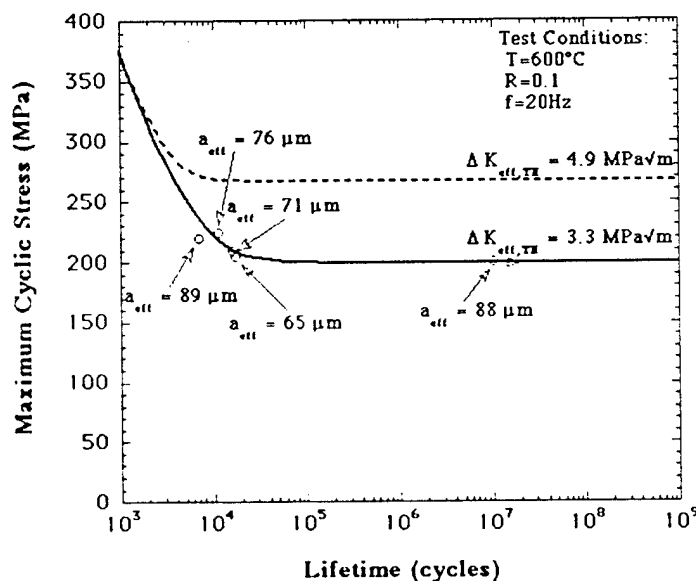
Figure 11: Comparison of stress-lifetime curves calculated from the ATANH equation with $\Delta K_{eff,TH}$ values of 4.9 MPa√m and 3.3 MPa√m. Use of the lower threshold value results in good estimation of both the endurance limit and short lifetime behavior of specimens with effective crack lengths on the scale of 75 μm.

In general. the depth of the indent-tip crack is usually much greater at the specimen surface than in the interior. This is likely due to the lack of material constraint at the specimen surface compared to the interior. This phenomenon would lead to an overestimate of the depth of the indent-tip crack from pre-test measurements compared to the actual "average" crack depth along the indent-tip front. In the duplex 48-2-2 alloy. 83% of the specimens examined had indent-tip crack depth pre-test measurements along the specimen surface that were longer than that in the interior. Similarly. in the near-lamellar WMS alloy 54% of the specimens examined had cracking that was greater at the surface than in the interior.

In addition. internal impact damage was observed in specimens without surface damage. In at least one 48-2-2 specimen and two WMS specimens with low severity impacts. evidence of internal semi-elliptical. indent tip cracks was found. The presence of internal

...t-tip cracks can be critical. Qualitative assessment of the fatigue crack shape data
...sts that fatigue cracks in both the 48-2-2 and WMS alloy prefer to propagate from
...ns along the indent-tip where cracking is already present due to the impact. In each
...where only an internal indent-tip crack is present, the fatigue crack appears to have
...gated from that initial source of damage resulting in semi-elliptical internal cracks.

...ermore, in specimens where surface cracks were observed, the fatigue cracks
...red to grow preferentially along the side of the specimen with the greatest degree of
...ident-tip cracking. This is particularly significant in the WMS alloy since here surface
connected cracks did not extend the full length of the indent tip. The result is that in 75%
of the 48-2-2 specimens and 100% of the WMS specimens the fatigue crack which
eventually lead to failure could be described as either a semi-elliptical corner or surface
crack. The implications that this analysis could have on the threshold-based model will
be discussed below.

The results of this reassessment of the assumptions regarding impact damage can be
analyzed on the Kitagawa plot. A correction for the overestimate of the effective crack
length by surface measurement would tend to shift the data toward smaller effective
crack lengths on the Kitagawa plot. As can be seen in Figure 12, this has the effect of
reducing the discrepancy between actual fatigue data and the through-thickness,
threshold-based prediction in the 48-2-2 alloy. At smaller effective crack lengths, the
data is actually shifted toward the right on the Kitagawa diagram. This is a result of the
underestimation of the degree of internal cracking in specimens that had no surface
cracks. This shift would serve to reduce the apparent small crack effect.

However, this approach to correcting for erroneous crack measurement fails to take into
account the fact that many of the cracks are not growing in fatigue as through thickness
cracks. Rather many of the fatigue cracks appear to propagate from the indent tip as
quarter-elliptical corner cracks. The result is a reduction in the geometry factor for
calculating the stress intensity of the fatigue crack, and a shift to the right of the threshold
prediction as shown in Figure 12. For the purposes of calculation, it was assumed that
the effective crack length represented the corner crack depth and that the aspect ratio
remained constant during fatigue crack growth. From the fractographic analysis the
average aspect ratio of fatigue cracks was found to be approximately 0.75. Finally, the
new threshold prediction is based on a Raju-Newman stress intensity solution for corner
cracks (Newman and Raju, 1981). The pre-test data appears to asymptotically approach
this new threshold line, though insufficient data is available to confirm the agreement at
larger crack sizes. Despite apparently good agreement with this corner crack model, it
fails to take into account the full effect of the indent, which can arguably be treated as a
through-thickness crack. Therefore, a threshold prediction based on a true representation
of the impact damage would fall somewhere between the through-thickness and corner
crack predictions.

A similar analysis was conducted for the WMS alloy. Figure 13 shows the modified
Kitagawa plot with corrections made for post-test measurement of the effective crack
length. As in the 48-2-2 alloy data at large effective crack lengths tends to be shifted

toward smaller crack sizes due to overestimation of impact damage from surface measurements. Also, data at smaller effective crack lengths is shifted toward larger crack sizes due to underestimation of the internal damage in these specimens. A second threshold-based prediction line is shown in Figure 13 based on a corner crack assumption. The same aspect ratio of 0.75 is used for the WMS alloy. There is a high degree of correlation between data at larger effective crack lengths and the corner crack threshold-based prediction, though additional data would be needed at larger crack sizes to confirm this agreement.
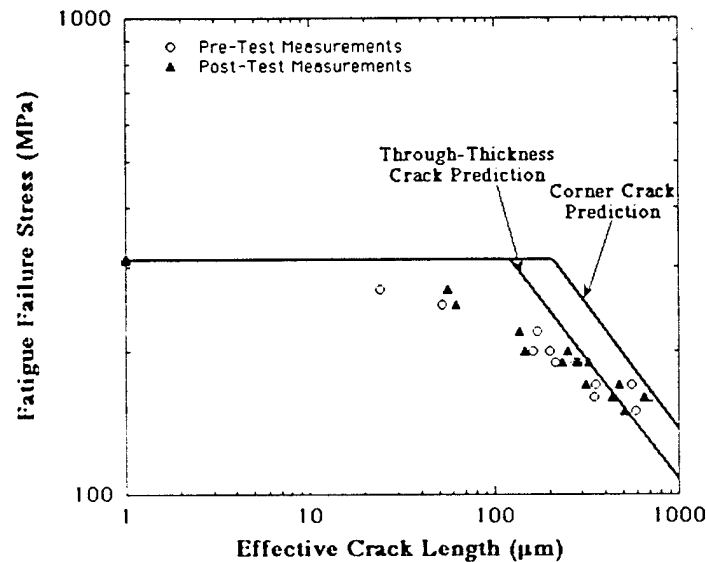
Figure 12: Kitagawa plot for the 48-2-2 alloy tested at 600°C showing the effects of crack measurements made before and after fatigue testing. Corrections are made for an inability to accurately measure the true internal crack size prior to testing. Also a new threshold-based prediction is shown assuming the fatigue crack propagates as a corner crack.

However, as in the 48-2-2 alloy, a true threshold-based prediction of the actual impact damage would lie between the through-thickness and corner crack predictions. In this case, there would likely still be some deviation between the actual fatigue results and this "ideal" threshold prediction, suggesting that residual stress effects may still be relevant. Given that this "ideal" threshold prediction would be quite difficult, the designer may be better suited in taking the corner crack and through-thickness crack predictions as upper and lower bounds of the true behavior. This approach would still necessitate an understanding of the small crack effect, but might eliminate the need for residual stress modeling. More testing is necessary to address this question.
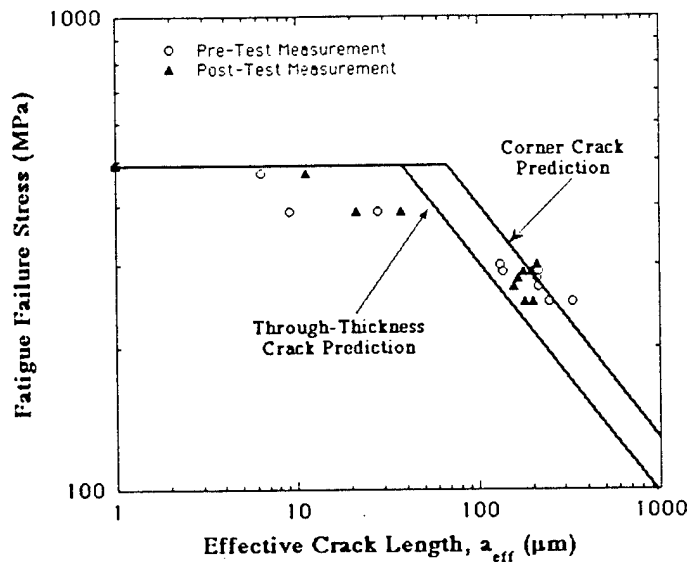
Figure 13: Kitagawa plot for the WMS alloy tested at 600°C showing the effects of pre- and post-test measurements of the effective crack length. Adjustment is made for errors introduced from surface measurements. Also, the threshold line is shifted to show the effects of changing the geometry factor associated with crack shape.

8.8. Conclusions

1. Step loading fatigue tests on a Ti-47.9Al-2.0Cr-1.9Nb duplex alloy (48-2-2) and a Ti-47.3Al-2.2Nb-0.6Mn-0.45W-0.46Mo-0.23Si near-fully lamellar alloy (WMS) have shown that simulated assembly-related (shop floor) impact damage reduces the fatigue strength in a way that is generally characterizable using a threshold-based approach. However, several discrepancies between the actual fatigue data and the model exist which warrant further investigation. These include residual stress effects, small crack behavior and erroneous assumptions regarding the nature of impact damage from pre-test measurements.

2. Numerical analysis of the potential effect of residual stresses on fatigue strength revealed that residual stresses may explain, at least partially, the higher than expected fatigue failure stresses at large effective crack lengths, particularly in the WMS alloy. The effect of residual stresses in the 48-2-2 alloy was found to be small and constrained to specimens impacted at only the most severe levels. In the WMS alloy however, the residual stress effect was found to be 2-3 times higher and affected the fatigue strengths of specimens with significantly smaller damage zones and thus less severe impacts. The higher residual stress effect is likely due to a higher yield strength and resistance to the formation of indent tip cracks. Thus the WMS alloy has a higher fatigue failure stress for a given large effective crack length compared to the 48-2-2 alloy despite a threshold-based prediction to the contrary.

3. The 600°C constant amplitude stress-lifetime response of impact damaged 48-2-2 specimens was modeled in an effort to predict small-crack near-threshold crack growth behavior. The ATANH equation, based on a regression fit of long-crack

fatigue crack growth data, accurately predicted the endurance limit of severely impacted specimens with effective crack lengths in the long-crack regime. However, an accurate fit of results from specimens with effective crack lengths in the small-crack regime could only be obtained by using the ATANH model with a threshold stress intensity range constrained to a value of 3.3 MPa√m. This arbitrary value was estimated form a Small Crack equation that could model the endurance limit, and thus near-threshold conditions, of such small cracks but not shorter lifetime behavior. This set of circumstances suggests that small cracks in the duplex 48-2-2 alloy may begin propagating at threshold values considerably lower than long cracks, but accelerate suddenly in a manner similar to long cracks.

4. Post-fatigue test fractographic analysis has revealed that several assumptions regarding the nature of impact damage are incorrect. Namely that the extent of internal damage is generally overestimated from surface measurements when indent tip cracks are present on the specimen surface, and that it is underestimated when they are not. Additionally, fatigue cracks appear to propagate from the damage zone as semi-elliptical corner and surface cracks rather than through-thickness cracks. These errors are generally more pronounced in the WMS alloy. Examination of the effect of these errors on the threshold-based model suggest that the true fatigue response falls somewhere between a threshold prediction based on a through-thickness crack assumption and one base on a corner crack assumption. Such a model would be difficult to develop, suggesting that the through-thickness and corner crack predictions may serve as lower and upper bounds of the actual behavior respectively. Furthermore, an intermediate prediction would reduce but not eliminate the apparent residual stress effect, particularly in the WMS alloy. Nor do any of the threshold predictions address the small crack effect for low severity impacts.

8.9. Future Work

The final phase of experimental work is to examine the influence of damage that is more simulative of foreign object damage on the fatigue properties of gamma TiAl. In particular the 48-2-2 alloy and a 47 XD alloy will be machined into an altered dogbone specimen with a chamfered edge in the gage section. This geometry is meant to represent the leading edge of a turbine blade. Damage will be introduced into the specimens by quasi-statically indenting the face of the chamfer with a 1.6mm ball-bearing to simulate a leading edge impact. This work will be done in conjunction with the surface damage project at Carnegie-Mellon University. Step loading fatigue tests will be used to evaluate the reduction in fatigue strength caused by the simulated foreign object damage. A threshold-based model will be evaluated for predicting this reduction using long-crack fatigue crack growth data for both the 48-2-2 and 47 XD alloys. Examination of the fracture surfaces of failed specimens will be necessary to determine the crack shape and size resulting from impacts. This data will be used to determine the stress-intensity factor of the initial damage and relate that value to the long-crack threshold stress intensity range. Since all tests will be conducted at 600°C, heat tinting developed on the fracture surface will facilitate the quantitative fractographic analysis.

Several other experiments are being considered as well. An examination of the effect of crack size on threshold stress intensity in the 47 XD alloy is one possibility. In this case constant amplitude fatigue tests would be conducted on specimens with varying levels of simulated shop floor damage. Modeling of the fatigue lifetime of these specimens would provide an indication of the change in threshold with crack length and the nature of the near-threshold behavior of the material with given damage levels. Another possible experiment is the examination of the effect of shop floor damage on the 45 XD alloy using step-loading fatigue tests. These results could then be compared to those obtained for the WMS and 48-2-2 alloys.

8.10. Acknowledgments

References

Austin, C.M., Kelly, T.J., McAllister, K.G. and Chesnutt, J.C.: *Structural Intermetallics, 1997*, M.V. Nathal et al., eds., The Minerals, Metals and Materials Society, Warrendale, PA, pp.413-425.

Campbell, J.P., Venkateswara Rao, K.T. and Ritchie, R.O.: *Materials Science and Engineering A*, 1997, 239/240, pp. 722-728.

Collins, J.A.: *Failure of Materials in Mechanical Design*, John Wiley and Sons, New York, 1993, pp. 379-381.

Elber, W., *Damage Tolerance in Aircraft Structures*, ASTM STP 486, American Society for Testing and Materials, Philadelphia, 1971, pp. 230-242.

Huang, S.C.: U.S. Patent 5,076,858, 1991.

Huang, S.C. and Chesnutt, J.C.: *Intermetallic Compounds: Vol. 2, Practice*, 1994, J.H. Westbrook and R.L. Fleischer, eds., John Wiley and Sons, New York, pp. 73-90.

Hudak, S.J., Jr., Chell, C.G., Rennick, T.S., McClung, R.C. and Davidson, D.L.: *Proc. 4th National Turbine Engine HCF Conference*, 1999, Universal Technology Corp., Dayton, OH, in press.

Kitagawa, H. and Takahashi, S.: in *Proc. of 2nd Intl. Conf. on Mechanical Behavior of Metals*, Boston, MA, 1976, pp. 627-631.

Larsen, J.M., Rosenberger, A.H., Worth, B.D., Li, K., Maxwell, D.C., and Porter, J.W.: in *Gamma Titanium Aluminides 1999*, Y-W. Kim, D.M. Dimiduk and M.H. Loretto, eds., The Minerals, Metals and Materials Society, Warrendale, PA, in press.

Larsen, J.M., Worth, B.D., Annis, C.G., Jr., and Haake, F.K.: *Int. J. of Fracture*, 1996, vol. 80, pp. 237-255.

Larsen, J.M., Worth, B.D., Balsone, S.J., Rosenberger, A.H. and Jones, J.W.: *Fatigue '96, Proc. of 6th Int. Fatigue Cong., Vol. III*, G. Lutjering and H. Nowack, eds., Pergamon Press, 1996, pp. 1719-1730.

Lerch, B.A., Draper, S.L., Baaklini, G.Y. and Pereira, J.M.: in *HITEMP Review 1999: Advanced High Temperature Engine Materials Technology Project*, NASA CP 1999-208915, Vol. 2, in press.

Newman, J.C., Jr. and Raju, I.S.: Stress Intensity Factor Equations for Cracks in Three Dimensional Finite Bodies, NASA Technical Memorandum 83200, 1981, pp.1-49.

Nicholas, T., Barber, J.P. and Bertke, R.S.: *Experimental Mechanics*, 1980, Vol. 20, no. 10, pp. 357-364.

Perrin, I.J.: *Gas Turbine Engine Technology: Proc. of 4th Int. Charles Parsons Turbine Conf.*, Institute of Metals, London, 1998, pp. 148-158.

Roder, O., Peters, J.O., Thompson, A.W. and Ritchie, R.O.: *Proc. 4th National Turbine Engine HCF Conference*, 1999, Universal Technology Corp., Dayton, OH, in press.

Rosenberger, A.H., Worth, B.D. and Balsone, S.J.: *Fatigue '96: Proc. of 6th Int. Fatigue Cong., Vol. III*, G. Lutjering and H. Nowack, eds., Pergamon Press, 1996, pp. 1785-1790.

Sadananda, K. and Vasudevan, A.K.: *Materials Science and Engineering A*, 1995, 192/193, pp. 490-501.

Trail, S.J. and Bowen, P.: *Materials Science and Engineering A*, 1995, 192/193, pp.427-434.

Venkataswara Rao, K.T., Kim, Y-W., Muhlstein, C.L. and Ritchie, R.O.: *Materials Science and Engineering A*, 1995, 192/193, pp. 474-482.

9. Program Organization, Interactions and Research Transitions

9.1 Personnel Supported

Faculty, graduate students and postdoctoral research associates supported by the PRET Program, are listed along with their project and university affiliation.

Limitations Imposed by Ductility on Engine Components
>   Prof. Jack Beuth (CMU-ME), Mr. Jorge Milke (CMU-ME), Mr. Kanit Nangkala (CMU-ME)

Resistance to Foreign Object and Surface Damage
>   Prof. Paul Steif (CMU-ME), Mr. Volus McKenna (CMU-ME)

Microstructural Origins of Property Variability
>   Prof. Tresa Pollock (CMU-MSE), Mr. R. Raban (CMU-MSE), Mr. Andrew Elliott (CMU-MSE)

Fatigue Behavior of Gamma Titanium Aluminides
>   Prof. Wayne Jones (UM-MSE), Mr. Trevor Harding (UM-MSE), Mr. Ryan Smith (UM-MSE).

Quantification of Microstructure and Strain Monitoring Techniques
>   Prof. Marc DeGraef (CMU-MSE), Mr. Nicholas Biery (CMU-MSE)

Casting and Processing Defects and Impurities
>   Prof. Alan Cramb (CMU-MSE), Dr. Linda Rishel (CMU-MSE), Mr. Bob Evans (CMU-MSE)

Microstructure Development in Gamma Titanium Aluminide Welds: Approaches to Mechanical Property Optimization
>   Prof. William A. Baeslack (OSU-Welding), Mr. Joe Breeding (OSU-Welding), Dr. Han Zhang(OSU-Welding)

9.2 Publications

1. T.M. Pollock, D.R. Mumm, K. Muraleedharan and P.L. Martin, "In-Situ Observations of Crack Initiation and Growth at Notches in Ti-48 Al-2Cr-2Nb", Scripta Metall. Mater. 35, 1311-1316, (1996).

2. L. L. Rishel, T. M. Pollock, A. W. Cramb and D. E. Larsen, 'Proc. of the International Symposium on Liquid Metal Processing and Casting', ed. A. Mitchell and P. Auburtin, Vacuum Metallurgy Division of AVS, 1997, 214-225.

3. K. Muraleedharan, L. L. Rishel, M. De Graef, A. W. Cramb, T. M. Pollock and G. T. Gray III, "The Effects of Cooling Rate during Casting on Microstructure Development in Ti-48Al-2Cr-2Nb", 'Proc. of the International Symposium on Structural Intermetallics', TMS, Warrendale, PA, 1997, 215 - 224.

4. Steif, P.S., Jones, J. W., Harding, T., Rubal, M.P., Gandelsman, V. Z., Biery, N., Pollock, T. M., "Surface Damage Due to Impact and Fatigue Strength Reduction in Gamma Titanium Alumindes," Proc. of the International Symposium on Structural Intermetallics, TMS, Warrendale, PA, (1997), 435 - 442.

5. P.S. Steif, M.P. Rubal, G.T. Gray, III, and J.M. Pereira, "Damage in Gamma Titanium Aluminides Due to Small Particle Impacts", J. Mech. Phys. Solids, Vol. 46, 2069-2086, (1998).

6. T.S. Harding, J.W. Jones, T.M. Pollock and P.S. Steif, "The Effects of Impact Damage on the Fatigue Properties of Gamma TiAl", Proc. of Paris Symposium on "High Cycle Fatigue of Structural Materials", TMS, Warrendale, PA, 499, (1997).

7. Knaul, D.A., Beuth, J.L. and Milke, J.G., Modeling and Measurement of the Notched Strength of Gamma Titanium Aluminides Under Monotonic Loading,~ Metallurgical and Materials Transactions, Vol. 30A, 1999, pp. 949-959.

8. De Graef, M. and Biery, N. and Rishel, L. and Pollock, T.M. and Cramb, A., "On the relation between cooling rate and solidification microstructure in as-cast titanium aluminides," to appear in Proc. Gamma Titanium Aluminides Symposium, TMS Annual Conference 1999.

9. Biery, N. and De Graef, M. and Pollock, T.M., "Study of localized strain at notches in gamma-TiAl alloys using displacement mapping and microstructural characterization," to appear in Proc. Gamma Titanium Aluminides Symposium, TMS Annual Conference 1999.

10. Biery, N. and Pollock, T.M. and Nuhfer, N.T. and De Graef, M., "Displacement mapping during in-situ straining in the SEM," Microscopy and Microanalysis, Vol. 5 (suppl. 2), 334-335, 1999.

11. L.L. Rishel, N.E. Biery, R. Raban, V.Z. Gandelsman, T.M. Pollock and A.W. Cramb, "Cast Structure and Property Variability in Gamma Titanium Aluminides", J. Intermetallics, 6, 629, (1998).

12. L.L. Rishel, T.M. Pollock and A.W. Cramb, "Induction Skull Melting of Gamma Titanium Aluminides", Proc. AVS Conf. on Liquid Metal Processing and Casting, 287, (1999).

13. R. Raban, L.L. Rishel and T.M. Pollock, "The Dependence of Tensile Ductility on Investment Casting Parameters in Gamma Titanium Aluminides", Proc. MRS Symp. on High Temperature Ordered Intermetallics VIII, in press.

14. T. S. Harding, J.W. Jones, T.M. Pollock and P.S. Steif, "Room Temperature Fatigue Response of γ-TiAl to Impact Damage," *Scripta Materialia*, **40**, (4), 445-449, 1999.

15. T.S. Harding, J.W. Jones, J.M. Larsen and P.S. Steif, "Influence of Impact Damage on the Elevated Temperature Fatigue Behavior of Gamma Titanium Aluminide Alloys," *Proceedings of Second International Symposium on Gamma Titanium Aluminide*, Y.W. Kim, et al., eds., TMS, Warrendale, PA, 1999.

9.3 Interactions in the PRET Program

Key to the goals of the PRET program is collaboration and communication between the industry and university teams as well as among the different universities working on closely tied projects. The degree of interaction between university and industry can be viewed on the basis of ongoing collaborative activities and the "transitions" of research that have occurred to date, as well as those which are planned for the remainder of the program. Details regarding these interactions and transitions are provided in the following sections. Additional communication of the results of this program has occurred via presentations at technical meetings and in journal publications; these are also listed below.

9.3.1 Transitions and Impact on Industry Programs

There has been a strong interaction between the PRET program and industry/outside laboratory collaborators in a number of different research areas. Below we list results which have been transitioned thus far in the program.

• The CMU ISM has been used to carry out an investigation of the induction skull melting of gamma titanium aluminides. The effect of melt atmosphere on the rate of vaporization of Al and the thermal response of the system have been quantified and shared with Howmet Corporation. This work has shown that melting in Argon atmospheres which suppress the vaporization of Al are cleaner, hotter and result in higher yields than melts conducted in vacuum levels which do not prevent the vaporization of Al from gamma titanium aluminides. These results have important implications for the production processing of gamma titanium aluminides.

• During the past year, collaborative efforts were performed with GE Aircraft Engines in Cincinnati, Ohio, the Air Force Research Laboratory at WPAFB, and with PCC Structurals in Portland, Oregon. GE Aircraft Engines has provided all base and filler materials, and electron beam and inertia-friction welds examined in this study, and have provided significant additional technical support during the course of this project. The Materials Directorate at ARFL has performed all heat treatment support. Finally, the

most recent interaction with PCC has led to their performance of all GTA welds in their sophisticated GTA welding system that allows full preheat and postweld stress-relief control. Technical interactions between W. A. Baeslack III and J. Breeding of OSU and the personnel at PCC were initiated during a visit in June, and will continue over the next year.

• The PRET program approach to studying damage and fatigue strength, which focuses realistic simulations of damage, is influencing the development of new design practices at aircraft engine companies to account for damage on intermetallic components.

• Fundamental information on the kinetics of aluminum vaporization generated in the PRET program has been utilized by General Electric for control of ingot alloy chemistry.

• The results of studies on the influence of casting cooling rates on microstructure and tensile ductility are being used by General Electric and PCC to explore some alternative thermal cycles for processing blades.

• To obtain information on cooling rates in Howmet production furnaces for comparison to PRET skull melting facilities and to generate another large lot of test material, molds were instrumented and casting experiments were conducted by PRET and Howmet personnel in their facilities in March 1998. Modeling results from previous collaborative experiments with Howmet have also been transitioned

• Thermal treatments studied in the PRET program in the welding project have been incorporated into the electron beam welding process cycle at General Electric.

• Data from the project on deformation of notched specimens of varying geometries was used as a part of the final GE90 low pressure turbine blade design review by General Electric in February of 1997. It is highly unusual for GE to use university-developed data as part of a formal design review; in their opinion this is the most tangible manner by which success in a university-industry program can be measured.

• The induction skull melting unit that was installed as a part of the program at CMU has been used for several sets of collaborative university-industry experiments. Most recently, joint experiments to study impurities and aluminum vaporization during melting have been conducted in collaboration with GE personnel in this facility. Other industrial users of this facility include Howmet, Timet, and Amorphous Technologies. Large ingots donated by Rockwell have been extremely useful in developing melting practice in this facility.

• PRET research has shown that slow cooling rates during casting prevent the establishment of optimum microstructure, particularly in larger sections. In response to a request from industrial partners, solidification modeling activities to assess limitations placed by cooling rates on larger section sizes have been completed. These studies were aimed at assessing possible problems with larger structural components of aircraft

engines. The computations were possible due to the instrumented casting experiments conducted by Dr. L. Rishel (PRET postdoctoral researcher) at Howmet.

• In the first year of the program we prepared a Web page on "Preparation and Analysis of Gamma Titanium Aluminide Microstructures". This page, prepared by K. Muraleedharan of CMU, documents a wide variety of polishing, electropolishing and etching solutions and techniques, along with microstructural documentation. All industrial partners have commented on the utility of this information, and a new etchant developed for TiAl in this program has been utilized by a large number of people outside the program.

9.3.3 Additional Collaborations

The PRET program has benefitted from a number of additional collaborations. These are briefly described below:

    (a) Wright Patterson - James Larsen, Andrew Rosenberger, Kezhong Li
This collaboration has been useful from the point of view of integrating PRET and Wright Patterson capabilities for experimental and analytical approaches to lifetime prediction for this class of materials. In addition, collaborations have occurred in the area of welding.
    (b) NASA - Susan Draper, Michael Pereira, Michael Nathal
Collaboration in the area of impact damage. High speed impacts continue to be conducted at the NASA impact facility. The impacts on blade simulative specimens carried out as part of a GE-NASA program are being simulated theoretically in the PRET program would the goal of establishing general criteria for the size of cracks produced by impacts.
    (c) UES - Dilip Banerjee
A copy of the PROCAST casting modelling program has been provided to Carnegie Mellon for analysis of cooling rate data generated in Howmet experiments and for analysis of future CMU casting experiments.
    (d) Los Alamos National Laboratory - George Gray III, John Bingert
High rate (Hopkinson bar) compression experiments have been conducted over a range strain rate and temperature on the baseline 47.9% Al alloy and on the WMS alloy. Constitutive equations which describe material behavior were also developed and have been incorporated into FE simulations.
    (e) UC San Diego - Professor Ken Vecchio
Small particle impact and rebound experiments were conducted on plates of WMS material. The measurements of rebound velocity give an additional opportunity to gauge the accuracy of finite element simulations of impact and the underlying constitutive equations.

9.3.4 Mechanisms of Interaction and Communication

A number of approaches have been considered to facilitate university-industry communication within the program, including:

- "Extended" University - Industry Personnel Exchanges
- "Short" University - Industry Exchanges for Collaborative Experiments
- University - Industry Meetings for Planning and Information Exchange
- Electronic Communication

With regard to personnel exchanges, "extended" exchanges and "short" exchanges have both sucessfully facilitated joint university-industry experiments. Several extended exchanges, two weeks to four months in duration have occurred. The outcomes of some of these exchanges are apparent in the transitions section above. Numerous "short" exchanges up to a week in duration have routinely occurred. Each company in the program has had from two to seven different people visit one or more of the universities involved. Conversely, university personnel have spent some time at each of the companies involved. These visits have involved shorter experiments, data sharing and planning for future project activities. Industry personnel involved in these exchanges are listed below:

> Allied Signal - Jerry LaSalle, Santosh Das, Rich Bellows, Jim Hall, Prabhir Bhowal
>
> Allison Engine Co. - Sushil Jain, Bob Ress, Amit Chaterjee, Richard Mullen, Farshad Mirzadeh, Judith Dodd
>
> General Electric - Curt Austin, Tom Kelly, Peg Jones, Kevin McAllister, Omer Erdmann, Ken Wright, Alan Gilchrist, Deb DeMania
>
> Howmet Corporation - Paul McQuay, Don Larsen, Chris Jensen
>
> PCC, Inc. - Srivats Ram, Jim Barrett
>
> Rockwell - Pat Martin, Dallis Hardwick

To facilitate information transfer we use a central server for the PRET program. The server is a DEC Alpha workstation (operating system Digital UNIX 4.0) with 96 Mbytes of RAM and about 12 Gbytes of diskspace. The server is located in the PRET office in Doherty Hall at CMU. The server is known as titan.mems.cmu.edu (IP address 128.2.55.42) and is integrated into the departmental workstation cluster. All PRET members have a user account on titan. The widely available telnet program can be used to remotely login to the server. The server has been heavily used for remote sharing of results between groups of collaborators in the program.

The standardized e-mail address for every member, regardless of geographic location, is lastname@titan.mems.cmu.edu which makes it particularly easy to send e-mail back and forth since one does not have to remember anybody's real e-mail address. In addition, we have defined a number of mailing groups, characterized by a "fake" username. Mailing groups have been set up for all companies; for all faculty, and for students and postdocs. All currently defined groups are posted on the gamma homepage.

The γ-Home Page

The γ-home page can be found at the Uniform Resource Locator (URL) http://titan.mems.cmu.edu/. Early on in the program we have decided to only support Netscape browsers, since they make up almost 90 percent of the inquiries. The homepage has gone through a number of different stages and is now becoming more stable.

The home page is divided into a public area, where we post information accessible to anybody on the Web, and a restricted area which requires a username and password. The public area houses such things as the slides of the Annual Reviews, information about polishing and etching conditions and e-mail addresses and groups. The restricted area consists of pages for each of the sub-projects), mailing archives, and general information for the program members.

Beginning in the Fall of 1997 we have also distributed a quarterly "newsletter" that alerts industry partners to new developments and provides "pointers" to more detailed information on the server.

9.3.5 PRET Presentations

Listed below are PRET presentations at international and other meetings that involve audiences outside the program. Presentations among team members are not listed for brevity.

1. "A University - Industry Partnership for Research and Transition of Gamma Titanium Aluminides", T.M. Pollock, Tri-Service Review of Titanium Contracts, Dayton, OH, Sept. 1995.

2. AFOSR PRET Review, Carnegie Mellon, Pittsburgh, PA, May 1996. This meeting was attended by all industrial participants, including individuals from materials and design organizations, by most of the collaborators listed in the previous section and a large number of attendees from Wright Labs. Presentations by all faculty.

3. PRET Program Overview, T.M. Pollock, AFOSR Structural Metals Workshop, Bar Harbor, ME, August 1996.

4. Microstructural Development and Phase Transformations in Cast Ti-48Al-2Cr-2Nb, K. Muraleedharan, M. De Graef and T.M. Pollock, TMS Fall Meeting, Cincinnati, OH, October 7-10, 1996 by K. Muraleedharan.

5. "The Effect of Casting Conditions on the Quality of Investment Cast Gamma Alloy Plates", L. L. Rishel, T. M. Pollock, A. W. Cramb, presented at the Fall TMS meeting, Cincinnati, OH, October 7-10, 1996 by L. L. Rishel.

6. "The Effect of Casting Conditions on the Development of Defects in Investment Cast Gamma Alloy Plates", L. L. Rishel, T. M. Pollock, A. W. Cramb and D. E. Larsen, presented at the International Symposium on Liquid Metals Processing and Casting, Santa Fe, NM, February 16-19, 1997, by L. L. Rishel.

7. "Microstructure Evolution During Postweld Heat Treatment of Gas Tungsten-Arc Welds in Cast Ti-48Al-2Cr-2Nb Alloy", 126th TMS Annual Meeting and Exposition, Orlando, FL, February 1997, by W. Baeslack.

8. The Gamma to Alpha Transformation in Ti-Al Alloys,. K. Muraleedharan, T. M. Pollock, P. Wang and V. K. Vasudevan, 126th TMS Annual Meeting and Exposition, Orlando, FL, February 1997, by K. Muraleedharan.

9. "The Effects of Postweld Heat Treatment on Microstructural Evolution and Mechanical Properties of Fusion Welds in Gamma Titanium Aluminides", 8th ASM Advanced Aerospace Materials and Processes Conference and Exposition, Williamsburg, VA, May 1997, by W. Baeslack.

10. AFOSR/PRET Review, Carnegie Mellon, Pittsburgh, PA, May 1997. This meeting was attended by all industrial participants, including most of the industrial in the previous section. Also in attendance were "additional collaborators" listed in the previous section, key personnel from Wright Labs and representatives from the UC-Berkeley URI, and SWRI. Presentations by all faculty and students.

11. "Damage in Gamma Titanium Aluminides Due to Small Particle Impacts," P.S. Steif, M.P. Rubal, G.T. Gray, III, and J.M. Pereira. Symposium on Dynamic Deformation and Failure Mechanics of Materials, Pasadena, CA, (1997), by P. Steif.

12. "Microstructure Evolution During Postweld Heat Treatment of Fusion and Inertia-Friction Welds in Ti-48Al-2Cr-2Nb", TWI, Cambridge, United Kingdom, June 1997, by W. Baeslack.

13. "Microstructure Evolution During Postweld Heat Treatment of Inertia-Friction Welds in Ti-48Al-2Cr-2Nb", 3rd ASM Synthesis, Processing and Modelling of Advanced Materials, Paris, France, June 1997, by W. Baeslack.

14. "Modeling and Measurement of the Notched Strength of Gamma Titanium Aluminides Under Monotonic Loading," by D.A. Knaul and J.L. Beuth, presented at McNU '97: Joint ASME, ASCE and SES Summer Meeting, Northwestern University, June 30, 1997, by J. Beuth.

15. "The Effects of Cooling Rate during Casting on Microstructure Development in Ti-48Al-2Cr-2Nb", K. Muraleedharan, L. L. Rishel, M. De Graef, A. W. Cramb, T. M. Pollock and G. T. Gray III, International Symposium on Structural Intermetallics, Sept. 1997, by K. Muraleedharan.

16. "Surface Damage Due to Impact and Fatigue Strength Reduction in Gamma Titanium Alumindes," Steif, P.S., Jones, J. W., Harding, T., Rubal, M.P., Gandelsman, V. Z., Biery, N., Pollock, T. M., 1997, International Symposium on Structural Intermetallics, Sept. 1997, by P. Steif.

17. "Application of Surface Displacement Mapping to Ductility Issues in Gamma TiAl Based Alloys", N.E. Biery, M. De Graef and T.M. Pollock, TMS Fall Meeting, Indianapolis, IN, Sept. 1997, by N. Biery.

18. "The Effects of Impact Damage on the Fatigue Properties of Gamma TiAl", T. Harding, J.W. Jones, T.M. Pollock and P.S. Steif, Proc. of Paris Symposium on "Fatigue of Structural Materials", TMS Fall Meeting, Indianapolis, IN, Sept 1997, by T. Harding.

19. "The Effect of Casting Conditions on the Occurrence of Surface Connected Porosity in Investment Cast Plates of Titanium Aluminide Alloys", Howmet Corporation, Operhall Research Center, Whitehall, MI, March 1998, by L. Rishel.

20. "Vaporization Kinetics of Aluminum from Ti-48.6Al-2Cr-2Nb Melts in the Vacuum Induction Skull Remelting Process", Howmet Corporation, Operhall Research Center, Whitehall, MI, March 1998, by L. Rishel.

21. "The Effect of Casting Conditions on the Occurrence of Surface Connected Porosity in Investment Cast Plates of Titanium Aluminide Alloys", Annual TMS Meeting, San Antonio, TX, February 1998, by L. Rishel.

22. "Strength and Ductility of Notched Gamma Titanium Aluminides," by J.L. Beuth and D.A. Knaul, presented at the TMS Annual Meeting, San Antonio, TX, February 15-19, 1998.

23. "Simulating Particulate Damage on TiAl Turbine Blades", UC Berkeley, Berkeley, CA, July 1998, by P. Steif

24. "PRET Program Overview", Allison Engine Company, Indianapolis, IN, Sept. 17th, 1997, by T. Pollock.

25. "Processing and Properties of Cast Gamma Titanium Aluminides", Pittsburgh Chapter of ASM International, November 20, 1997, by T. Pollock.

26. "Processing and Properties of Cast Gamma Titanium Aluminides", Kyoto Workshop on High Temperature Intermetallics, Kyoto, Japan, May 12, 1998, by T. Pollock

27. "Microstructural Control in Gamma Titanium Aluminides", Gordon Conference on Physical Metallurgy, Plymouth, NH, June 1998, by T. Pollock.

28. "Impact Damage and the High Temperature Fatigue Behavior of γ-TiAl,", T. S. Harding, J.W. Jones, T.M. Pollock, M.P. Rubal and P.S. Steif, ASM/TMS Annual Meeting, Rosemont, IL, October 1998, T.S. Harding.

29. "Fatigue Life Prediction in Impact-damaged Gamma TiAl,", T. S. Harding, J.W. Jones, T.M. Pollock, M.P. Rubal and P.S. Steif, ASM/TMS Annual Meeting, Rosemont, IL, October 1998, by T.S. Harding.

30. "Application of Surface Displacement Mapping to Ductility Issues in Gamma-TiAl Based Alloys", N. Biery, M. De Graef, T.M. Pollock, TMS Fall Meeting, Indianapolis, IN, Sept. 15, 1997, by N. Biery

31. "The Effects of Postweld Heat Treatment on the Structure and Properties of EB and GTA Welded Ti-48Al-2Cr-2Nb", Presented at GE Aircraft Engines, Cincinnati, OH, February, 1998., by W. Baeslack.

32. "Postweld Heat Treatment of Electron Beam Welded Ti-48Al-2Nb-2Cr (at.%) Titanium Aluminide", 79th Annual AWS Convention, Detroit, MI, April 1998, by W. Baeslack.

33. "Microstructure Evolution during the Inertia Friction Welding and Postweld Heat Treatment of Cast Ti-48Al-2Nb-2Cr", 5th Conference on Trends in Welding Research, Pine Mountain, GE, June, 1998, by W. Baeslack.

34. "Postweld Heat Treatment Effects on Microstructure Evolution and Mechanical Properties of Electron Beam Welded Cast Ti-48Al-2Nb-2Cr", Third Pacific Rim International Conference on Advanced Materials and Processing, Honolulu, Hawaii, July, 1998, by W. Baeslack.

35. AFOSR PRET Review, Carnegie Mellon, Pittsburgh, PA, May 1998. This meeting was attended by all industrial participants, including most of the industrial in the previous section. Also in attendance were "additional collaborators" listed in the previous section, key personnel from Wright Labs and representatives from the UC-Berkeley URI. Presentations by all faculty and students.

36. "Processing and Properties of Cast Gamma Titanium Aluminides", Johns Hopkins University, Baltimore, MD, Oct. 21, 1998, (by T. Pollock).

37. "The Influence of Cooling Rate on Property Variability in Gamma Titanium Aluminides", Dec. 2nd, 1998, Materials Research Society, Boston, MA, (by T. Pollock).

38. "Tensile Ductility and Property Variability in Cast Gamma Titanium Aluminides", TMS Annual Meeting, San Diego, CA, March 2, 1999, (by T. Pollock).

39. "Gamma Titanium Aluminides as Structural Materials", Penn St. University, Sept. 13th, 1999, (T. Pollock, invited)

40. "Apparent Size Effects in Notched Titanium Aluminides Under Monotonic Loading," by J.L. Beuth, J.G. Milke and D.A. Knaul, presented at the MRS Fall Meeting, Boston, Nov. 30- Dec. 4, 1998 (by J. Beuth).

41. "Constraints of Ductility on Notched Component Design," by J.L. Beuth, D.A. Knaul and J.G. Milke, presented to representatives of Pratt and Whitney, Inc. at Carnegie Mellon University, December 17, 1998 (by J. Beuth).

42. "Notch Strengthening in Titanium Aluminides Under Monotonic Loading," by J.G. Milke and J.L. Beuth, presented at Wright-Patterson Air Force Base, Dayton, OH, July 22, 1999 (by J. Beuth).

43. "Induction Skull Melting of Titanium Aluminides", International Symposium on Liquid Metal Processing and Casting, February 23, 1999, (by L. Rishel).

44. "Vaporization Kinetics of Aluminum from Ti-48.9Al-2Cr-2Nb Melts in the Vacuum Induction Skull Remelting Process", Fall TMS Meeting, Rosemont, IL, October, 1998 (by L. Rishel).

45. "On the relation between cooling rate and solidification microstructure in as-cast titanium aluminides," M. De Graef, N. Biery, L. Rishel, T.M. Pollock, and A.W. Cramb, to appear in Proc. Gamma Titanium Aluminides Symposium, TMS Annual Conference 1999, by N. Biery.

46. "Study of localized strain at notches in gamma-TiAl alloys using displacement mapping and microstructural characterization," N. Biery, M. De Graef, and T.M. Pollock, to appear in Proc. Gamma Titanium Aluminides Symposium, TMS Annual Conference 1999, by N. Biery.

47. "Displacement mapping during in-situ straining in the SEM," N. Biery, T.M. Pollock, N.T. Nuhfer, and M. De Graef, Microscopy and Microanalysis, Vol. 5 (suppl. 2), 334-335, 1999, by N. Biery.

48. "Overview of Work in PRET Fatigue Program", T.S. Harding, J.W. Jones, *NASA Lewis Research Center*, Cleveland, OH, May 1999, by T. Harding.

49. "Influence of Impact Damage on the Elevated Temperature Fatigue Behavior of Gamma Titanium Aluminide Alloys," T.S. Harding, J.W. Jones, J.M. Larsen and P.S. Steif, *Second International Symposium on Gamma Titanium Aluminides, TMS Annual Meeting*, San Diego, CA, March 1999, by T. Harding.

50. "Impact Damage and the High Temperature Fatigue Behavior of γ-TiAl," T. S. Harding, J.W. Jones, T.M. Pollock, M.P. Rubal and P.S. Steif, *ASM/TMS Fall Meeting*, Rosemont, IL, October 1998, by T. Harding.

51. "Fatigue Life Prediction in Impact-damaged Gamma TiAl," T. S. Harding, J.W. Jones, T.M. Pollock, M.P. Rubal and P.S. Steif, *ASM/TMS Fall Meeting*, Rosemont, IL, October 1998, by T. Harding.

52. "Postweld Heat Treatment and Aluminum Content Effects on the Fusion Zone Microstructure and Mechanical Properties of Electron Beam Welded Ti-48Al-2Cr-2Nb", W. Baeslack, Chris Jensen, Han Zhang, and Tom Kelly, presented at 1999 TMS Annual Meeting, San Diego, by X. D. Zhang (substituted for W. Baeslack).

9.4 Inventions and Patent Disclosures

None

9.5 Honors and Awards

In the period of this contract, the following awards have been received:

Prof. Jack Beuth

> Best Presentation Award for the Talk ASTM 6th Symposium on Composites Fatigue and Fracture, May 16-17, 1995.

> Received the 1998 Ralph R. Teetor Educational Award from the Society of Automotive Engineers (SAE International). The award was presented at the 1998 SAE International Congress and Exposition, Detroit, Michigan, February 23-26, 1998.

Mr. Nick Biery

> Microscopy Society of America Presidential Fellowship, to attend the MSA meeting in Portland (August 1999).

Prof. Alan Cramb

> Benjamin Richard Teare Award for Excellence in Engineering Education Carnegie Mellon, 1995.

> Appointed to the Pohang Iron and Steel Company (POSCO) Professorship in the Department of Materials Science and Engineering at Carnegie Mellon University, 1997.

Prof. Marc De Graef

Poster Competition Award (Physical Sciences, 2nd prize) at
the 53rd Annual Meeting of the Microscopy Society of America,
Kansas City (August 1995)

Carnegie Mellon University G.T. Ladd Award for Excellence in Research
(October 1996)

R.E. Peterson Award for outstanding applications paper from the Society for
Experimental Mechanics (1998) for the following paper: Wissuchek D.J.,
Mackin T.J., De Graef M., Lucas G.E., and Evans A.G., "A simple
method for measuring surface strains around cracks," Journal of
Experimental Mechanics, **36**, pp. 173-179 (1996).

Mr. Trevor Harding

University of Michigan MSE Department Outstanding Graduate Student
Instructor Award

American Society for Engineering Education (Michigan Chapter)
Outstanding Graduate Student Instructor Award for the College of
Engineering

Best Paper Award, American Society for Engineering Education, Graduate Studies
Division, 1999 National ASEE Conference, Charlotte, NC, June 1999

Rackham Graduate School Pedagogical Award, 1999-2000

University of Michigan Rackham Predoctoral Fellowship, 1999-2000

American Society for Engineering Education Apprentice Faculty Grant, 1999

College of Engineering Distinguished Leadership Award, 1999

College of Engineering Distinguished Achievement Award, 1999

Dept. of Materials Science and Engineering Best Overall Teaching Assistant,
1998

Robert Cadell Memorial Achievement Award, 1998

Mr. Chris Jensen

     1st Place Award, Student Poster Competition, 78th Annual AWS Convention, Los Angeles, CA, April 1997. Poster Title: Postweld Heat Treatment Effects on the Structure and Properties of Gas Tungsten-Arc Welded Ti-48Al-2Cr-2Nb

Prof. Tresa Pollock

     ASM International Bradley Stoughton Educator Award, 1995.

     Appointed to the Alcoa Professorship in the Department of Materials Science and Engineering at CMU, 1997.

     Oustanding Materials Engineer Award, Purdue University, 1997.

     ASM International Research Silver Medal Award, 1999.

Prof. Paul Steif

     Carnegie Institute of Technology Philip L. Dowd Fellowship Award, 1997.